UNIVERSITY OF SOUTHAMPTON

FACULTY OF ENGINEERING AND PHYSICAL SCIENCES
School of Electronics and Computer Science

Numerical Modelling of Lightning Strikes to Wind Turbine Blades: Analysis of Equipotential Bonding for CFRP Spars

by

Antonio Andrea Maria Laudani

ORCID: 0000-0002-0423-5363

Thesis for the degree of Doctor of Philosophy

November 2021

UNIVERSITY OF SOUTHAMPTON

ABSTRACT

FACULTY OF ENGINEERING AND PHYSICAL SCIENCES

School of Electronics and Computer Science

Thesis for the degree of Doctor of Philosophy

Numerical Modelling of Lightning Strikes to Wind Turbine Blades: Analysis of Equipotential Bonding for CFRP Spars

Antonio Andrea Maria Laudani

Modern wind turbine blades are equipped with a lightning protection system to intercept the lightning and conduct its current, preventing the direct attachment to internal conductors. In such conditions, resin thermal degradation develops at the equipotential bonding (EB) connections between down conductors (DCs) and carbon fibre reinforced polymer (CFRP) spars. This problem was investigated in this work by combining experimental studies and finite element method (FEM) simulations.

The experimental work focused on the characterisation of the input material properties to be used in the FEM models. An experimental-numerical procedure was established to determine the electrical contact resistivity of EB joints. Besides, the thermal degradation of a commercial epoxy was studied to determine its reaction kinetics.

The developed FEM models solve a weakly coupled formulation of the electromagnetic-thermal problem to predict lightning current paths and thermal damage at the bonding interfaces. The validation of the models against conducted current test data showed that they can assist in the design of EB joints. High current densities and temperatures were predicted at the sparking

locations found during the test, which allowed a qualitative prediction of potential thermal degradation areas upon the solution of the Arrhenius equation. In addition, such models can be used to assess the potential risk of flashover between the blade conductors due to high electric fields.

Finally, typical EB materials were compared using the developed FEM models to provide guidelines and suggestions for the implementation of EB joints. It was seen that materials with high in-plane electrical conductivities, such as ECF and BIAX CFRP, can reduce the electric field below the insulation breakdown strength and prevent flashovers. Besides, hot spots at the bonding interfaces can be controlled by changing the arrangement of the EB layers, or by using a material with low contact resistivity and high thermal diffusivity like ECF.

Table of Contents

Table of Figures

Table of Tables

Research Thesis: Declaration of Authorship

Print Name:	Antonio Andrea Maria Laudani

Title of thesis:	Numerical Modelling of Lightning Strikes to Wind Turbine Blades: Analysis of Equipotential Bonding for CFRP Spars

I declare that this thesis and the work presented in it are my own and have been generated by me, as the result of my own original research.

I confirm that:

- This work was done wholly or mainly while in candidature for a research degree at this University.
- Where any part of this thesis has previously been submitted for a degree or any other qualification at this University or any other institution, this has clearly been stated.
- Where I have consulted the published work of others, this is always clearly attributed. Where I have quoted from the work of others, the source is

always given. Except for such consultations and quotations, this thesis is entirely my own work.

- I have acknowledged all main sources of help.
- Where the thesis is based on work done by myself jointly with others, I have exactly made clear what was done by others and what I have contributed myself.
- Parts of this work have been published as:

Journal Papers

1. A. A. M. Laudani, L. Carloni, O. T. Thomsen, P. L. Lewin, and I. O. Golosnoy, "Efficient Method for the Computation of Lightning Current Distributions in Wind Turbine Blades using the Fourier Transform and the Finite Element Method," *IET Sci. Meas. Technol.*, vol. 14, no. 7, pp. 786–799, 2020.
2. A. A. M. Laudani *et al.*, "Estimation of Contact Resistivity in Lightning Protection Equipotential Bonding Joints of Wind Turbine Blades," *IEEE Trans. Electromagn. Compat.*, vol. 63, no. 4, pp. 1163–1178, 2021.
3. O. Vryonis, A. A. M. Laudani, T. Andritsch, I. O. Golosnoy, and A. S. Vaughan, "Lightning Protection of Wind Turbine Blades — How Supersizing Has Created New Challenges for Nanodielectrics Research," *IEEE Electr. Insul. Mag.*, vol. 37, no. 6, pp. 6–20, 2021.
4. A. A. M. Laudani *et al.*, "Numerical Simulation of Lightning Strike Damage to Wind Turbine Blades and Validation against Conducted Current Test Data," *Compos. Part A Appl. Sci. Manuf.*, vol. 152, p. 106708, 2022.

Conference Papers

1. A. A. M. Laudani, I. O. Golosnoy, and O. T. Thomsen, "Numerical computation of lightning time-domain voltages using the Fourier analysis and the finite element method," in Tenth International Conference on Computational Electromagnetics, 2019, pp. 1–6.

2. A. A. M. Laudani, I. O. Golosnoy, O. T. Thomsen, and P. L. Lewin, “Novel numerical models for the simulation of the electromagnetic response of CFRP wind turbine spars subjected to lightning strikes,” in *International Conference on Lightning and Static Electricity*, 2019, pp. 1–9.
3. A. A. M. Laudani, I. O. Golosnoy, J. Kremer, E. C. Senis, O. T. Thomsen, and P. L. Lewin, “Experimental Characterisation of Contact Resistivity for CFRP Wind Turbine Spars Equipotential Bonding,” in *IEEE Holm Conference on Electrical Contacts*, 2019, pp. 278–285.

Signature:		Date:	

Acknowledgments

This project was funded by Nordex Energy GmbH and the University of Southampton, grant agreement 0179210, and by the EU Horizon 2020 Marie Sklodowska-Curie Actions – Innovative Training Networks (ITN), grant agreements 642771 (SPARCARB project) and 734629 (PATH project).

I would like to thank my supervisors, Dr Igor O. Golosnoy, Prof. Ole T. Thomsen, and Prof. Paul L. Lewin, for their invaluable expertise. I would particularly like to express my deepest gratitude to Igor, who has been more than a primary supervisor. Although on a few occasions he has been tough, but fair, he has always supported and guided me throughout the years of my PhD. Thanks for teaching me how to review and judge my own work critically, which is never easy.

Thanks go to Dr Hendrik Klein and Jochen Kremer from Nordex Energy GmbH. I would particularly like to single out Jochen for his guidance and insight on lightning protection aspects from an industrial point of view. In addition, I would like to acknowledge Thomas Theur, Nick Ohlerich, and Lars Pospischil for the technical support during the design and manufacturing of the samples assessed in this work.

I would like to thank my fellow PhD students of the SPARCARB project, Dr Orestis Vryonis, Dr Evangelos C. Senis, and Dr Timothy M. Harrel, for the excellent collaboration during the project. Special thanks to Orestis and Evangelos for being my closest friends in Southampton too.

Thanks also to Dr Thomas Andritsch for the viable discussion and feedback after my Second Progression Review.

Thanks to the Tony Davies High Voltage Laboratory, Neil Palmer, Brian Rodgers, Alan Welford, and Charlie Reed, for the technical support and for providing the necessary equipment.

I would like to thank Dexmet Corporation for providing the expanded copper foil material free of charge.

To my colleagues and friends, Maria Angelica, Alex, Christian, Franco, Nazareno, and Giannis. It has been a pleasure to meet you and share this path together.

Thanks to my family, my parents, my brothers, and my aunt, who have always encouraged me from home. Thanks also to Franco, Nuccia, Giulio, and Francesca for their support.

Special thanks go to my partner, Kryspina, who helped me finding the light in my life again. I will never be able to thank you enough for the gift you are going to give me in a month.

This work is dedicated to my parents. I would not be who I am without your teachings. You have always worked hard to allow me to achieve my goals and dreams.

Nomenclature

BDF	Backward differentiation formula
BIAX	Biaxial
BMI	Bismaleimide
C_DC-EB	Contact region between the down conductor and equipotential bonding layers
C_EB-Spar	Contact region between the equipotential bonding layers and spar
C_EB-P.Spar	Contact region between the EB layers and primary spar
C_EB-S.Spar	Contact region between the EB layers and secondary spar
CFRP	Carbon fibre reinforced polymer
DC	Down conductor
DFT	Discrete Fourier transform

EB	Equipotential bonding
ECF	Expanded copper foil
FEM	Finite element Method
FFT	Fast Fourier transform
GFRP	Glass fibre reinforced polymer
HV	High voltage
IDFT	Inverse discrete Fourier transform
IEC	International Electrotechnical Commission
IED	Infinite element domain
IR	Infrared
LE	Leading edge
LPS	Lightning protection system
PET	Polyethylene terephthalate
PS	Pressure side
PVC	Polyvinyl chloride
SS	Suction side
TE	Trailing edge
TGA	Thermogravimetric analysis
TLM	Transfer length method

UD	Unidirectional
VARTM	Vacuum assisted resin transfer moulding
$\boldsymbol{A}$	Magnetic vector potential [Wb/m]
A	Pre-exponential factor of the apparent single reaction [1/s]
$A_{C\_DC\text{-}EB}$	Contact surface between the DC and EB layers [m^2]
$A_{C\_EB\text{-}Spar}$	Contact surface between the EB layers and spar [m^2]
$A_{C\_DC\text{-}EB}^{Chamfer}$	Contact surface between the DC and EB layers for the chamfered samples [m^2]
A_i	Pre-exponential factor of the *i*-th degradation mechanism [1/s]
$\boldsymbol{B}$	Magnetic flux density [T]
C'	Capacitance per unit length [F/m]
C_p	Specific heat capacity at constant pressure [J/(kg·K)]
$\boldsymbol{E}$	Electric field strength [V/m]
E_a	Activation energy of the apparent single reaction [J/mol]
$E_{a,i}$	Activation energy of the *i*-th degradation mechanism [J/mol]
$E_{applied}$	Applied uniform electric field [V/m]

$E_{bd,unif}$	Breakdown strength in uniform electric field conditions [V/m]
$E_{bd\_non\text{-}unif}$	Breakdown strength in non-uniform electric field conditions [V/m]
$E_{bd\_non\text{-}unif,max}$	Maximum breakdown strength in non-uniform electric field conditions [V/m]
$E_{critical}$	Critical electric field [V/m]
E_i	Inception electric field [V/m]
E_{max}	Maximum electric field [V/m]
E_{mean}	Average electric field [V/m]
E_y	Transverse electric field [V/m]
$E_{y,max}$	Maximum transverse electric field [V/m]
F_s	Sampling frequency [Hz]
$\boldsymbol{H}$	Magnetic field strength [A/m]
I_0	Peak current [A]
$\widetilde{I_k}$	Frequency-domain k-th current complex coefficient [A]
I_k	Magnitude of the k-th current complex coefficient [A]
$Int_{DC\text{-}EB\_Exp}$	Experimental y-axis intercept of the DC-EB sample [Ω]
$Int^{Corr}_{DC\text{-}EB\_Exp}$	Experimental y-axis intercept of the DC-EB sample corrected from the contact resistance of the measuring electrodes [Ω]

$Int_{DC\text{-}EB\text{-}Spar\_Exp}$	Experimental y-axis intercept of the DC-EB-Spar sample [Ω]
$Int^{Corr}_{DC\text{-}EB\text{-}Spar\_Exp}$	Experimental y-axis intercept of the DC-EB-Spar sample corrected from the contact resistance of the measuring electrodes [Ω]
$Int_{DC\text{-}EB\_FEM}$	FEM y-axis intercept of the DC-EB sample [Ω]
$Int_{DC\text{-}EB\text{-}Spar\_FEM}$	FEM y-axis intercept of the DC-EB-Spar sample [Ω]
$\boldsymbol{J}$	Conduction current density [A/m^2]
L'	Self-inductance per unit length [H/m]
L_{BLADE}	Partial self-inductance of the blade [H]
L_{RP}	Partial self-inductance of the return path [H]
L_S	Sample length [m]
L_{TOT}	Total (loop) self-inductance of the system composed of the rotor blade and the return path [H]
LWD	Long way of the diamond [m]
M'	Mutual inductance per unit length [H/m]
$M_{BLADE\text{-}RP}$	Mutual inductance between the blade and return path [H]
N	Number of samples
Q_{LONG}	Charge transferred by lightning long strokes [C]
Q_{rh}	Joule heat [W/m^3]

Q_{SHORT}	Charge transferred by lightning short strokes [C]
R	Molar gas constant [J/(mol·K)]
R'	Resistance per unit length [Ω/m]
$R_{C\_DC\text{-}EB}$	Contact resistance between the DC and EB layers [Ω]
$R_{C\_DC\text{-}EB}^{Chamfer}$	Contact resistance between the DC and EB layers for the chamfered samples [Ω]
$R_{C\_EB\text{-}Spar}$	Contact resistance between the EB layers and spar [Ω]
$R_{C\_Electrodes}$	Contact resistance of the measuring electrodes [Ω]
R_{DC}	Resistance of the DC [Ω]
$R_{DC\text{-}EB\_Tot}$	Total resistance of the DC-EB sample [Ω]
$R_{DC\text{-}EB\text{-}Spar\_Tot}$	Total resistance of the DC-EB-Spar sample [Ω]
R_{EB1}	Resistance of the EB layer at the top of the DC [Ω]
R_{EB2}	Resistance of the EB layer at the bottom of the DC [Ω]
R_{EB3}	Resistance of the horizontal EB layer [Ω]
R_{EB4}	Resistance of the EB layer on the side of the spar [Ω]
R_{EB5}	Resistance of the EB layer at the bottom of the spar [Ω]
R_{EB6}	Resistance of the EB layer at the top of the spar [Ω]
R_{Spar}	Resistance of the spar [Ω]

R_{Tot}	Total resistance of the system depicted in Figure 3.5*a* [Ω]
SWD	Short way of the diamond [m]
T	Temperature [K]
T_a	Temperature of the apparent single reaction [K]
T_{ext}	Ambient temperature [K]
Th_{EB}	EB thickness [m]
T_i	Temperature of the *i*-th degradation mechanism [K]
T_m	Temperature at maximum degradation rate [K]
T_{onset}	Degradation onset temperature [K]
V	Electric scalar potential [V]
V_{bd}	Breakdown voltage [V]
V_i	Inception voltage of partial discharges [V]
$\widetilde{V_k}$	Frequency-domain k-th voltage complex coefficient [V]
V_k	Magnitude of the k-th voltage complex coefficient [V]
W/R	Specific energy [J/Ω]
d	Distance [m]
$\frac{\mathrm{d}i}{\mathrm{d}t}$	Rate of rise of current [A/s]
$\frac{\mathrm{d}\alpha}{\mathrm{d}t}$	Degradation rate or reaction rate [1/s]

$\frac{d\Gamma}{dt}$	First time derivative of the mass fraction of the polymer [%/s]
$\frac{d^2\Gamma}{dt^2}$	Second time derivative of the mass fraction of the polymer [%/s^2]
$\frac{d^3\Gamma}{dt^3}$	Third time derivative of the mass fraction of the polymer [%/s^3]
f_k	Frequency points [Hz]
h	Heat transfer coefficient [W/(m^2·K)]
i_m	Time-domain m-th current sample [A]
$i(t)$	Instantaneous current [A]
j	Square root of −1
$\boldsymbol{k}$	Thermal conductivity tensor [W/(m·K)]
k	Frequency index (bin number)
k_0	Correction factor for the peak current
k_{11}	Longitudinal thermal conductivity [W/(m·K)]
k_{22}	Transverse thermal conductivity [W/(m·K)]
k_{33}	Through-thickness thermal conductivity [W/(m·K)]
m	Time sampling index
$m_p(t_0)$	Initial polymer mass [kg]

$m_{p,i}(t)$	Instantaneous polymer mass of the i-th degradation mechanism [kg]
$m_{p,i}(t_\infty)$	Final polymer mass of the *i*-th degradation mechanism [kg]
$\boldsymbol{n}$	Outward normal
n	Reaction order
$\boldsymbol{q}_{cond}$	Heat flux by conduction [W/m^2]
$\boldsymbol{q}_{conv}$	Convective heat flux [W/m^2]
$\boldsymbol{q}_{rad}$	Radiative heat flux [W/m^2]
t	Time [s]
t_1	Rise time coefficient [s]
t_2	Decay time coefficient [s]
$t_{Flex\ 1}$	Time at the first inflection point [s]
$t_{Flex\ 2}$	Time at the second inflection point [s]
t_m	Discrete time variable [s]
t_{offset}	Heidler function offset time [s]
t_s	Observation time [s]
t_{step}	Sampling interval (time step) [s]
$v(t_m)$	Time-domain voltage [V]
Γ	Mass fraction of the polymer [%]

ΔV	Potential difference [V]
Δx	Sample thickness for thermal conductivity measurements [m]
$\alpha(t)$	Degree of thermal degradation of the apparent single reaction
$\alpha_i(t)$	Degree of thermal degradation of the *i*-th degradation mechanism
β	Heating rate [K/s]
γ	Chamfer angle [°]
ε	Emissivity
ε_0	Vacuum permittivity
ε_r	Relative permittivity
η	Field utilization factor
μ_0	Vacuum permeability [H/m]
μ_r	Relative permeability
ρ	Density [Kg/m^3]
ρ_C	Electrical contact resistivity [$\Omega \cdot m^2$]
$\rho_{C\_DC\text{-}EB}$	Contact resistivity between the DC and EB layers [$\Omega \cdot m^2$]
$\rho_{C\_EB\text{-}Spar}$	Contact resistivity between the EB layers and spar [$\Omega \cdot m^2$]

$\rho_{C\_EB\text{-}P.Spar}$	Contact resistivity between the EB layers and primary spar, no chamfer [$\Omega \cdot m^2$]
$\rho_{C\_EB\text{-}P.Spar\_Chamfer\ a}$	Contact resistivity between the EB layers and primary spar, chamfer a [$\Omega \cdot m^2$]
$\rho_{C\_EB\text{-}P.Spar\_Chamfer\ b}$	Contact resistivity between the EB layers and primary spar, chamfer b [$\Omega \cdot m^2$]
$\rho_{C\_EB\text{-}P.Spar\_Chamfer\ c}$	Contact resistivity between the EB layers and primary spar, chamfer c [$\Omega \cdot m^2$]
$\rho_{C\_EB\text{-}S.Spar}$	Contact resistivity between the EB layers and secondary spar, no chamfer [$\Omega \cdot m^2$]
$\rho_{C\_EB\text{-}S.Spar\_Chamfers\ d,\ e,\ g}$	Contact resistivity between the EB layers and secondary spar, chamfers d, e, g [$\Omega \cdot m^2$]
$\rho_{C\_EB\text{-}S.Spar\_Chamfer\ f}$	Contact resistivity between the EB layers and secondary spar, chamfer f [$\Omega \cdot m^2$]
$\rho\ C_p \frac{\partial T}{\partial t}$	Time derivative of the internal energy per unit volume [W/m^3]
$\boldsymbol{\sigma}$	Electrical conductivity tensor [S/m]
σ_{11}	Longitudinal electrical conductivity [S/m]
σ_{22}	Transverse electrical conductivity [S/m]
σ_{33}	Through-thickness electrical conductivity [S/m]
σ_{SB}	Stefan-Boltzmann constant [$W/(m^2 \cdot K^4)$]
τ_1	Front duration [s]

τ_2	Time to half value [s]
τ_{LONG}	Duration of long strokes [s]
$\varphi_{I,k}$	Argument of the k-th current complex coefficient [rad]
$\varphi_{V,k}$	Argument of the k-th voltage complex coefficient [rad]
ω	Angular frequency [rad/s]
∇	Gradient operator
$\nabla\bullet$	Divergence operator
∇x	Curl operator

Chapter 1
Introduction

1.1 Overview

Over the last two decades, the electrical energy developed by the wind energy sector has experienced a significant increment from 23,900 to ~650,000 MW (see Figure 1.1). This growth is not only due to an increase in wind farm installations but also to a larger power capacity generated by each wind turbine, which can arrive up to 14 MW [1]. The increasing demand for higher rated power outputs led to larger wind turbines, which can reach up to 220 m in rotor diameter and 250 m in overall height in the case of GE Haliade-X [1]. In such a scenario, wind turbines become particularly sensitive to lightning strikes, with rotor blades as a component with the highest likelihood of being struck and damaged by lightning (see Figure 1.2). Considering that rotor blades account for 15-20% of the total wind turbine cost [2], [3], and that each year ~6% of the worldwide wind turbines report lightning damage to rotor blades [4], the losses incurred by wind farms owners may become significant [5]–[8]. For instance, it was shown that for 1.5-6 MW wind turbines, the average cost to repair a damaged blade is 12,000-15,000 €, i.e., 2-4% of the annual maintenance cost. Furthermore, this amount needs to be summed to the revenue loss caused by

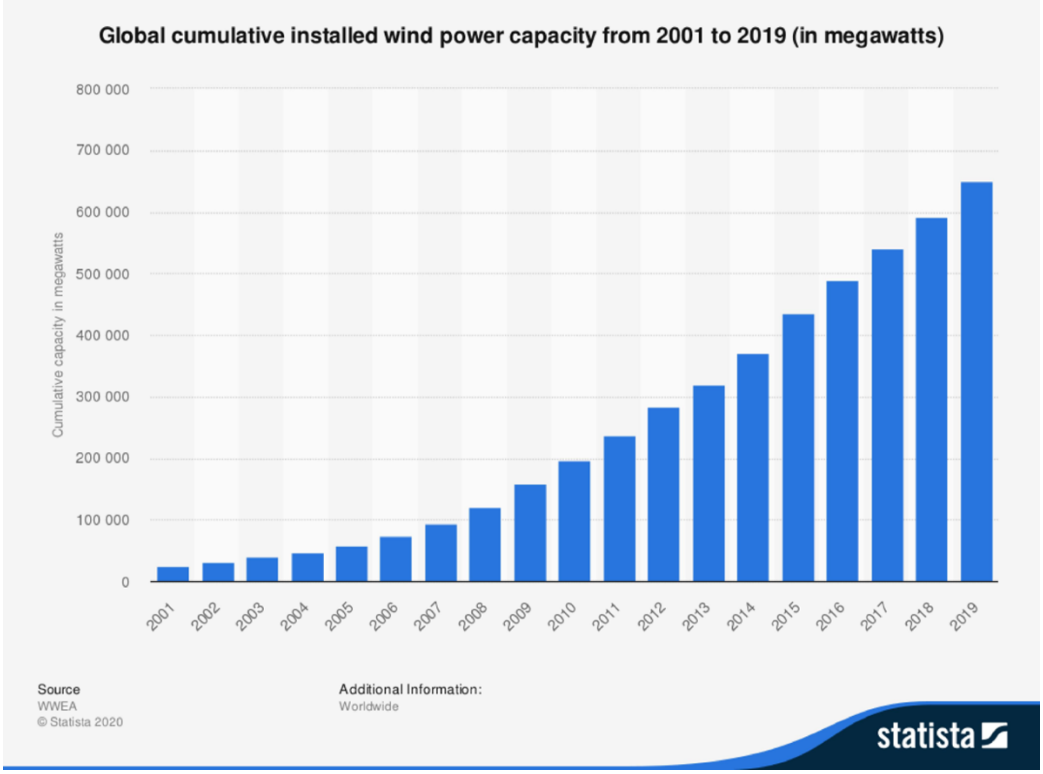

Figure 1.1 – Global cumulative wind capacity [9].

Figure 1.2 – Wind turbine damaged by a lightning strike [10].

the downtime, in which the wind turbine is not operative and productive. On the one hand, the average downtime for an onshore wind turbine is around 30 hours, but it can reach up to 10 days for the most critical damages. On the other hand, downtime periods longer than two weeks can be required for offshore wind

turbines. In fact, special transportation equipment needs to be employed to access the remote location, as well as repair operations are carried out with suitable weather conditions only. Indicatively, the downtime loss ranges from 0.06 to 0.11% of the yearly revenue [11].

Wind turbine blades are equipped with a lightning protection system (LPS) to avoid lightning damage. It is composed of metal receptors placed over the blade surface near the tip, and metal down conductor (DC) cables or braids located within the blade. The former are aimed to intercept the lightning leaders in such a way as to avoid the direct attachment to internal conductors. The latter are intended to conduct the lightning current from the attachment point to the grounding system [12].

1.2 Research Motivation

With rotor blades exceeding 100 m in length [1], it has become essential to reduce their weight without affecting the structural integrity. For this reason, carbon fibre reinforced polymer (CFRP) materials have been introduced in the rotor blade structure, which ensure high specific strength and stiffness [13]–[16]. They are mainly employed for the manufacturing of spar caps (see Figure 1.3), which support bending loads due to the wind pressure. CFRP spars allow a weight reduction of 25-30% compared with more traditional glass fibre reinforced polymer (GFRP) ones, although the total blade cost increases by up to 25% [3], [17].

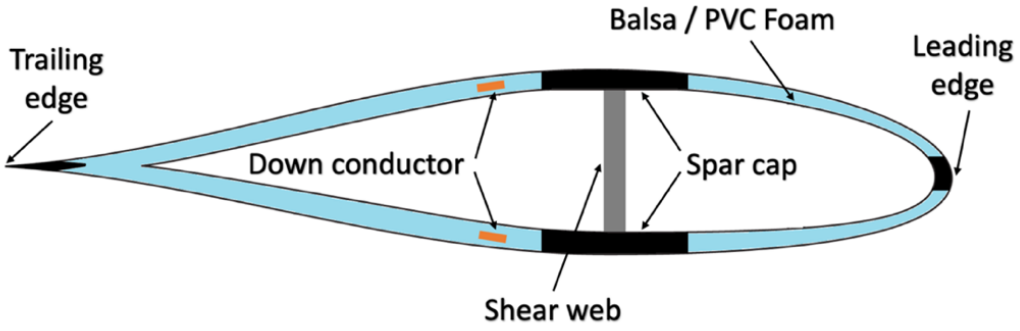

Figure 1.3 – Typical wind turbine blade cross-section [14].

The incorporation of CFRPs introduces additional challenges for the protection of the blade against lightning strikes [5], [18]–[23]. In fact, despite the low electrical conductivity (between 3 and 5 orders of magnitude lower than metals), such materials can be subjected to direct lightning attachment, which causes shell puncturing and severe structural damage [24]. Although multi-receptor LPS solutions can prevent direct attachment to the CFRP components, rotor blades can still experience severe structural damage via high voltage (HV) breakdown of the blade insulating material. Internal flashovers are induced by a high electric field between the DC and a floating conducting element such as the CFRP spar [12], [25], [26]. A solution to prevent internal arcs would be to bond electrically the DC to the spar such that to split the lightning current between the two elements and obtain the same electric potential. However, the conduction of lightning current through the CFRP spar might result in overheating and thermal damage because of the following two reasons. The first one is the large electrical contact resistance observed at the equipotential bonding (EB) connections between the DC and spar. Such interface resistances generate elevated temperatures at the jointed surfaces, which lead to the thermal degradation of some of the resin used for the bonding. The produced gas filled voids separate the rotor blade conductors carrying the lightning current and trigger sparks (see Figure 1.4) once the contact is open [27], [28]. The second one is the spreading resistance of the spar due to the strong anisotropic nature of CFRP materials (up to 4 orders of magnitude variation between longitudinal and through-thickness electrical conductivities). In fact, non-uniform current density distributions can be experienced by the spar if the current is not injected adequately, which lead to the overheating of the spar surface layers [29]. In order to reduce the spreading effect, recent studies have presented different methods to improve the bulk properties of CFRP materials in the transverse and through-thickness directions [30]–[35], e.g., by the dispersion of conducting nanofillers within the matrix [36]–[39]. Thus, it is essential to minimise both contact and spreading effects to prevent thermal damage. This is done by a correct arrangement, dimensioning, and material choice of EB connections.

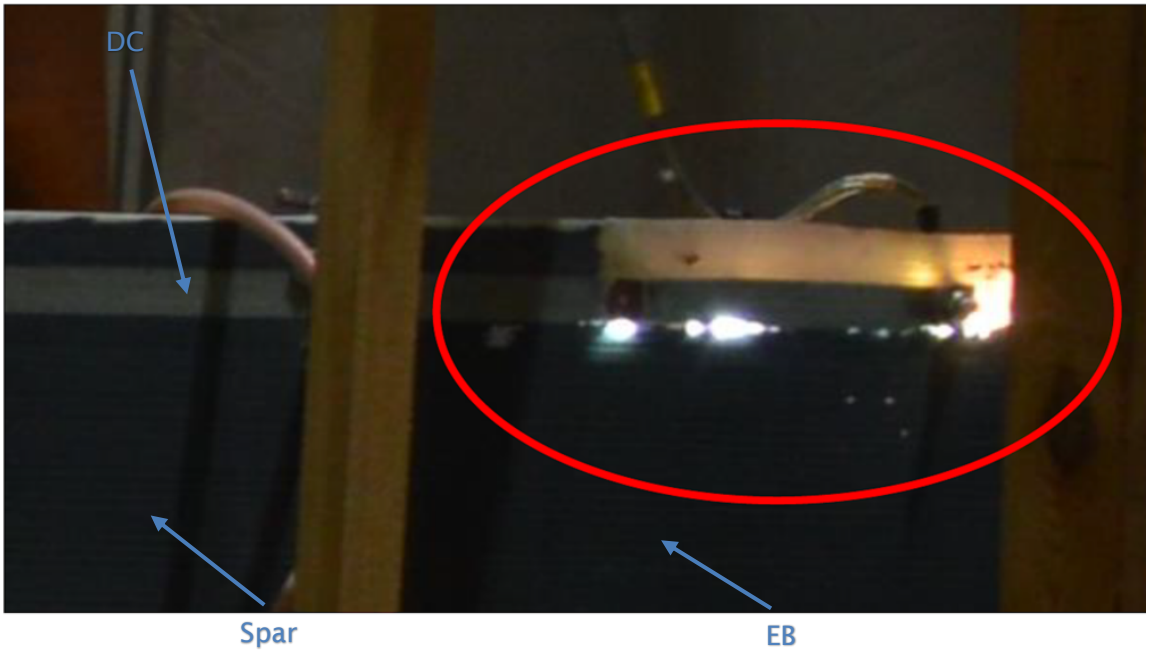

Figure 1.4 – Sparks (circled in red) occurring at the EB region.

Although previous publications [12], [40]–[43] have pointed out the need of EB connections between the DC and spar, no work has so far investigated the damage at the EB interfaces and how to design such connections to avoid it. For this reason, two key questions on the design of wind turbine blade EB connections have remained unanswered for more than a decade: (1) can CFRP spars and EB joints withstand lightning currents without experiencing thermal damage? (2) how should equipotential connections be designed? [18].

1.3 Research Aim and Objectives

The aim of this PhD project is to investigate the response under lightning strikes of wind turbine blades equipped with EB connections. A combination of experimental studies and numerical simulations is carried out to accomplish the following objectives:

- To determine the causes and mechanisms of resin thermal degradation in rotor blade EB joints and propose techniques to quantify the triggering factors of this process.

- To develop finite element method (FEM) models capable of assisting in the design of EB connections by predicting voltage, current, and temperature distributions along the blade.
- To explore, through the developed numerical models, different EB concepts and materials to provide suggestions and guidelines for the implementation of such complex joints.

1.4 Thesis Contribution to the Research Field

This thesis makes significant contributions to the field of lightning protection of wind turbine blades by the following achievements:

- It presents an experimental procedure capable of estimating the electrical contact of EB joints. In addition, it investigates the mechanisms responsible for resin thermal degradation and sparks in EB joints and their reaction kinetics. Both electrical contact and thermal degradation can be modelled in FEM simulations to develop more reliable EB solutions.
- It studies the response of wind turbine blades under lightning strikes by 3D, time-domain FEM simulations. The advantage of the FEM over other approaches, such as equivalent circuits using the lumped-element model, is the capability of computing spatial current density distributions in the rotor blade cross-section. This would allow the identification of high current density and temperature areas at the EB interfaces, which might lead to resin thermal degradation and sparks. Besides, numerical modelling would allow to reduce the testing cost, which can be in excess of 100,000 €/test including material and manufacturing of testing samples. Once validated, the models can be re-employed several times during the design stage at little extra cost [12], [43], [44]. Finally, such models can be customised to predict the response under lightning strikes of other systems, such as wind turbine nacelle and hub components or aerospace composite joints.

- It provides guidelines and suggestions on the design of equipotential connections by the procedures and models outlined in the previous two points, to answer the two open questions of this research topic. That is, whether CFRP spars and EB joints can withstand lightning currents without experiencing thermal damage and how to design equipotential connections.

1.5 Thesis Outline

This PhD thesis is structured as follows.

Chapter 2 revises the state of the art for the field of lightning protection of wind turbine blades. The core of this review is dedicated to the numerical methodologies, and the required input material properties, for the simulation of lightning strikes to rotor blades.

Chapter 3 is aimed to characterise the electrical contact resistivity of wind turbine blade EB joints. Such values need to be implemented in the FEM models to predict accurate current density and temperature distributions and investigate the thermal damage experienced at the bonding interfaces.

Chapter 4 investigates the thermal degradation process of a commercial epoxy resin, to determine the degradation mechanisms responsible for voids formation and sparks in EB joints and their reaction kinetics.

Chapter 5 presents the numerical methodologies developed in this research project to simulate lightning strikes to wind turbine blades. A procedure is proposed to inject the lightning current by imposing a voltage boundary condition. The latter improves the convergence of the solution, reducing the computational time.

Chapter 6 is meant to assess whether the developed numerical methodologies can replicate the reality and thus assist in the design phase of EB systems. To

do so, the current and temperature distributions predicted by the FEM models are compared against conducted current test data performed according to the international electrotechnical commission (IEC) 61400-24:2019 standard procedures.

Chapter 7 investigates, by the developed FEM models, the electromagnetic-thermal response of a 50 m rotor blade under different lightning impulses, to propose guidelines and suggestions for the implementation of EB connections. The blade is first subjected to the subsequent short stroke current to predict the electric field distribution and verify the potential occurrence of internal flashovers between the DC and spar. Then, the blade is subjected to the first positive short stroke current to investigate the high-current performance of different EB concepts.

In the final chapter, conclusions are drawn to summarise the main points and finding of this thesis, as well as potential future investigations are briefly discussed.

Chapter 2

Literature Review

This chapter reviews the engineering challenges related to lightning protection of wind turbine blades and the previous attempts to solve them, in order to place this research within the context of existing literature. To this end, the first half introduces the foundations of the problem, such as fundamentals on wind turbine blades (components, materials, and manufacturing), lightning damage to rotor blades, and the protection system and practises to prevent damage. After that, the core of the review is focused on the numerical methodologies used in past studies to investigate lightning strikes to rotor blades. In addition, an overview is given on the input material properties required to simulate these phenomena and the procedures to characterise them. Finally, the chapter is concluded by reviewing the different lightning impulses used for the design of wind turbine blade LPSs and the IEC 61400-24:2019 standard lightning current.

2.1 Wind Turbine Blades: Components, Materials, and Manufacturing

Rotor blades are the wind turbine components aimed to convert the wind energy into shaft torque. As depicted in Figure 2.1, they comprise two aerodynamic shells, i.e., the pressure side (PS) and the suction side (SS), bonded together at

both leading edge (LE) and trailing edge (TE). The shells are reinforced by primary and secondary spars, which are the structural components aimed to support the operating loads [13]–[16].

The main loads (see Figure 2.2) that drive the structural design of a wind turbine are [13], [14], [16]:

- Wind pressure loads, which produce flapwise and edgewise bending.
- Gravitational loads, which generate edgewise bending.
- Torsional loads, which are created by the flapwise and edgewise bending that are not applied at the shear centre of the blade.

The most employed manufacturing route of wind turbine blades is vacuum assisted resin transfer moulding (VARTM) or variations of this process. It requires to place fabric layers of dry fibres (aligned along the blade length direction) into a mould. As the blade is thicker at the root but becomes progressively thinner towards the tip, not all the fabric layers run for the entire blade length. The fabrics are then covered and sealed by a vacuum bag and low-viscosity resin is infused under vacuum. Finally, after the infusion process is completed, the resin is cured at 70-80 °C [13]–[16]. An alternative method to the standard VARTM process has been adapted from the aircraft industry and is based on prepreg technology. It consists of fibres pre-impregnated with resin which bonds them together. This process results in superior and less variable material properties than VARTM, but it is more expensive [13]–[16].

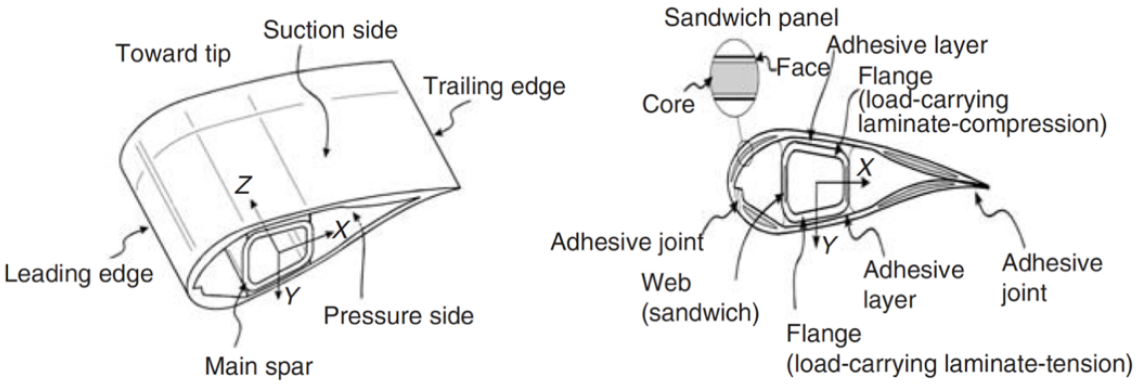

Figure 2.1 – Design details and components of a typical wind turbine blade section [13].

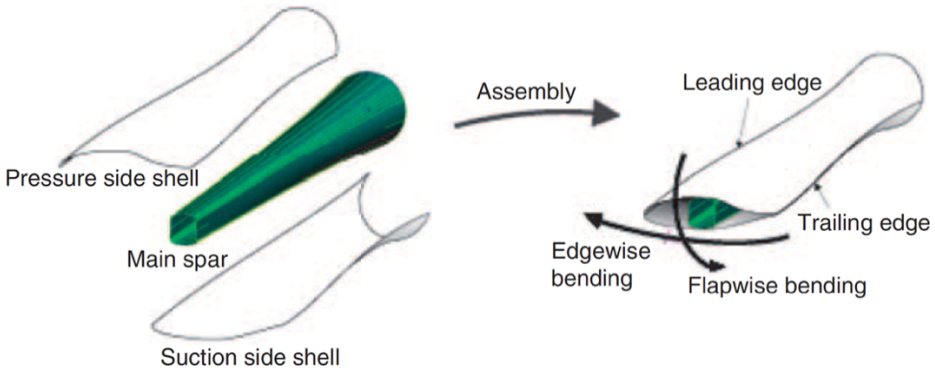

Figure 2.2 – Principal loads acting on a wind turbine blade [13].

The primary functions, materials, and manufacturing routes of each rotor blade component are outlined in the following subsections.

2.1.1 Primary Spar

There are two main configurations of primary spar [13]–[16]: the main spar (box spar) configuration, composed of two main spar flanges and two main spar webs (see Figure 2.3*a*); and the I-beam configuration, which consists of two spar caps integrated (encapsulated) into the GFRP shells and either one or two shear webs (see Figure 2.3*b*).

The primary function of the spar caps (or the main spar flanges in the box spar configuration) is to support the flapwise bending moments. For this reason, it presents unidirectional (UD) reinforcement fibres aligned along the blade longitudinal direction. In addition, biaxial (BIAX) CFRP layers ($\pm 45^{\circ}$ orientation with respect to the blade longitudinal direction) might be utilised to improve the buckling resistance [13]–[16]. Typically, for blades shorter than 40 m the spar caps are made of GFRP materials, while longer blades are manufactured from CFRP or from hybrid CFRP/GFRP materials. CFRP materials are preferred over GFRPs as they allow 25-30% weight reduction and thus a higher blade efficiency, although they increase the total cost of the blade by up to 25% [3], [17]. The main manufacturing processes of the spar caps are resin infusion, pultrusion, or prepreg technology, and can be either encapsulated within or bonded through

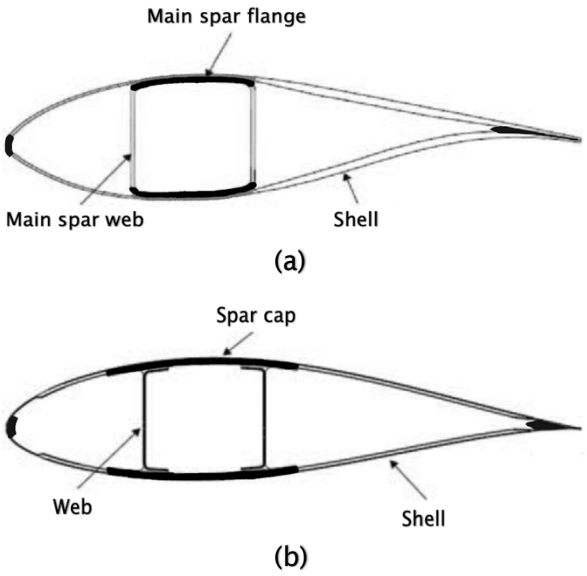

Figure 2.3 – Different rotor blade concepts [13]**:** (a) design with main spar (box spar) and (b) design with spar caps and shear webs.

structural adhesives to the shells [13]–[16]. On the other hand, the shear webs (or the main spar webs in the box spar configuration) withstand the flapwise shear loads. They are sandwich structures typically composed of two BIAX GFRP layers and a polymeric or balsa wood core [13]–[16].

2.1.2 Secondary Spar

Secondary spars are usually positioned on the TE side and, alike primary spars, they are composed of spar caps to support the flapwise bending moments and shear webs to withstand the flapwise shear loads. Secondary spar caps are typically manufactured out of CFRP, hybrid CFRP/GFRP, or GFRP materials, whereas secondary shear webs are sandwich structures [13], [45].

2.1.3 Reinforcements

Reinforcement components are located at both LE and TE where the two shells are bonded together, and they are made of either CFRPs or GFRPs. Their principal function is to carry the edgewise bending moments and shear loads [13], [45].

2.1.4 Shell

The purpose of the shells is to provide the aerodynamic aerofoil shape that converts the wind flow pressure into aerodynamic forces responsible for the rotation of the blades [13]–[16]. In addition, the shells also transfer the edgewise shear loads from the primary spar to the secondary spar [45]. Figure 2.4 shows that the shells are sandwich structures composed of a core material encapsulated within two layers of GFRP. Typically, the core material can be balsa wood, polyvinyl chloride (PVC) foam, polyethylene terephthalate (PET) foam, bismaleimide (BMI) foam, or a combination of them [13]–[16], [46].

Rotor blades are the most expensive components of the wind turbine since they are made of polymer matrix composite materials. Although market costs of rotor

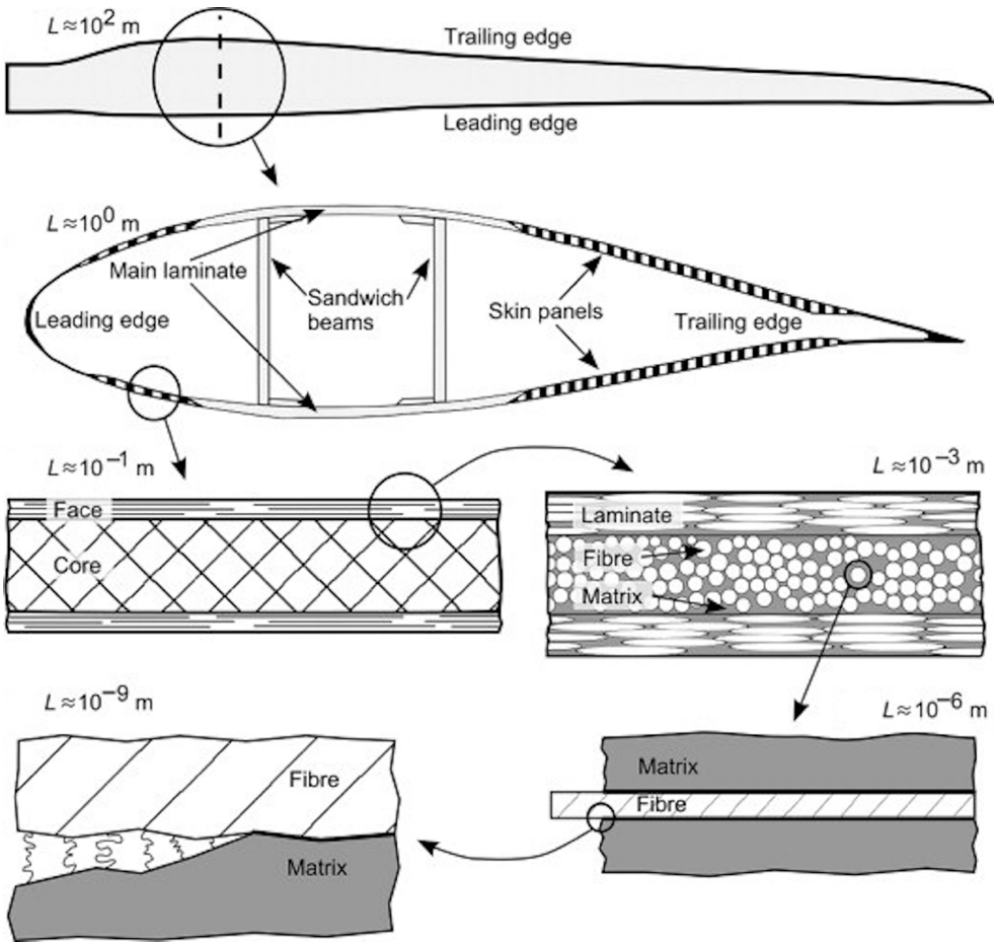

Figure 2.4 – Detailed view of the blade shells [15].

blade materials are not easily accessible, some studies attempted to predict and compare the cost of different rotor blade solutions. For instance, [47]–[49] compared the costs of several manufacturing processes, such as hand lay-up, vacuum infusion, and prepreg. [50] estimated the costs of both thermoplastic and thermoset blades, while the costs of CFRP and GFRP spar caps were analysed in [3]. Of particular interest is the study conducted by Griffith and Johanns [51], as it presented the manufacturing cost of the entire blade, including the shells, core material, primary spars, and secondary spars. Blade lengths between 40 and 100 m were considered, and the following costs were taken into account: materials; capital equipment; and labour (see Table 2.1).

2.2 Lightning Direct Attachment to Wind Turbine Blades

During thunderstorms, tall structures such as wind turbines experience a significant electric field enhancement which leads to streamers formation from all the conductive elements of the blade, such as electronic wires and CFRP spars [52]. In addition, streamers might also develop from the insulating blade shells because of the deposition of charged rain droplets [53]. Streamers tend to propagate more easily along the inner and outer surfaces of the blade shell (see Figure 2.5*a*) where a smaller electric field is required [54]–[57], rather than through the air, especially if the surfaces are wet and polluted [12]. When the ambient electric field is sufficiently high, the streamer may develop into either an answering leader (downward lightning) or an upward leader (upward lightning), intercepting the lightning leader. This causes a direct puncture of the lightning to the blade shell (see Figure 2.5*b*) and severe structural damage [40].

Table 2.1 – Blade Cost breakdown of a GFRP spar cap blade and a CFRP spar cap blade [51].

Overall blade cost	40 m all GFRP blade	100 m all GFRP blade	100 m CFRP spar blade
Materials	52.0%	72.0%	75.0%
Capital equipment	41.0%	13.5%	12.0%
Labour	7.0%	14.5%	13.0%
TOTAL COST [$]	57,843	631,793	704,692

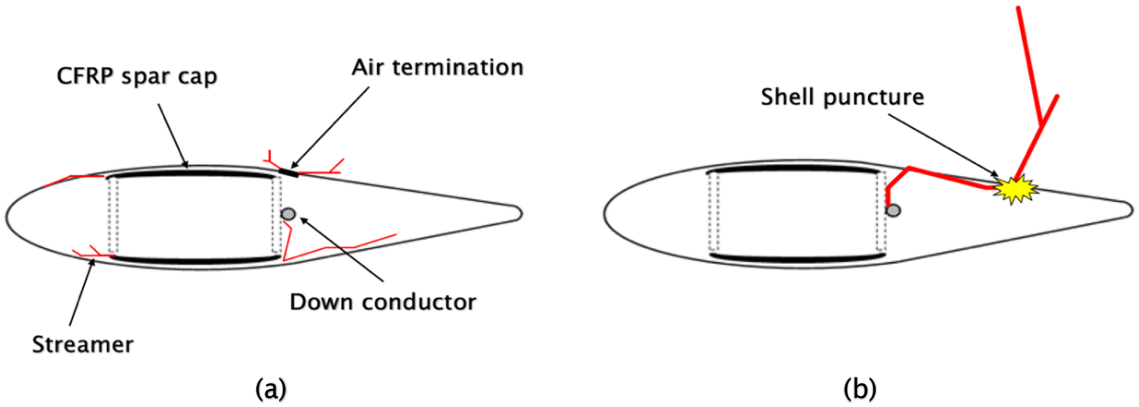

Figure 2.5 – Direct attachment mechanism [22]: (a) streamers propagation from blade conductive components and (b) shell puncture.

A study carried out in the USA [22] analysed the lightning strike incidence on wind turbine blades, i.e., which part is more sensitive to lightning shell puncturing. It was found out that 60% of the damage was located at the last meter of the blade, whilst 90% of the damage was localised within the last 4 m of the blade (see Figure 2.6). The following damage modes were observed in [22]:

- Delamination, when the shell plies separate from one another due to the large heating generation at the striking point (see Figure 2.7). It is the most common damage mode and can occur in any location of the blade.
- Debonding, which is the localised detachment of the two shell halves (see Figure 2.8). It usually occurs at the tip, at the LE, and at the TE, while the lightning strike point is usually located within the last six meters of the blade.
- Shell detachment, i.e., the total separation of the two shell halves for several meters (see Figure 2.9). It is usually preceded by debonding, which then evolves into shell detachment because of the blade rotation and of the large force applied by the wind during a thunderstorm. This damage mode is very rare, and the lightning strike point is located at the last meter of the blade.

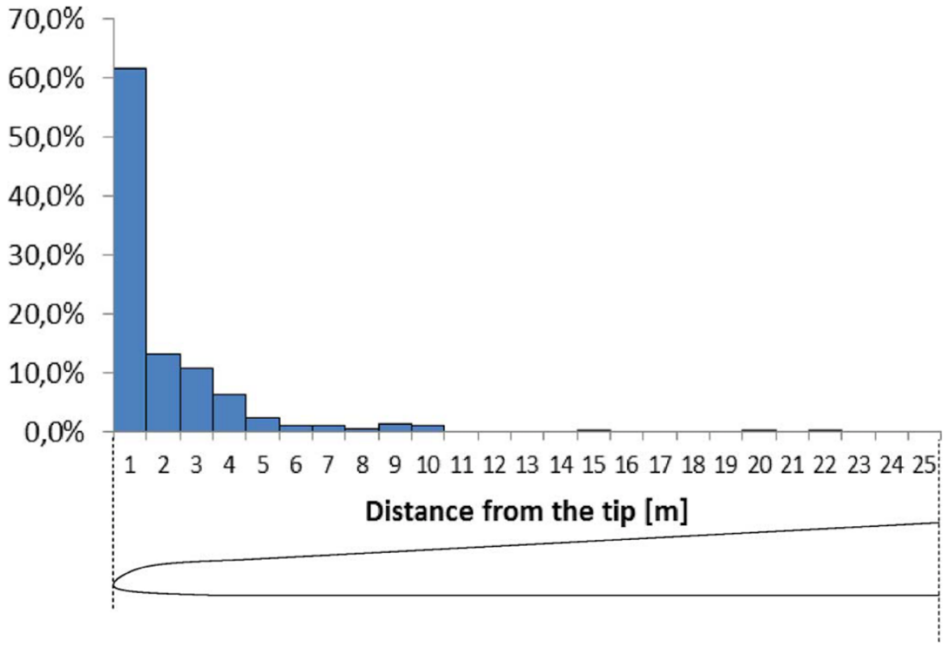

Figure 2.6 – Lightning strike incidence along the length of the blade [22].

Figure 2.7 – Delamination of the shell plies [22].

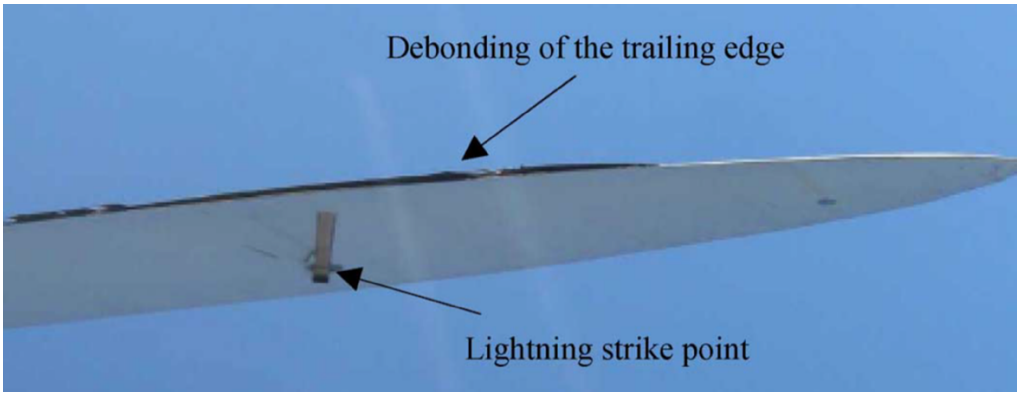

Figure 2.8 – Debonding of the two shell halves [22].

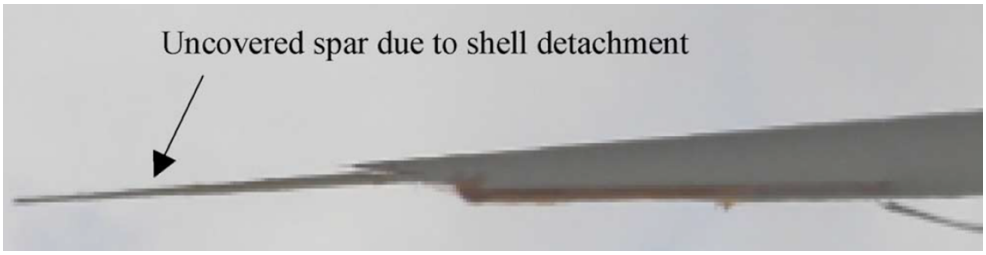

Figure 2.9 – Shell detachment [22].

Once the lightning punctures the blade shell, its current flows through the component that has initiated either the answering leader or the upward leader. If the conductive component is the CFRP spar, then severe structural damage may occur, such as matrix pyrolysis, matrix cracks, delamination, and carbon fibre and matrix pyrolysis residue sublimation [58].

2.3 LPSs of Wind Turbine Blades

In order to avoid the lightning direct attachment to the blade shell and the consequent damage described in the previous section, modern rotor blades are equipped with an LPS. It is composed of three parts: the air termination system, which intercepts the lightning leader; the transmission system, i.e., the DC, which conducts the lightning current from the attachment point to the blade root; and the EB system, which prevents flashovers between the blade conductors. As depicted in Figure 2.10, different LPS solutions have been implemented over the years by the main wind turbine blade manufacturers. Configuration A is used on blades equipped with a tip brake system. The lightning attaches at the air termination system, and its current is conducted by a steel wire controlling the tip brake, which acts as a DC. Configuration B is the most employed one, which is composed of an air termination system and a dedicated transmission system. Configuration C is a variant of solution B as it presents two DCs, one located at the LE and one at the TE. Finally, configuration D is mainly employed in the aerospace sector and has been extended to rotor blades. It requires the use of metal meshes placed over the blade surface, which act as both air termination system and transmission system [12].

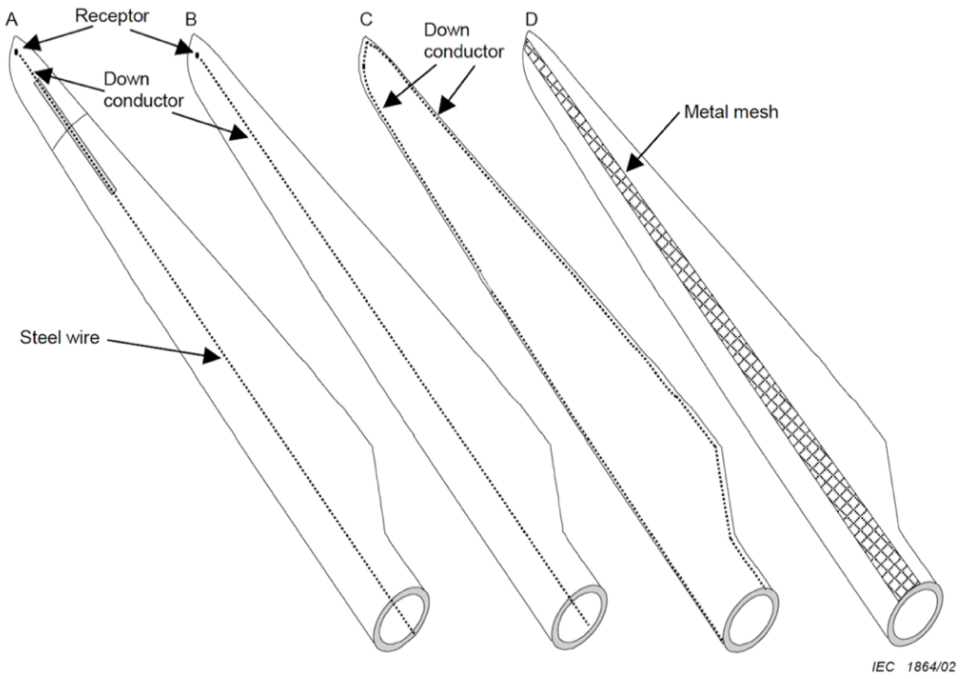

Figure 2.10 – Different LPS configurations. Configuration A employs the tip brake steel wire as a DC. Configuration B presents a dedicated DC cable or braid. Configuration C has two dedicated DC cables or braids, one located at the LE and one at the TE. Configuration D uses a metal mesh placed over the blade surface [12].

2.3.1 Air Termination System

The aim of the air termination system is to enhance the electric field and either to emit answering leaders that intercept the downward-approaching lightning leaders or to trigger upward lightning leaders. It is composed of one or more receptors, which can be either metal tips (see Figure 2.11*a*) or metal disks/screws (see Figure 2.11*b*). Receptors are mounted on the blade tip since this is the area with the highest probability of being struck by a lightning [8], [59]–[61], as seen in Section 2.2. In addition, the air termination system capturing efficiency also depends on the size and number of receptors, as investigated in [53], [62]–[65]. The IEC 61400-24:2019 standard [12] reports the procedures for a correct design of the air termination system, such as materials, nominal cross-section areas, geometries, implementation, and maintenance. For

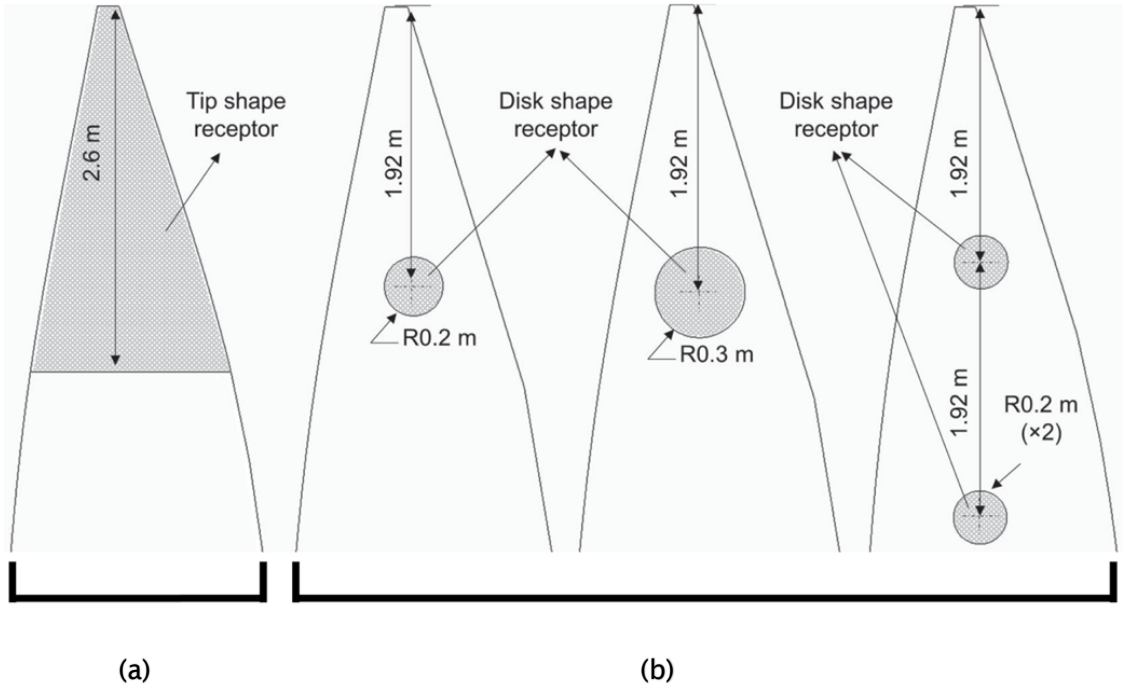

Figure 2.11 – Air termination system configurations [53]: (a) tip shape and (b) disk/screw shape.

instance, it is required to insulate all the conductive parts of the blade in such a way as to delay the formation of streamers from these components and favour the lightning attachment to the receptors [40] [12]. In practice, this is done by encapsulating the blade conductors within layers of GFRP material, which presents a breakdown strength of ~20 MV/m [66]. If the IEC guidelines are implemented, most of the lightning energy is conducted through the receptor and transferred to the transmission system, avoiding damage (however, it might still be required to replace the receptors after several strikes because of erosion at lightning arc roots). If they are not followed, the air termination system might be subjected to severe damage, such as [19], [21], [67], [68]:

- receptor melting and evaporation, due to the development of Joule heating while the lightning current is conducted through the air termination system (see Figure 2.12*a*).
- receptor loss, when it is blown off from the blade. This is usually due to the high air pressure inside the blade cavity (see Figure 2.12*b*).

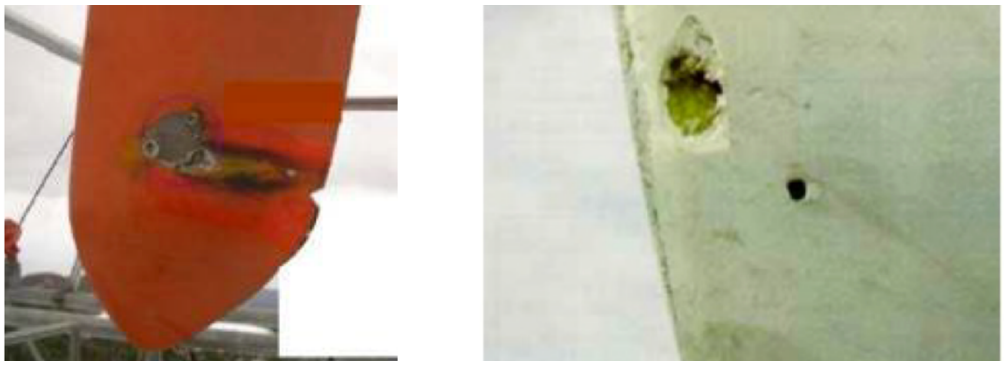

Figure 2.12 – Air termination system damage: (a) receptor ablation [19] and (b) receptor loss [21].

2.3.2 Transmission System

The transmission system, i.e., the DC, is intended to transfer the lightning current from the air termination system to the grounding system (see Figure 2.13). It can be either a braid encapsulated within the blade shell, or a cylindrical cable installed in the blade cavity, usually made of copper or aluminium. In order to avoid any structural damage, DCs should be designed in such a way as to resist electrical and thermal loads due to the lightning current. In the event of a lightning strike, DCs can present melting at imperfect connection points where the contact resistance is large [19], [68], [69].

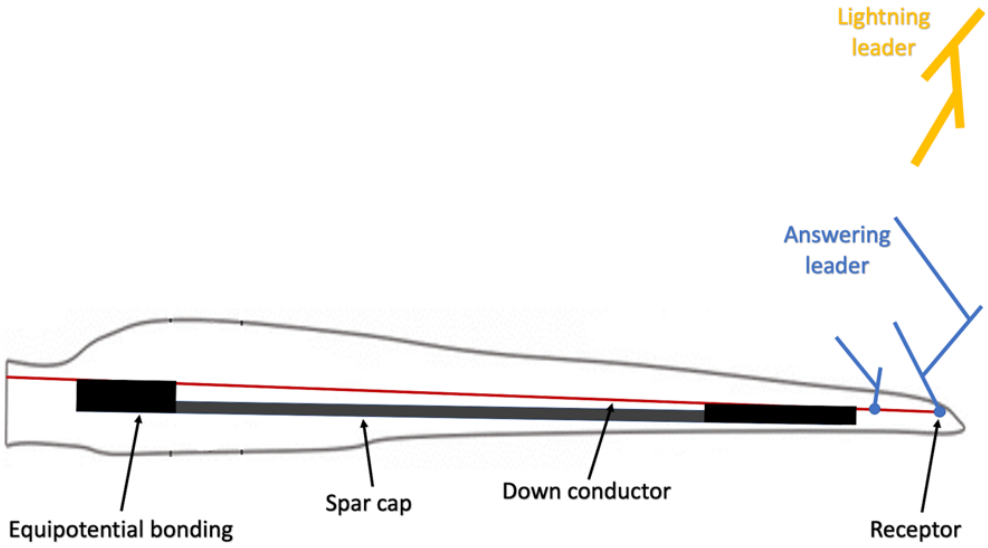

Figure 2.13 – LPS of a wind turbine blade.

2.3.3 EB System

As said, after the lightning attaches at the receptor, all the current flows through the receptor and is transferred to the DC, which then conducts the current to the blade root. In such conditions, HV breakdown of the blade insulating material between the DC and a floating conducting element of the blade might develop (according to the blade design and the position of the DC, the insulation can be air, GFRP, core material, or a combination of them). Such events occur when the applied electric field across the two electrodes is larger than the insulation breakdown strength. In such conditions, a conductive channel composed of positive ions and electrons develops in the insulating system which bridges the two conductors and allows the flow of electric current [70]. For wind turbine blades, critical flashovers are those between the DC and CFRP spars since the latter would experience severe damage, which would compromise the structural integrity of the rotor blade [12], [25], [26]. A solution to prevent HV breakdown events would be to bond electrically the DC to the spar such that to split the lightning current between the two elements and maintain the same electric potential. However, additional challenges and design considerations are introduced once the lightning current is allowed to flow within the blade structure. In fact, LPS equipotential connections of wind turbine blades are adhesive joints as the EB layers are glued to the DC and spar by resin during the infusion process of the blade (on the other hand, bolts are not employed for such connections since holes are generally avoided in CFRP structural elements). As a result, large temperatures are often observed because of the large contact resistance, which decompose some of the resin around the bonding points. The produced gas filled voids separate the rotor blade conductors carrying the lightning current and trigger sparks once the contact is open [27], [28]. Although EB connections between the DC and CFRP spars are key components of modern LPSs, the literature does not present any work on their design, nor the causes of resin thermal degradation at the bonding interfaces and how to prevent it.

Typically, two different EB configurations can be employed: the continuous-bonding configuration, which presents one strip only that connects the two conductors throughout the blade length (see Figure 2.14*a*); and the bonding-patches configuration, which consists of several strips implemented in strategic positions along the blade (see Figure 2.14*b*). The bonding-patches configuration, compared with the continuous-bonding one, would allow to save material, thus reducing the blade weight and cost.

EB materials should fulfil the following criteria and technical requirements:

- Electrical conductivity of at least 10^4 S/m in the in-plane directions to obtain the same electric potential on both DC and spar.
- Good fatigue strength to avoid failure and the consequent loss of the connection between the conductors.
- Low weight, to preserve the performance of the blade [71].
- Low cost, to maintain the price of the blade competitive [71].
- Desirable to select them from the materials already implemented in the rotor blade structure, to facilitate the manufacturing process [72].

Based on the criteria and requirements outlined above, the following materials are typically used for rotor blade EB applications [72]:

- Expanded copper foil (ECF), which is a copper sheet presenting several diamond shape openings of the same size (see Figure 2.15*a*). In order to manufacture expanded metal foils, the original solid sheet is

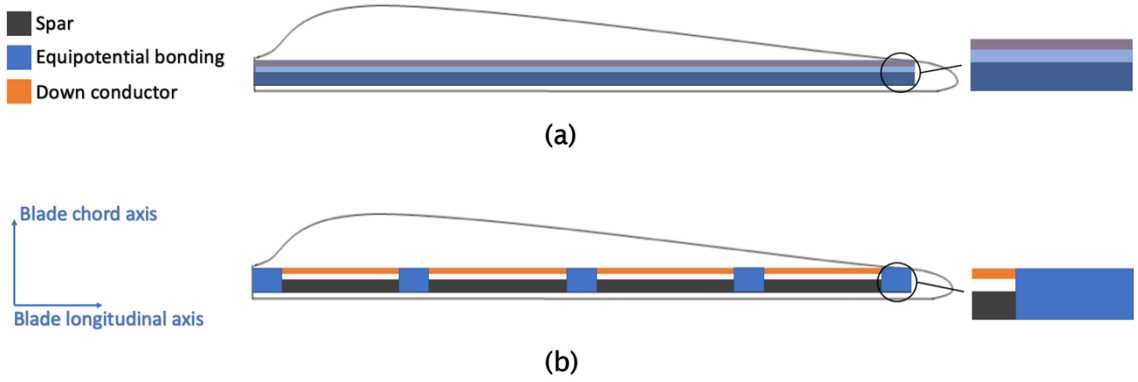

Figure 2.14 – EB configurations: (a) continuous-bonding and (b) bonding-patches.

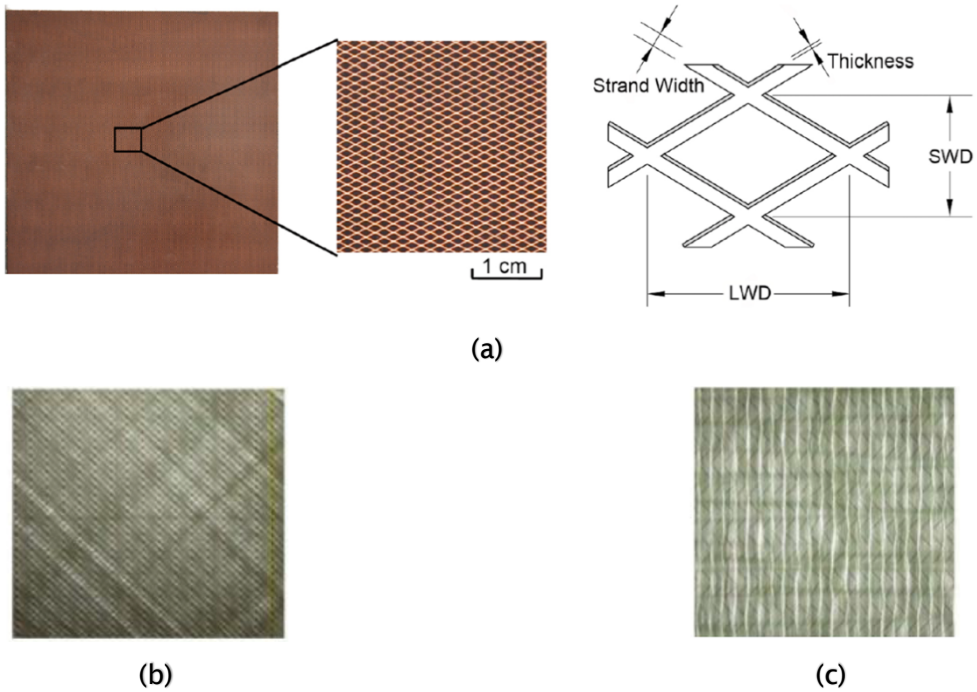

Figure 2.15 – Selected EB materials: (a) ECF [73], (b) BIAX CFRP [72], and (c) UD CFRP [72].

simultaneously slit and stretched through cutting tools which define the shape and number of the holes [74]. The choice of copper is justified by its excellent electrical and thermal conductivities equal to 5.91 x 10^7 S/m and 391 W/mK, respectively, as well as it presents a good fatigue limit of 115 MPa. Although aluminium is also an excellent electrical and thermal conductor, it is characterised by a poor fatigue life and its use as an EB material is usually avoided [75], [76].

- BIAX CFRP fabric, which presents fibres at +45° and -45° with respect to the blade longitudinal direction (see Figure 2.15*b*). This fibre architecture is typically chosen for EB applications as it results in quasi-isotropic (in-plane isotropic) material properties [77]. Compared with metals, CFRP materials are poor electrical and thermal conductors (from 3 to 5 orders of magnitude smaller conductivities). However, CFRPs present higher specific strength and stiffness, as well as a better fatigue limit (although it cannot accurately be determined because of the different damage modes CFRPs can experience [78]–[80]).

- UD CFRP fabric, which has all the fibres oriented along one direction (see Figure 2.15*c*). UD CFRP presents a relatively good electrical conductivity along the fibre direction, while it decreases by 3 orders of magnitude along the transverse direction and by 4 orders of magnitude along the through-thickness direction. In order to support the rotor blade operating loads, the UD fibres are aligned along the blade longitudinal direction, i.e., parallel to the spar fibres.

2.4 Modelling Methodology of Lightning Strikes

2.4.1 Electric Potential and Current Distributions

The simulation of lightning strikes to wind turbine blades has mainly relied on the lumped-element model [40], [42], [43], in which the spatially distributed blade is represented by a series of equivalent lumped-element circuits connected by perfectly conducting wires. More specifically, the blade is divided into sections of equal length (see Figure 2.16), and the conductors of each blade section are represented by lumped elements, i.e., resistance per unit length, *R'* [Ω/m], self-inductance per unit length, *L'* [H/m], mutual inductance per unit length, *M'* [H/m], and capacitance per unit length, *C'* [F/m]. By applying the classical circuit theory, this method allows to compute lightning current splits between the DC and spars, as well as potential differences to verify the risk of flashover. The lumped-element model can be used when transmission line effects are negligible, which is a safe assumption in the case of lightning strikes to rotor blades [40], [43]. This approach has also been employed by the aerospace industry to predict lightning current splits between metal and CFRP components of fastened joints [81]–[84]. Although this method is not computationally demanding, it presents some limitations that reduce its applicability to study lightning strikes to wind turbine blades. The first limitation is due to the procedure to determine the lumped elements of the blade

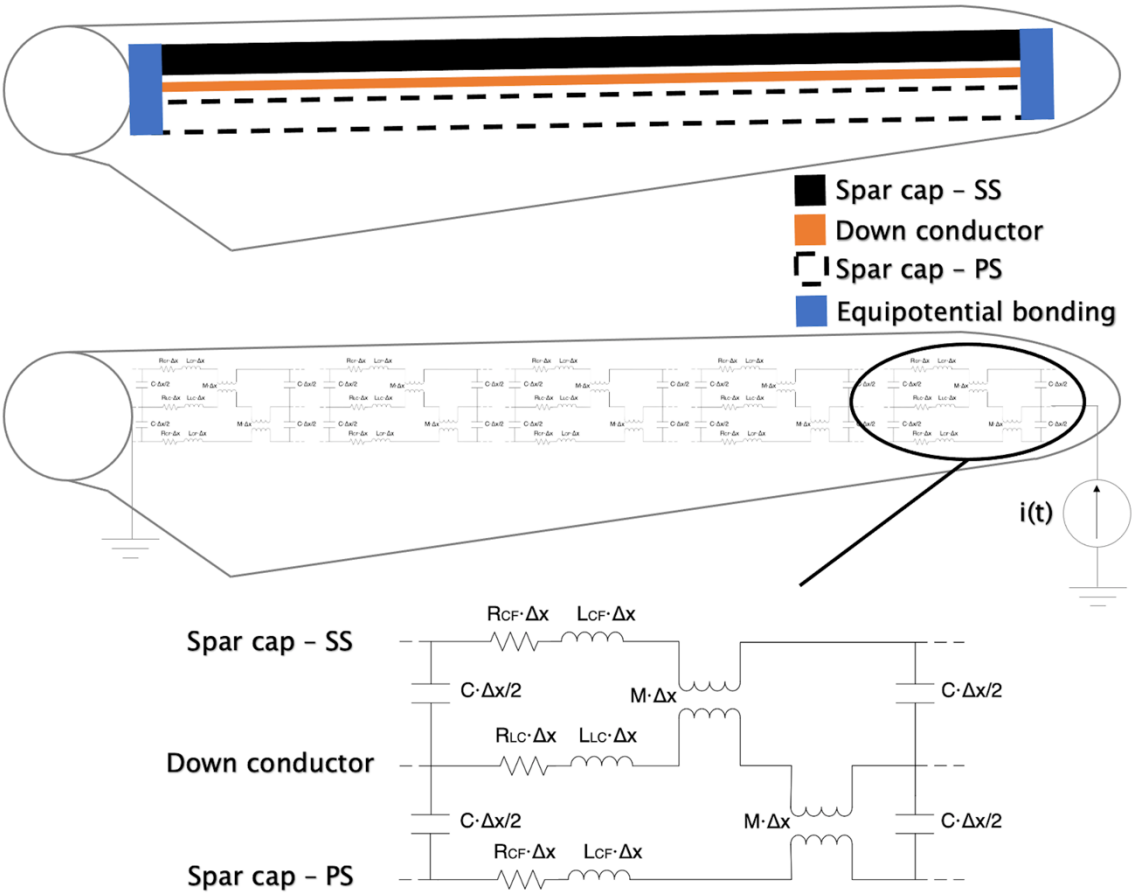

Figure 2.16 – Wind turbine blade representation by lumped-element circuits [40], [43].

conductors, which is usually done by 2D FEM simulations. For instance, resistances, self-inductances, and mutual inductances are calculated at a reference frequency only (i.e., 25 kHz for first positive short strokes and 1 MHz for subsequent short strokes), neglecting the remaining frequency content of the lightning current. Furthermore, EB connections are modelled as ideal short circuits, that is, both the impedance of the EB joints and the current crowding around the EB interfaces caused by the CFRP anisotropy are disregarded [40], [43]. This procedure only allows a rough estimation of the electrical parameters, which in turn reduces the accuracy of the solution. The second drawback is related to the assumptions made when using this method, which are not always realistic. For instance, the risk of flashover between the blade conductors can only be verified upon the definition of an average electric field, given by the electric potential difference divided by the distance, which is then compared to

the breakdown strength of the blade insulation. In other words, it is assumed that wind turbine blades are subjected to uniform electric field conditions under lightning strikes. However, this is not the case since the blade conductors present sharp corners where the electric field is magnified, which might potentially lead to HV breakdown of the insulation. Such areas cannot be predicted by the lumped-element model as it returns electric potential distributions rather than electric field distributions. Thus, the definition of the average electric field only is not a sufficient information to evaluate the potential risk of flashover within the blade. In addition, this method computes the net lightning current split between the DC and spar, while it is not capable of predicting spatial current density distributions in the EB joint cross-section. This information is fundamental to identify critical areas that might lead to thermal damage within the joint. Therefore, this method is not suitable for the purpose of this research project.

Spatial current density and electric field distributions across the blade can be predicted by the electromagnetic field diffusion problem. That is, by solving for both the Ampère-Maxwell equation and the current conservation law while considering both potential and induced electric fields [85], [86]. In this research project the equations mentioned above are solved by the FEM [87] (see Chapter 5). Despite the accuracy and the widespread availability in commercial software packages, the use of the FEM for rotor blade lightning strike studies has been limited to frequency-domain analyses [25] or to simplified geometry and model formulation [88]. More specifically, the work presented in [88] did not consider key features of modern blade geometries, such as CFRP spars and equipotential connections, disregarding the current split between the DC and spar. Consequently, it solved for the potential electric field only, neglecting the induced electric field due to the time-varying magnetic field. However, the induced electric field cannot be discounted since it is the main contributor of the voltage drop across the rotor blade, as well as it drives the current split between the blade conductors [26], [40], [42].

2.4.2 HV Breakdown in Non-Uniform Electric Field Conditions

When assessing the occurrence of HV breakdown of solid insulating materials in non-uniform electric field conditions (such as those experienced by wind turbine blades), it is necessary to identify a failure criterion. In uniform electric field conditions, the HV breakdown occurs when [70], [89]

$$E_{applied} = \frac{\Delta V}{d} = E_{bd\_unif} \tag{2.1}$$

where $E_{applied}$ [V/m] is the applied uniform electric field, ΔV [V] is the potential difference between the two electrodes, d [m] is the distance between the two electrodes, and E_{bd_unif}[V/m] is the breakdown strength of the insulating medium in uniform electric field conditions.

In non-uniform electric field conditions, the concept of field utilization factor is introduced, which expresses the degree of non-uniformity of the electric field due to the electrode size, geometry, and arrangement [70], [89]–[92]:

$$\eta = \frac{E_{mean}}{E_{max}} = \frac{\Delta V/d}{E_{max}} \tag{2.2}$$

where η is the field utilization factor, E_{mean} [V/m] is the average electric field, and E_{max} [V/m] is the maximum electric field.

The following electric field non-uniformities are identified (see Figure 2.17):

- $0.8 < \eta < 1$ very weakly non-uniform electric field conditions
  For very weakly non-uniform electric fields, it is still assumed that the breakdown occurs when Equation (2.1) is satisfied [89].
- $0.2 < \eta < 0.8$ weakly non-uniform electric field conditions
  For weakly non-uniform electric fields, the breakdown voltage decreases and can analytically be determined according to the following expression [70]:

$$V_{bd} = E_{bd\_unif}\, d\, \eta \tag{2.3}$$

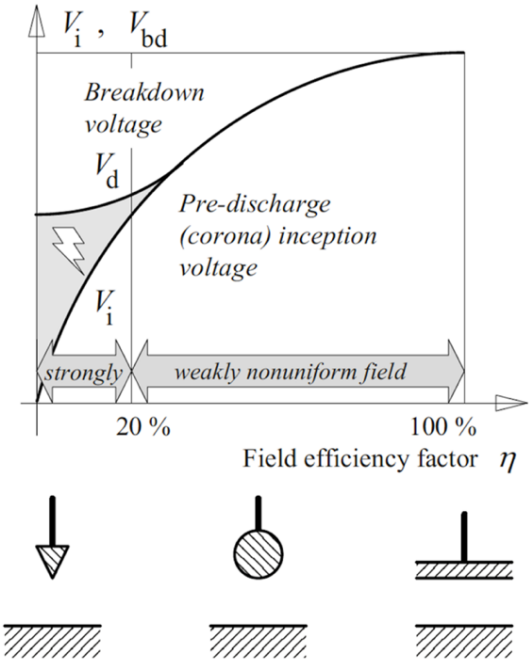

Figure 2.17 – Different degrees of electric field non-uniformity [89].

where V_{bd} [V] is the breakdown voltage.

However, experimental measurements [70] typically show different values of V_{bd} than those obtained using Equation (2.3), which suggests that the breakdown strength also varies as a function of η, and more specifically it increases [70], [89], [93]. The new value of breakdown strength in non-uniform electric field conditions, $E_{bd\_non\text{-}unif}$ [V/m], can be determined by experimental measurements of the breakdown voltage [70], [93]. In weakly non-uniform electric field conditions, the streamer formation leads directly to the breakdown (i.e., no pre-discharge is observed) when [89]

$$E_{max} = E_{bd\_non\text{-}unif} \tag{2.4}$$

- $0 < \eta < 0.2$ strongly non-uniform electric field conditions

  For strongly non-uniform electric fields generated by slow impulses, pre-discharges occur which cause the accumulation of space charge in front of the high-field electrode. In such conditions, the breakdown voltage is larger than the inception voltage of partial discharges, V_i [V], (see Figure 2.17) as the space charge cloud shields the high-field electrode and

reduces its sharp radius of curvature [70], [89], [94]. Pre-discharges develop at the location of maximum electric field only and the inception criterion is given by [70], [89]

$$E_{max} = E_i = E_{bd\_non\text{-}unif,max} \tag{2.5}$$

where E_i [V/m] is the inception electric field and $E_{bd\_non\text{-}unif,max}$ [V/m] is the maximum breakdown strength in non-uniform electric field conditions.

The pre-discharge becomes a streamer discharge and starts to propagate in the low-field region if the electric field at the opposite electrode is larger than a threshold limit, $E_{critical}$ [V/m], while it fades away if it is lower. However, for strongly non-uniform electric fields generated by very rapid voltage impulses like lightning ones, there is not enough time to form a space charge in front of the high-field electrode, and what has been discussed above does not hold anymore. In this case even the first electron avalanche causes the complete breakdown once the inception criterion is satisfied ($E_{max} = E_{bd\_non\text{-}unif,max}$) [89], [95], [96].

2.4.3 Temperature Distributions and Thermal Damage

No previous study has investigated the thermal damage at the EB interfaces due to the conduction of lightning current within the blade after the attachment to the receptor. On the other hand, extensive research has been conducted to predict the thermal damage due to lightning direct attachment to CFRP structures of either wind turbine blades [97]–[99] or aircraft [100]–[107], which is a completely different problem. Some of these studies employed a strongly coupled formulation of the electromagnetic-thermal problem, in which temperature dependent electrical conductivity tensors were considered. In fact, it is known that the electrical conductivity of CFRPs grows with an increase in temperature due to the activation of electrons from valence to conduction bands. Significant increases are observed when the temperature is larger than ~400 °C [100], [103], [105]–[108]. However, a weakly coupled formulation of the

electromagnetic-thermal problem, i.e., no dependence of the electrical conductivity on temperature, should allow a realistic description of the lightning thermal damage at the EB interface of wind turbine blades. In fact, for the problem under consideration, the source term in the heat transfer equation [109], [110] is the Joule heat generated by the flow of lightning current through the blade. Several studies, such as [21], [40], [42], [111], have shown that CFRP spars only conduct a small share of the total lightning current, and low temperatures are observed in the bulk CFRP.

In order to solve the electromagnetic field diffusion problem by the FEM, it is required to know some input material properties of the LPS conductors, which are the electrical conductivity tensor, σ [S/m], the electrical contact resistivity, ρ_C [$\Omega \cdot m^2$], the relative permittivity, ε_r, and the relative permeability, μ_r. Similarly, to solve the heat transfer problem, the following material properties are needed: the density, ρ [kg/m^3]; the specific heat capacity at constant pressure, C_P [J/(kg·K)]; and the thermal conductivity tensor, $\boldsymbol{k}$ [W/(m·K)]. The next section outlines the procedures to determine these properties and their typical values in the case of CFRP materials.

2.5 Properties of CFRP Materials for Lightning Strike Analysis

A composite material, like CFRPs, is made of two distinct materials with significantly different physical and chemical properties called constituents, which result in a material with enhanced properties once combined [112]–[114]. CFRP materials have found several fields of application, such as aerospace, wind energy, and automotive, thanks to the following advantages over conventional materials: high specific strength and stiffness; high fatigue resistance; high corrosion resistance; high level of design flexibility; and high optimisation degrees [115]. The first constituent material is the reinforcement, which usually is in the form of long fibres, short fibres, or particles. The reinforcement phase

is aimed to support the applied mechanical, electrical, and/or thermal loads. The second constituent material is the matrix, which usually is a thermoset or a thermoplastic resin. The objective of the matrix material is to transfer the load to the fibres, as well as to protect them from environmental abrasion and contamination. It is possible to have two main configurations of CFRP plates: the lamina, which is an individual layer (also called ply) of carbon fibres bonded together through the polymer matrix; and the laminate, which is the stacking and bonding of individual laminas [112]–[114].

CFRP materials are characterised by anisotropic material properties because of the anisotropy of carbon fibres. It is therefore essential to define a local coordinate system within each lamina to identify the material symmetry directions (see Figure 2.18), called principal-axis coordinate system (1,2,3):

- Longitudinal direction, parallel to the fibres.
- Transverse direction, perpendicular to the fibres.
- Through-thickness direction, perpendicular to the layer plane.

On the other hand, the global-axis coordinate system (x,y,z) specifies the reference directions of the CFRP laminate or structure, which might not coincide with the laminas principal directions [116], [117], as shown in Figure 2.18.

The properties of CFRP materials are determined using the homogenisation anisotropic approach [112], [118]–[121], which considers the complex bi-phase structure of a piece of CFRP as a homogeneous block having bulk properties (see Figure 2.19). This macroscopic method can be employed if the following two conditions are met [120]: the thickness of the CFRP block is much larger than the carbon fibres diameter (~1-10 μm [122]); and the carbon fibres are uniformly distributed throughout the matrix resin. Special CFRP arrangements, such as UD and BIAX, are orthotropic as they present three orthogonal planes of material symmetry, i.e., the material matrices do not vary when reflected around such planes. As a result, material properties like electrical and thermal conductivities can be represented by diagonal tensors.

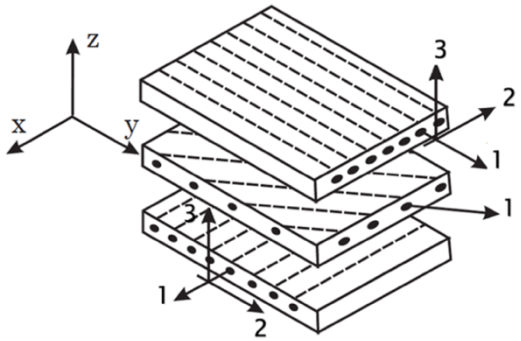

Figure 2.18 – Principal-axis (1,2,3) and global-axis (x,y,z) coordinate systems [114].

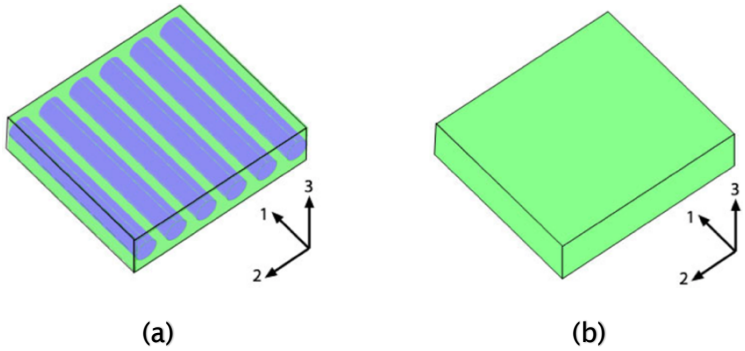

Figure 2.19 – CFRP lamina schematic: (a) micromechanical approach and (b) macromechanical (homogeneous) approach [30].

The next subsections review the experimental techniques, analytical models, and approximations to determine the CFRP material properties identified in Section 2.4. As said, these properties are needed by the FEM models to predict lightning current density and temperature distributions across the blade. Therefore, they play a key role in the overall accuracy of the numerical predictions.

2.5.1 Electrical Properties of CFRP

In order to predict realistic lightning current flow patterns in CFRP structures, it is essential to have an accurate representation of the bulk electrical conductivity tensor. From room temperature to ~400 ˚C, the CFRP electrical conductivity typically ranges from 20,000 to 45,000 S/m along the fibre direction, whilst it drops by up to 3 and 4 orders of magnitude along the transverse and through-

thickness directions, respectively [30], [31], [33], [100], [103], [105]–[108], [123]. Several studies have presented experimental procedures to characterise the orthotropic electrical conductivity tensor of CFRP materials, such as [30]–[33], [124]. The first step when performing resistance measurements on CFRP samples is to prepare reliable ohmic contacts (measuring electrodes) for the injection and extraction of the electric current [125]. In order to measure the real electrical conductivity of the bulk CFRP, sanding operations are first required to remove the thin resin film from the external surfaces of the sample. Uhlig [123] conducted an experiment in which he observed an increase of 1 order of magnitude in through-thickness electrical conductivity when the thin polymer layer was removed. After that, conducting materials are applied on the exposed carbon fibres to obtain the desired ohmic contacts. Conductive silver paint is the most employed material thanks to its ease of use and effectiveness [30]–[33], [126]. The paste is first spread with a brush on the sanded surfaces of the CFRP and then let to cure for 30 min at ambient temperature. Measuring electrodes can alternatively be realised by copper electroplating processes [72] or by fasteners inserted into holes coated with conductive paint (widely employed in the aerospace sector) [127], [128]. The second step requires to inject a direct current and measure the total resistance of the sample. This can be done by either the four-probe method [30], [124] or the two-probe method [31]–[33]. The former utilises four electrodes: two for the injection/extraction of the current; and two for the measurement of the voltage drop across the specimen (see Figure 2.20*a*). The latter makes use of two probes only for both the injection/extraction of the current and the measurement of the voltage drop (see Figure 2.20*b*). The measuring electrodes are placed sufficiently far away from the current injection point to allow the spreading of the current through the sample cross-section and obtain accurate readings. In fact, since the through-thickness electrical conductivity is 4 orders of magnitude smaller than the one along the fibres, the injected current might be confined in the first layers of the specimen (see Figure 2.21). This would overestimate the sample resistance and would not reflect the real electrical conductivity of the CFRP [129].

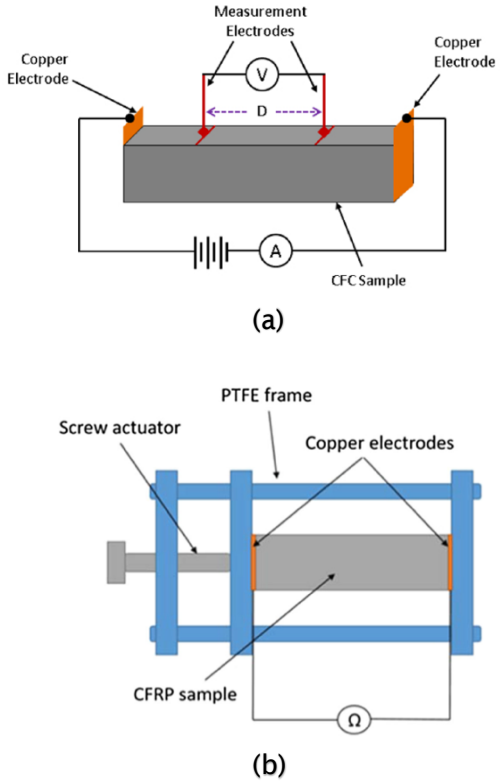

Figure 2.20 – Circuit schematics for CFRP resistance measurements: (a) four-probe method [30] and (b) two-probe method [33].

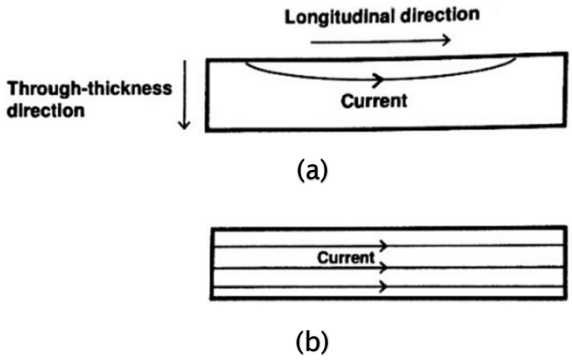

Figure 2.21 – Current distribution in the sample cross-section [129]: (a) insufficient penetration and (b) complete penetration.

As said in Section 2.4.3, no dependence of the electrical conductivity on the temperature should be considered in this project as only a small share of the total lightning current is conducted by the spars, and temperatures lower than 400 °C are found in the bulk CFRP. In addition, the variation of the CFRP electrical conductivity with electric field is disregarded, as well as its dependence on

frequency since the largest lightning frequency is ~13 MHz in the case of the subsequent short stroke [26].

Another important material property for accurate FEM predictions of current density and temperature distributions is the contact resistivity at the EB interfaces. In fact, such joints are realised by resin, which generates steep electric potential differences (see Figure 2.22) because of the high contact resistance and dissipates part of the lightning energy in the form of Joule heating. Only a few studies, like [42], [130], have provided values of contact resistance for metal-CFRP interfaces, although the authors have not clarified how these values were obtained. Therefore, one of the objectives of this research project is to develop an effective methodology capable of estimating the electrical contact of composite joints to fill this gap in the knowledge. To this end, it would be beneficial to review the experimental procedures designed to characterise the contact resistance in other applications, such as metal-semiconductor contacts [131]–[137]. These studies employed the transfer length method (TLM), which consists of measuring the total resistance of the sample, i.e., conductor bulk resistance + semiconductor bulk resistance + contact resistance, at different lengths. After that, to isolate the sought contact resistance from the bulk ones, the linear relationship between the measured total resistance and sample length is exploited. This is done by linearly interpolating the experimental measurements, and the y-axis intercept is twice the sought value of contact resistance (see Figure 2.23). However, typical EB configurations are much more complex than the systems analysed in [131]–[137], and the TLM alone is not capable of isolating the contact resistance from the bulk resistances by taking the y-axis intercept. More precisely, some of the bulk resistances of the jointed parts (DC, EB layers, and spar) are contained in the y-axis intercept (see Section 3.1.3). Thus, it is somehow required to estimate these bulk resistances to isolate the contact resistance. On the one hand, this might be straightforward for isotropic parts like the DC made of copper, in which

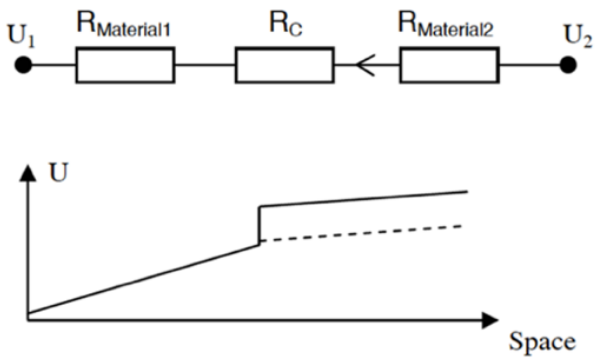

Figure 2.22 – Sharp voltage drop at the bonding interfaces due to the high contact resistance [65].

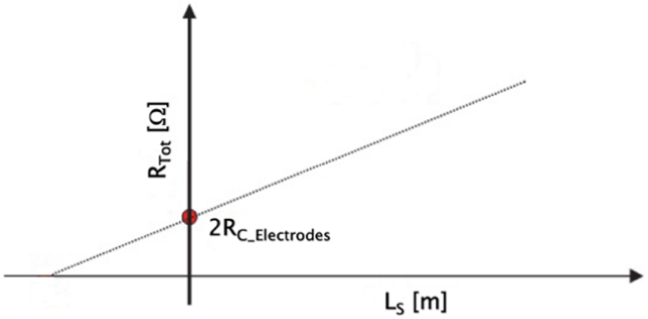

Figure 2.23 – TLM interpolation schematic.

the effective area occupied by the current is the entire cross-section and the Ohm's law can be used to estimate its resistance. On the other hand, the strong anisotropy of CFRPs causes a non-uniform current distribution in the cross-section of the spar, which behaves as a spreading resistance [138], [139]. Therefore, a suitable method needs to be identified to compute the spreading resistance in CFRP parts and isolate the contact resistance term from the y-axis intercept.

Finally, it is necessary to specify the relative permittivity to solve electric current problems. When a conductor is connected to a current source, an electric current flows within it. According to the Ohm's law an electric field needs to exist inside the conductor to have a current density. The relative permittivity of good electrical conductors is assumed equal to 1 when solving electric current problems since polarisation is overshadowed by conduction [140]. That is, the displacement current is negligible compared with the conduction current since

$\sigma \gg \omega\, \varepsilon_0\, \varepsilon_r$, where ω [rad/s] is the angular frequency and ε_0 is the vacuum permittivity. Polarisation effects are also negligible in continuous fibre CFRP materials, despite relative permittivity values in the range of 10^1 and 10^3 [141]–[143]. In fact, CFRP laminates used in engineering applications present a fibre volume fraction of 50-70%, which is significantly larger than the percolation threshold of ~40 vol% [29]. This produces several electrical contact points between the carbon fibres that allow conduction along both transverse and through-thickness directions [29]. Therefore, it is common practice in numerical simulation studies, e.g., [31], [108], [144], to assume a relative permittivity of 1 for CFRPs, which results in accurate electric field and current density predictions.

2.5.2 Magnetic Properties of CFRP

In order to predict the induced electric field due to the Maxwell-Faraday equation, and thus the induced current, it is required to know the relative permeability of the different wind turbine blade components. Previous research [145]–[148] has shown that CFRPs exhibit a weak diamagnetic behaviour and a negligible anisotropy at frequencies lower than 1 GHz. Considering that the maximum lightning frequency is ~13 MHz in the case of the subsequent short stroke, the relative permeability of CFRPs can be assumed equal to 1.

2.5.3 Thermal Properties of CFRP

The density and the specific heat capacity at constant pressure of CFRP materials are usually determined through the parallel rule of mixture [149], [150]. For typical wind turbine blade CFRP materials, the density is between 1,300 and 1,600 Kg/m^3 [112], [151], while the specific heat capacity at constant pressure is in the range of 1,100 and 1,400 J/(kg·K) [108], [152]–[154].

The last CFRP property required to solve the heat transfer problem is the thermal conductivity tensor. From room temperature to ~400 °C, typical thermal conductivity values along the fibre direction are between 2.4 and 2.6 W/(m·K),

whereas transverse and through-thickness thermal conductivities range from 0.5 to 0.9 W/(m·K) [33], [100], [103], [105]–[108], [123], [155]. The longitudinal thermal conductivity is typically determined through the parallel rule of mixture [149], [150]. On the other hand, transverse and through-thickness thermal conductivities are usually estimated experimentally through the guarded hot plate method [33]. This steady-state technique requires to expose the assessed CFRP samples (disk shape specimens) to a 1D heat flow generated by two metal plates (see Figure 2.24): the hot plate, which is in contact with a heat source; and the cold plate, which is in contact with a cooling block. To avoid lateral heat losses, the apparatus is embedded into insulating foam material. The temperature is measured through a thermocouple, while the applied heat flux and voltage are measured by a sensor and a voltmeter, respectively. Finally, to reduce the thermal contact resistance and to mitigate surface roughness and air gaps, a paste is spread at the interfaces between the plates and the sample. Samples with different thickness, Δx [m], are assessed to determine the paste thermal conductance (y-axis intercept in Figure 2.24) and remove it from the estimated thermal conductivity (slope of the linear plot in Figure 2.24).

2.5.4 Pyrolysis in CFRP

Pyrolysis is the irreversible thermal degradation of organic (carbon-based) materials occurring spontaneously at high temperatures and is considered the first step of combustion [30], [149], [154]. During the pyrolysis process, 80-90%

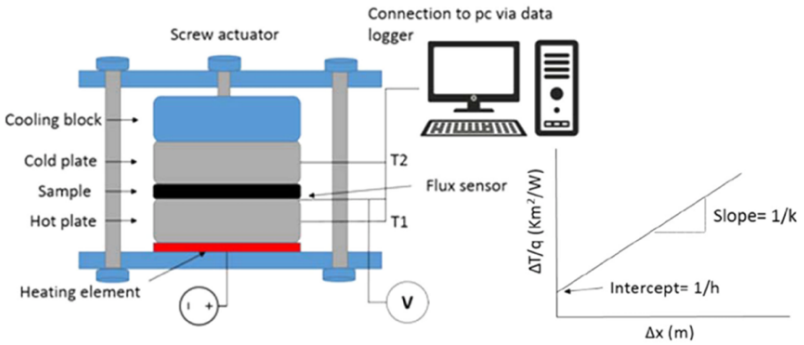

Figure 2.24 – Transverse and through-thickness thermal conductivities test setup schematic [33].

of the polymer mass decomposes into gases (H_2O, CO, and CO_2), while the remaining into porous char consisting of carbon (85-98 wt%) [154], [156]. Polymer thermal degradation is often investigated by thermogravimetric analysis (TGA). It measures the variation of the polymer mass as a function of time and temperature while it is exposed to a controlled environment. There are two main types of TGAs: isothermal TGA, in which the sample weight is measured while subjected to a constant temperature; dynamic TGA, in which the sample weight is measured at different temperatures under a constant heating rate. Temperatures assessed by commercial TGA apparatuses range from ambient to 1,000 °C, while typical heating rates are between 0.1 and 200 °C/min [157]–[159]. The heating rate affects the pyrolysis process by scaling the reaction rate, and thus the degradation temperature, up and down [30], [102], [149], [160]. Previous studies have characterised the thermal degradation process of epoxy resins and epoxy resin based CFRPs assuming that the degradation develops into an apparent single reaction [161]–[165]. However, it has been shown that the pyrolysis process of cured epoxy resins develops into multiple different mechanisms [159], [166], [167]. More specifically, epoxies display an initial degradation process between 100 °C and 250 °C, which involves release of water [159], [168]. This initiation mechanism has been identified as a dehydration reaction between the hydroxyl groups formed during the curing process [36] and hydrogens originally found on the molecular main chain [168], [169]. The latter process causes the formation of chemical groups that are weaker and less thermally stable than the original ones [166], which in turn result in a degradation mechanism occasionally mentioned as “head-to-head” degradation mechanism in the related literature [159]. Eventually, another mechanism occurs via “random scission” processes of C-C bonds [166]. The two latter mechanisms take place between 200 and 800 °C. They exhibit similar activation energies and at sufficiently high heating rates they might overlap and even invert their sequence [159]. Finally, note that prior to any of the three described mechanisms, water molecules in the form of absorbed moisture might be released (not to be confused with the described dehydration process) [167],

[170]. In this thesis the epoxy pyrolysis process is modelled by the deconvoluted description outlined above (see Chapter 4), to account for the degradation mechanisms occurring at low temperatures. The latter are believed to cause thermal degradation and consequent sparking in rotor blade EB joints.

2.6 Types of Lightning Impulses

A lightning is a long electric arc generated by a type of cloud called Cumulonimbus or Thundercloud, which develops in the atmosphere during thunderstorms [171]–[173]. Wind turbine blades are exposed to both downward (cloud-to-ground) and upward (ground-to-cloud) lightning strikes, which are a combination of short and long strokes and transfer a total charge of 300 C. Short strokes (see Figure 2.25*a*) last less than 2 ms and transfer 100 C, while long strokes (see Figure 2.25*b*) last up to 0.5 s and transport 200 C. Lightning strokes can be described by a set of electrical and time parameters [12]. The electrical

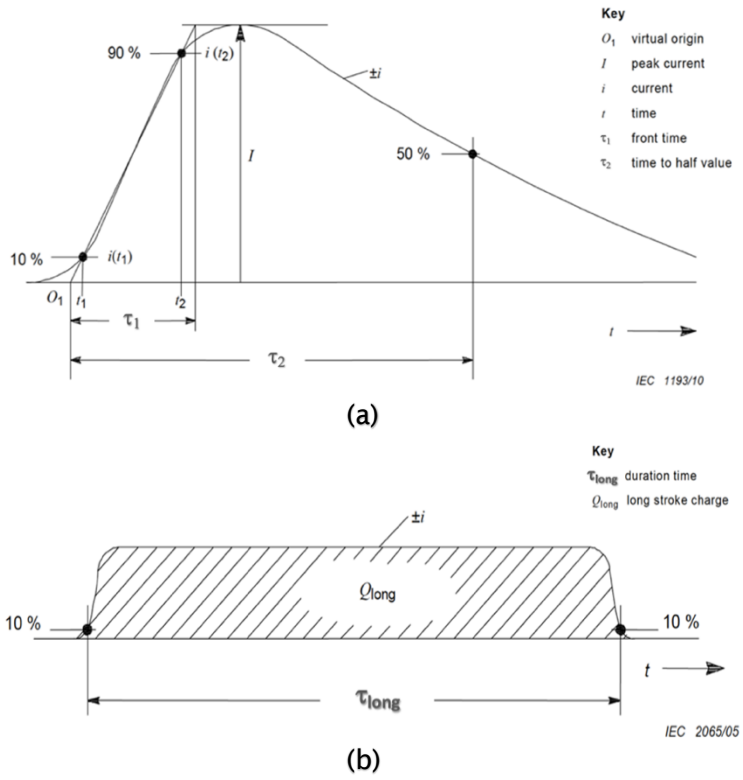

Figure 2.25 – Waveforms of lightning currents: (a) short stroke and (b) long stroke [12].

parameters are the peak current, I_0 [A], the transferred charge, Q_{SHORT} and Q_{LONG} [C], and the specific energy, W/R [J/Ω]. In contrast, the time parameters are the front duration, τ_1 [s], the time to half value, τ_2 [s], and the duration of long strokes, τ_{LONG} [s]. Different lightning strokes exist according to the value of these parameters (see Tables 2.2 and 2.3), which are outlined in the next subsections.

2.6.1 Downward Negative Lightning

A downward negative lightning develops from the cloud to the Earth's surface and transfers negative charge. Downward negative lightning strikes account for the 90% of all the downward strikes and are composed of a first short stroke followed by a combination of subsequent short and long strokes. Figure 2.26 illustrates a typical waveform of the downward negative lightning current [12]. The peak current of the first negative short stroke can achieve 100 kA with a mean value of 30 kA, while the transferred charge is equal to 100 C. The front duration and time to half value are 1 μs and 200 μs, respectively.
Subsequent short strokes of downward negative lightning have a peak current

Table 2.2 – Waveform parameters of different downward lightning impulses [12].

Lightning Impulse	Current Parameter	
First positive short stroke	**Peak current, I_0 [kA]**	200
	Charge, Q_{SHORT} [C]	100
	Specific energy, W/R [MJ/Ω]	10
	Front duration, τ_1 [μs]	10
	Time to half value, τ_2 [μs]	350
First negative short stroke	**Peak current, I_0 [kA]**	100
	Front duration, τ_1 [μs]	1
	Time to half value, τ_2 [μs]	200
Subsequent short stroke	**Peak current, I_0 [kA]**	50
	Front duration, τ_1 [μs]	0.25
	Time to half value, τ_2 [μs]	100
Long stroke	**Current value [kA]**	0.2–1.2
	Charge, Q_{LONG} [C]	200
	Duration, τ_{LONG} [s]	0.5

Table 2.3 – Waveform parameters of upward lightning impulses [12].

Lightning Impulse	Current Parameter	
Upward lightning	**Peak current, I_0 [kA]**	20
	Total charge, Q_{TOT} [C]	300
	Total duration, τ_{TOT} [s]	0.5
	Number of superimposed impulses	50

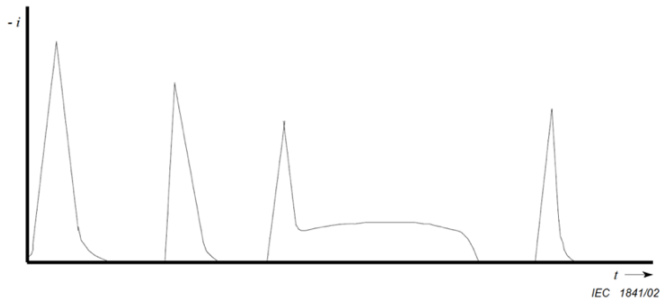

Figure 2.26 – Typical waveform of a downward negative lightning [12].

of 50 kA and time parameters equal to 0.25 μs (front duration) and 100 μs (time to half value). Consequently, subsequent short strokes present the largest rate of rise of current, $\frac{di}{dt}$ [A/s], equal to 200 kA/μs, which generates the highest voltage drop across the rotor blade. Therefore, such an impulse is considered to assess the occurrence of the electrical breakdown of the insulation between the DC and spar [12].

2.6.2 Downward Positive Lightning

A downward positive lightning develops from the cloud to the Earth's surface and transfers positive charge. Downward positive lightning strikes are just 10% of all the downward strikes and are composed of one short stroke and one long stroke, as shown in Figure 2.27. The time parameters of the first positive short stroke are 10 μs (front duration) and 350 μs (time to half value). Moreover, its electrical parameters are the highest in terms of peak current, transferred charge, and specific energy, which are equal to 200 kA, 100 C, and 10 MJ/Ω, respectively. As a result of the high specific energy carried by this type of

lightning, it generates the largest amount of Joule heating. Therefore, the first positive short stroke is considered for the design of EB connections between the DC and CFRP spars [12].

The long stroke (continuing current) is characterised by a transferred charge equal to 200 C and a duration of 0.5 s.

2.6.3 Upward Lightning

Wind turbines present heights of 100 m or more and are frequently exposed to upward lightning strikes. In fact, the electric field at this altitude is sufficiently enhanced by the cloud charge to develop upward leaders. In addition, the initiation of upward leaders is also favoured by the continuous rotation of the blades [8], [18], [174], [175]. Upward lightning strikes can transfer both positive and negative charges, although positive ground-to-cloud lightning is very rare [12]. As depicted in Figure 2.28, a typical profile of upward discharges consists of a superposition of long and short strokes. More specifically, it always starts with a long stroke to which short strokes are superimposed. The maximum peak current of the short stroke is 20 kA, while the transferred charge is 300 C [12].

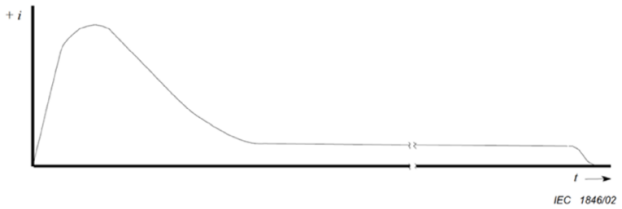

Figure 2.27 – Typical waveform of a downward positive lightning [12].

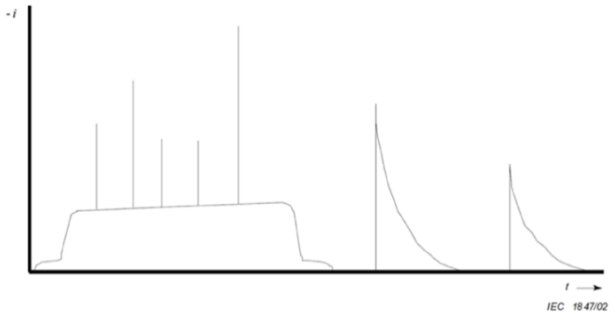

Figure 2.28 – Typical waveform of an upward lightning [12].

To summarize, two different waveforms are considered depending on the type of potential damage it is desired to assess: the subsequent short stroke of downward negative lightning, to investigate the occurrence of flashovers between the DC and CFRP spars; and the first positive short stroke, to evaluate the high-current performance of EB connections and the occurrence of thermal damage at their interfaces.

2.6.4 Mathematical Approximation of Lightning Short Stroke Waveforms: Heidler Function

A good representation of the lightning short stroke waveforms (first and subsequent short strokes given in Table 2.2) is provided by the Heidler function [176], [177], which is the standard lightning waveform employed for rotor blade simulation studies [12]:

$$i(t) = \frac{I_0}{k_0} \frac{\left(\frac{t}{t_1}\right)^{10}}{1 + \left(\frac{t}{t_1}\right)^{10}} \mathrm{e}^{\left(-\frac{t}{t_2}\right)} \tag{2.6}$$

where $i(t)$ [A] is the instantaneous current, t [s] is the time, k_0 is the correction factor for the peak current, t_1 [s] is the rise time coefficient, and t_2 [s] is the decay time coefficient. Table 2.4 summarises the Heidler function coefficients [44], [176]–[178], while Figure 2.29 depicts the rise and decay fronts of the first positive short stoke given by the Heidler function. Note that the rise and decay time coefficients of Equation (2.6) are longer than the front duration and time to half value given in Table 2.2. In fact, the inherent shape of the Heidler function presents an initial offset interval, t_{offset} [s], in which the current is zero. This offset time varies according to the different types of short strokes [44], [176]–[178].

One of the major challenges when simulating lightning strikes to rotor blades by the FEM is the injection in the model of the lightning current, as it splits among the different conductive paths of the blade. These lightning current

Table 2.4 – Heidler function coefficients of lightning short strokes [44], [176]–[178].

Lightning Impulse	Peak Current I_0 [kA]	Correction Factor k_0	Rise Time t_1 [µs]	Decay Time t_2 [µs]
First positive short stroke	200	0.93	19	485
First negative short stroke	100	0.986	1.82	285
Subsequent short stroke	50	0.993	0.454	143

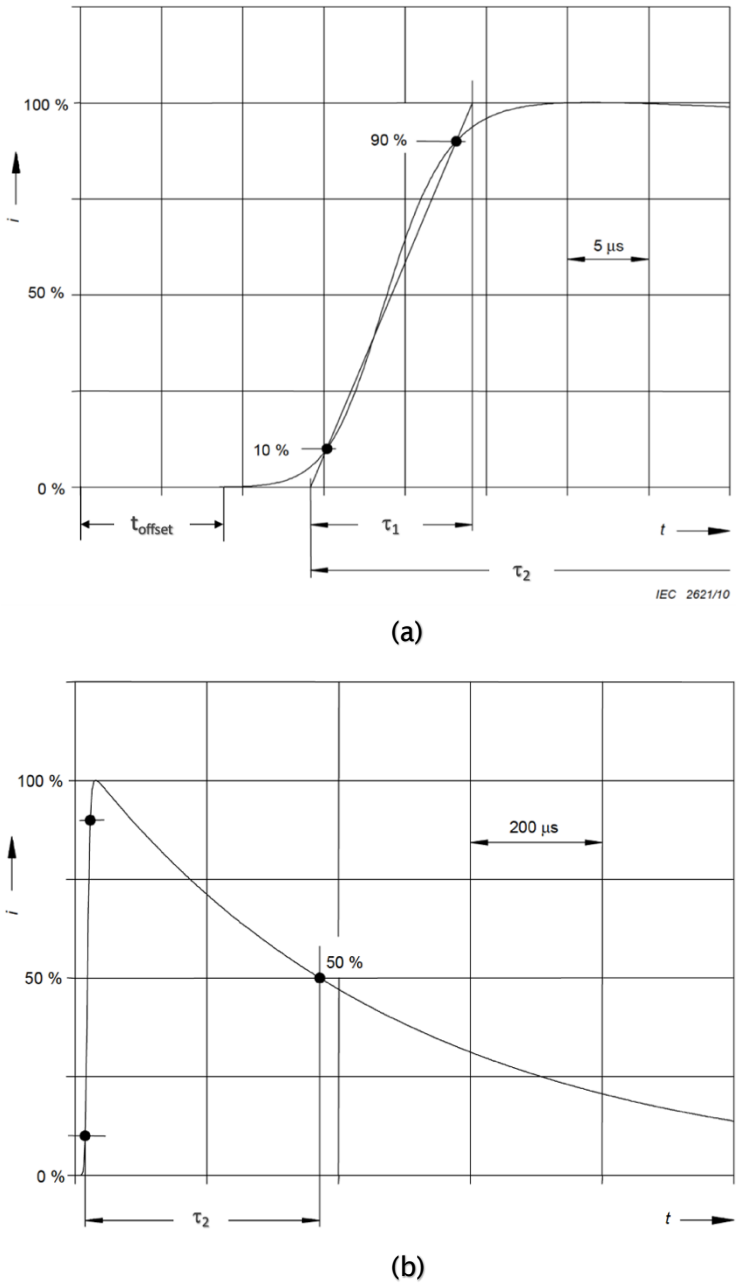

Figure 2.29 – Heidler function first positive short stroke [44]: (a) rise front and (b) decay front.

redistributions are driven by both resistive and inductive effects [40], [43], and it is thus required to solve for both electric scalar and magnetic vector potentials. This can be done by coupling them through an imposed integral constraint on the total transport current, i.e., the Heidler function. However, the computational cost to solve such a combined problem is large for fast rising currents such as lightning ones. Therefore, a procedure is needed to solve the electromagnetic problem in the time-domain without imposing the integral constraint on the total transport current, in such a way as to achieve better convergence and a smaller computational time.

2.7 Summary

This chapter was intended to revise the engineering problems related to lightning protection of wind turbine blades and the previous attempts to solve them. One of the main challenges in the design of modern LPSs of wind turbine blades is the implementation of EB joints. Although several studies have pointed out the need of EB connections to avoid flashovers between the blade conductors, no previous research has investigated how to design such joints, nor the causes of thermal damage at their interfaces and how to prevent it. The core of this literature review was dedicated to the numerical methodologies, and the required input material properties, for the simulation of lightning strikes to rotor blades. Previous studies have mainly employed lumped-element circuits simulations to study lightning strikes to rotor blades, although this approach presents some limitations that reduce its accuracy and applicability. For instance, the lumped parameters are typically determined through 2D FEM simulations, disregarding both the impedance of the EB joints and the current crowding around the EB interfaces due to the CFRP anisotropy. In addition, this approach is not capable of predicting current density distributions in the EB joint, which are fundamental to identify critical areas where thermal damage and sparks might develop. An effective tool to predict such quantities can be the FEM, which is widely available in commercial software packages and is employed

in this project. The main input material properties to predict, by the FEM, realistic lightning current paths and temperature distributions in the EB joint cross-section are the electrical conductivity, thermal conductivity, and electrical contact resistivity. While extensive research has been conducted on the investigation of CFRP electrical and thermal conductivities, no study has so far attempted to characterise the electrical contact resistivity of EB joints.

To conclude, the following lines of enquiry have been identified, which are answered in the next chapters of this PhD thesis (given below in brackets):

- The causes and mechanisms of resin thermal degradation at the EB interfaces have not fully been investigated yet. More precisely, no experimental method has so far been proposed to characterise the electrical contact at the EB interfaces (Chapter 3). In addition, the polymer thermal degradation process of commercial EB resins used in rotor blades has not been explored to define the degradation mechanisms responsible for voids formation and sparking (Chapter 4).
- A numerical procedure is required to solve the electromagnetic problem in the time-domain without imposing an integral constraint on the transport current (Chapter 5).
- Fundamental questions regarding the design of wind turbine blade EB connections have remained unanswered for several years, that is, whether CFRP spars and EB joints can withstand lightning currents without experiencing thermal damage and how to design equipotential connections (Chapters 6 and 7).

Chapter 3
Electrical Contact of Lightning Protection EB Joints

As discussed in both the Introduction and Literature Review, the lightning current is allowed to flow within the spar through the equipotential connections. In such conditions, it is important to study the electrical contact behaviour between the different parts of the adhesive joint. In fact, the physical connections between the DC and spar through the EB layers are realised by resin during the infusion process of the blade. For instance, Figure 3.1 depicts the interface between the DC and EB layer, which exhibits resin-rich areas. The latter result in large values of contact resistance and temperature, which lead to the thermal degradation of some of the resin used for the bonding. The produced gas filled voids in turn cause sparks and delamination once the contact is open [27], [28]. For this reason, the aim of this chapter is to present a reliable procedure that allows to characterise the electrical contact resistivity at the bonding interfaces for a range of EB concepts. The implementation of these values in the FEM simulations is crucial to predict accurate current density and temperature distributions and investigate the thermal damage experienced at these interfaces.

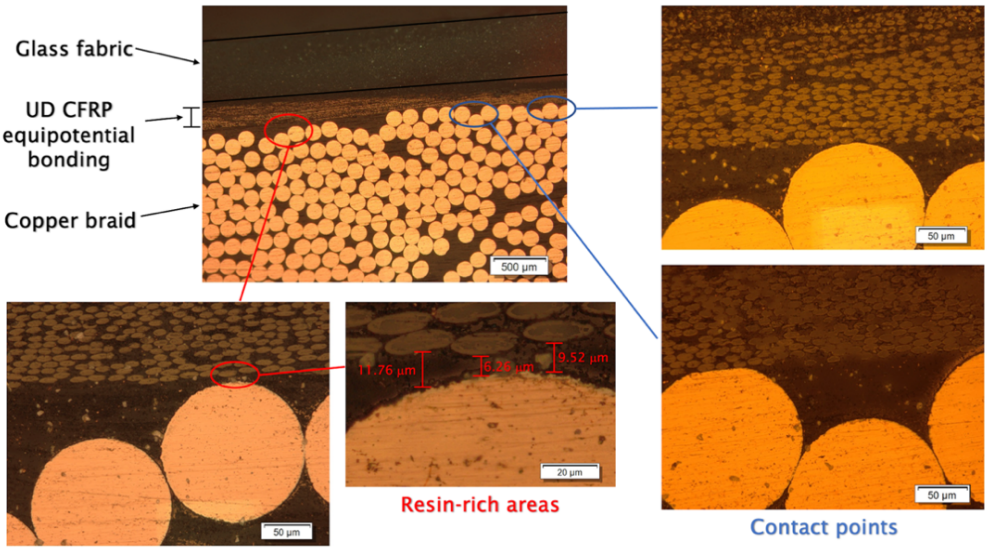

Figure 3.1 – Resin rich areas and contact points at the interface between DC and EB.

3.1 Experimental Procedure

3.1.1 Materials

As a polymer matrix, a two-component epoxy system was employed during the infusion process, which was supplied by Hexion. It comprised Hexion RIMR035c epoxy resin and Hexion RIMH037 curing agent. For the CFRP spar, a UD non-crimp carbon fabric with an areal density of 870 g/m^2, supplied by Saertex, was utilised. Three different EB materials were employed to connect the copper LPS DC to the CFRP spar: UD non-crimp carbon fabric (600 g/m^2); BIAX non-crimp carbon fabric (218 g/m^2); and ECF 4Cu14-125. Both UD and BIAX non-crimp carbon fabrics were supplied by Saertex, whereas the ECF was supplied by Dexmet Corporation [74]. The latter consisted of copper Alloy C11000 [179] and was characterised by a nominal thickness of 0.101 mm, strand width of 0.356 mm, long way of the diamond (LWD) and short way of the diamond (SWD) approximately equal to 3.175 mm and 1.397 mm, respectively. Finally, the samples were encapsulated within a BIAX non-crimp glass fabric with an areal density of 1,010 g/m^2, supplied by Saertex.

3.1.2 Sample Geometry and Manufacturing

Figure 3.2 depicts a typical arrangement of the wind turbine blade internal components. The system was composed of a DC, a spar made of UD CFRP, and two EB layers connecting the DC to the spar. Two main contact regions needed to be investigated:

- the contact region between the DC and EB layers (C_DC-EB), which is composed of two interfaces, i.e., top and bottom surfaces of the DC.
- the contact region between the EB layers and spar (C_EB-Spar), which is composed of three interfaces, that is, side, top, and bottom surfaces of the spar.

For a more accurate estimation of the electrical contact behaviour, it was decided to separate the contribution of the two contact regions to the total interface resistance, i.e., two distinct values of contact resistance were estimated for the two contact regions. This was achieved by designing two different types of specimens:

- the DC-EB specimen (see Figure 3.3*a*), which is composed of a DC and two EB layers. It allowed to determine the contact resistance between the DC and EB connections.
- The DC-EB-Spar specimen (see Figure 3.3*b*), which consists of a DC, two EB layers, and a constant thickness CFRP spar. It enabled to characterise the contact resistance between the EB connections and spar after measuring the interface resistance between the DC and EB connections. Typical spar geometries of rotor blades present chamfer profiles for mechanical purposes. From a lightning protection point of view, it is beneficial to place EB layers on these surfaces since the current can directly be injected into each spar layer and thus through the entire spar cross-section. Therefore, three additional DC-EB-Spar samples (see Figure 3.4) were designed to investigate the effects of the chamfer angle, $\gamma\,[^{\circ}]$, on the contact resistance.

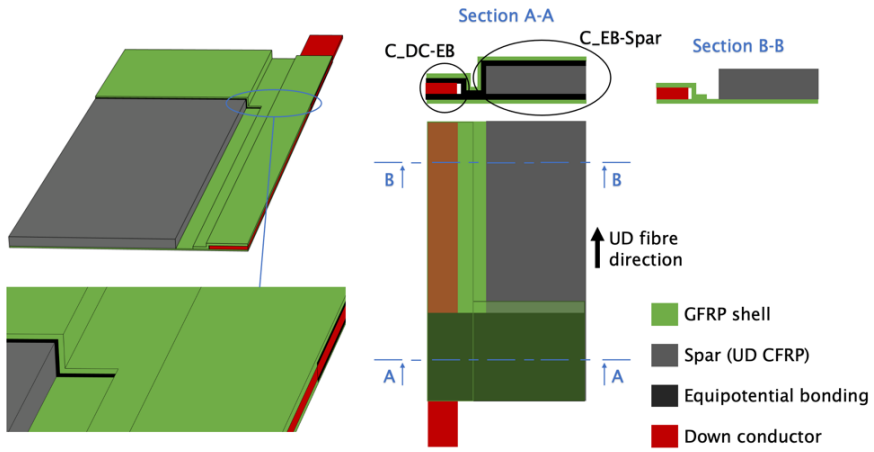

Figure 3.2 – Typical arrangement of wind turbine blade internal components.

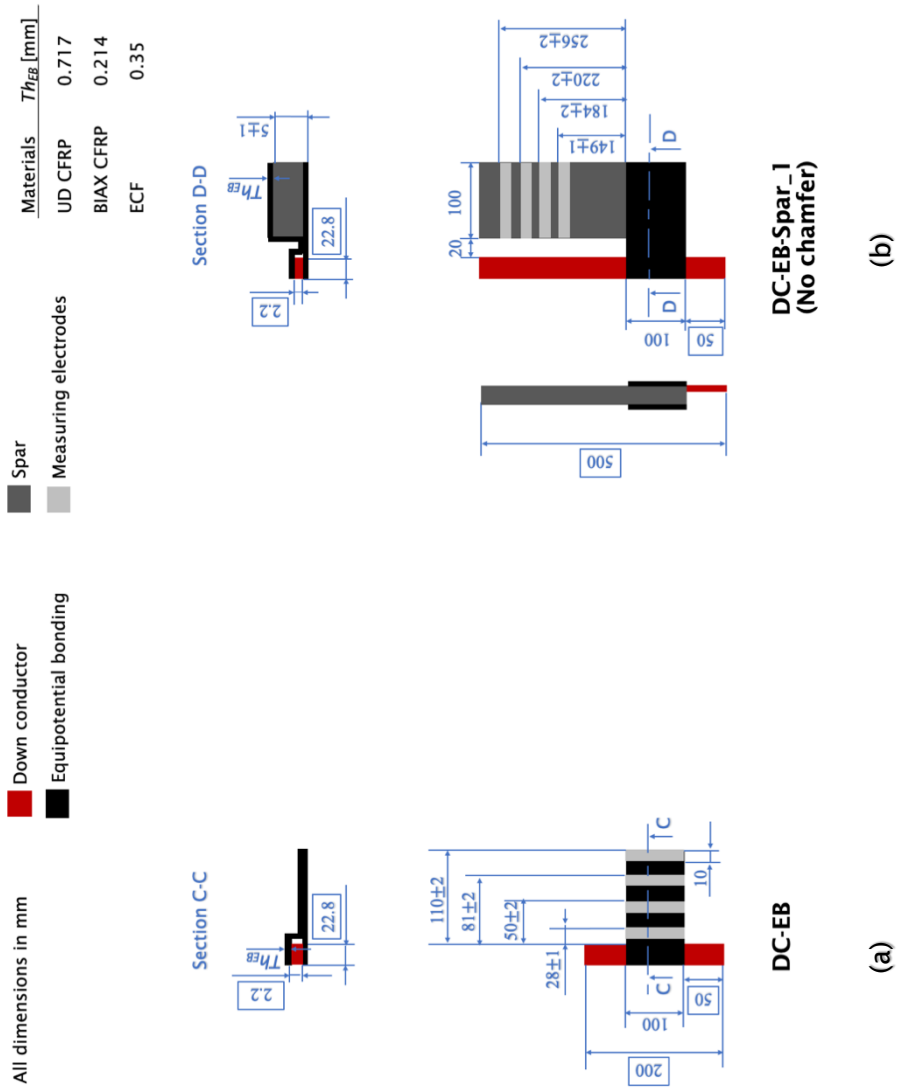

Figure 3.3 – Geometry of: (a) DC-EB and (b) DC-EB-Spar_1 (no chamfer).

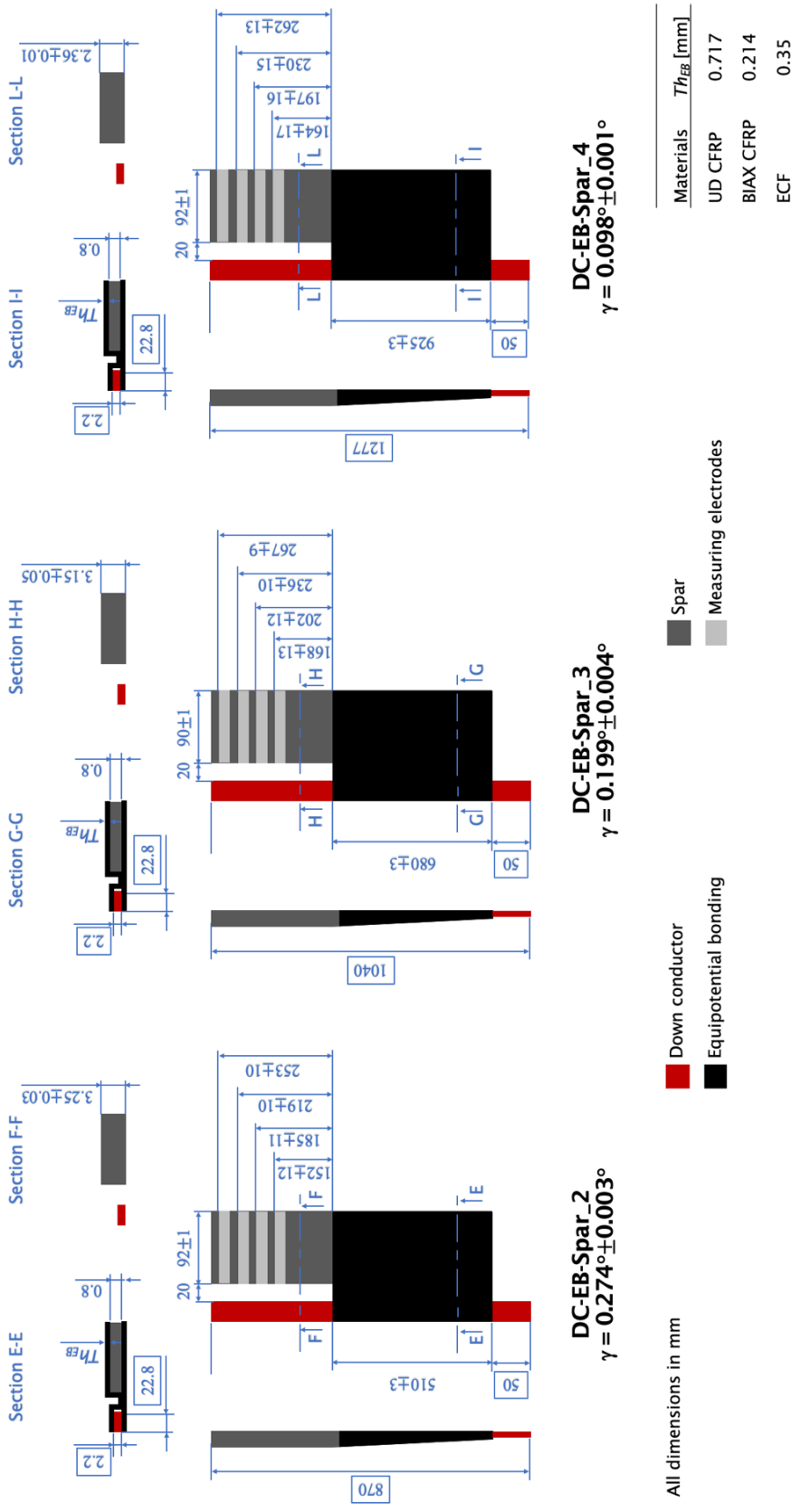

Figure 3.4 – Geometry of chamfered samples: DC-EB-Spar_2, DC-EB-Spar_3, and DC-EB-Spar_4.

The samples were manufactured by the industrial sponsor of this project, Nordex Energy GmbH, through the VARTM process, which is the standard manufacturing route for wind turbine blades. It is essential to employ the same blade production strategies and materials for the experiment to be representative, since the quality of the contact (i.e., the contact resistivity) depends on these factors [13]–[16]. The UD CFRP spar sample was obtained by stacking layers of dry carbon fabric (five layers for the DC-EB-Spar_1 samples, four layers for both the DC-EB-Spar_2 and DC-EB-Spar_3 samples, and three layers for the DC-EB-Spar_4 samples) into a flat mould, whereas a copper braid (LPS DC) with a cross-section of 50 mm^2 [12] was positioned in parallel to the laminate. EB layers were then placed in the desired positions to connect the DC to the spar, as shown in Figure 3.2. Finally, to be consistent with the actual structure of the rotor blade, the whole system (i.e., CFRP spar, DC, and EB) was encapsulated into GFRP fabric layers and infused at the same time under vacuum. The samples were cured for 6 h at 70 °C following the instructions of the resin supplier. The fibre volume fraction of the laminates was approximately 53%. Four specimens per each configuration were manufactured and assessed in order to account for any variation in the contact quality caused by the manufacturing process.

3.1.3 Characterisation of Total Resistance

Before conducting the experiment, it was essential to prepare the sample surfaces that were intended to act as electrodes. First, the top surface of the sample was sanded down in order to remove the excess epoxy resin and expose the carbon fibres [30], [32], [123]. The sanding process was performed by means of 180 grit silicon carbide abrasive paper until carbon fibres were visible, followed by 300 and 600 grit to finish the surface. Small amount of water was also used to trap the created epoxy resin dust. Finally, the epoxy and carbon fibre residue were removed through acetone and left to dry for an hour. Second, measuring electrodes were obtained on the sanded

areas by means of copper tapes. To reduce the measuring electrodes contact resistance, the copper tapes were attached to the sample surface using conductive silver paint with a bulk electrical conductivity of $1x10^5$ S/m, which was supplied by RS Components. The silver paste was left to cure for 30 min at ambient temperature, as specified by the supplier [180].

The maximum direct current injected in both DC-EB and DC-EB-Spar samples was limited to 50 mA to mitigate Joule heating effects and avoid any damage. In addition, some studies have shown that both the bulk electrical resistivity [181]–[183] and the electrical contact resistivity [184]–[186] of CFRPs decrease with increasing temperatures. Thus, by conducting the experiment at ambient temperature, the electrical contact was characterised in the worst-case scenario, i.e., the case with the highest electrical contact resistivity. Under such conditions, the total resistance of both DC-EB and DC-EB-Spar samples was measured through the AIM TTi BS-407 low resistance ohmmeter using the two-probe method depicted in Figure 3.5*a*. It employs two wires and two probes for both the injection of the current and the measurement of the voltage drop across the specimen. The sample was connected to the circuit using two crocodile clip test leads; the first wire was connected to the DC to inject the current, whereas the second one to the measuring electrode to ground it. The two-probe method was chosen since it includes the sought values of contact resistance into the total measurements. A pressure equal to 20 MPa was applied through a hydraulic press on the metal electrodes during the measurements in order to mitigate the effects of the surface roughness and improve the ohmic contact [138]. The amount of pressure was driven by the reduction of the experimental uncertainties, as shown in Section 3.3.1. The hydraulic press cylinder needed to be centred over the electrode surface in order to deliver the correct pressure. In addition, an aluminium block insulated from the current path was placed between the sample and the press cylinder to spread the applied force over the entire electrode surface. All measurements were conducted at a temperature of 25 °C and with a relative humidity of 55%.

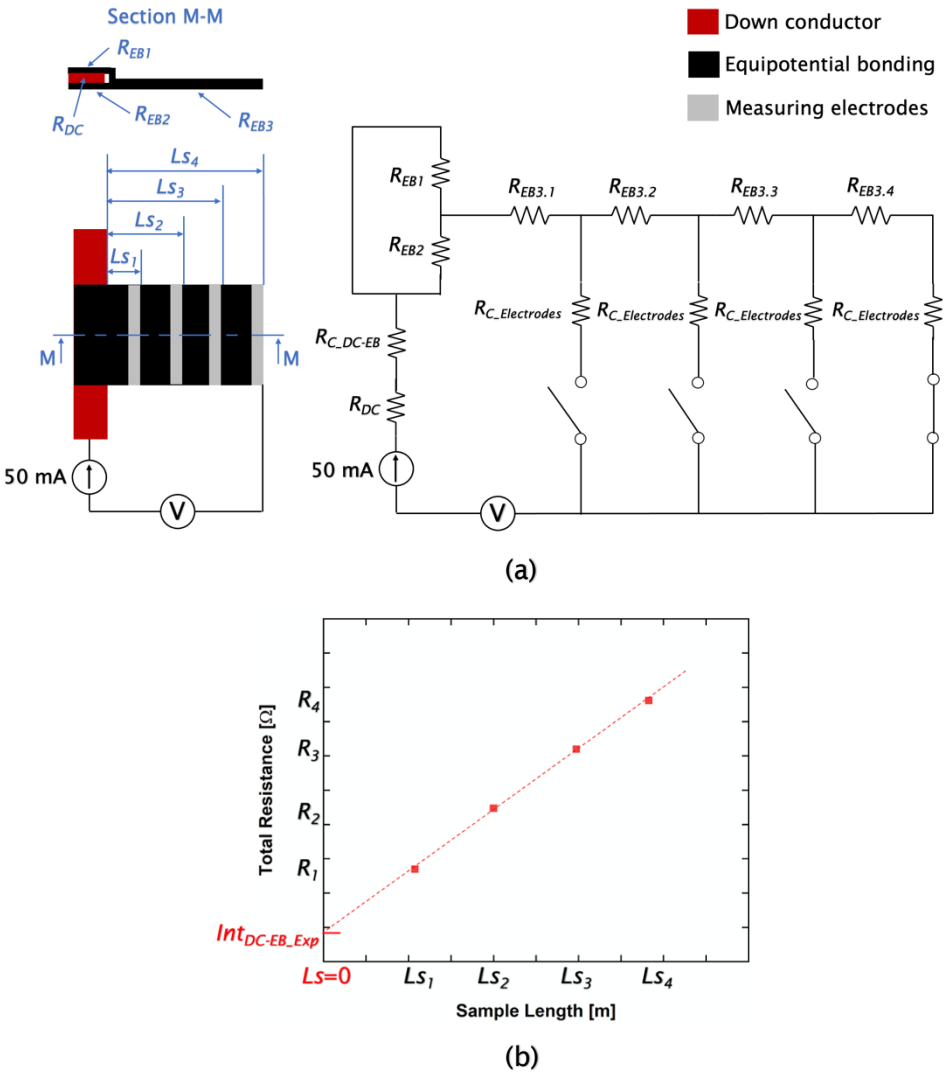

Figure 3.5 – Characterisation of $R_{C\_DC\text{-}EB}$: (a) electric circuit arrangement and (b) interpolation procedure.

The experiment was first performed on the DC-EB sample depicted in Figure 3.5*a*, which was designed to characterise the contact resistance between the DC and EB layers. This system is equivalent to the electric circuit shown in Figure 3.5*a* when considering the contact resistance between the conductors and the contact resistance of the measuring electrodes. The developed procedure required to measure the total resistance at different lengths of the specimen, which was assumed linearly distributed since the resistance of the EB strip is directly proportional to the strip length:

$$R_{DC\text{-}EB\_Tot}(L_S) = R_{DC} + R_{C\_DC\text{-}EB} + \frac{1}{\frac{1}{R_{EB1}} + \frac{1}{R_{EB2}}} + R_{EB3}(L_S) + R_{C\_Electrodes} \quad (3.1)$$

where $R_{DC\text{-}EB\_Tot}$ [Ω] is the total resistance of the DC-EB sample, Ls [m] is the sample length, R_{DC} [Ω] is the resistance of the DC, $R_{C\_DC\text{-}EB}$ [Ω] is the contact resistance between the DC and EB layers (the value to be determined), R_{EB1} [Ω] is the resistance of the EB layer at the top of the DC, R_{EB2} [Ω] is the resistance of the EB layer at the bottom of the DC, R_{EB3} [Ω] is the resistance of the horizontal EB layer, and $R_{C\_Electrodes}$ [Ω] is the contact resistance of the measuring electrodes.

By moving the measuring electrode over the surface of the EB layer we were varying the resistance R_{EB3}, which was zero when $Ls = 0$ (see Figure 3.5*b*). This point corresponded to the y-axis intercept, which was determined after interpolating the measured resistance values:

$$Int_{DC\text{-}EB\_Exp} = R_{DC} + R_{C\_DC\text{-}EB} + \frac{1}{\frac{1}{R_{EB1}} + \frac{1}{R_{EB2}}} + R_{C\_Electrodes} \quad (3.2)$$

where $Int_{DC\text{-}EB\_Exp}$ [Ω] is the experimental y-axis intercept of the DC-EB sample.

As shown in Equation (3.2), the expression of the y-axis intercept included the contact resistance of the measuring electrodes, i.e., $R_{C\_Electrodes}$. This resistance needed to be quantified and subtracted from the y-axis intercept value to avoid an overestimation of the sought contact resistance, i.e., $R_{C\_DC\text{-}EB}$. This was realised by measuring the total resistance of the sample when injecting the current in one measuring electrode and extracting it from the following ones (see Figure 3.6*a*). The values of total resistance measured by this circuit were equal to

$$R_{Tot}(L_S) = R_{EB3}(L_S) + 2R_{C\_Electrodes} \quad (3.3)$$

where R_{Tot} [Ω] is the total resistance of the system depicted in Figure 3.6*a*.

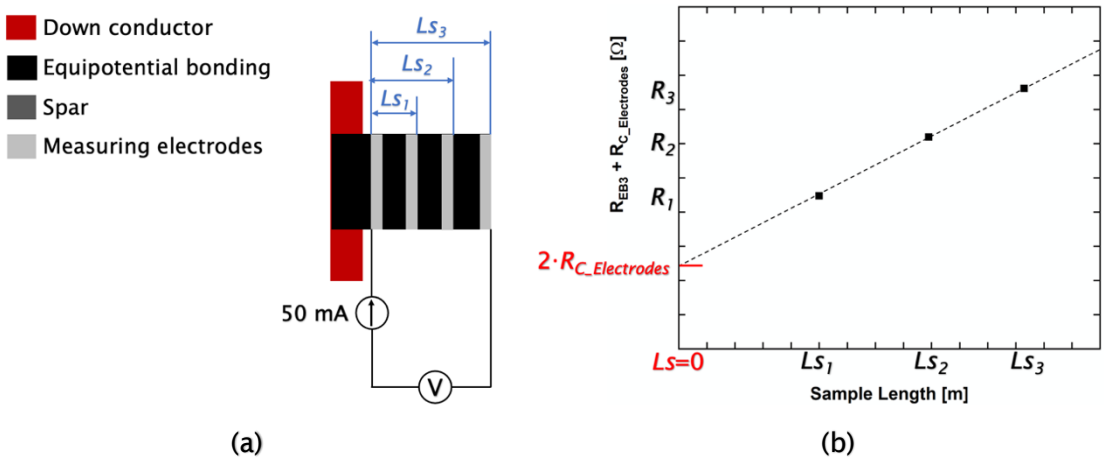

Figure 3.6 – Characterisation of $R_{C\_Electrodes}$ for the DC-EB sample: (a) electric circuit arrangement and (b) interpolation procedure.

The values of measured resistance were interpolated and the y-axis intercept (see Figure 3.6*b*) represented the contact resistance of the measuring electrodes, which was subtracted from Equation (3.2):

$$Int^{Corr}_{DC\text{-}EB\_Exp} = R_{DC} + R_{C\_DC\text{-}EB} + \frac{1}{\frac{1}{R_{EB1}} + \frac{1}{R_{EB2}}} \tag{3.4}$$

where $Int^{Corr}_{DC\text{-}EB\_Exp}$ [Ω] is the experimental y-axis intercept of the DC-EB sample corrected from the contact resistance of the measuring electrodes.

The same procedure was repeated to characterise the total resistance of the DC-EB-Spar sample (see Figure 3.7*a*):

$$R_{DC\text{-}EB\text{-}Spar\_Tot}\,(L_S) = R_{DC} + R_{C\_DC\text{-}EB} + \frac{1}{\frac{1}{R_{EB1}} + \frac{1}{R_{EB2}}} + R_{EB3} + R_{C\_EB\text{-}Spar} + \\ + \frac{1}{\frac{1}{R_{EB4}} + \frac{1}{R_{EB5}} + \frac{1}{R_{EB6}}} + R_{Spar}(L_S) + R_{C\_Electrodes} \tag{3.5}$$

where $R_{DC\text{-}EB\text{-}Spar\_Tot}$ [Ω] is the total resistance of the DC-EB-Spar sample, $R_{C\_EB\text{-}Spar}$ [Ω] is the contact resistance between the EB layers and spar (the value to be determined), R_{EB4} [Ω] is the resistance of the EB layer on the side of the spar,

R_{EB5} [Ω] is the resistance of the EB layer at the bottom of the spar, R_{EB6} [Ω] is the resistance of the EB layer at the top of the spar, and R_{Spar} [Ω] is the resistance of the spar.

The experimental y-axis intercept of the DC-EB-Spar sample was

$$Int_{DC\text{-}EB\text{-}Spar\_Exp} = R_{DC} + R_{C\_DC\text{-}EB} + \frac{1}{\frac{1}{R_{EB1}} + \frac{1}{R_{EB2}}} + R_{EB3} + R_{C\_EB\text{-}Spar} + \\ + \frac{1}{\frac{1}{R_{EB4}} + \frac{1}{R_{EB5}} + \frac{1}{R_{EB6}}} + R_{C\_Electrodes} \quad (3.6)$$

where $Int_{DC\text{-}EB\text{-}Spar\_Exp}$ [Ω] is the experimental y-axis intercept of the DC-EB-Spar sample.

The contact resistance of the measuring electrodes was determined as in Figure 3.7*b* and subtracted from Equation (3.6):

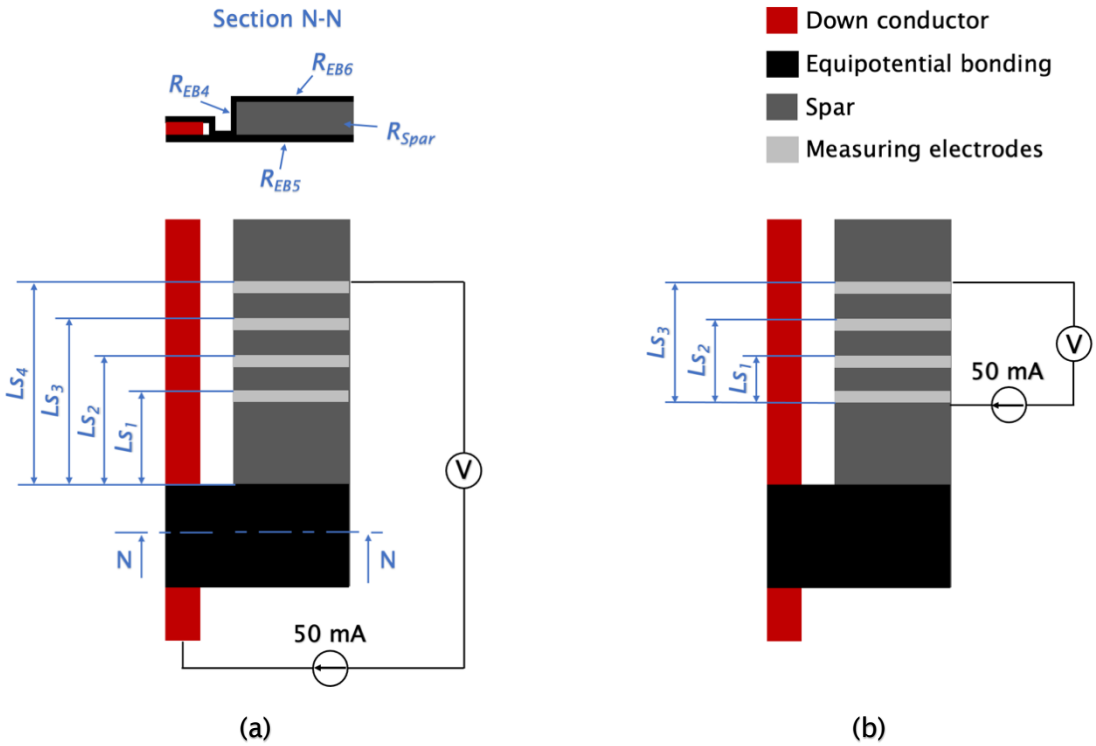

Figure 3.7 – Electric circuit arrangement of the DC-EB-Spar sample for: (a) the characterisation of $R_{C\_EB\text{-}Spar}$ and (b) the characterisation of $R_{C\_Electrodes}$.

$$Int^{Corr}_{DC\text{-}EB\text{-}Spar\_Exp} = R_{DC} + R_{C\_DC\text{-}EB} + \frac{1}{\frac{1}{R_{EB1}} + \frac{1}{R_{EB2}}} + R_{EB3} + R_{C\_EB\text{-}Spar} + \\ + \frac{1}{\frac{1}{R_{EB4}} + \frac{1}{R_{EB5}} + \frac{1}{R_{EB6}}} \tag{3.7}$$

where $Int^{Corr}_{DC\text{-}EB\text{-}Spar\_Exp}$ [Ω] is the experimental y-axis intercept of the DC-EB-Spar sample corrected from the contact resistance of the measuring electrodes.

The values of interface resistance contained in Equations (3.4) and (3.7) can be determined if the resistance of the individual conductors (R_{DC}, R_{EB}, and R_{Spar}) are somehow estimated. This was done by numerical simulations using the electrical conductivity of the employed materials as input parameters.

3.2 Numerical Procedure

Section 3.1.3 presented the experimental procedures employed for the characterisation of the contact resistance of wind turbine blade EB joints. The experimental y-axis intercepts given in Equations (3.4) and (3.7) contained the information of the interface resistances to be determined ($R_{C\_DC\text{-}EB}$ and $R_{C\_EB\text{-}Spar}$) as well as the bulk resistances of the DC, EB, and spar (R_{DC}, R_{EB}, and R_{Spar}). The latter needed to be computed and subtracted from the y-axis intercepts in such a way as to isolate the sought contact resistances. This was not a trivial task since the system presented CFRP components, which behave as spreading resistances [138], [139]. In fact, the spreading of the current within these parts is not identical in the three principal directions because of the strong anisotropy of CFRP materials (up to 4 orders of magnitude variation between longitudinal and through-thickness electrical conductivities). Spreading effects require several complex assumptions for rough analytical estimations. On the other hand, more accurate predictions of current distributions and spreading resistances can be obtained using the FEM [187]–

[189] by specifying the materials' electrical conductivity as input parameters. To this end, the experiment was simulated using COMSOL Multiphysics 5.5.

3.2.1 FEM Implementation

Model Formulation

The objective of the numerical simulations was to quantify the bulk resistances (R_{DC}, R_{EB}, and R_{Spar}) and subtract them from the experimental y-axis intercepts to determine the sought contact resistances ($R_{C\_DC\text{-}EB}$ and $R_{C\_EB\text{-}Spar}$). Therefore, the electric current problem was solved when considering ideal contact between the conductors while solving for the electric potential assuming current conservation [190], [191]:

$$\nabla \bullet (-\boldsymbol{\sigma} \nabla V) = 0 \tag{3.8}$$

where $\nabla\bullet$ is the divergence operator, ∇ is the gradient operator, and V [V] is the electric scalar potential.

Geometry and Material Properties

The geometries of the specimens under testing, i.e., DC-EB and DC-EB-Spar, were modelled in COMSOL Multiphysics 5.5 to predict the spreading resistance. As an example, Figure 3.8*a* illustrates the geometry of the DC-EB-Spar_2 model. The electrical conductivities of the spar, EB, and DC materials are given in Appendix A.

Boundary Conditions

Electric insulation ($\boldsymbol{n} \bullet \boldsymbol{J} = 0$, where $\boldsymbol{n}$ is the outward normal and $\boldsymbol{J}$ [A/m^2] is the conduction current density) was assumed at all outer boundaries of the model, except for the current injection and ground surfaces of the DC and spar, respectively. As an example, the boundary conditions of the DC-EB-Spar_2 model are shown in Figure 3.8*a*.

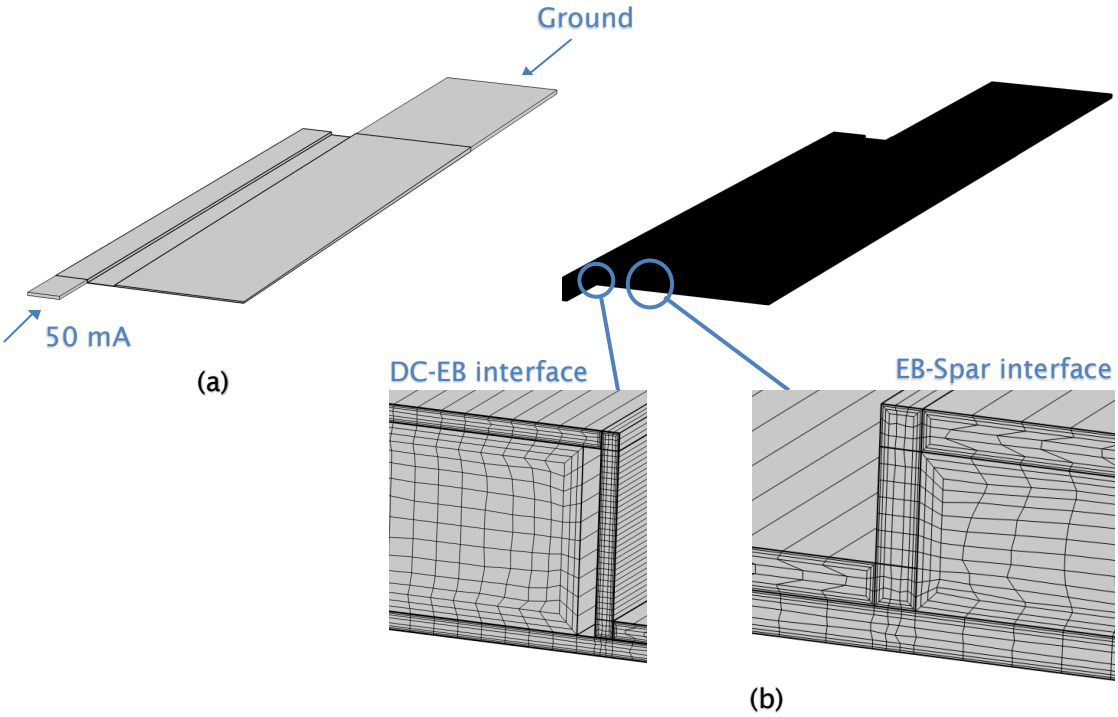

Figure 3.8 – FEM modelling: (a) geometry and boundary conditions and (b) mesh.

Mesh

The automatic mesh refinement option was used to minimise the errors [190], [191] and the final meshes of DC-EB and DC-EB-Spar models consisted of 37,000 and 73,000 hexahedral and boundary layer elements, respectively. Boundary layers were employed to capture non-uniform current density distributions around the bonding interfaces due to the anisotropy of CFRPs. As an example, the mesh of the DC-EB-Spar_2 model is shown in Figure 3.8*b*.

3.2.2 Contact Resistance and Contact Resistivity

When simulating the experiment for the DC-EB sample while assuming ideal contact, the FEM y-axis intercept was equal to (see Figure 3.9)

$$Int_{DC\text{-}EB\_FEM} = R_{DC} + \frac{1}{\frac{1}{R_{EB1}} + \frac{1}{R_{EB2}}} \tag{3.9}$$

where $Int_{DC\text{-}EB\_FEM}$ [Ω] is the FEM y-axis intercept of the DC-EB sample.

On the other hand, the FEM y-axis intercept of the DC-EB-Spar sample when considering ideal contact was

$$Int_{DC\text{-}EB\text{-}Spar\_FEM} = R_{DC} + \frac{1}{\frac{1}{R_{EB1}} + \frac{1}{R_{EB2}}} + R_{EB3} + \frac{1}{\frac{1}{R_{EB4}} + \frac{1}{R_{EB5}} + \frac{1}{R_{EB6}}} \tag{3.10}$$

where $Int_{DC\text{-}EB\text{-}Spar\_FEM}$ [Ω] is the FEM y-axis intercept of the DC-EB-Spar sample.

By taking the difference between Equations (3.4) and (3.9), it was possible to determine the contact resistance between the DC and EB layers:

$$R_{C\_DC\text{-}EB} = Int^{Corr}_{DC\text{-}EB\_Exp} - Int_{DC\text{-}EB\_FEM} \tag{3.11}$$

Similarly, by taking the difference between Equations (3.7) and (3.10), and subtracting the contact resistance $R_{C\_DC\text{-}EB}$ found by Equation (3.11), it was possible to determine the contact resistance between the EB layers and spar:

$$R_{C\_EB\text{-}Spar} = Int^{Corr}_{DC\text{-}EB\text{-}Spar\_Exp} - Int_{DC\text{-}EB\text{-}Spar\_FEM} - R_{C\_DC\text{-}EB} \tag{3.12}$$

Finally, commercial FEM packages (COMSOL Multiphysics as well as others) model electrical contacts as homogeneous surface conditions [190], [191]. Consequently, it was required to determine the contact resistivity by multiplying the interface resistance by the contact surface [192]–[197]:

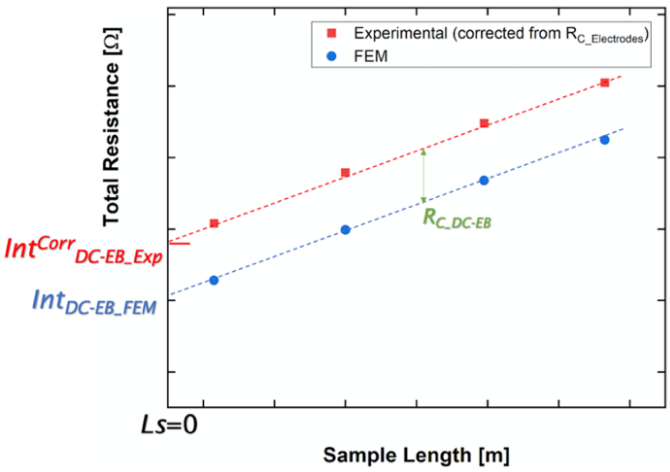

Figure 3.9 – Schematic of the procedure to estimate the contact resistance.

$$\rho_{C\_DC\text{-}EB} = R_{C\_DC\text{-}EB}\, A_{C\_DC\text{-}EB} \tag{3.13}$$

and

$$\rho_{C\_EB\text{-}Spar} = R_{C\_EB\text{-}Spar}\, A_{C\_EB\text{-}Spar} \tag{3.14}$$

where $\rho_{C\_DC\text{-}EB}$ [$\Omega \cdot m^2$] is the contact resistivity between the DC and EB layers, $A_{C\_DC\text{-}EB}$ [m^2] is the contact surface between the DC and EB layers, $\rho_{C\_EB\text{-}Spar}$ [$\Omega \cdot m^2$] is the contact resistivity between the EB layers and spar, and $A_{C\_EB\text{-}Spar}$ [m^2] is the contact surface between the EB layers and spar.

Note that since the contact area between the DC and EB layers is the same for both DC-EB and DC-EB-Spar_1 samples (i.e., 0.00456 m^2, see Figure 3.3), $R_{C\_DC\text{-}EB}$ was directly subtracted in Equation (3.12) to isolate the term $R_{C\_EB\text{-}Spar}$. However, this contact area is larger in the chamfered samples (see Figure 3.4), and the contact resistance $R_{C\_DC\text{-}EB}$ to be subtracted in Equation (3.12) needed to be determined from the contact resistivity $\rho_{C\_DC\text{-}EB}$ as in Equation (3.15):

$$R_{C\_DC\text{-}EB}^{Chamfer} = \frac{\rho_{C\_DC\text{-}EB}}{A_{C\_DC\text{-}EB}^{Chamfer}} \tag{3.15}$$

where $R_{C\_DC\text{-}EB}^{Chamfer}$ [Ω] is the contact resistance between the DC and EB layers for the chamfered samples and $A_{C\_DC\text{-}EB}^{Chamfer}$ [m^2] is the contact surface between the DC and EB layers for the chamfered samples.

3.3 Results and Discussion

3.3.1 Error Analysis

The possible sources of random and systematic error of the developed procedure were identified in order to take suitable control measures and minimise them.

Resistance Measurements: Random and Systematic Errors

According to the manufacturer datasheet, the AIM TTi BS-407 low resistance ohmmeter presents 0.1% accuracy [198], which contributed to the random error of the measurements. However, systematic errors might be introduced by the employed ohmmeter if not calibrated. The instrument calibration was evaluated before starting the experiment by measuring (using the same test leads and crocodile clips) three different shunt resistances (1, 10, and 68 Ω), and the returned values were within 0.1% of the nominal ones. Four samples per each bonding configuration were assessed to account for the manufacturing random error introduced by geometrical variations, variability in volume fraction of the constituent materials, etc. The sample-to-sample differences in experimental y-axis intercept (standard deviations in Table 3.1) were up to 0.2, 5, and 13% for UD, BIAX, and ECF EB configurations, respectively. On the other hand, multiple measurements on the same sample produced an uncertainty of less than 0.1%. Since the manufacturing process was clearly the main source of random error, it was decided not to investigate the variation of measured resistance on the same sample.

Before conducting the experiment, it was important to consider the position of the measuring electrodes realised over the spar laminate. As the current is injected into the spar from its side, top, and bottom surfaces through the EB layers, it might initially remain confined in the outer layers because of the strong anisotropy of CFRP materials (see the current density streamlines in Figure 3.10). In such conditions, the linear relationship between the total resistance and length assumed in Equations (3.1) and (3.5) would not be satisfied. To avoid this, it is necessary to place the measuring electrodes at a sufficient distance from the injection area (i.e., the EB region), in such a way that the current can spread through the entire spar thickness. The correct positions of the measuring electrodes were found by FEM simulations before the experiment. The ground boundary condition (i.e., the measuring electrode in the experimental setup) was adjusted over the spar surface and the

variation of the total resistance as a function of the sample length was investigated. Figure 3.10 shows, in the case of BIAX_DC-EB-Spar_1, that the linearity between the total resistance and length is lost when the distance between the EB layers and the ground position is smaller than 60 mm. Consequently, it was decided to place the measuring electrodes in the last 100 mm of the spar where the current is uniformly distributed through the spar thickness and the linearity between total resistance and length satisfied.

To prevent incorrect readings due to a poor ohmic contact with the carbon fibres, it was required to apply pressure over the measuring electrode surface. The systematic error due to surface roughness was reduced to around 1% when applying 20 MPa, as shown in Figure 3.11. Note that the change in resistance when applying 20 MPa is 2 orders of magnitude smaller than the measured sample resistance. However, it is comparable to the contact resistance to be determined, which would be overestimated if the application of pressure was neglected.

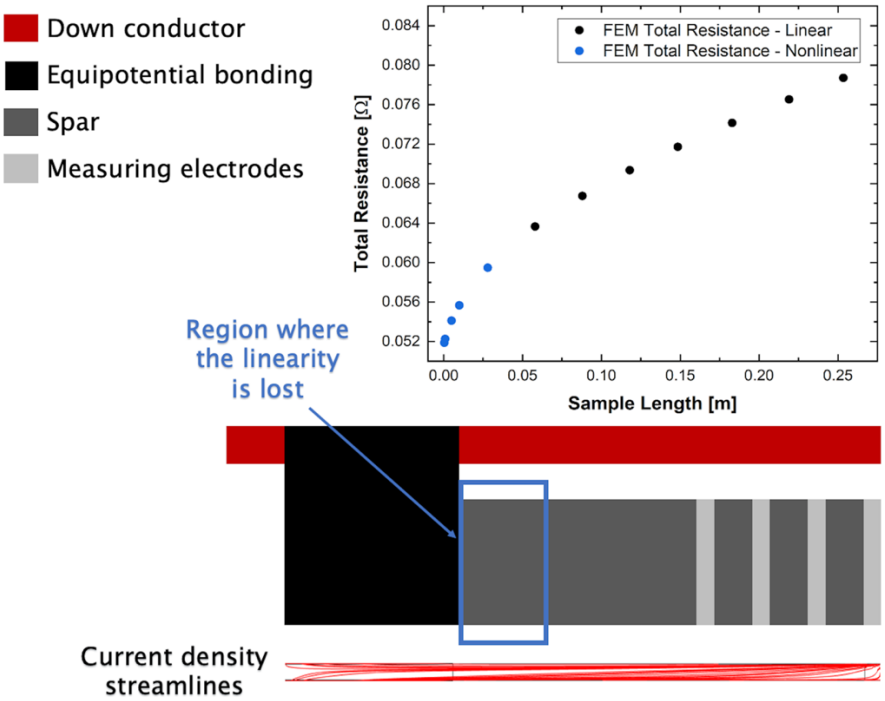

Figure 3.10 – Positions of measuring electrodes to satisfy the linear relationship between measured resistance and length, and current streamlines within the spar.

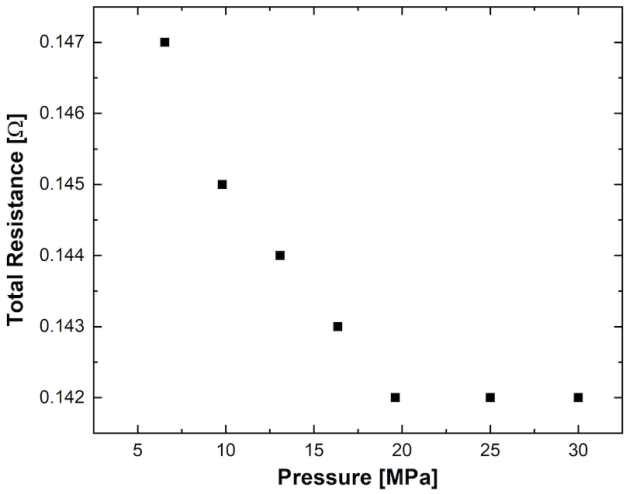

Figure 3.11 – Variation of total resistance as a function of pressure.

The contact resistance of the measuring electrodes (that is, $R_{C\_Electrodes}$) needed to be deducted from the y-axis intercept to avoid inaccurate estimations of the sought interface resistances (i.e., $R_{C\_DC\text{-}EB}$ and $R_{C\_EB\text{-}Spar}$). The measuring electrodes contact resistance comprises the following terms: the contact resistance between the silver paint-copper tape and carbon fibres; the contact resistance between the silver paint-copper tape and test leads crocodile clips; and the contact resistance between the test leads. Highly conductive materials were utilised to reduce the resistance of the measuring electrodes: silver paint with an electrical conductivity of 1×10^5 S/m; and copper tape with an electrical conductivity equal to 5.998×10^7 S/m. Such materials have effectively been employed for CFRP resistance measurements in previous research [30]–[33], [126]. Despite the employment of materials with high electrical conductivity, the measuring electrodes contact resistances were still significant, e.g., up to 60% of the y-axis intercept in the ECF EB configurations (see Table 3.1).

Systematic Error Introduced by the Experimental-Numerical Approach

The main systematic error source of the developed procedure (combination of experimental and numerical methods) was represented by the estimation of the spreading resistance around the contacts. In fact, the prediction of this resistance depends on the assumptions and modelling strategies

implemented in the numerical simulations. First, the uncertainty was introduced when assuming ideal contact condition, which was used to calculate the combined resistance of DC, spar, and EB layers given in Equations (3.9) and (3.10). Such a condition assumes that all the contact points at the interface regions do not experience any resistance, which affects the distribution of the current in the spar and thus the value of spreading resistance. Second, commercial FEM packages model electrical contacts as homogeneous surface conditions, that is, all the points of the interface are in contact and experience the same contact quality. This is not the case of real bonding interfaces as they do not experience contact at all points, nor with the same quality. In fact, there are areas of the interface where the conducting parts are in contact with each other and other areas where they are separated by the resin. The homogeneous contact condition influenced the way the current entered and distributed within the spar and thus the prediction of the spreading and spar resistances in the simulations.

The procedure uncertainty was quantified by comparing the experimental total resistances with the FEM ones computed with the contact resistances included in the model. According to the results given in Figures 3.12 to 3.14 and Table 3.1, the observed discrepancies were more prominent for the ECF and UD CFRP samples, which were ~10% of their calculated contact resistances. On the other hand, BIAX CFRP presented uncertainties close to 5% of its contact resistances. The percentage uncertainty of the contact resistivity was assumed equal to the percentage uncertainty of the contact resistance since the percentage uncertainty of the contact area was negligible. Experimental and FEM results also differed in the value of the spar resistance (i.e., the slope of the linear fitting) since the spar spreading resistance was affected by the modelling strategies of the numerical analysis, as outlined in the previous paragraph. When comparing ECF and BIAX EB configurations, it is noted that they were characterised by slightly different experimental slopes

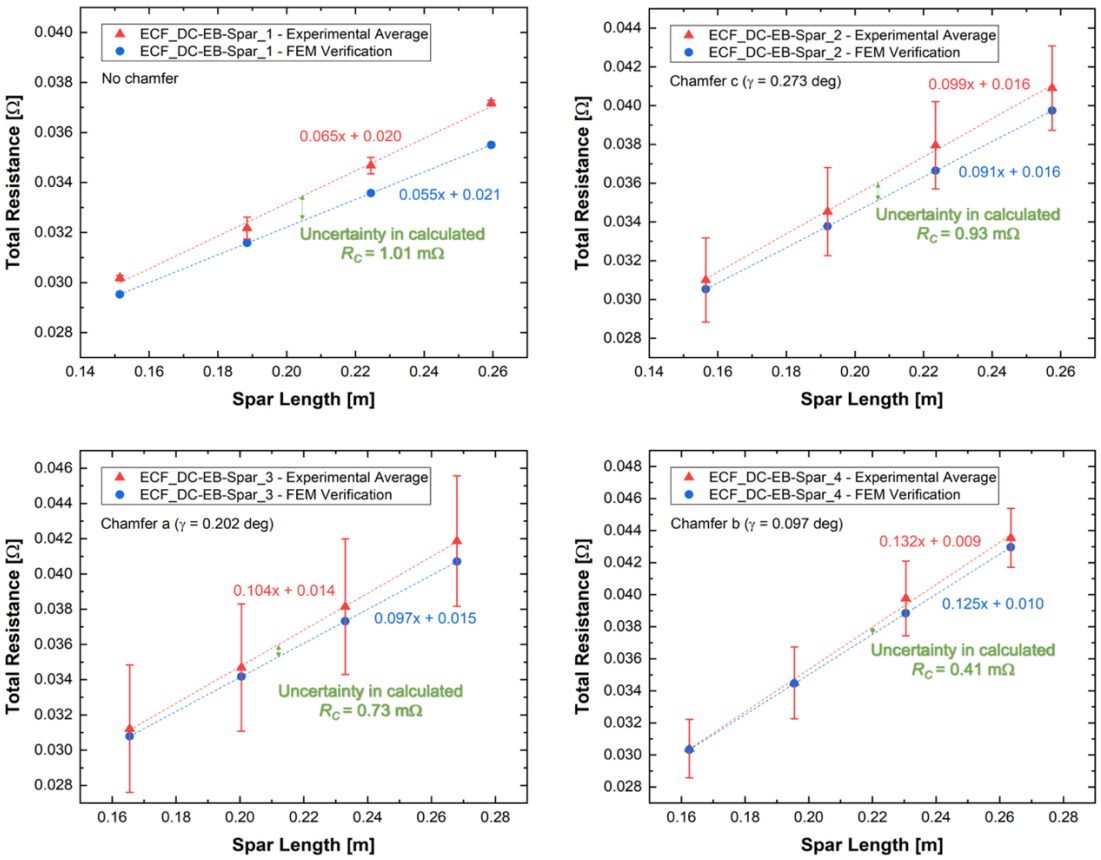

Figure 3.12 – ECF EB configurations: experimental and FEM total resistances. The error bars denote the standard deviation.

and thus by different spar resistances. The small difference between the experimental slopes of ECF and BIAX CFRP (i.e., the small increase in apparent spar resistance in ECF EB configurations) should be due to the inherent shape of the ECF sheets (see Figure A.1), which consists of several wires and diamond openings. The latter reduce the contact surface between the ECF and spar layers and increase the spreading resistance in the spar and thus the measured spar resistance. This conclusion is supported by the fact that the FEM slopes (i.e., the FEM spar resistances) of both ECF and BIAX CFRP were similar. The difference between the slopes of ECF and BIAX CFRP could not accurately be captured by the numerical simulations since the ECF layers were modelled as uniform sheets having anisotropic (effective) electrical

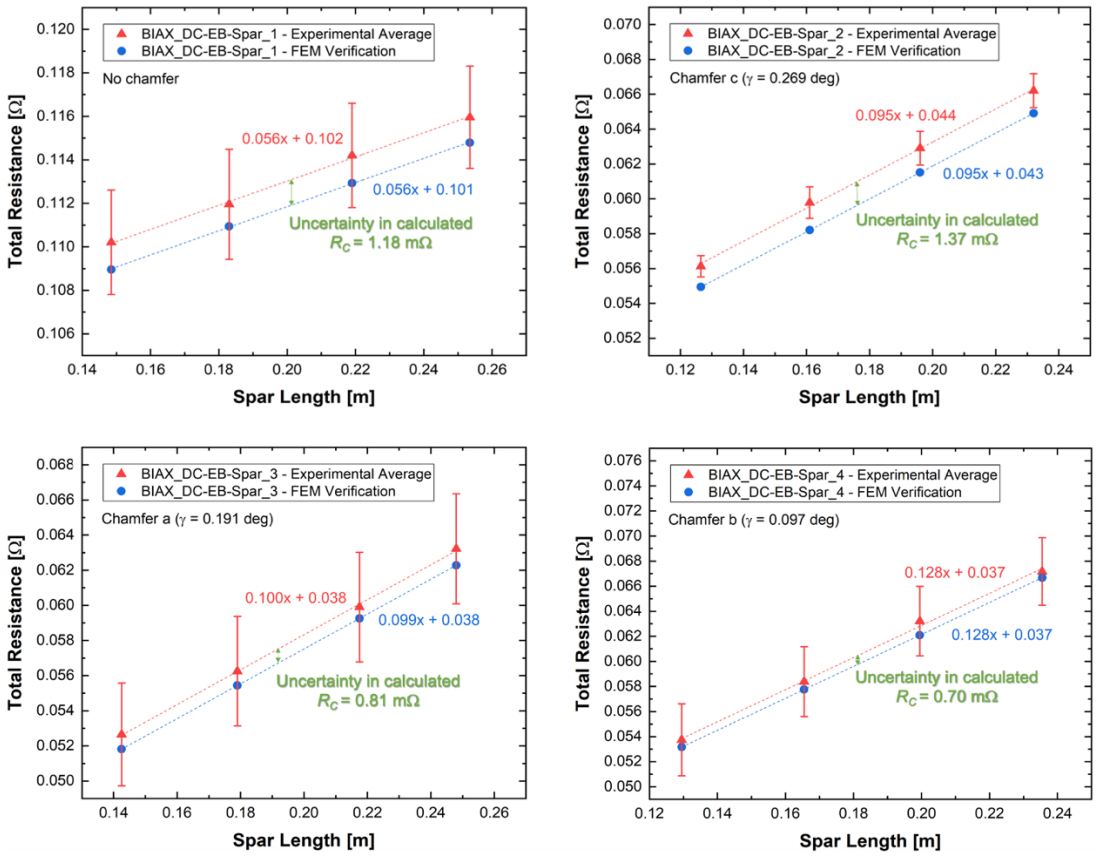

Figure 3.13 – BIAX EB configurations: experimental and FEM total resistances. The error bars denote the standard deviation.

conductivity rather than the actual open-area structure. Higher accuracy would be obtained if the real ECF geometry was modelled, although it would be completely unpractical. For this reason and considering the low contact resistances provided by ECF material, it was decided to accept the 10% uncertainties in the calculated contact resistances. On the other hand, the slope of the UD EB configurations was nearly ten times larger than the slopes of both ECF and BIAX EB configurations because of a highly non-uniform current density distribution in the spar. This was due to the low transverse electrical conductivity of the UD CFRP material, which did not allow the current to spread on the entire contact surfaces with the spar. This increased the spar and total resistances of the UD EB configurations by ~1 order of magnitude.

To conclude, the assumptions and modelling strategies adopted in the

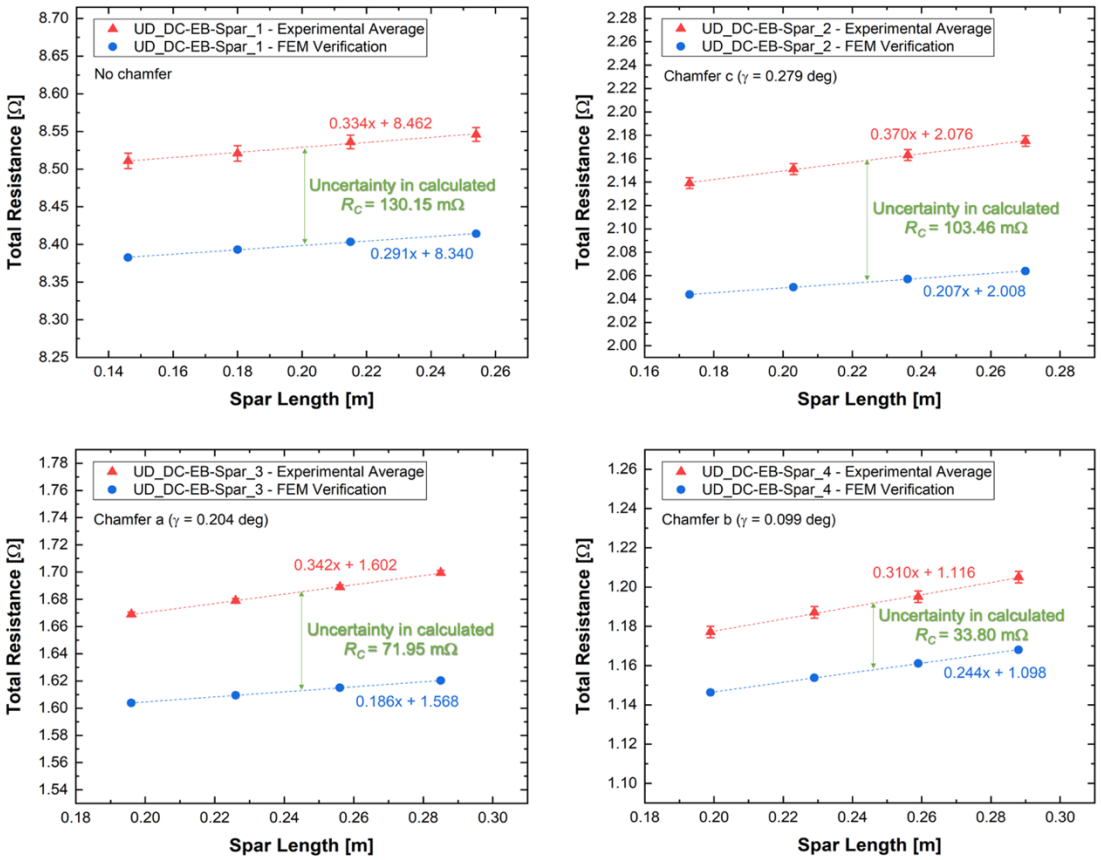

Figure 3.14 – UD EB configurations: experimental and FEM total resistances. The error bars denote the standard deviation.

numerical simulations (i.e., the initial ideal contact condition and the homogeneous modelling of electrical contact) did not significantly affect the results since the uncertainties of the procedure were approximately 1 order of magnitude smaller than the contact resistances. Therefore, it is safe to assume that the presented methodology (combination of experimental and numerical techniques) is reliable and allows to characterise the electrical contact of wind turbine blade EB joints.

3.3.2 Y-Axis Intercept, Contact Resistance, and Contact Resistivity

Y-axis intercept, contact resistance, and contact resistivity results (average and standard deviation) are given in Table 3.1. The mean and standard

Table 3.1 – Results of DC-EB and DC-EB-Spar samples: y-axis intercept, contact resistance, and contact resistivity.

Configuration	Int_{Exp} [mΩ]	Int^{Corr}_{Exp} [mΩ]	Int_{FEM} [mΩ]	R_C [mΩ]	ρ_C [mΩ·m²]
UD_DC-EB	888.90 ± 1.08	876.55 ± 4.96	836.78	39.77 ± 2.13	0.18 ± 0.01
BIAX_DC-EB	32.39 ± 4.11	22.65 ± 6.08	15.82	6.83 ± 0.20	0.03 ± 0.001
ECF_DC-EB	5.05 ± 0.04	4.95 ± 0.04	2.96	1.99 ± 0.17	0.01 ± 0.001
UD_DC-EB-Spar_1	8,496.18 ± 13.80	8,462.15 ± 14.95	6,031.81	2,390.57 ± 130.15	49.01 ± 2.67
UD_DC-EB-Spar_2 (γ = 0.279°)	2,095.40 ± 4.58	2,075.56 ± 4.60	1,317.43	750.33 ± 103.46	69.67 ± 9.61
UD_DC-EB-Spar_3 (γ = 0.204°)	1,621.36 ± 1.22	1,601.81 ± 1.58	1,029.99	565.97 ± 71.95	70.05 ± 8.91
UD_DC-EB-Spar_4 (γ = 0.099°)	1,131.20 ± 2.69	1,115.31 ± 2.90	824.94	286.04 ± 33.80	47.79 ± 5.65
BIAX_DC-EB-Spar_1	128.96 ± 1.76	101.91 ± 2.60	61.90	33.19 ± 1.18	0.68 ± 0.02
BIAX_DC-EB-Spar_2 (γ = 0.269°)	80.37 ± 0.56	44.33 ± 0.66	25.71	17.28 ± 1.37	1.64 ± 0.13
BIAX_DC-EB-Spar_3 (γ = 0.191°)	72.29 ± 2.19	38.44 ± 3.12	25.43	12.01 ± 0.81	1.52 ± 0.10
BIAX_DC-EB-Spar_4 (γ = 0.097°)	66.23 ± 2.08	37.27 ± 3.14	29.28	7.25 ± 0.70	1.25 ± 0.12
ECF_DC-EB-Spar_1	38.93 ± 0.34	20.11 ± 0.35	8.17	9.94 ± 1.01	0.20 ± 0.02
ECF_DC-EB-Spar_2 (γ = 0.273°)	40.49 ± 1.36	15.58 ± 2.19	5.54	9.64 ± 0.93	0.92 ± 0.09
ECF_DC-EB-Spar_3 (γ = 0.202°)	40.59 ± 1.92	13.90 ± 3.19	5.90	7.72 ± 0.73	0.94 ± 0.09
ECF_DC-EB-Spar_4 (γ = 0.097°)	22.84 ± 0.74	8.84 ± 1.21	5.56	3.06 ± 0.41	0.53 ± 0.07

deviation values were quantified by conducting the experiment on four samples per each bonding configuration.
Both the contact region between the DC and EB layers and the contact region between the EB layers and spar showed the same trend in terms of contact resistivity. In fact, the best contact was assured by ECF and BIAX CFRP, which presented contact resistivities from 1 to 2 orders of magnitude smaller than UD CFRP. In addition, the contact resistivity on the spar surfaces was larger than the one on the DC surfaces for all the assessed materials. This indicates that a worse contact was obtained at the spar interfaces.

3.3.3 Final Considerations on the Assessed EB materials

Lower values of contact resistance are found on the chamfered surfaces for all the assessed EB materials. This is due to the fact that more contact points are obtained between the EB layers and spar carbon fabrics. In fact, while in the non-chamfered samples (DC-EB-Spar_1) the contact occurs on the side, top, and bottom surfaces of the spar only, in the chamfered specimens the contact is also established with the cross-section of each spar layer. In addition, Figure 3.15 shows that the smaller the chamfer angle is, the better the contact becomes (i.e., lower contact resistance), which might suggest that the number of contact points grows as the spar thickness varies gradually.

Final considerations are made on the assessed materials based on the electrical contact results given in Table 3.1. However, no definitive conclusion can be drawn on their performance as an EB material without verifying their response under simulated lightning currents [12], [24] (see Chapter 7). ECF exhibits the lowest values of contact resistivity and thus the best contact behaviour compared with the other materials. Although the contact resistivities provided by BIAX CFRP are ~1 order of magnitude higher than the ECF ones, it can still be considered a good candidate for EB applications

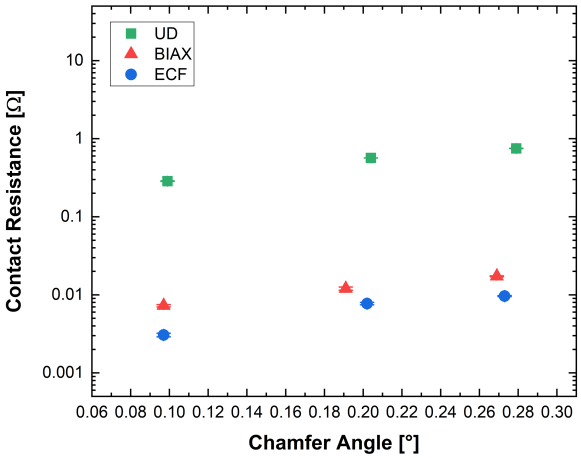

Figure 3.15 – Variation of $R_{C\_EB\text{-}Spar}$ as a function of chamfer angle.

thanks to the high in-plane electrical conductivities. However, the same does not hold for UD CFRP since it presents contact resistivities that are 2 orders of magnitude larger than the ECF contact resistivities. One reason for the superior contact behaviour provided by the ECF layers is the morphology of this material. In fact, the thick and stiff ECF strands exert a higher pressure over the spar carbon fibres during the vacuum infusion process, which squeezes the resin into the diamond openings. In this way more contact points are obtained between the ECF wires and the spar carbon fibres, reducing the local contact resistance. Furthermore, the high electrical conductivity of this material (from 3 to 7 orders of magnitude larger than the CFRP electrical conductivities) assures lower local resistances at the physical contact points [73], [199], [200]. On the other hand, carbon fibres are more flexible due to their small diameter (~1-10 μm [122]). As a consequence, most of the resin concentrates in between the EB and spar layers (i.e., the contact interfaces) and forms resin-rich interlaminar regions. In addition, the formation of interlaminar resin areas is also favoured by fibre volume fractions larger than 50% as carbon fibres are arranged in close proximity to one another and impede the resin to infiltrate in between them [33], [201], [202]. Hence, in the case of carbon fibre-based EB layers, a higher concentration of resin at the contact areas leads to larger values of local resistance at the contact points. In the case of UD CFRP, the contact

performance is further diminished by the low transverse electrical conductivity of this material, which does not allow the current to spread over the entire interface surfaces, reducing the amount of local contact points. The limitation in conduction capability of CFRP materials caused by both the carbon fibres anisotropy and the presence of resin-reach interlaminar regions is a well-known issue. Recent research has proposed various methods for improving the electrical conductivity of CFRPs [33]–[35]. For this particular case, the electrical contact behaviour might be improved by the dispersion of conducting nanofillers within the epoxy matrix [36]–[39]. These particles would reduce the local resistance at the contact points, as well as they would enhance the transverse electrical conductivity. The latter would also facilitate the current spreading on the spar contact surfaces in the case of UD EB.

Finally, past research shows that the contact resistivity of CFRPs decreases with increasing temperatures [184]–[186]. Furthermore, this change appears to be inversely proportional to the change in through-thickness electrical conductivity of the bulk CFRP. For instance, a drop in contact resistivity of ~10-20% from 20 to 150 °C roughly corresponds to an increase of ~10-20% in bulk through-thickness electrical conductivity [181], [182], [184], [185]. On the other hand, this study considers the ambient temperature case in order to investigate the scenario with the highest contact resistivity. As a result, the Joule heating at the interface regions would be overestimated when ambient temperature values of contact resistivity are implemented in FEM models to predict the lightning current damage in the joint. Therefore, the use of ambient temperature contact resistivities in numerical simulations should mainly be limited to the identification of the damage onset and location, while no exact information can be provided on the extent of damage.

3.4 Summary

This chapter presented an alternative approach to estimate the electrical contact behaviour of complex joints such as equipotential connections used

for wind turbine blades lightning protection. For such assemblies, the use of the standard two-probe method alone results to be unsuccessful because of the spreading effects in CFRP components and of the complicated geometrical arrangement (the samples are encapsulated within insulating GFRP layers representing the blade shell). In order to overcome them and determine the contact resistance, the developed procedure combines experimental measurements with FEM simulations.

The experiment was conducted at ambient temperature to assess the electrical contact in the worst-case scenario, i.e., the case with the highest electrical contact resistivity. The procedure showed good accuracy when applied to three different EB materials, i.e., UD CFRP, BIAX CFRP, and ECF. The observed uncertainties between the experimental and numerical total resistances were within 10%. These discrepancies were due to the assumptions and modelling strategies made in the FEM simulations. That is, the initial ideal contact condition (to compute the bulk resistances of the conducting parts) and the homogeneous electrical contact condition. Both ECF and BIAX CFRP assured better contacts than UD CFRP thanks to their high in-plane electrical conductivities (larger than 10^4 S/m). For all the assessed EB materials, the contact resistance was reduced on the chamfered surfaces and lower values of contact resistance were found as the chamfer angle was decreased. This trend indicated that more contact points were established between the EB layers and the chamfered layers of the spar.

Finally, it is known that the contact resistivity decreases with increasing temperatures. As a result, the implementation of ambient temperature values in FEM models to predict lightning current damage would lead to an overestimation of the Joule heating at the bonding interfaces. Thus, the use of ambient temperature contact resistivities should mainly be limited to estimate the damage onset and location in the joint.

Chapter 4

Thermal Degradation of Epoxy Resin

In this chapter the Hexion epoxy resin system is subjected to TGA to determine the degradation mechanisms responsible for voids formation and sparks in EB joints and their reaction kinetics. The latter are needed in the FEM simulations to model the thermal degradation process due to lightning strike induced temperature profiles and predict the locations where sparks might develop.

4.1 Experimental Procedure

4.1.1 Sample Preparation

The epoxy resin samples were obtained by curing the Hexion epoxy system under vacuum. First, a flat mould was treated with 2-3 layers of release agent to facilitate the de-moulding procedure. The Hexion RIMR035c epoxy resin was mixed with the Hexion RIMH037 hardener at a 100:20 ratio as suggested by the manufacturer, and then degassed for 30 min in a vacuum chamber. A vacuum tube connected to a pump was placed in position to remove the air from the mould. After the completion of the degassing, the resin was poured

into the mould while simultaneously applying vacuum. Finally, the resin was cured for 6 h at 70 ˚C [36]–[39] following the instructions of the manufacturer.

4.1.2 Characterisation of Polymer Thermal Degradation by TGA

The TGA experiment was performed using a Perkin Elmer Pyris 1 TGA analyser [203], which is composed of (see Figure 4.1): a hang-down quartz wire; a balance connected to the hang-down wire, which quantifies the weight of the assessed specimen; a platinum sample pan hanged on the quartz wire; a furnace where the degradation reaction occurs; and a thermocouple to measure the temperature. The Perkin Elmer Pyris 1 TGA analyser can heat the assessed sample from ambient temperature to 1,000 ˚C at a constant heating rate that can range from 0.1 to 200 ˚C/min. In addition, the pyrolysis process can take place in either oxygen or nitrogen environment [203], [204].
The TGA analyser was calibrated by a manufacturer technician before the experiment. The assessed samples were subjected to the following heating procedure:

- Isothermal at 60 ˚C for 2 min in nitrogen environment.
- Heating from 60 to 900 ˚C at a constant heating rate in nitrogen environment.
- Isothermal at 900 ˚C for 30 min in air environment, to burn residues and avoid blocking the device vents.
- End condition, i.e., cooling from 900 to 60 ˚C.

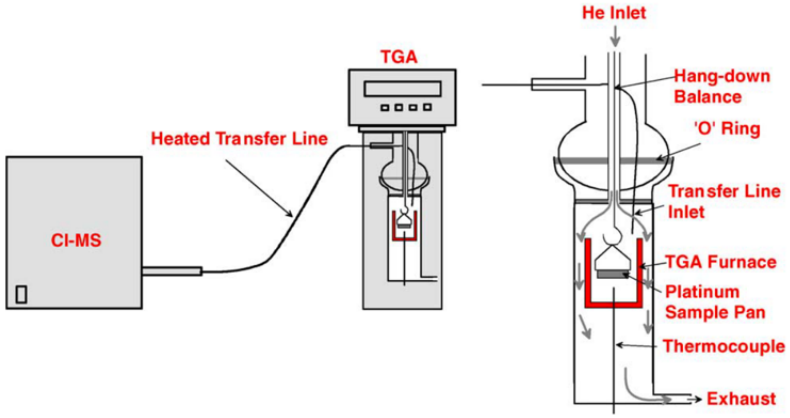

Figure 4.1 – Schematic of the Perkin Elmer Pyris 1 TGA analyser internal components [204].

The above heating method was performed for the following heating rates: 0.2, 0.5, 1, 2, 5, 10, 20, 50, 100, 150, and 200 °C/min.

4.2 Modelling of Thermal Degradation

4.2.1 Arrhenius Equation

Although the pyrolysis process of cured epoxy resins is usually described as an apparent single reaction, in reality, it develops into four different mechanisms [159], [166], [167] (see Section 2.5.4). These are, hereafter, abbreviated as follows: mechanism 1 (release of absorbed moisture), mechanism 2 (dehydration reaction), mechanism 3 (allylic bonds), mechanism 4 (random scission).

Previous lightning protection studies [108], [161], or similar high heating rate applications like polymer laser processing [205], [206], have modelled the pyrolysis process through the Arrhenius equation:

$$\frac{\mathrm{d}\alpha}{\mathrm{d}t} = \underbrace{A\,[1-\alpha(t)]^{n}\,e^{-\frac{E_a}{RT_a}}}_{\text{Apparent single reaction model}} = \underbrace{\sum_{i=1}^{4} A_i\,[1-\alpha_i(t)]\,e^{-\frac{E_{a,i}}{RT_i}}}_{\text{Deconvoluted reactions model}} \tag{4.1}$$

where $\frac{\mathrm{d}\alpha}{\mathrm{d}t}$ [1/s] is the degradation rate or reaction rate (speed of pyrolysis), A [1/s] is the pre-exponential factor of the apparent single reaction, $\alpha(t)$ is the degree of thermal degradation of the apparent single reaction, n is the reaction order, E_a [J/mol] is the activation energy of the apparent single reaction, R [J/(mol·K)] is the molar gas constant, T_a [K] is the temperature of the apparent single reaction, A_i [1/s] is the pre-exponential factor of the i-th degradation mechanism, $\alpha_i(t)$ is the degree of thermal degradation of the i-th degradation mechanism, $E_{a,i}$ [J/mol] is the activation energy of the i-th degradation mechanism, and T_i [K] is the temperature of the i-th degradation mechanism.

The degree of thermal degradation of each mechanism is defined as [207]

$$\alpha_i(t) = \frac{m_p(t_0) - m_{p,i}(t)}{m_p(t_0) - m_{p,i}(t_\infty)}, \qquad \alpha(t) = \sum_{i=1}^{4} \alpha_i(t) \tag{4.2}$$

where $m_p(t_0)$ [kg] is the initial polymer mass, $m_{p,i}(t)$ [kg] is the instantaneous polymer mass of the *i*-th degradation mechanism, and $m_{p,i}(t_\infty)$ [kg] is the final polymer mass of the *i*-th degradation mechanism.

4.2.2 Reaction Kinetics: Kissinger Method

The parameters E_a, n, and A define the pyrolysis process and are called reaction kinetics. In this study they were computed by the TGA and DTGA curves using the Kissinger method [208]. It is a differential method based on the fact that, for a given heating rate, the first time derivative of the TGA curve (i.e., the DTGA curve) reaches a maximum at a certain temperature [209]:

$$\ln\left(\frac{\beta}{T_m^2}\right) = \text{const} - \frac{E_a}{R}\frac{1}{T_m} \tag{4.3}$$

where β [K/s] is the heating rate and T_m [K] is the temperature at maximum degradation rate.

The activation energy is the energy required for the degradation reaction [208], [209]. It was determined from the slope of the linear plot given in Equation (4.3) after measuring experimental values of T_m at different β [208]. The reaction order expresses the degree of asymmetry of the DTGA curve [208]. It was assumed equal to 1 when considering the deconvoluted description of the degradation process. On the other hand, it was larger than 1 for the apparent single reaction description, and it was determined from the tangents at the inflection points of the DTGA curve [208]:

$$n = 1.26\sqrt{\left|\frac{\left(\frac{d^2\Gamma}{dt^2}\right)_{t=t_{Flex\ 2}}}{\left(\frac{d^2\Gamma}{dt^2}\right)_{t=t_{Flex\ 1}}}\right|} \tag{4.4}$$

where Γ [%] is the mass fraction of the polymer, $\frac{d^2\Gamma}{dt^2}$ [%/s^2] is the second time derivative of the mass fraction of the polymer, t_{Flex1} [s] is the time at the first inflection point, and t_{Flex2} [s] is the time at the second inflection point.

The inflection points were found where the second time derivative of the DTGA curve is zero [208], [210], [211]:

$$\frac{d^2}{dt^2}\left(\frac{d\Gamma}{dt}\right) = \frac{d^3\Gamma}{dt^3} = 0 \rightarrow (t_{Flex1}, t_{Flex2}) \tag{4.5}$$

where $\frac{d\Gamma}{dt}$ [%/s] is the first time derivative of the mass fraction of the polymer and $\frac{d^3\Gamma}{dt^3}$ [%/s^3] is the third time derivative of the mass fraction of the polymer.

The first, second, and third time derivatives were computed from the TGA plots using OriginLab commercial software. To remove the experimental noise, the first time derivative plots of the low heating rate procedures were smoothed by the standard adjacent averaging method. The inflection points and the second time derivative values at the inflection points were found manually using the generated third and second time derivatives plots, respectively.

Finally, the pre-exponential factor defines the rate at which the pyrolysis reaction occurs and was found by [208]:

$$A = \frac{\frac{E_a\beta}{RT_m^2}}{\left[1 + (n-1)\frac{2RT_m}{E_a}\right]e^{-\frac{E_a}{RT_m}}} \tag{4.6}$$

4.3 Results and Discussion

4.3.1 TGA and DTGA Curves - Apparent Single Reaction Model

The TGA curves describing the epoxy thermal degradation process are shown in Figure 4.2a for the assessed heating rates. Values of degradation onset temperature, T_{onset} [K], can be extrapolated from the TGA curves according to the procedure reported in the ASTM E2550-17 standard [212]. They are given by the intersection of the baseline (horizontal line) and the tangent line after the degradation occurs [213]–[216]. On the other hand, the first derivative of the TGA curves (see the DTGA curves plotted in Figure 4.2b) allows to determine the temperature at maximum degradation rate. Both T_{onset} and T_m values increase with higher heating rates [102], [149], [160], as shown in Figure 4.2.

4.3.2 TGA and DTGA Curves – Deconvoluted Reactions Model

The experimental DTGA curves have been deconvoluted into individual curves representing the different degradation mechanisms (see Figure 4.3); similar approaches have been employed in previous studies [217], [218]. The Voigt shape has resulted in a better agreement between the convolution of the

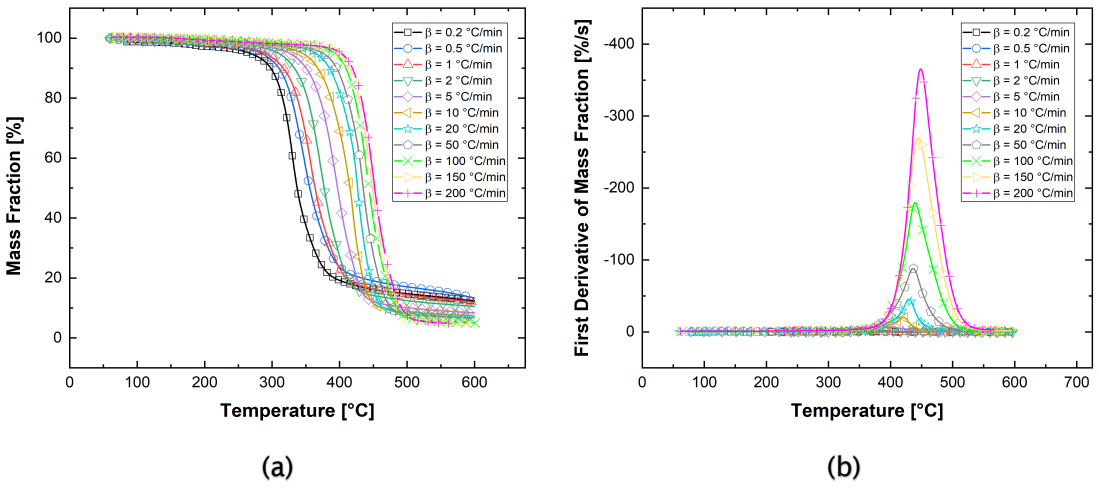

Figure 4.2 – Thermal degradation of epoxy resin: (a) TGA curves and (b) DTGA curves.

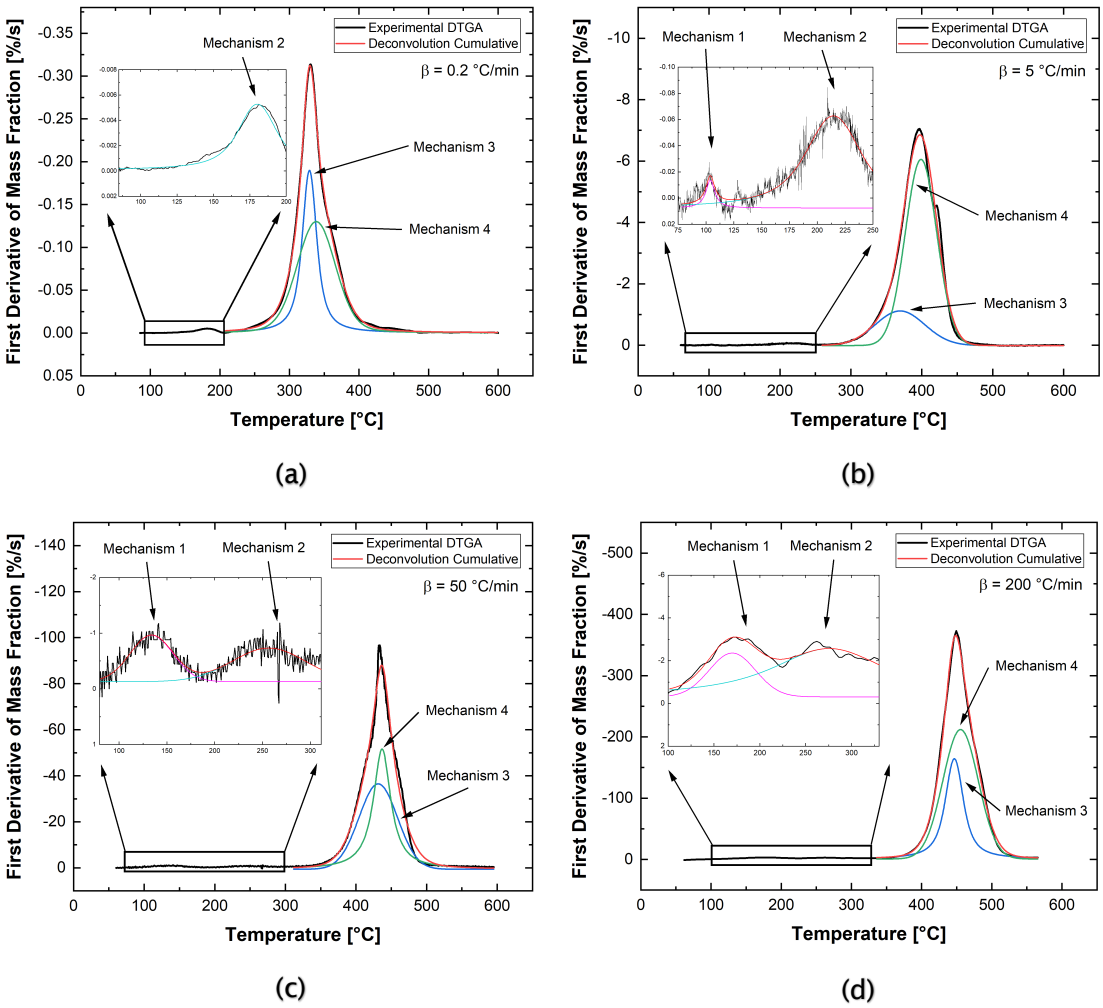

Figure 4.3 – Deconvoluted reactions DTGA curves at: (a) 0.2 ˚C/min, (b) 5 ˚C/min, (c) 50 ˚C/min, and (d) 200 ˚C/min.

individual curves (red profiles) and the experimental DTGA curves (black profiles), compared with other shapes such as Gaussian and Lorentzian.

As expected, the results show that the degradation process starts with either mechanism 1 or 2, depending on the heating rate. It appears that mechanism 1 is only visible at heating rates above 5 ˚C/min, where its T_m appears to be ~100 ˚C. This mechanism does not constitute an epoxy degradation reaction *per se*, and its magnitude and/or presence might be situational and largely affected by environmental factors. In view of these considerations, it has been decided not to consider it when investigating the thermal damage in Chapter 6. Finally, Figure 4.3 shows that the majority of the mass loss is caused by

mechanisms 3 and 4. However, mechanism 2 cannot be ruled out as a potential degradation mechanism, although its contribution to the total degradation is 2-3%. This is because even such a small amount of gas is sufficient to introduce voids that separate the rotor blade current carrying conductors and trigger sparks (see Section 6.3.3).

4.3.3 Degradation Reaction Kinetics

The degradation reaction kinetics, calculated by the Kissinger method outlined in Section 4.2.2, are provided in Table 4.1 for both the apparent single reaction and the deconvoluted reactions models. Although these parameters were computed at low heating rates using a laboratory TGA analyser, they are employed in Chapter 6 to model the resin pyrolysis process caused by lightning temperature profiles, as done in similar studies [108], [161], [205], [206].

4.4 Summary

The objective of this chapter was to study the thermal degradation process of the Hexion epoxy resin system, a commercial resin used in wind turbine blade manufacturing, to determine its reaction kinetics. The latter are implemented in the FEM models to predict the thermal damage due to lightning temperature profiles computed in the simulation.

Past studies have shown that polymers decompose into different mechanisms,

Table 4.1 – Degradation reaction kinetics for both the apparent single reaction and the deconvoluted reactions models.

Reaction Kinetics	Apparent	Deconvoluted Reactions			
	Single Reaction	Mech. 1	Mech. 2	Mech. 3	Mech. 4
A [1/s]	$2.20 \pm 0.47 \times 10^{12}$	13.11×10^{6}	2.00×10^{12}	4.76×10^{12}	2.19×10^{13}
n	1.17 ± 0.09	1	1	1	1
E_a [kJ/mol]	185.78	64.86	137.36	188.06	200.22

which develop at different ranges of temperature. However, the TGA analyser assumes that the pyrolysis process develops through an apparent single reaction described by an asymmetric DTGA curve. Thus, to derive the degradation mechanisms and their reaction kinetics, the experimental DTGA curves were deconvoluted into individual curves representing the different mechanisms. The results showed that the pyrolysis process was initiated at temperatures lower than expected by release of water molecules formed via a thermally activated dehydration reaction (mechanism 2). However, the majority of the mass loss was caused by the main degradation mechanisms related to the scission of polymer chains (mechanisms 3 and 4). Finally, it was noted that before any of those mechanisms occurs, water molecules in the form of absorbed moisture might be released (mechanism 1). This mechanism does not constitute an epoxy degradation reaction *per se*, and its magnitude and/or presence might be situational and largely affected by environmental factors. For this reason, it was decided not to consider it when investigating the thermal damage in Chapter 6.

Chapter 5
Numerical Modelling Framework of Lightning Strikes to Wind Turbine Blades

One of the objectives of this research project is to develop FEM models capable of simulating the time-domain electromagnetic-thermal response of wind turbine blades subjected to lightning strikes. In fact, the advantage of the FEM is the capability of computing spatial current density distributions in the rotor blade cross-section. This would allow the identification of high current density and temperature regions at the EB interfaces, which might lead to resin thermal degradation and sparking within the EB joint. To this end, this chapter provides the methodologies for the numerical simulation of such phenomena. A procedure is presented to inject the lightning impulse in the rotor blade without imposing an integral constraint on the transport current.

5.1 Assumptions of the Modelling Framework

The following assumptions were made to model, by the FEM, the electromagnetic-thermal response of wind turbine blades subjected to lightning strikes:

- As seen in the Literature Review, the rotor blade is composed of two shells glued together. Since the geometries of the two shells are very similar (see Figures 2.1 to 2.4), they are characterised by comparable impedances. In such conditions, it is reasonable to assume that one half of the lightning current distributes in the upper shell (i.e., in the upper DC, EB, and spar), and the other half in the lower shell (i.e., in the lower DC, EB, and spar). Thus, only half of the blade was modelled, and the peak value of the injected current was halved.
- It was assumed that the air termination system can withstand several lightning strikes without experiencing any damage, in such a way that most of the lightning energy is conducted through the receptor and transferred to the DC (see [12] for the guidelines on receptor design).
- Transmission line effects are neglected, which has previously been shown to be a reasonable assumption [40], [43].
- The displacement current density term was neglected in the electromagnetic formulation since lightning strikes are low frequency applications [130], [219]–[221]. For instance, at 800 kHz the displacement current density in composite materials is smaller than the conduction current density by 11 orders of magnitude along the fibre direction and by 7 orders of magnitude along the through-thickness direction.
- As outlined in Section 2.4.2, for strongly non-uniform electric fields generated by rapid voltage impulses like lightning ones, there is not enough time to form a space charge and even the first electron avalanche causes the complete breakdown. In such conditions, the inception criterion of HV breakdown is $E_{max} = E_{bd\_non\text{-}unif,max}$. However,

the breakdown strength in non-uniform electric field conditions is not known for typical rotor blade core materials (balsa wood, PVC foam, PET foam, etc.) and needs to be characterised experimentally. On the other hand, the breakdown strength of these materials in uniform electric field conditions is known from literature values. Furthermore, it was said that the breakdown strength is lower in uniform electric field conditions than in non-uniform electric field conditions. Thus, the former was assumed as breakdown inception criterion, $E_{max} = E_{bd\_unif}$, since it is more conservative.

- The heat transfer problem was solved by imposing a weak coupling with the electromagnetic problem, that is, no dependence of the electrical conductivity on temperature was considered. In fact, the studies revised in the Literature Review have shown that CFRP spars only conduct a small share of the total lightning current [21], [40], [42], [111], and low temperatures are found in the bulk CFRP spars. In addition, the modelling approach employed in this project considered ambient temperature contact resistivities (i.e., the scenario with highest values), although past research has proven that the contact resistivity of CFRPs decreases with increasing temperatures [184]–[186]. This is a conservative choice as the Joule heat released at the bonding interfaces and thus the temperature would be overestimated. It follows that, if resin thermal degradation at the EB interfaces is not predicted when considering ambient temperature contact resistivities, then this would also be the case if temperature dependent values were implemented. In this way a strongly coupled electromagnetic-thermal formulation is avoided, which would drastically increase the computational cost. However, since ambient temperature contact resistivities overrate the Joule heating, it is simply possible to identify the damage onset and location, whereas no exact information can be provided on the extent of damage.

5.2 FEM Model Formulation

5.2.1 Electromagnetic Field Diffusion

The electromagnetic field diffusion problem was computed by solving the following set of equations, either in the time-domain or frequency-domain according to the problem under study [86]:

Time-domain	Frequency-Domain
$\begin{cases} \nabla \times \boldsymbol{H} = \boldsymbol{J} = \boldsymbol{\sigma}\left(-\nabla V - \dfrac{\mathrm{d}\boldsymbol{A}}{\mathrm{d}t}\right) \\ \nabla \cdot \boldsymbol{J} = 0 \end{cases}$	$\begin{cases} \nabla \times \boldsymbol{H} = \boldsymbol{J} = \boldsymbol{\sigma}(-\nabla V - \mathrm{j}\omega \boldsymbol{A}) \\ \nabla \cdot \boldsymbol{J} = 0 \end{cases}$

(5.1)

while the following relations are known:

$$\begin{cases} \boldsymbol{B} = \nabla \times \boldsymbol{A} \\ \boldsymbol{B} = \mu_0 \mu_r \boldsymbol{H} \end{cases} \tag{5.2}$$

where ∇x is the curl operator, $\boldsymbol{H}$ [A/m] is the magnetic field strength, $\boldsymbol{A}$ [Wb/m] is the magnetic vector potential, j is the square root of –1, $\boldsymbol{B}$ [T] is the magnetic flux density, and μ_0 [H/m] is the vacuum permeability.

5.2.2 Heat Transfer

The heat transfer problem was computed by solving for the heat transfer equation [110]:

$$\rho\, C_p \frac{\partial T}{\partial t} + \nabla \cdot \boldsymbol{q_{cond}} = Q_{rh} \tag{5.3}$$

where $\rho\, C_p \frac{\partial T}{\partial t}$ [W/m^3] is the time derivative of the internal energy per unit volume, T [K] is the temperature, $\boldsymbol{q_{cond}} = -\boldsymbol{k}\nabla T$ [W/m^2] is the heat flux by conduction, and Q_{rh} [W/m^3] is the Joule heat.

The Joule heat due to the resistance of the individual blade components (i.e., DC, EB, and spars), as well as due to the contact resistance at the EB interfaces, was computed in the electromagnetic problem and applied to the heat transfer analysis through a weak coupling [190], [222]:

$$Q_{rh} = \boldsymbol{J} \bullet \boldsymbol{E} \tag{5.4}$$

where $\boldsymbol{E}$ [V/m] is the electric field strength.

Finally, the Arrhenius equation given in Equation (4.1) was solved in the heat transfer problem via a weak coupling, using the degradation reaction kinetics presented in Table 4.1 and the temperature predicted at each time step.

5.3 FEM Boundary Conditions

5.3.1 Magnetic and Electric Insulation

An insulating volume surrounding the rotor blade is required in electromagnetic analyses, which is the computational domain within which the Ampère-Maxwell equation is solved. The outer boundaries of the insulating volume act as a current return path, which is needed to ensure that the current flows in a closed loop (see Figure 5.1) respecting the current conservation law. The current return path was defined by assuming magnetic and electric insulation at the insulating volume outer boundaries [190]:

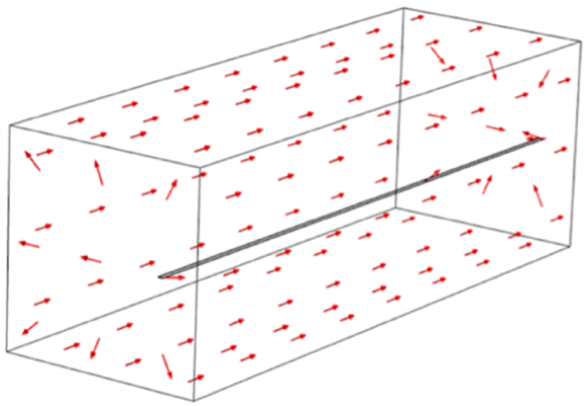

Figure 5.1 – Current return path for the injected lightning current.

$$\begin{cases} \boldsymbol{n} \times \boldsymbol{A} = 0 \\ \boldsymbol{n} \cdot \boldsymbol{J} = 0 \end{cases} \tag{5.5}$$

5.3.2 Electrical Contact

Electrical contact was modelled at the EB interfaces by assuming [190]

$$\begin{cases} \boldsymbol{n} \cdot \boldsymbol{J_1} = -\frac{1}{\rho_C}(V_1 - V_2) \\ \boldsymbol{n} \cdot \boldsymbol{J_2} = -\frac{1}{\rho_C}(V_2 - V_1) \end{cases} \tag{5.6}$$

5.3.3 Lightning Transient Voltage

As said in Section 2.6.4, one of the major challenges when simulating lightning strikes to rotor blades by the FEM is the injection in the model of the lightning current, as it splits among different conductive paths of the blade. Such lightning current redistributions are driven by both resistive and inductive effects, that is, by both potential electric field and induced electric field generated by the time-variable magnetic field. One way of predicting them consists of solving the electromagnetic field diffusion problem when the electric scalar and magnetic vector potentials are coupled through an imposed integral constraint on the total transport current (i.e., the Heidler function). A numerical solution of such a combined problem is complex for fast rising currents such as lightning impulses and tests on commercial software packages indicate that multiple iterations at each time step are required to find consistent solutions. Moreover, the computational cost of such analyses is even larger for high aspect-ratio structures like rotor blades, which require fine meshes for accurate predictions. On the other hand, better convergence and a smaller computational time would be achieved by imposing a transient voltage boundary condition across the blade DC. This allows independent calculations of the potential component of the electric field (and of the associated current density) in the magnetic vector potential problem.

However, such voltage waveforms are not known from lightning observation studies and depend on the lightning current in a non-linear manner, i.e., they cannot simply be scaled up and down from a single reference case. Consequently, a numerical procedure was developed to compute the voltage which drives the sought lightning current through the assessed structure.

The first step of the developed approach is to compute the spectrum of the lightning current. In the second step, the electromagnetic problem is solved in the frequency-domain to determine the voltage related to each component of the lightning current spectrum. This can easily be completed since the problem is linear at each fixed frequency, i.e., voltage and current are directly proportional through the impedance. In the third step, the voltage components are transformed back to the time-domain, obtaining the sought transient voltage profile. Finally, the electromagnetic problem is solved in the time-domain by applying the determined lightning voltage waveform as a boundary condition. To accomplish this algorithm, the following input data need to be known: the expression of the transport current to compute its spectrum; and the geometry and material properties of the structure under study to evaluate its impedance at different frequencies. As an example, in the following paragraphs the lightning voltage waveform is computed when considering the first positive short stroke current, the rotor blade geometry given in Section 7.2.1, and the material properties listed in Appendix A.

Fourier Transform

The Heidler function given in Equation (2.6) is composed of two terms with very different time coefficients: the rise term, which is a power curve; and the decay term, which is the exponential decay. The Fourier integral of this function cannot be analytically calculated, and the spectrum of the standard lightning waveform can be determined by either numerical integration or the discrete Fourier transform (DFT) [177], [223]. The latter is the preferred method since it is more efficient when performed using the fast Fourier

transform (FFT) algorithm, provided that the total number of samples is an integer power of 2 [224].

The DFT converts a discrete time periodic signal (an array of time-domain samples) into a sum of sinusoidal components (an array of frequency-domain components) [224], [225]. Since the standard lightning current is a non-periodic continuous function, it was first required to sample it. This was done by choosing an appropriate sampling interval (time step), t_{step} [s], and number of samples, N, to ensure that the sampling reflected the characteristics of the lightning waveform. Then, the observation time, t_s [s], was [224], [225]

$$t_s = Nt_{step} \tag{5.7}$$

whereas the frequency points, f_k [Hz], were defined as

$$f_k = \frac{k}{t_s} = \frac{k}{Nt_{step}}, \qquad k = \overline{0, N-1} \tag{5.8}$$

where k is the frequency index (bin number).

The discrete spectrum of the Heidler function was given by:

$$\widetilde{I}_k = I_k \, e^{j\varphi_{I,k}} = \frac{1}{N} \sum_{m=0}^{N-1} i_m e^{-j2\pi \frac{k}{N} m} \tag{5.9}$$

where $\widetilde{I}_k$ [A] is the frequency-domain k-th current complex coefficient, I_k [A] is the magnitude of the k-th current complex coefficient, $\varphi_{I,k}$ [rad] is the argument of the k-th current complex coefficient, i_m [A] is the time-domain m-th current sample, and m is the time sampling index.

The total number of frequency components is equal to the number of time-domain samples. According to the Nyquist Theorem [224], the frequency bandwidth is half the sampling frequency, F_s [Hz]. Thus, all the frequency components larger than $F_s/2$ are aliased when the signal is transformed back to the time-domain. Therefore, when performing the DFT of non-periodical signals, the sampling frequency must be chosen carefully to prevent significant errors. In addition, special attention should be paid to [224]

- The selection of the sampling interval, which is chosen to represent the high frequency components of the Heidler function. For this reason, at least 20 time points need to be placed along the rising front. Such an empirical approach allows to pass the "knee" on the current magnitude plot given in Figure 5.2*a*, as well as to ensure that the magnitudes of the aliased components are small enough to be ignored.
- The number of samples, which defines t_s as given in Equation (5.7) and is chosen to capture the slow decaying tail of the Heidler function, i.e., the current $i(t_s)$ should decay below 10^{-18} of its peak value. This is a very conservative requirement and can be relaxed for lightning waveforms that present shorter tails. However, such an excessive extension of the observation time does not affect the computational time of the DFT since it is performed using the FFT algorithm (FEM simulations are instead stopped at 2 ms, which is the typical duration of a lightning short stroke [12]).

An adequate representation of the first positive short stroke was achieved when the sampling interval was 0.61 μs, the number of samples was 32,768, and the frequency bandwidth was ~800 kHz (see Figures 5.2*a* and 5.2*b*).

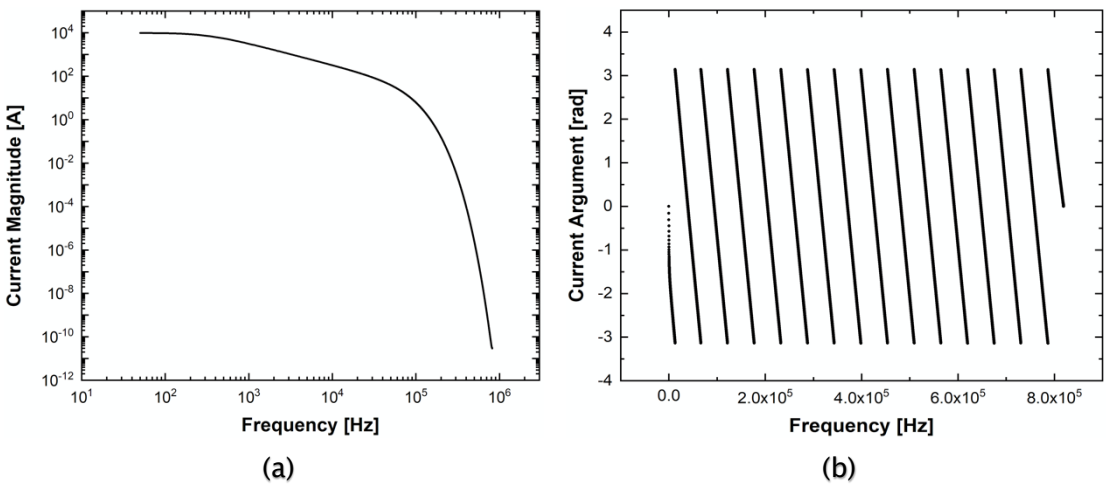

Figure 5.2 – First positive short stroke current spectrum: (a) magnitude and (b) argument.

Impedance Calculation: Frequency-Domain Electromagnetic Field Diffusion Problem

Once the spectrum of the transport current was determined, the next step was to predict the voltage spectrum (i.e., the voltage magnitude and phase related to each frequency component of the current spectrum). This was done by solving the electromagnetic field diffusion problem in the frequency-domain using the FEM [190], [191] (see Section 5.2.1).

Selection of Frequency Components and Interpolation Strategy

As shown in the Fourier Transform paragraph, the typical spectrum of the first positive short stroke current comprised 32,768 components. Solving the electromagnetic problem (in order to predict the voltage components at given frequencies) for all these components would be impractical, especially when considering real blade geometries characterised by a high aspect-ratio. Therefore, the electromagnetic problem was solved for a small set of components only to reduce the computational time, while the remaining voltage components were determined through interpolation.

The selection of the current frequency components for the electromagnetic solution plays an important role in the overall accuracy of the procedure as it might introduce significant errors during the interpolation process. First, the electromagnetic problem was only solved for 133 components out of 32,768, which were chosen in such a way as to cover the entire bandwidth of the current spectrum (note that only a small number of components was selected at high frequencies, see Figure 5.3). The corresponding voltage drops predicted by the FEM were then cubic interpolated to determine the remaining 32,635 voltage components and thus the voltage spectrum (see Figure 5.4). However, it was also required to know the phase (argument) of each voltage component to obtain the required time-domain voltage waveform. Consequently, a second component selection procedure was carried out to determine the voltage phase at different frequencies. To do so, the

approximately linear relationship between the current phase and frequency (see Figure 5.2*b*) was exploited. More specifically, a set of frequencies was chosen in such a way that they laid in all the branches of the bandwidth (see Figure 5.5). That is, the selected components needed to be spaced by ~2π rad. In fact, if the selected points were spaced by more than 2π rad, then some of the phase branches would be lost. After that, the electromagnetic problem was solved for these frequencies (416 in total) and the corresponding voltage phases are plotted in Figure 5.6 (blue points). Then, the frequencies

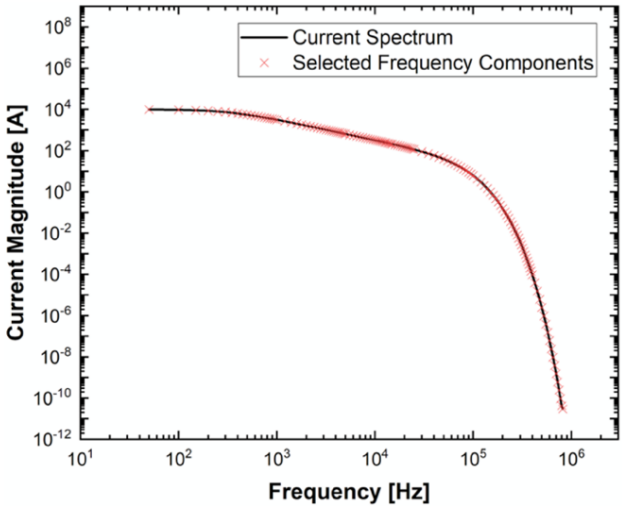

Figure 5.3 – First positive short stroke: selected current components to determine the voltage spectrum.

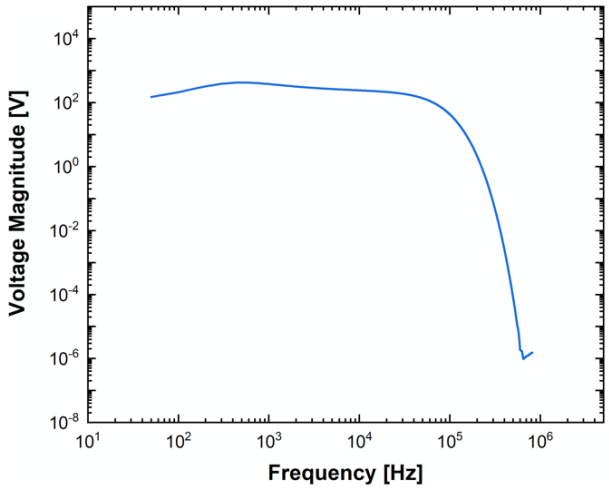

Figure 5.4 – First positive short stroke: voltage spectrum.

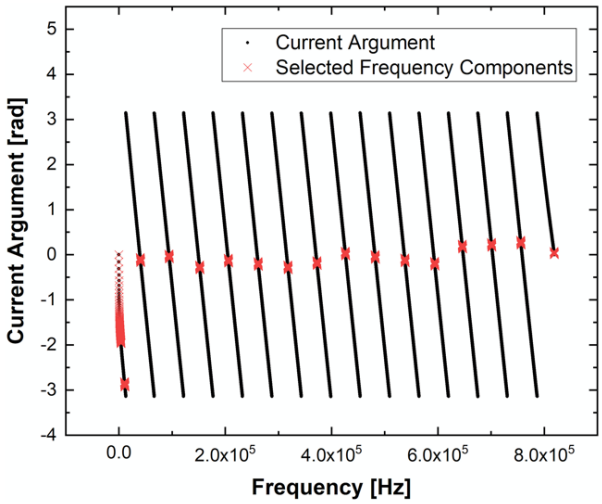

Figure 5.5 – First positive short stroke: selected current components to determine the voltage phase.

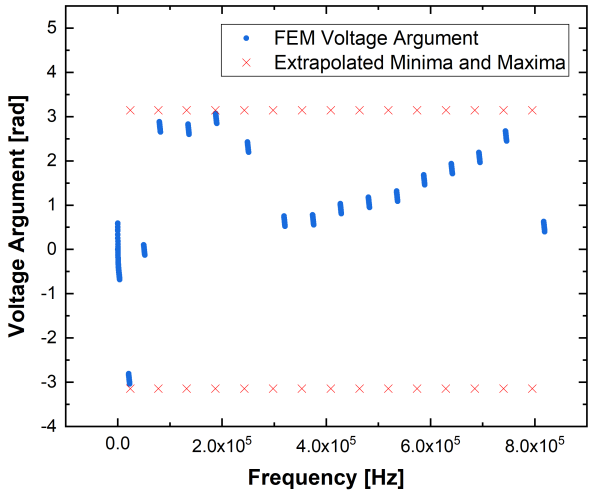

Figure 5.6 – First positive short stroke: FEM voltage phase and extrapolated minima and maxima.

at which the phase is minimum ($-\pi$ rad) and maximum (π rad) were linearly extrapolated (red crosses in Figure 5.6). The phases between the frequencies of minima ($-\pi$ rad) and maxima (π rad) were instead determined by linear interpolation, which are given in Figure 5.7 (blue plot). As a comparison, Figure 5.7 also shows the voltage phase obtained when solving the electromagnetic problem in a time-domain computational analysis (red plot) by imposing the transport current, i.e., the slow procedure. A good agreement

was obtained between the two, with some discrepancies in the frequency range of 250 and 600 kHz.

Time Dependent Voltage: Inverse Discrete Fourier Transform

Once all the frequency components of the driving voltage were found, the voltage spectrum was transformed to the time-domain using the inverse discrete Fourier transform (IDFT) [224]:

$$v(t_m) = N \sum_{k=0}^{N-1} \mathrm{Re}\left(\widetilde{V_k}\, e^{j\omega_k t_m}\right) = N \sum_{k=0}^{N-1} \mathrm{Re}\left(V_k\, e^{j\varphi_{V,k}}\, e^{j\omega_k t_m}\right) \tag{5.10}$$

where $v(t_m)$ [V] is the time-domain voltage, t_m [s] is the discrete time variable, $\widetilde{V_k}$ [V] is the frequency-domain k-th voltage complex coefficient, V_k [V] is the magnitude of the k-th voltage complex coefficient, and $\varphi_{V,k}$ [rad] is the argument of the k-th voltage complex coefficient.

The resulting time dependent voltage profile for the first positive short stroke case is depicted in Figure 5.8. This was finally applied as a time dependent boundary condition to solve the electromagnetic problem in the time-domain (see Section 5.2.1) and compute the associated current distribution within the blade conductors [190], [191].

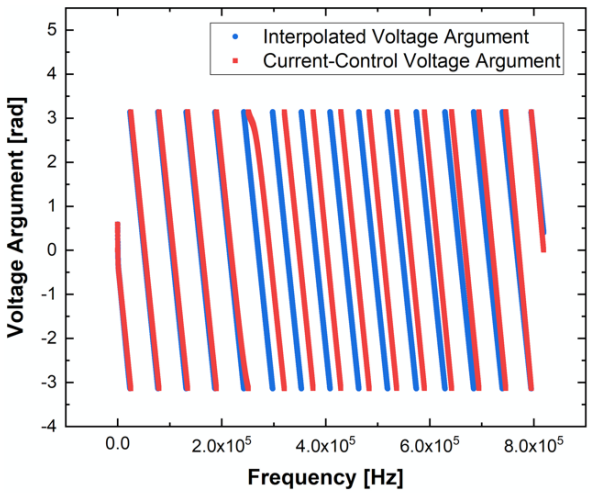

Figure 5.7 – First positive short stroke: interpolated voltage phase and current-control simulation voltage phase.

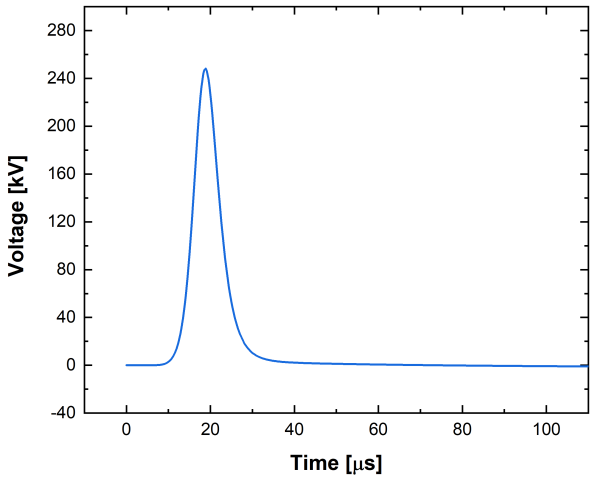

Figure 5.8 – First positive short stroke: voltage waveform.

Overall, the developed procedure was approximately two times faster than the time-domain computations with the imposed transport current. The expected time savings are even greater when different lightning impulses need to be analysed, e.g., first positive short stroke, first negative short stroke, and subsequent short stroke. In this case the expected gain for the whole analysis would be a factor of six since the calculation of the frequency dependent impedance, which is the most time-consuming part of the procedure, would need to be performed only once.

5.3.4 Convective Heat Flux

Convective heat flux was assumed at the rotor blade outer boundaries in contact with the ambient [110], [226]:

$$-\boldsymbol{n} \cdot \boldsymbol{q}_{conv} = h(T_{ext} - T) \tag{5.11}$$

where $\boldsymbol{q}_{conv}$ [W/m^2] is the convective heat flux, h [W/(m^2·K)] is the heat transfer coefficient, and T_{ext} [K] is the ambient temperature. The air heat transfer coefficient was equal to 25 W/(m^2·K) [226].

5.3.5 Thermal Radiation

Thermal radiation was assumed at the rotor blade outer boundaries in contact with the ambient [110], [226]:

$$-\boldsymbol{n} \cdot \boldsymbol{q}_{rad} = \varepsilon\sigma\left(T_{ext}^4 - T^4\right) \tag{5.12}$$

where $\boldsymbol{q}_{rad}$ [W/m^2] is the radiative heat flux, ε is the emissivity, and σ_{SB} [W/(m^2·K^4)] is the Stefan-Boltzmann constant. The emissivity of CFRP, GFRP, and copper surfaces were equal to 0.9 [161], [227], [228], 0.85 [227], [229], and 0.03 [230], respectively.

5.4 FEM Implementation

The modelling framework was implemented in COMSOL Multiphysics 5.5 using the following three built-in modules: the electric currents, the magnetic fields, and the heat transfer in solids. The backward differentiation formula (BDF) was employed for time-stepping, while the linear algebraic equations were solved by the MUMPS direct solver. The considered physics were independently solved by a segregated approach, which improved the numerical convergence and stability, reducing the computational time. The employed desktop computer was equipped with Intel Core™ i7-6700 @ 3.4 GHz CPU, 16.0 GB RAM, and NVIDIA GeForce GTX 1050 graphics card.

To improve the convergence of the FEM solution and reduce the computational time, it is suggested to assign a small, but non-zero, electrical conductivity to the insulating volume [190], [191]. It is recommended that this value is at least 2 orders of magnitude smaller than the lowest electrical conductivity of the conductors. The electrical conductivity of the insulating volume was varied from $1\text{x}10^{-4}$ to $1\text{x}10^{-15}$ S/m to study its impact on the solution accuracy when implementing the rotor blade presented in Section 7.2.1 subjected to the subsequent short stroke current. Figure 5.9 shows that

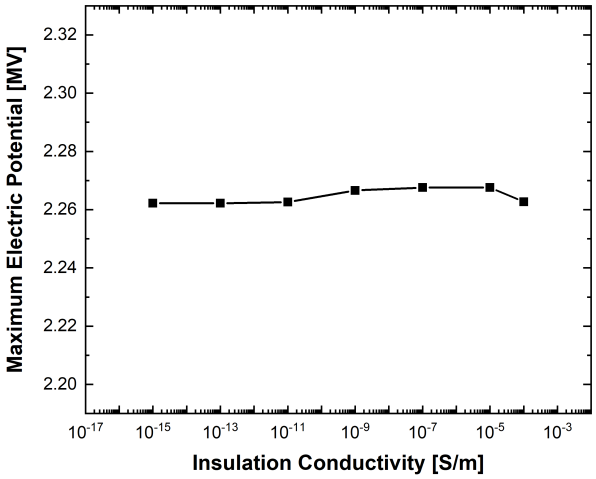

Figure 5.9 – Maximum electric potential as a function of the insulating volume electrical conductivity.

no significant change in maximum electric potential at the blade tip was observed below $1x10^{-4}$ S/m, which was chosen as the electrical conductivity of the insulating volume.

5.5 Summary

This chapter presented the numerical modelling framework to simulate the behaviour of wind turbine blades under lightning strikes. The developed FEM models solve the electromagnetic field diffusion problem since existing literature showed that transmission line effects can be neglected for wind turbine blade lightning strike problems. The displacement current density term was disregarded in the Ampère-Maxwell equation as lightning strikes are low frequency applications. To improve the convergence and reduce the computational time, lightning currents were injected in the models by imposing voltage boundary conditions. The latter are not known from field observation studies and thus they were computed by a procedure that combines Fourier transform with frequency-domain FEM simulations.

In addition, the FEM models solve both the heat transfer and Arrhenius equations to predict temperature distributions and thermal damage in EB joints. This was done by imposing a weak coupling between electromagnetic

and thermal problems, i.e., no dependence of the electrical conductivity on temperature was considered. In fact, previous studies showed that CFRP spars only conduct a small share of the total lightning current and low temperatures are found in the bulk CFRP.

Chapter 6

Validation of the Numerical Modelling Framework

The aim of this chapter is to establish whether the numerical modelling framework presented in Chapter 5 can replicate the reality and thus support the design phase of EB systems. To do so, the FEM models are validated against high-current test data in terms of current and temperature distributions. Moreover, if thermal damage and sparks are observed, it needs to be verified that the numerical models can predict high values of current density and temperature at the sparking areas.

6.1 Conducted Current Test

The conducted current test was performed by the industrial sponsor of this project, Nordex Energy GmbH, according to the IEC standard procedures [12].

6.1.1 Test Sample

The geometry of the assessed blade tip sample (arrangement and dimensions) is shown in Figure 6.1 and represents an airfoil shell section of a 70 m wind turbine blade. It was composed of a 25 mm^2 copper braid (LPS DC) in parallel

to a pultruded UD CFRP spar. The latter presented chamfered surfaces for mechanical purposes (note that the dimensions of each spar pultruded profile, i.e., width, thickness, length, and chamfer angle, are not given for confidentiality reasons. However, the overall dimensions of the spar are provided). The two conductors were electrically connected throughout the sample length (continuous-bonding configuration) by two layers of BIAX CFRP. To be consistent with the real blade structure, PET foam was placed between the DC and spar as a core material. In addition, the whole system (i.e., spar, DC, EB, and PET foam) was encapsulated within two layers of BIAX GFRP representing the blade shell (one placed on the top and one on the bottom of the sample). The sample was cured for 6 h at 75 ˚C following the VARTM manufacturing procedures [13]–[16]. Finally, the test sample impedance was not comparable to the full blade one since the specimen represented the blade

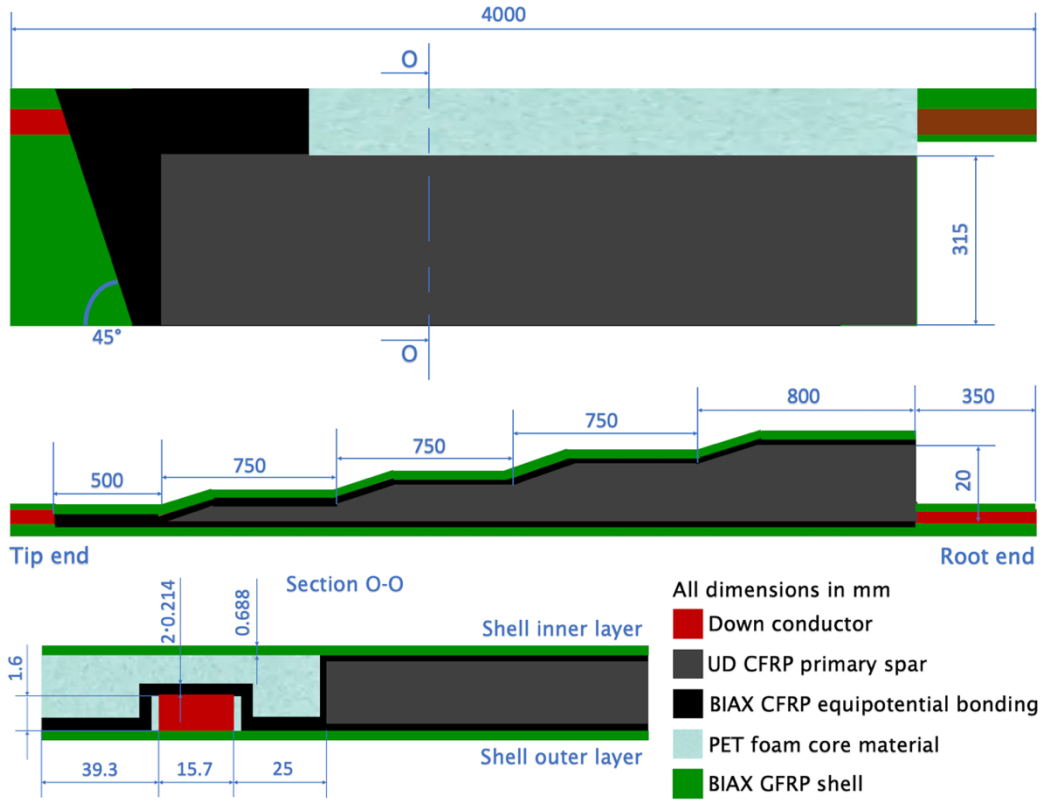

Figure 6.1 – Wind turbine blade sample under testing (not to scale). In the top view, both the shell inner layer and the top EB layer were intentionally omitted to show the DC and spar.

tip only. Thus, copper bars were bolted to the sample root end to account for the impedance of the remaining blade section that was not manufactured.

6.1.2 Test Current

The test current was the first positive short stroke (see Figure 6.2), having time parameters t_1 = 10 μs and t_2 = 350 μs, and peak current I_0 = 125 kA.

6.1.3 Test Setup

The test setup is shown in Figure 6.3, in which it is visible the test sample, the generator, the return cage, and the measuring apparatus. The latter included: four Rogowski coils (indicated by red circles in Figure 6.3) and two oscilloscopes to measure the current split between the DC and spar at different sample locations; four cameras to collect sample pictures; and an IR camera (with an acquisition frequency of 12.5 Hz) to record the sample temperature. The specimen was connected to the generator and return cage through copper bars.

6.1.4 Test Conditions

The test was conducted at a temperature of 16.6 °C and with a relative humidity of 50%.

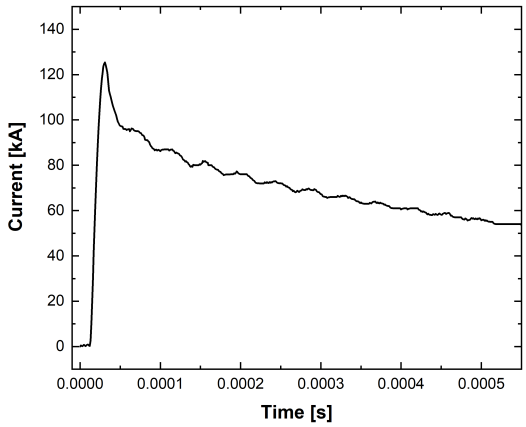

Figure 6.2 – Conducted current test: injected current.

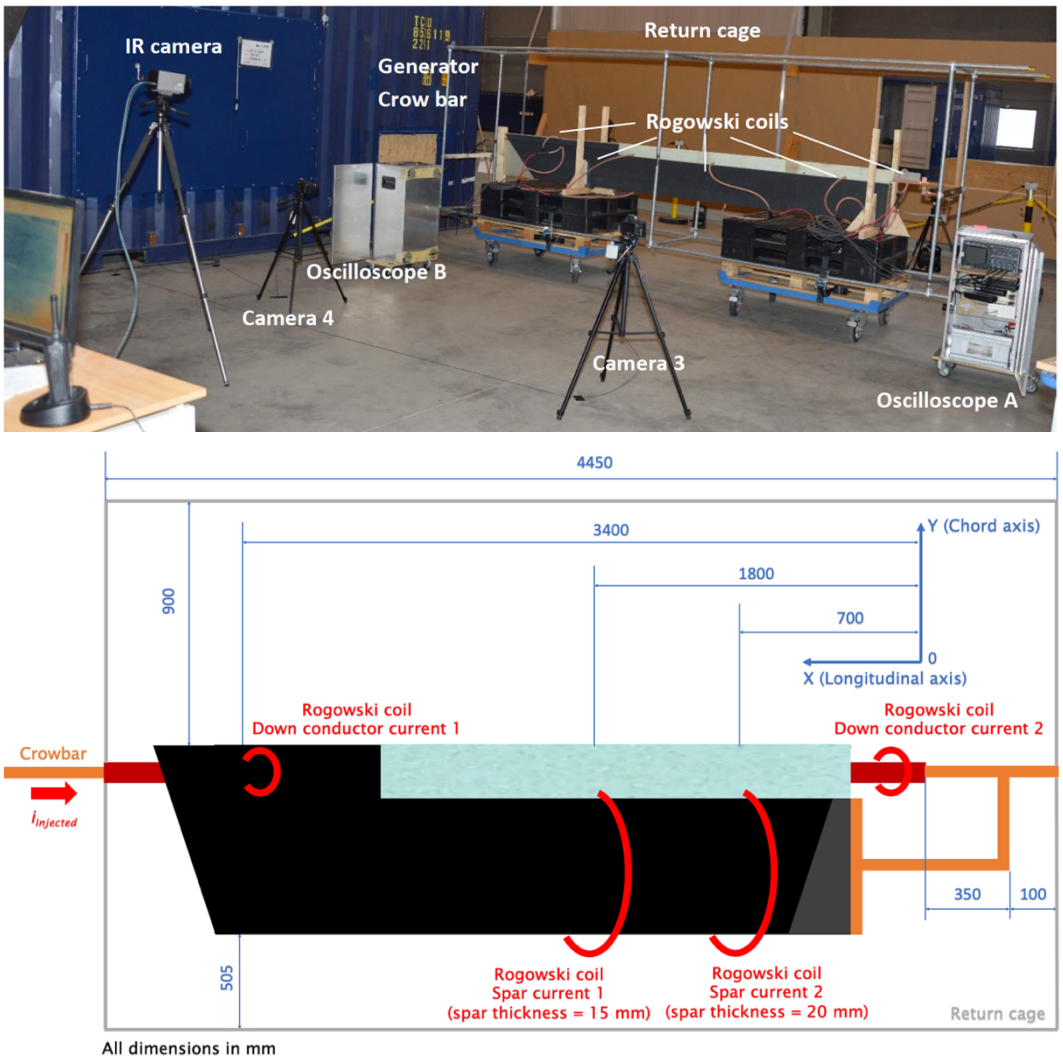

Figure 6.3 – Test setup of the conducted current test. Both the inner and outer layers of the shell were intentionally omitted to show the sample conductors.

6.2 FEM Modelling

6.2.1 Geometry and Material Properties

The geometry of the FEM model is shown in Figure 6.4. To facilitate the meshing procedure, the EB layers 45° cuts at the tip and root ends were disregarded. The return cage used in the test needed to be implemented in the FEM model as a return path to obtain a comparable impedance and be consistent with the test. Thus, the blade sample was placed within a

computational domain (insulating volume) of size 0.6 x 1.8 x 4.45 m^3. Finally, the material properties of the sample components are given in Appendix A.

6.2.2 Lightning Voltage Waveform

The test current given in Figure 6.2 was injected in the FEM model by applying a voltage across the DC inlet (current injection end) and outlet (grounded end), as shown in Figure 6.4. The applied lightning voltage waveform is given in Figure 6.5 and was obtained by the procedure presented in Section 5.3.3.

6.2.3 Mesh

The FEM model was meshed by hexahedral elements, which is the suggested finite element type for electromagnetic-thermal problems [231]–[233]. The hexahedral elements were obtained by the mapped and swept built-in features of COMSOL Multiphysics 5.5. In addition, boundary layers [191] were employed to reproduce the crowding (skin) effect in the DC [234] as well as to capture non-uniform current density distributions around the EB interfaces due to the CFRP anisotropy. A mesh convergence study (see Figure 6.6)

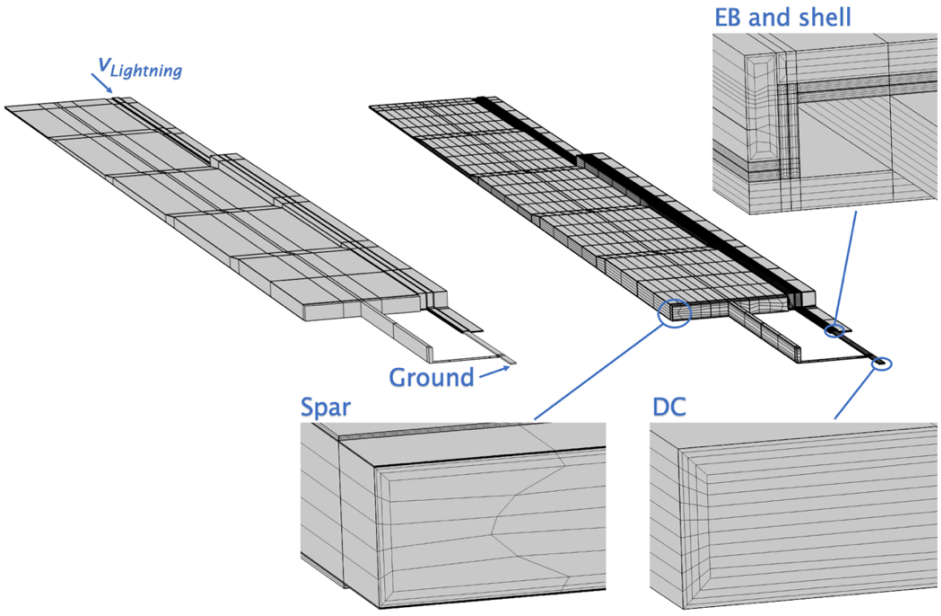

Figure 6.4 – FEM geometry and mesh (the insulating volume is intentionally hidden).

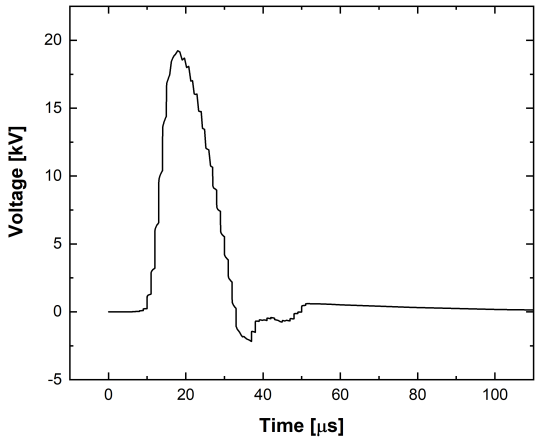

Figure 6.5 – Voltage waveform used in the FEM model to inject the test current.

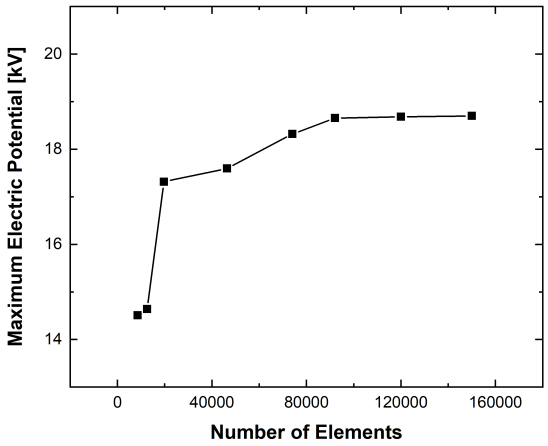

Figure 6.6 – Mesh convergence study.

was conducted to ensure that the solution was mesh independent. The minimum and maximum number of elements in the blade longitudinal (sweep), transverse, and through thickness directions were 1 and 4, 1 and 6, and 1 and 13, respectively. The final mesh consisted of ~97,170 hexahedral and boundary layer elements (see Figure 6.4).

6.3 Results and Discussion

6.3.1 Lightning Current Distribution within the Blade Conductors

The FEM simulation is capable of predicting the overall lightning current split between the blade conductors at different locations (see Figures 6.7*a* to 6.7*e*).

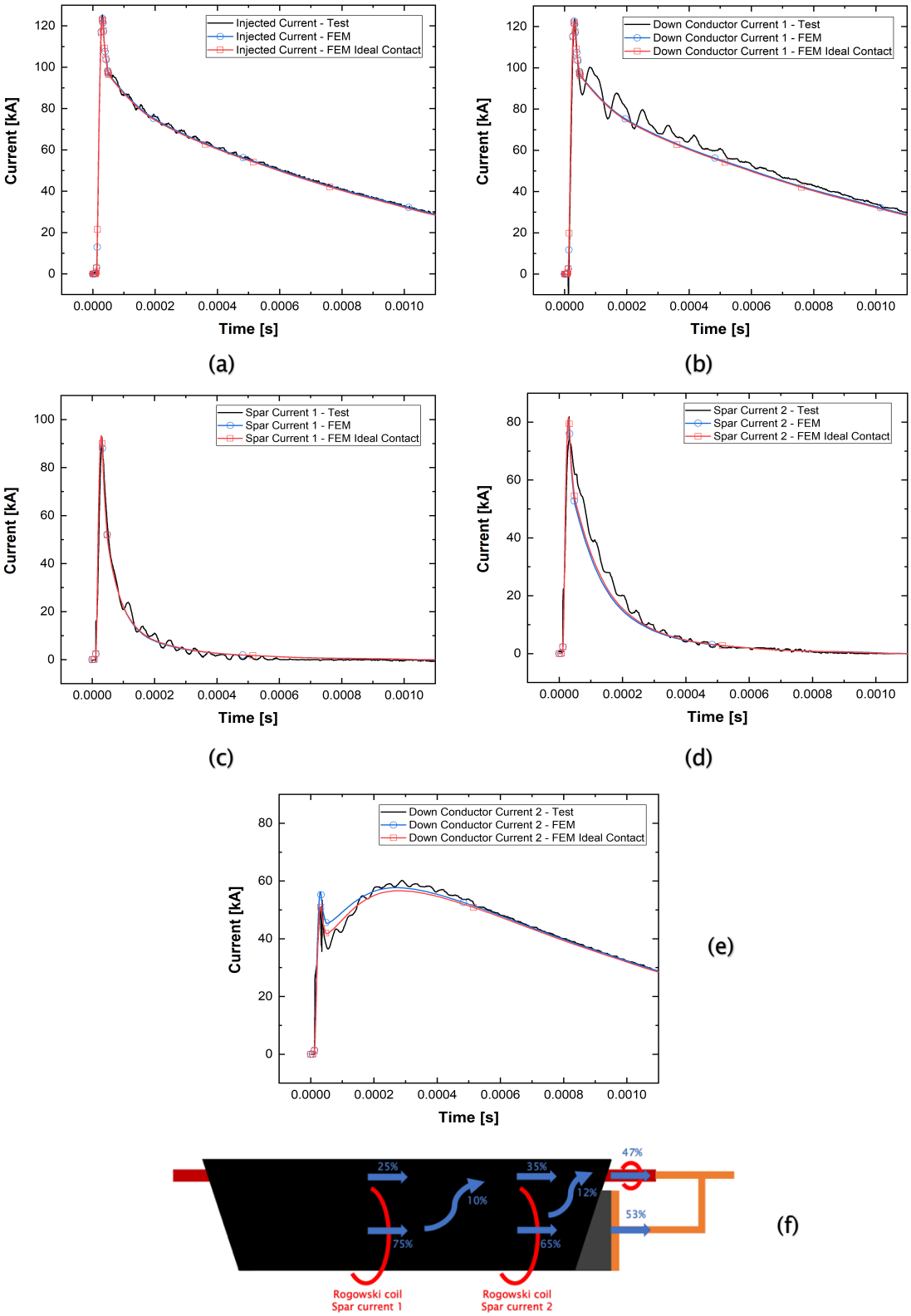

Figure 6.7 – Lightning current distribution: (a) injected current, (b) DC current 1, (c) spar current 1, (d) spar current 2, (e) DC current 2, and (f) peak current redistribution along the sample.

The FEM currents are obtained by integrating the current density over the conductors' cross-section at the x-coordinates given in Figure 6.3, indicating the locations of the Rogowski coils. The spar cross-sections at the specified x-coordinates can be derived from the overall spar width and thicknesses provided in Figures 6.1 and 6.3, respectively. As shown in Figures 6.7*a* to 6.7*e*, an excellent agreement is found between the test measurements and FEM predictions, with negligible deviations in terms of peak current and specific energy due to geometrical approximations. The results show that during the rise front the lightning current is mainly conducted by the spar because of its low inductance, whereas during the slow decay front the lightning current mainly flows through the DC due to its low resistance. In addition, Figure 6.7*f* illustrates how the peak current, measured by the Rogowski coils (see locations in Figure 6.3), is redistributed along the DC and spar. It is observed that the current leaves the spar and returns to the DC gradually along the sample length. More specifically, the peak of the current flowing in the middle of the spar (Spar Current 1) is 75% of the injected current peak, while it reduces to 65% at the end of the fourth chamfer profile (Spar Current 2). This means that 10% of the current is diverted back to the DC. Furthermore, the peak current in the DC at the root is 47% of the total, which means that an additional 12% leaves the spar for the DC at the root end.

High current density areas are predicted at x = 3.4 m (position of the spar first pultruded profile) around the bonding interfaces (see Figures 6.8 and 6.9). The high current density area at the EB-Spar interface is found where the current enters the spar first pultruded profile and might be due to the large spar chamfer angle. The high current density region at the DC-EB interface is instead caused by the crowding effect in the DC, which reduces the contact area established with the EB layers required to divert the current to the spar. These areas might lead to high temperatures and thermal damage due to Joule heating (note that only the conduction current density is modelled, while the displacement current density is neglected as outlined in Section 5.1).

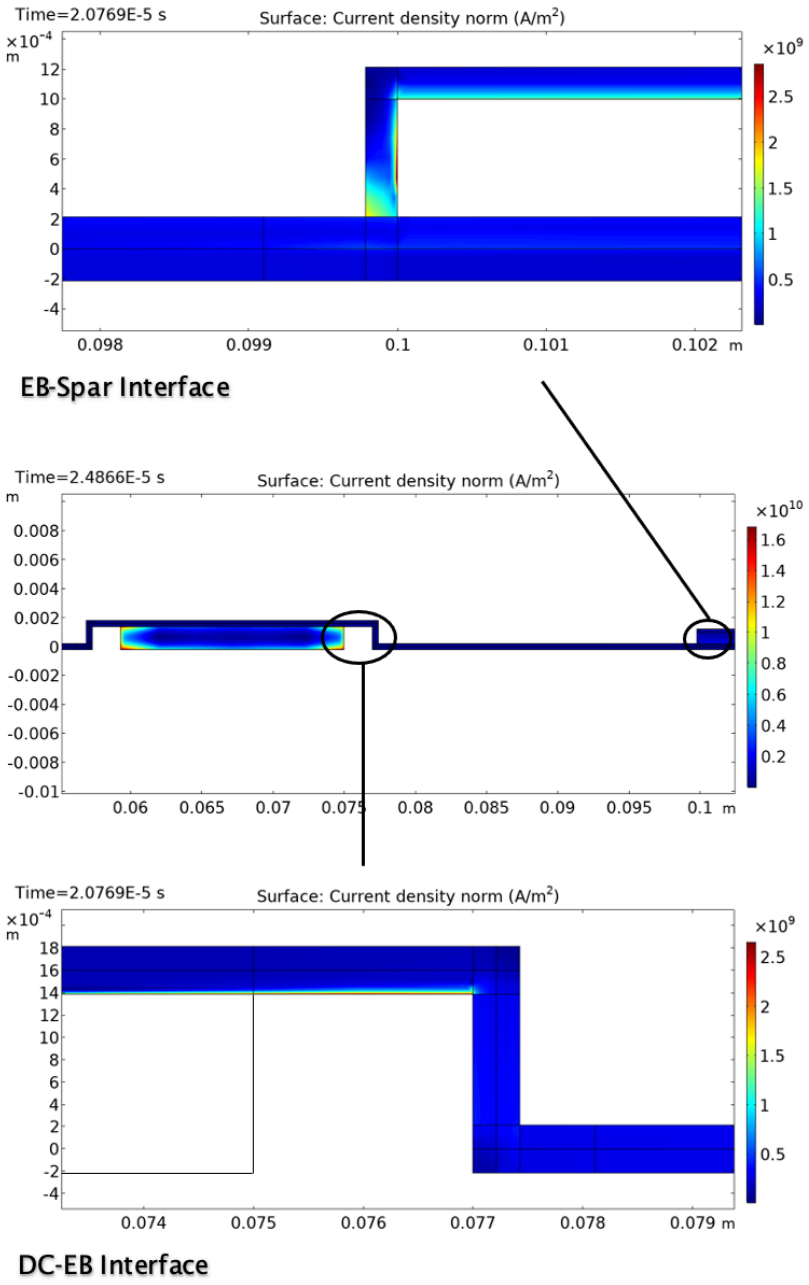

Figure 6.8 – FEM simulation: high current density areas with electrical contact formulation (at x = 3.4 m and at the time instance of maximum current density).

Finally, no significant difference in terms of overall current split is observed in Figure 6.7 when simulating the test with electrical contact resistivities implemented at the bonding interfaces (blue curves) and without, i.e., ideal contact is assumed (red curves). This is expected as the resulting contact resistances are between 2 and 4 orders of magnitude smaller than the overall

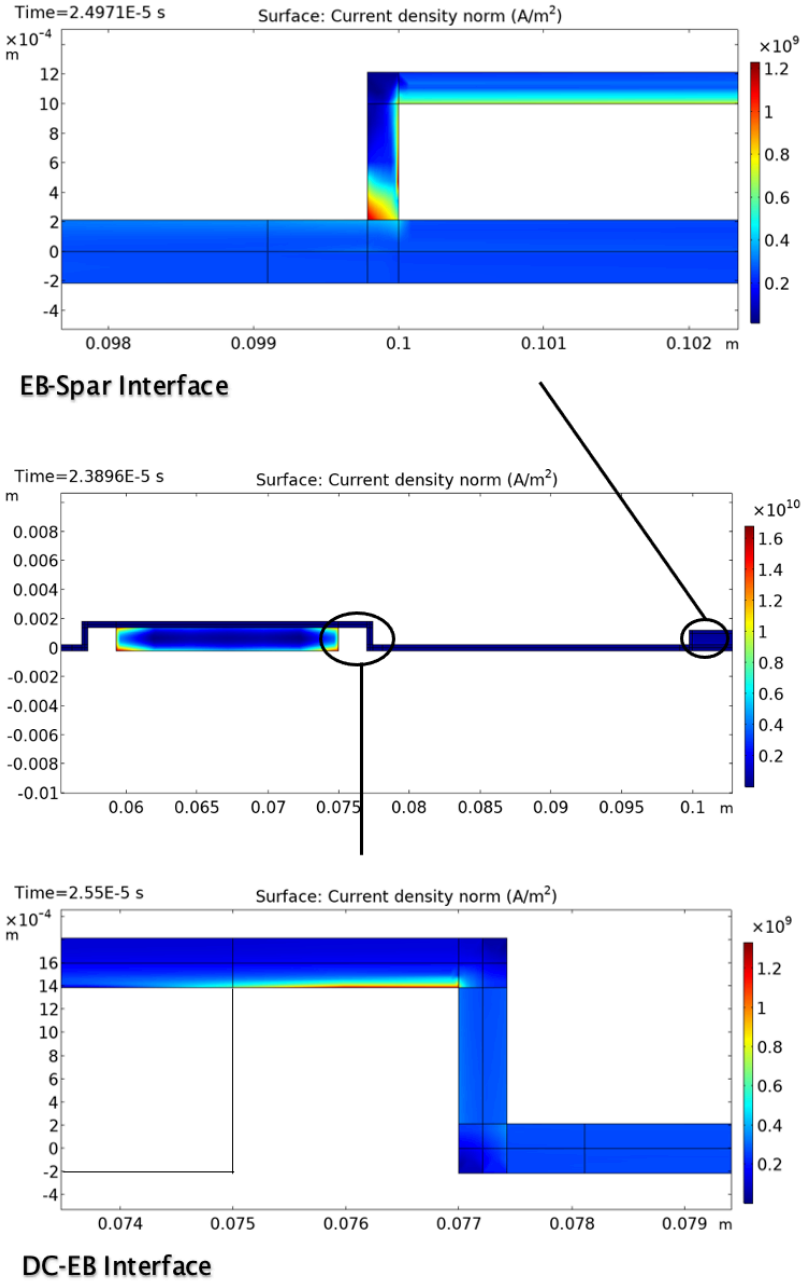

Figure 6.9 – FEM simulation: high current density areas with ideal contact formulation (at x = 3.4 m and at the time instance of maximum current density).

sample impedance. On the other hand, the implementation of the electrical contact affects the current density distribution in the EB joint cross-section. More precisely, the maximum value of current density increases by a factor of 2.5 at the EB-Spar interface and by a factor of 2 at the DC-EB interface when modelling the electrical contact (see Figures 6.8 and 6.9).

6.3.2 Temperature Distribution within the Blade Conductors

The temperature distributions within the rotor blade sample predicted by the FEM simulation are depicted in Figures 6.10 to 6.12. The maximum temperature within the spar is found at x = 3.4 m and does not exceed 90 °C (see Figure 6.10). This is due to the fact that the spar conducts the lightning current for a short interval [21], [40], [42], [111], as well as because the test sample presents EB layers over the spar chamfered surfaces. This allows the current to be injected through the entire spar cross-section, which reduces the Joule heating due to the CFRP anisotropy. As the spar maximum temperature is considerably below the temperature dependence range of

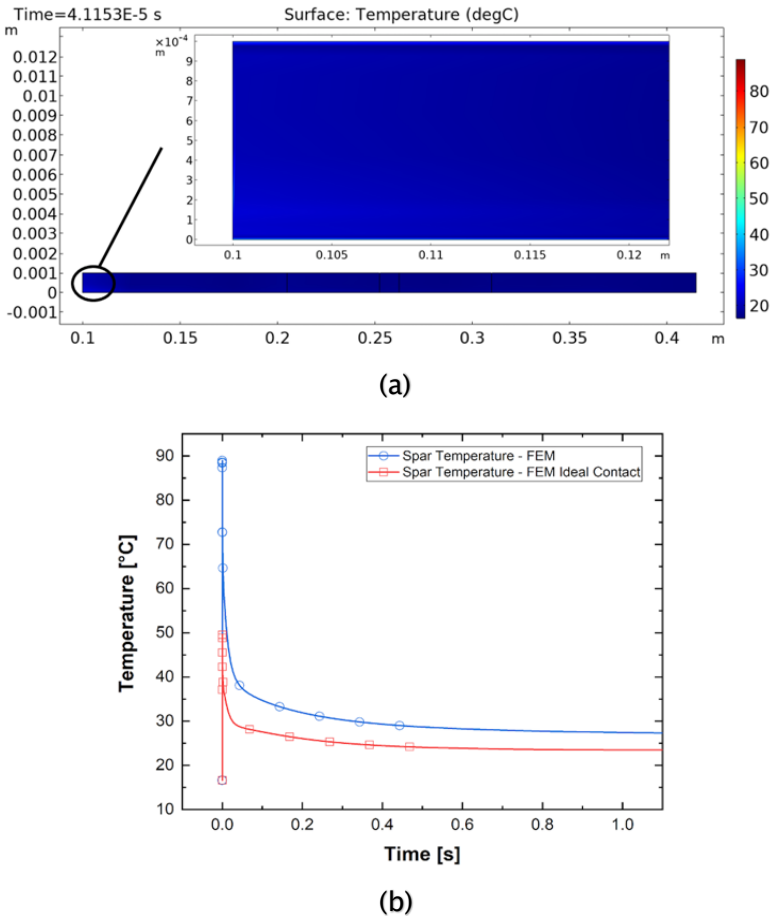

Figure 6.10 – FEM simulation: (a) temperature distribution in the spar with electrical contact formulation (at x = 3.4 m and at the time instance of maximum temperature) and (b) maximum temperature as a function of time in the spar with electrical and ideal contact formulations.

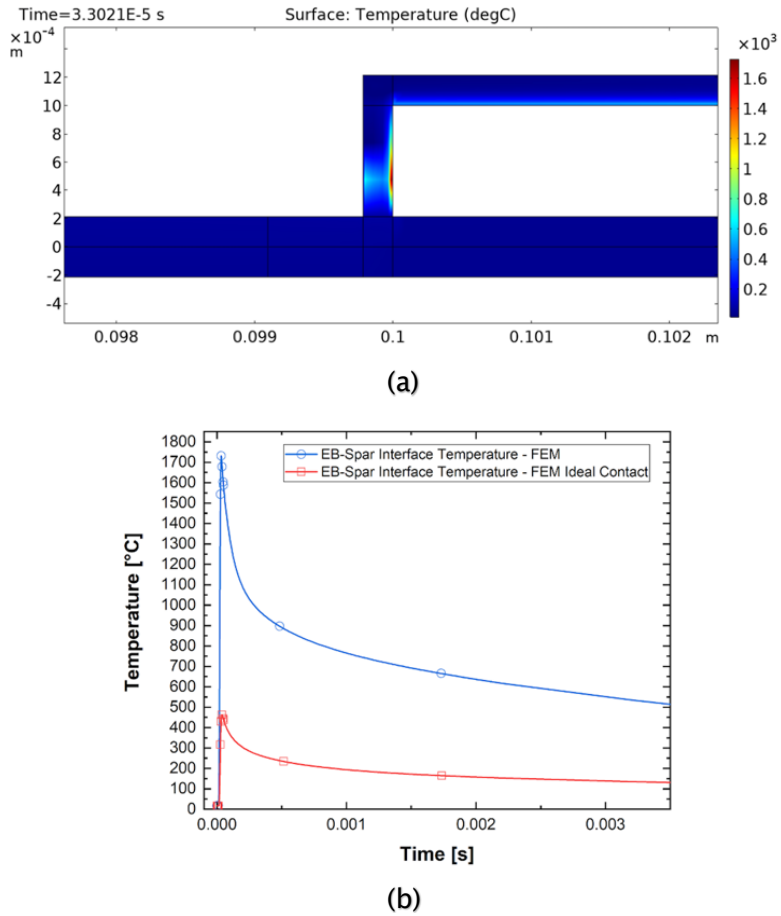

Figure 6.11 – FEM simulation: (a) temperature distribution at the EB-Spar interface with electrical contact formulation (at x = 3.4 m and at the time instance of maximum temperature) and (b) maximum temperature as a function of time at the EB-Spar interface with electrical and ideal contact formulations.

CFRP electrical and thermal conductivities [100], [103], [105]–[108], the weak coupling between the electromagnetic and heat transfer problems is a valid approach to model lightning strikes to wind turbine blades. On the other hand, large temperatures are achieved at the bonding interfaces in the area around x = 3.4 m because of high current density areas, as seen in Figure 6.8. More specifically, a peak temperature of ~1,730 ˚C is achieved after ~33 μs at the EB-Spar interface (see Figure 6.11), whereas a peak value of ~3,440 ˚C is observed after ~34 μs at the DC-EB interface (see Figure 6.12). After 38 s, the sample has cooled down and its temperature has approximately returned to ambient value.

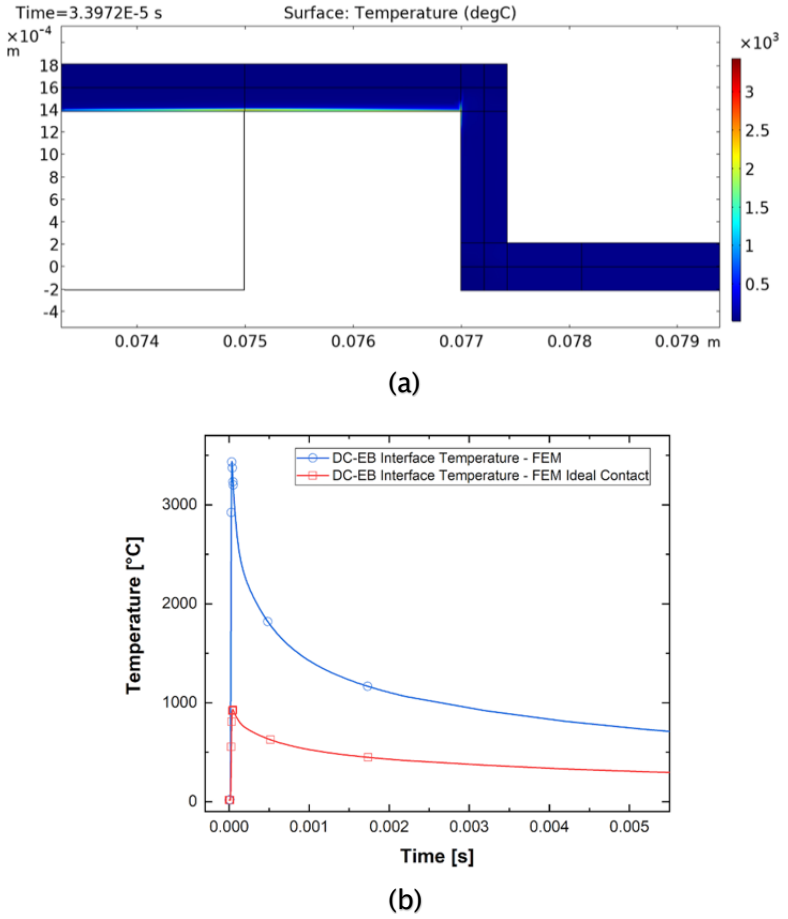

Figure 6.12 – FEM simulation: (a) temperature distribution at the DC-EB interface with electrical contact formulation (at x = 3.4 m and at the time instance of maximum temperature) and (b) maximum temperature as a function of time at the DC-EB interface with electrical and ideal contact formulations.

The temperature distribution on the external surface of the sample (i.e., the GFRP shell inner layer) was recorded during the test through the IR camera. The results show that the temperature peak is attenuated and delayed through the shell compared with the temperature peak at the EB interfaces. For instance, a maximum value of ~32 ˚C is achieved after 1.7 s at the shell inner layer (see Figure 6.13). Such a long delay is due to the low diffusivity of GFRP materials, which is equal to 2.5×10^{-7} m^2/s in the through-thickness direction. Hot areas at the shell inner layer are located between the DC and spar and along the edge of the first pultruded profile where the lightning current enters the spar (see Figure 6.13*a*). A good correlation is found with

the FEM simulation regarding the temperature distribution in these regions of the sample (see Figure 6.13*b*), although slight differences are noticed. For instance, the size of the hot area between the DC and spar (i.e., the red area in Figures 6.13*a* and 6.13*b*) is slightly smaller in the simulation (see Figure

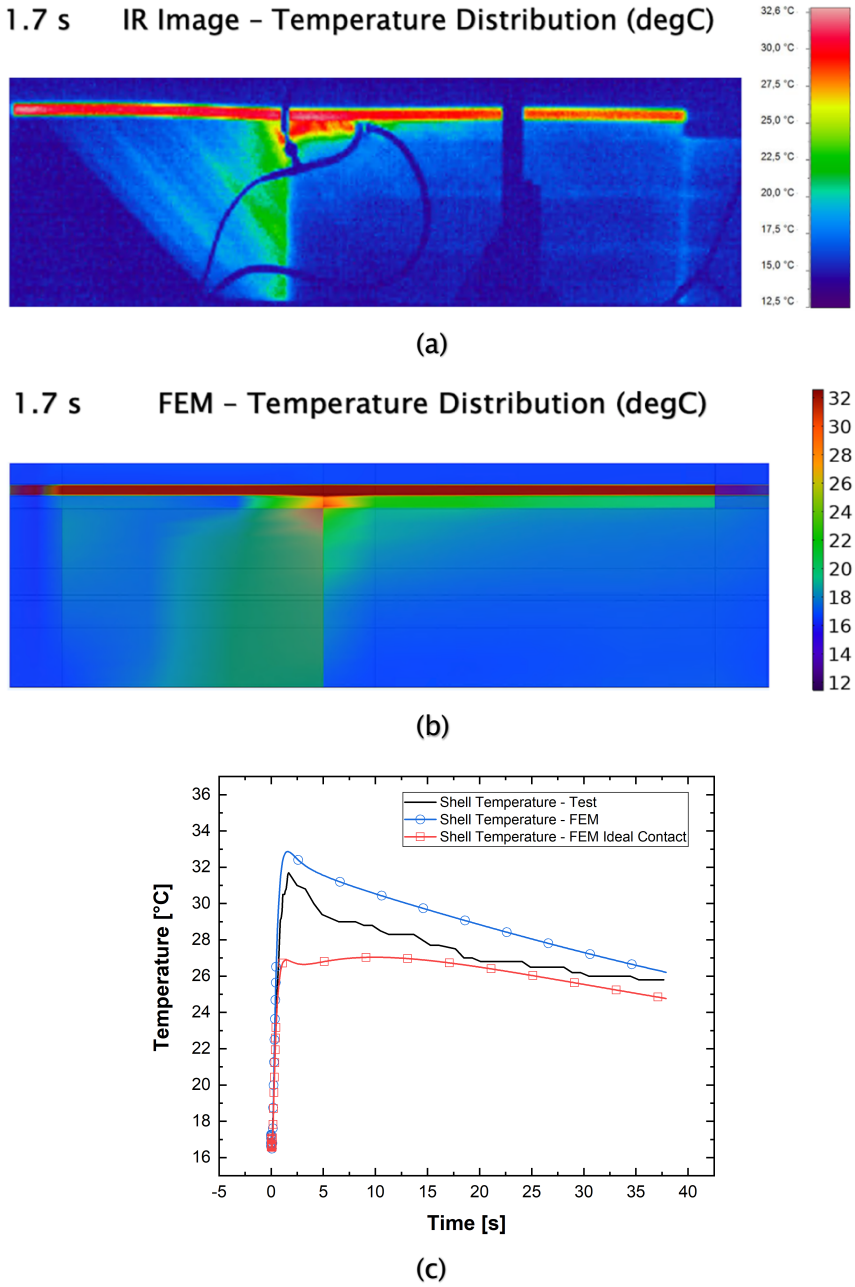

Figure 6.13 – Temperature results on the shell inner layer at the tip end: (a) temperature distribution observed in the test, (b) temperature distribution predicted by the FEM simulation with electrical contact formulation, and (c) maximum temperature as a function of time.

6.13*b*) than in the test (see Figure 6.13*a*). This may be due to the sparking events occurring in this area (see Section 6.3.3). The formation of voids and sparks may modify the contact area, which causes the current to spread over a larger area when it diverts towards the spar. The change in contact resistivity due to the sparks is not known and thus not implemented in the FEM model. In addition, the simulation predicts slightly higher temperatures in the region between the DC and spar (see Figure 6.13*c*). In fact, both the peak temperature at 1.7 s and the temperature at 38 s are slightly overestimated by ~1 °C in the FEM simulation. This is caused by two other numerical assumptions. The first one is made when modelling the epoxy degradation (see Section 6.3.3) since the change in system enthalpy due to the phase change is neglected, which would dissipate part of the Joule heat. However, the increase in the solution accuracy thanks to its implementation would not justify the significant growth of the computational time. The second one is represented by the employed contact resistivity values since they have been determined by room temperature tests, while it is known that the contact resistivity decreases with increasing temperatures [184]–[186]. Despite the approximations and assumptions mentioned above, the overall FEM computations of heat release and temperature are accurate as the predicted hot regions correspond to the ones measured experimentally.

Finally, note that much lower temperatures are achieved at the EB interfaces if ideal contact is assumed, e.g., up to ~465 °C at the EB-Spar interface (see Figure 6.11*b*) and ~930 °C at the DC-EB interface (see Figure 6.12*b*). In addition, major temperature disagreements are also found, with ideal contact, at the shell inner layer, where the heating and cooling profiles are noticeably different compared with the test observations (see Figure 6.13*c*). These discrepancies are expected as lower values of current density are achieved when considering the ideal contact formulation, as seen in Section 6.3.1. Therefore, it is essential to model the electrical contact at the EB interfaces in order to achieve accurate current density and temperature distributions.

6.3.3 Thermal Damage: Sparking and Delamination

Figure 6.14*a* depicts the test sample during the conduction of the simulated lightning current, as well as the positions of the sample components (the dashed lines indicate that the component is encapsulated within the GFRP shell). As shown in the figure given above, sparks have been observed at the sample tip end. They have developed along the DC edge on the spar side (no. 1) and along the edge of the first pultruded profile where the lightning current

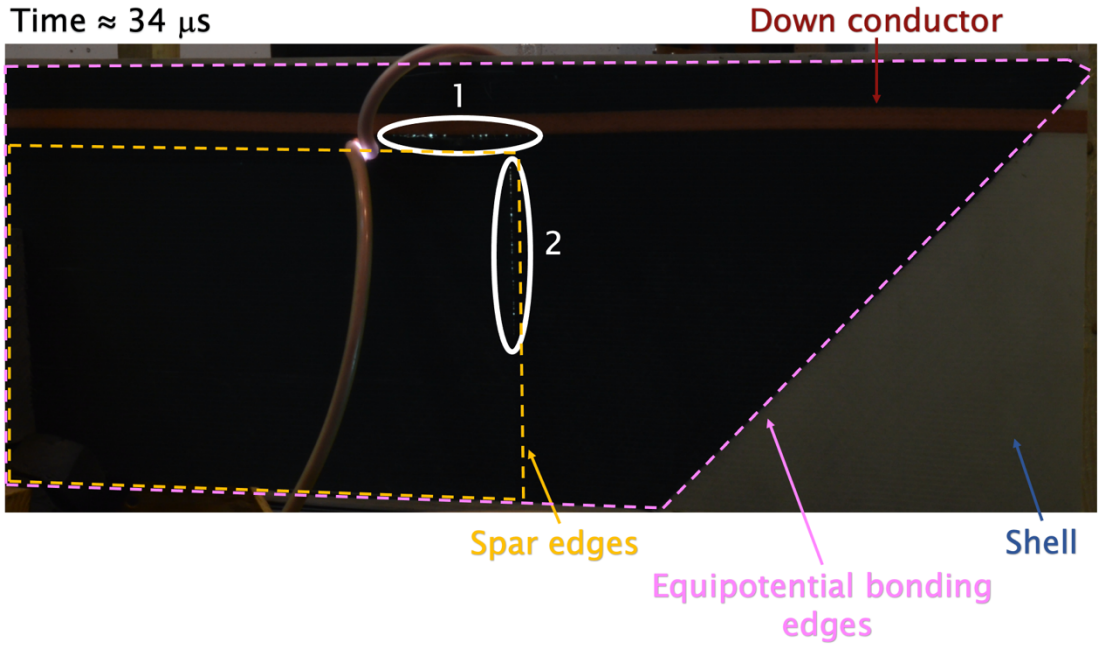

(a)

(b)

Figure 6.14 – Conducted current test: (a) sparking locations during the test and (b) delamination, after the test, between the inner surface of the GFRP shell outer layer and the BIAX EB layer, which is visible thanks to the transparency of GFRPs.

enters the spar (no. 2). In addition, a delamination of ca. 26.1x8.5 mm^2 has been observed in area no. 1 (see Figure 6.14*b*) below the sample surface. It occurs at the interface between the BIAX EB layer and the inner surface of the GFRP shell outer layer in the vicinity of the DC. This delamination is visible thanks to the transparency of GFRPs, and is most likely caused by the excessive heating at this location (see Figure 6.12) and by the thermal expansion mismatch between copper and composite materials [235], [236].

The sparks and delamination observed in the test are located above the DC-EB and EB-Spar interfaces in the area around x = 3.4 m. That is, where high current densities (see Figure 6.8) and temperatures (see Figures 6.11 and 6.12) are found within the sample cross-section. By solving the Arrhenius equation in the FEM model (see Section 5.2.2) using the thermal degradation kinetics and the temperature predicted at each time step, the degree of thermal degradation is computed. The results indicate the occurrence of polymer degradation at both DC-EB (see Figure 6.15) and EB- Spar (see Figure 6.16) interfaces in the area around 3.4 m, i.e., where sparks have been observed. More precisely, Figure 6.15 shows that sparking area no. 1 coincides with the red area (i.e., $0.9 \leq \alpha_i \leq 1$) of both mechanisms 3 and 4. On the other hand, polymer degradation is predicted near sparking area no. 2 for mechanism 2 only (see Figure 6.16), as the temperature in this area is below the onset temperatures of mechanisms 3 and 4 (note that the temperature in area no. 2 is 800-1,000 ˚C, while the 1,730 ˚C peak is achieved on the EB vertical layer only, see Figure 6.11). In other words, the degradation in sparking area no. 2 would not be predicted if the apparent single reaction approach (i.e., all mechanisms summed together) was used, which would contradict the test observations. Considering these results, it is therefore concluded that sparking phenomena triggered at the EB interfaces of wind turbine blades during lightning strikes are thermally activated. That is, epoxy degradation due to high temperatures results in formation of gas filled voids, which separate the current carrying conductors and trigger sparks [27], [28].

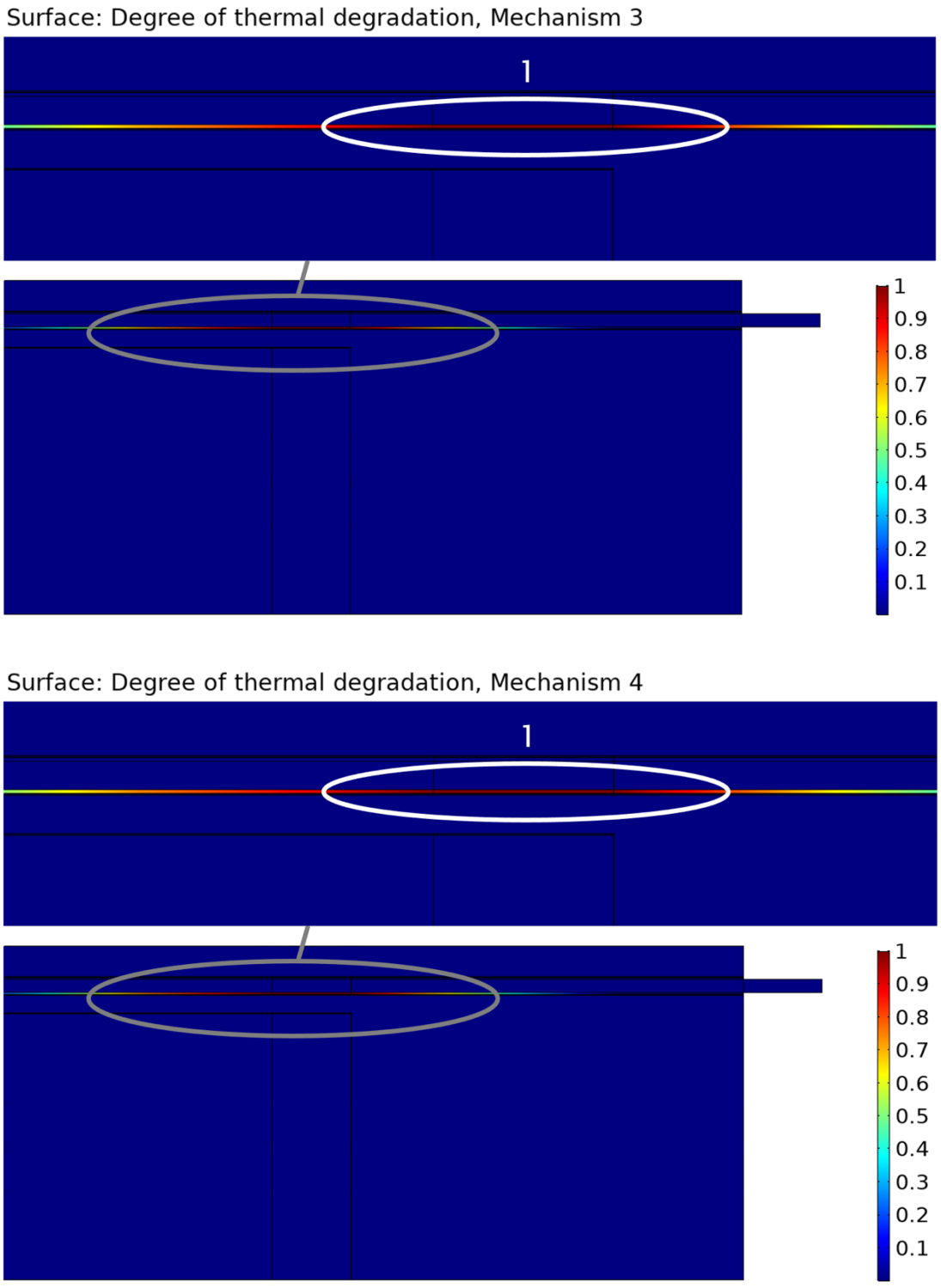

Figure 6.15 – FEM simulation: polymer thermal degradation at sparking area no. 1.

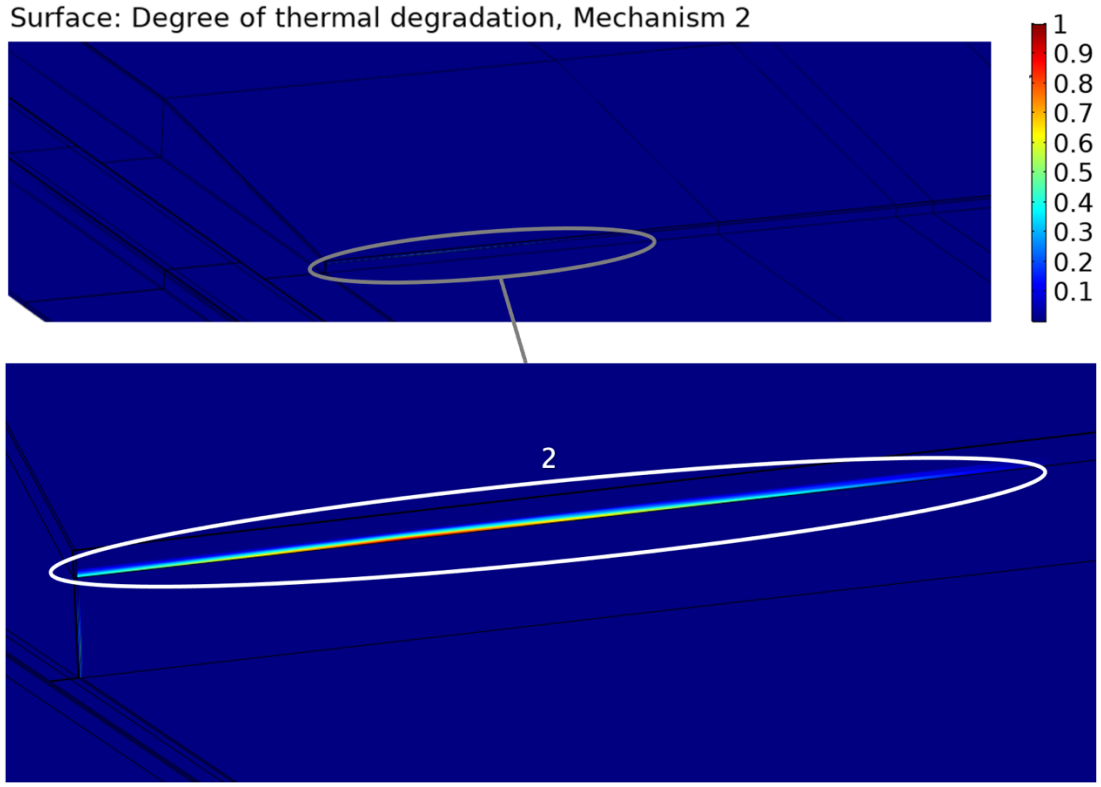

Figure 6.16 – FEM simulation: polymer thermal degradation at sparking area no. 2.

The results presented in Sections 6.3.2 and 6.3.3 answer one of the two EB design open questions identified in both the Introduction and Literature Review. That is, the bulk CFRP spar can withstand lightning currents since it only conducts a small share of it, whereas thermal damage can develop at the EB interfaces because of high contact resistances.

6.4 Summary

This chapter validated the numerical modelling framework presented in Chapter 5 against simulated lightning current tests, to evaluate its capability of assisting in the design of rotor blade EB connections. Lightning damage to modern wind turbine blades typically develops at the LPS EB interfaces. Such regions present resin-rich areas that lead to high-current densities and temperatures, with consequent resin thermal degradation and sparking events.

It was shown that numerical simulations are effective tools to study the thermal damage at the considered EB interfaces. In fact, the proposed FEM model predicted high current densities and temperatures at the sparking locations, which allowed a qualitative estimation of potential thermal degradation areas upon the solution of the Arrhenius equation. The predictions of high temperature and thermal degradation at the sparking locations indicated that the damage is thermally activated. That is, high temperatures cause epoxy pyrolysis, leading to voids formation, separation of the blade current carrying conductors, and inception of sparks. In addition, the results revealed that this is true even when the amount of mass converted into a gas fraction is as little as 2-3%, as in the case of mechanism 2. In fact, the latter was the only degradation mechanism predicted at sparking area no. 2, which would not be captured if the apparent single reaction description was used. On the other hand, the bulk CFRP spar could withstand the lightning current without experiencing thermal damage. These results answered one of the two EB design open questions identified in both the Introduction and Literature Review, i.e., EB joints can experience thermal damage under lightning currents, whereas the bulk CFRP spar can safely conduct them.

Finally, it was shown that the FEM formulations with and without the contact resistivities at the bonding interfaces did not present any significant variation in terms of lightning current split between the blade conductors. However, major differences were found between the two formulations in terms of local current density and temperature distributions, e.g., peak temperatures were up to 4 times smaller in the ideal contact formulation. Therefore, it is essential to implement the electrical contact in FEM models in order to compute accurate current density and temperature distributions and design reliable EB solutions.

Chapter 7

Electromagnetic-Thermal Behaviour of a Wind Turbine Blade Equipped with EB Joints

As said in both the Introduction and Literature Review, two crucial questions on the design of wind turbine blade EB connections have remained unanswered for several years, that is: whether CFRP spars and EB joints can withstand lightning currents without experiencing thermal damage and how equipotential connections should be designed. The first question was answered in Chapter 6, which showed that EB joints can experience thermal damage under lightning currents, whereas the bulk CFRP spar can safely conduct them. On the other hand, this chapter provides guidelines and suggestions on the implementation of EB connections to help answering the second open question. To do so, the FEM methodology presented in Chapter 5 is employed to investigate the electromagnetic-thermal behaviour of a 50 m rotor blade when equipped with different EB materials, which are ECF, BIAX CFRP, and UD CFRP. The blade is first subjected to the subsequent short stroke current to predict the electric field distribution and determine the minimum number and length of the bonding points. After that, the blade

equipped with the EB concepts established in the previous step is subjected to the first positive short stroke current to propose the best practises for the control and minimisation of the temperature at the EB interfaces. Note that this chapter is not intended to provide any final EB design to be implemented in rotor blades as it would require high-current test validation in order to get the IEC 61400-24:2019 standard certification [12].

7.1 EB Design Procedure

Typically, the design procedure of EB systems develops into two main steps (see Figure 7.1). First, it is required to solve the electromagnetic problem when the blade is subjected to the subsequent short stroke. In fact, the latter is the impulse that presents the largest rate of rise of current (200 kA/μs) and that results in the highest electric field distribution along the blade (see Section 2.6.1). In this step the prevention of internal flashovers dictates the number and length of EB connections, which are gradually introduced in the blade structure to minimise the increase in blade weight. If the computed electric field is smaller than the insulating material breakdown strength at all

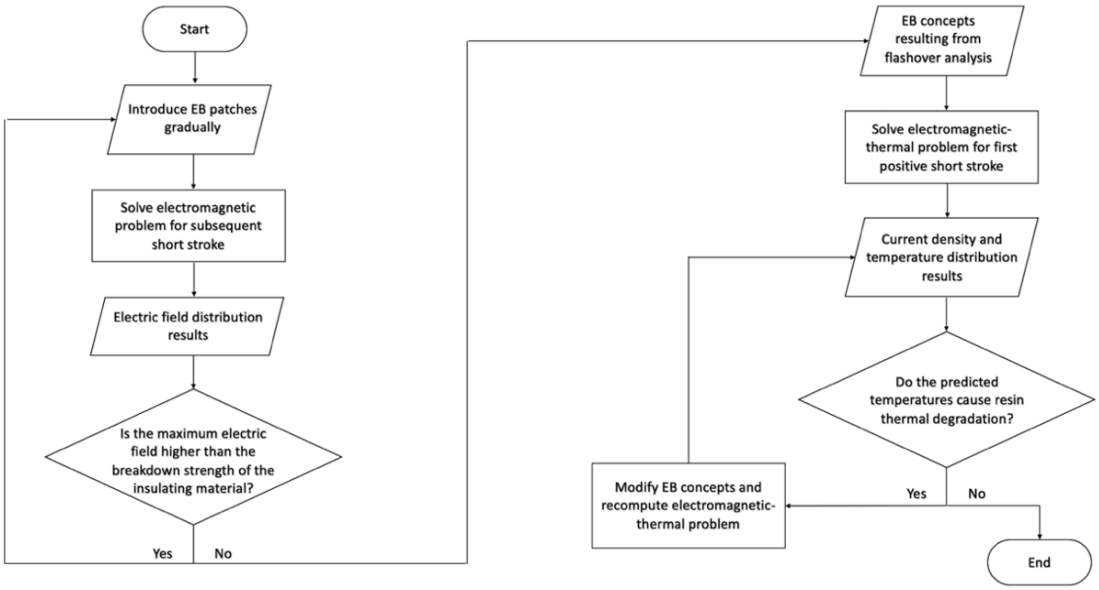

Figure 7.1 – Flowchart of the EB design procedure.

the blade locations, then the EB configuration can avoid flashovers. If not, the length and/or number of EB patches are increased and the electric field recomputed until it is below the insulation breakdown strength.

The EB concepts resulting from the first step, i.e., the flashover risk analysis, are then used as input designs for the second step, i.e., the current and temperature distributions analysis. The impulse considered in this step is the first positive short stroke as it generates the largest amount of Joule heating because of its high specific energy (see Section 2.6.2). The arrangement, length, and/or number of EB patches are gradually modified until the predicted temperatures are below the degradation onset temperature.

7.2 FEM Modelling

7.2.1 Wind Turbine Blade Geometry and Material Properties

The geometry of the 50 m rotor blade shell is shown in Figure 7.2, while its dimensions are summarised in Table 7.1. It was composed of a 40.1 m UD

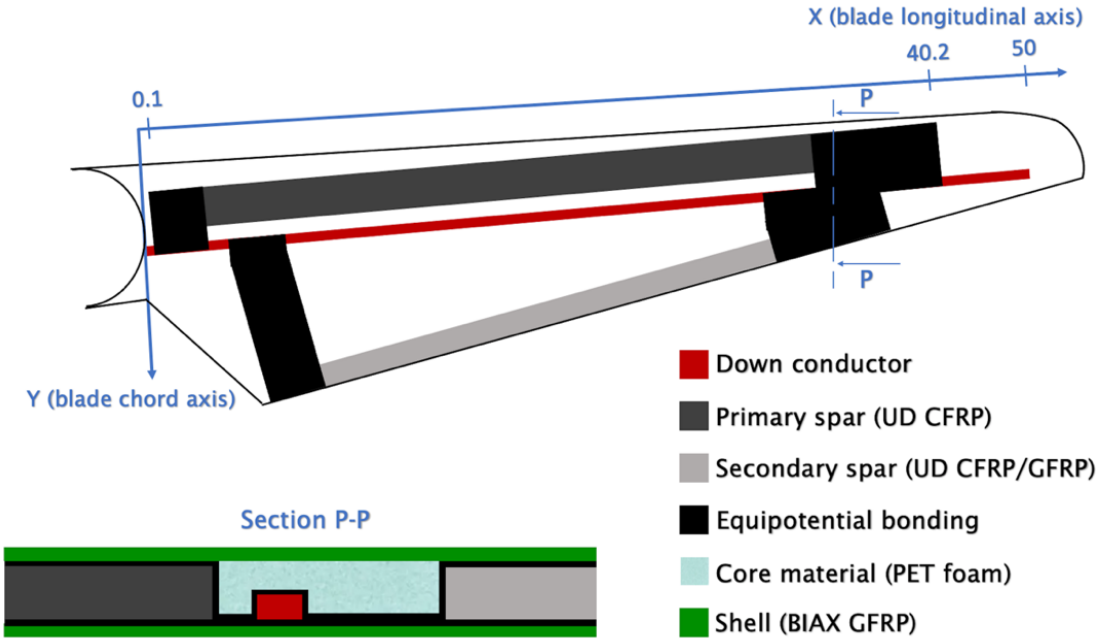

Figure 7.2 – Arrangement of the blade conductors (not to scale). The shell layers and the core material were intentionally omitted in the top view to show the DC, spars, and EB layers.

Table 7.1 – Wind turbine blade dimensions. The width and length of the EB layers vary according to the assessed EB solution.

	Primary spar	
Width [mm]		400
Thickness [mm]		0.828-27.32
Length [m]		40.1
Primary spar - DC distance [mm]		30
	Secondary spar	
Width [mm]		310
Thickness [mm]		0.818-28.63
Length [m]		35
Secondary spar - DC distance [mm]		62(Tip)-1,292(Root)
	EB	
Width [mm]		Variable
	UD CFRP	0.717
Thickness [mm]	**BIAX CFRP**	0.214
	ECF	0.35
Length [m]		Variable
	DC	
Width [mm]		22.8
Thickness [mm]		2.2
Length [m]		50
Cross-section [mm^2]		50
	Core material	
Width [mm]		113(Tip)-1,307(Root)
Thickness [mm]		29.3
Length [m]		35.75
	Shell	
Width [mm]		925(Tip)-2,160(Root)
Thickness [mm]		0.688
Length [m]		50.4

CFRP primary spar and a 35 m UD CFRP/GFRP secondary spar with variable thickness, as they presented chamfer profiles (see Figure 7.3). Both the primary and secondary spars were connected to the DC by EB layers (see Figure 7.2), which were made of UD CFRP, BIAX CFRP, or ECF. The DC was made of copper and its cross-section was 50mm^2, as specified in the IEC 61400-24:2019 standard [12]. Finally, the material properties of the blade components are given in Appendix A.

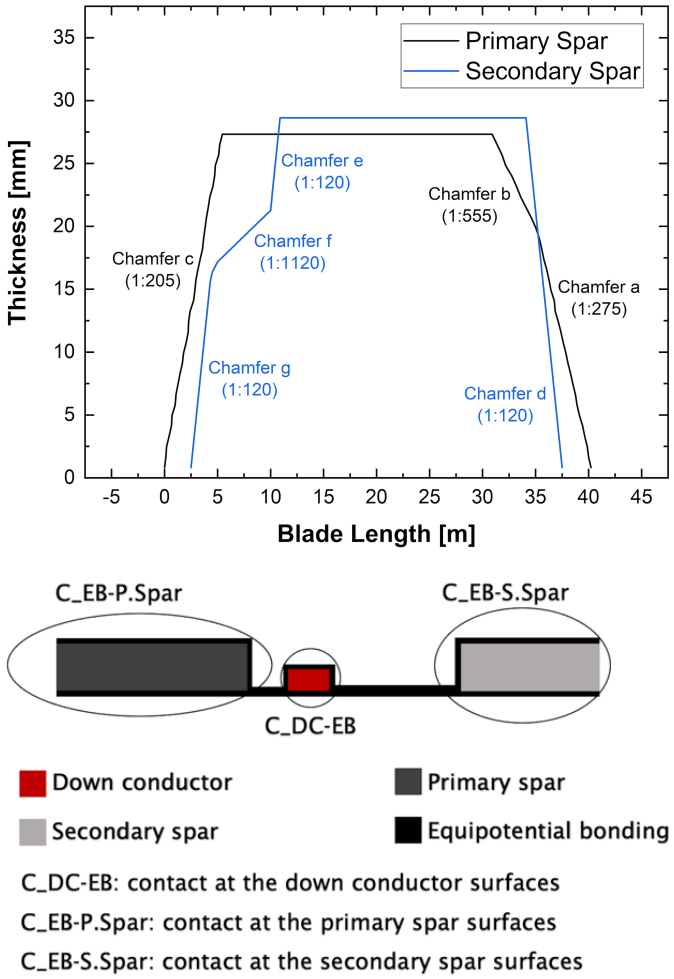

Figure 7.3 – Variation of primary and secondary spars thickness as a function of the blade position, and different contact regions.

7.2.2 Size of the Insulating Volume

The wind turbine blade structure was placed within a computational domain (insulating volume) of size 4 x 4 x 40.2 m^3. The outer surfaces of the insulating volume acted as a current return path, as defined by the boundary conditions given in Equation (5.5). The size of the return path is a key factor for the computation of the system total inductance, which is the main contributor to the voltage drop across the rotor blade and is given by:

$$L_{TOT} = L_{BLADE} + L_{RP} - 4M_{BLADE\text{-}RP} \tag{7.1}$$

where L_{TOT} [H] is the total (loop) self-inductance of the system composed of the rotor blade and the return path, L_{BLADE} [H] is the partial self-inductance of the blade, L_{RP} [H] is the partial self-inductance of the return path, and $M_{BLADE\text{-}RP}$ [H] is the mutual inductance between the blade and return path.

The mutual inductance $M_{BLADE\text{-}RP}$, and thus L_{TOT}, depends on the distance between the blade conductors and return path [237], [238]. More specifically, if this distance grows $M_{BLADE\text{-}RP}$ decreases and thus L_{TOT} increases, and vice versa [85], [237]–[239]. As said in Section 6.2.1, for simulations of lightning current tests the return path needs to be as large as the return cage used in the test to obtain a comparable impedance and consistent results. However, lightning strikes to wind turbine blades are not characterised by a finite return path, as the closed path for the current is cloud-wind turbine-ground-cloud. Therefore, infinite elements were employed in the insulating volume, which stretch its boundaries to an almost infinite distance from the blade, increasing the size of the return path (and thus the system total inductance). For instance, an increase of ~15% in maximum electric potential at the blade tip was observed when using infinite elements.

7.2.3 Mesh

The main domains (the orange area and the blade structure depicted in Figure 7.4) were meshed using hexahedral and boundary layer elements. On the other hand, infinite elements [190], [191] were placed on the outer layer of the insulating volume (violet area in Figure 7.4), which is the infinite element domain (IED).

A two-step mesh convergence study was conducted to ensure that the solution was mesh independent. In the first step, the number of elements was increased in the main domains only while keeping the number of infinite elements along the IED thickness equal to 5 [191], until convergence was achieved (see Figure 7.5*a*). The minimum and maximum number of elements in the blade longitudinal (sweep), transverse, and through thickness

directions were 1 and 5, 1 and 20, and 1 and 10, respectively. In the second step, the number of infinite elements along the IED thickness was increased from 5 to 400, while keeping the number of elements in the main domains constant (which was determined in the previous step). Convergence was reached when employing 20 elements along the IED thickness, as shown in Figure 7.5*b*. The final mesh consisted of ~150,000 infinite, hexahedral, and boundary layer elements (see Figure 7.6).

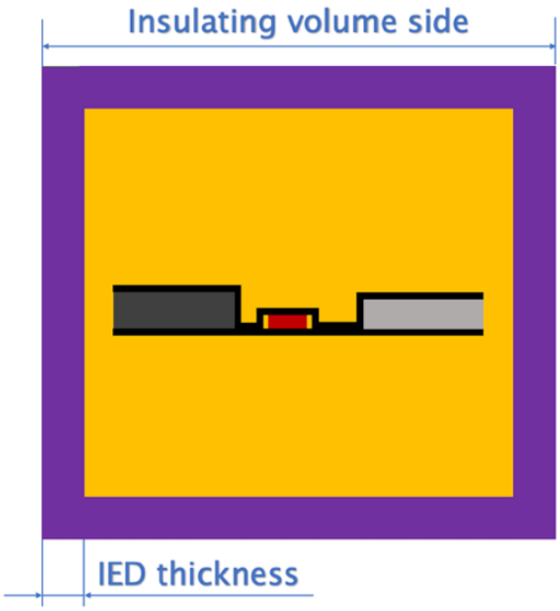

Figure 7.4 – Cross-section view of main and infinite element domains.

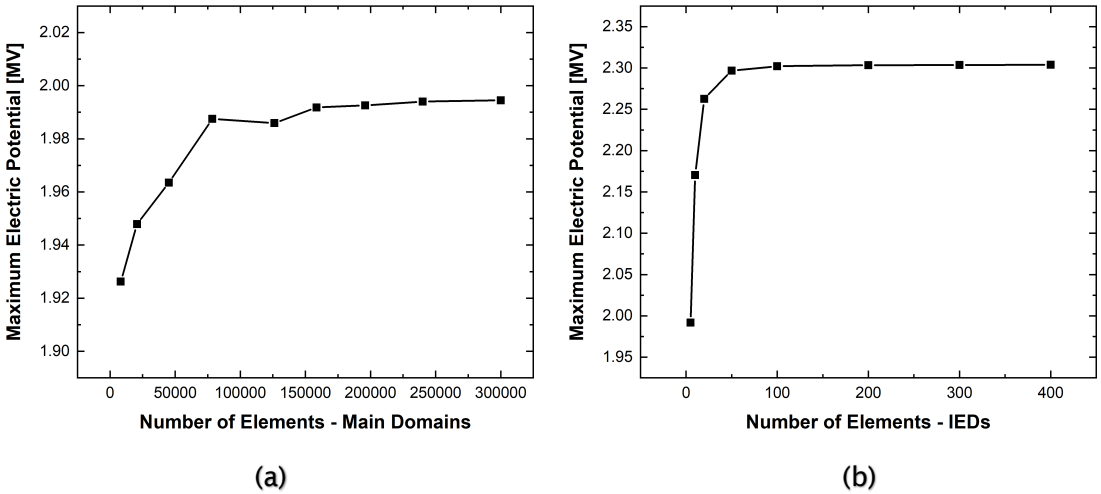

Figure 7.5 – Mesh convergence: (a) main domains and (b) IED.

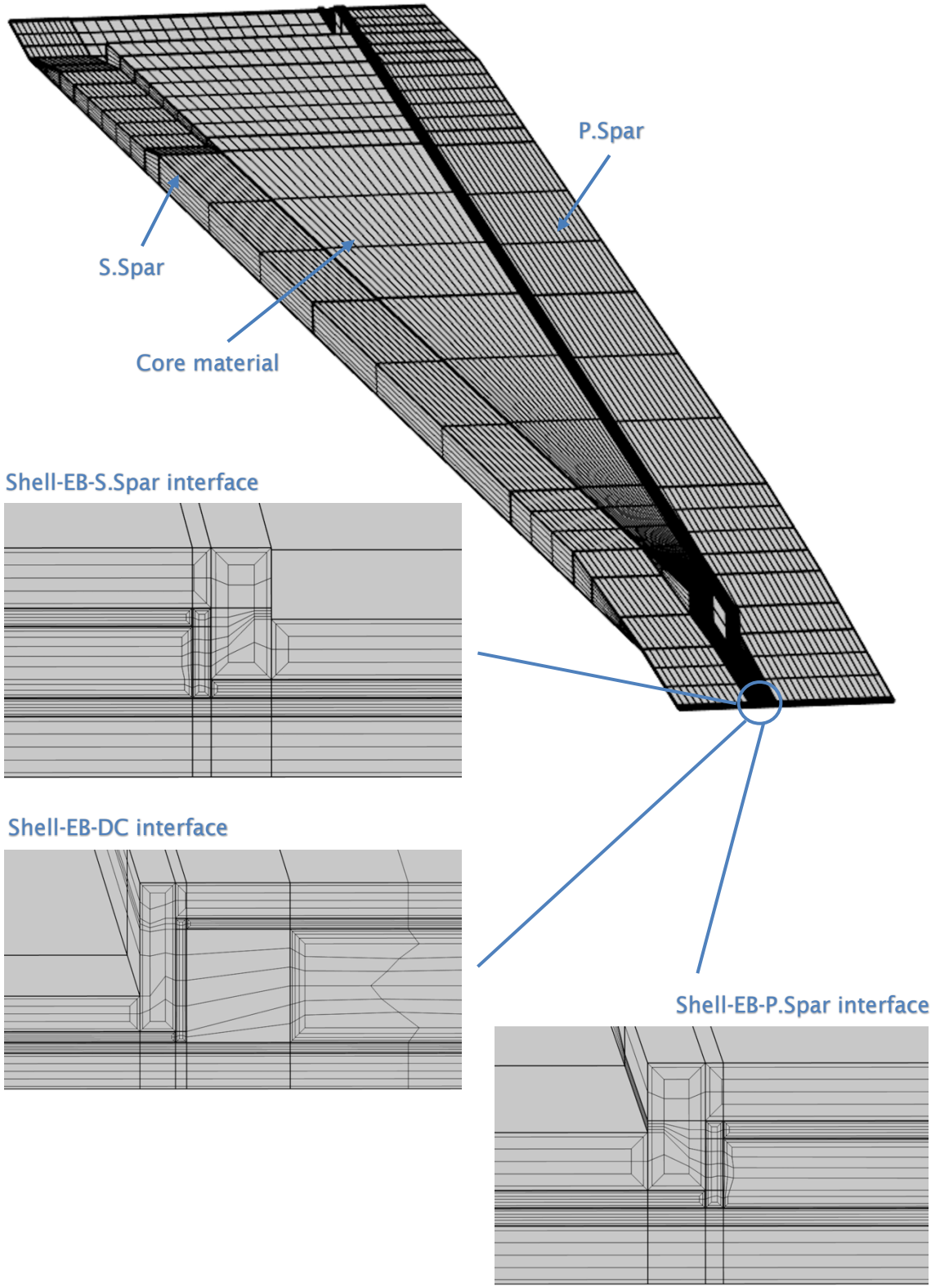

Figure 7.6 – FEM mesh (the insulating volume is intentionally hidden).

7.3 Results and Discussion

7.3.1 Electromagnetic Problem: Flashover Risk Analysis

The results of the flashover risk analysis are given in Figures 7.7 to 7.18 for the three assessed EB materials, i.e., ECF, BIAX CFRP, and UD CFRP (see Section 7.2.1). For each EB material, three different bonding configurations are assessed, which differ in terms of number and length of EB patches. Such concepts are shown in Figures 7.7, 7.11, and 7.15, together with the locations (numbers and lines in violet, light blue, and green) where the transverse component of the electric field, E_y [V/m], is maximum. For instance, in the case of ECF EB configuration 1, values of maximum transverse electric field, $E_{y,max}$ [V/m], are found at x = 35 m, x = 4.45 m, and x = 27.3 m. Note that this work only considers HV breakdown of the insulating material between the blade conductors, as it would cause severe structural damage to the blade. On the other hand, surface flashovers in the cavity of the rotor blade are not studied since they would cause minor or no damage at all.

The distributions of E_y in the gaps between the blade conductors (i.e., along the violet, light blue, and green lines in Figures 7.7, 7.11, and 7.15) show that the electric field is strongly non-uniform for almost all the considered EB configurations (see results in Subfigures *c*, *d*, and *f*). As expected, E_y is maximum near the conductors since the latter are very thin and sharp, whereas it approximately tends to E_{mean} in the middle of the gap. As seen in Section 2.4.2, for rapid voltage impulses like lightning ones even the first electron avalanche causes the complete breakdown once the inception criterion is satisfied [89], [95], [96]. To account for the most conservative scenario, the inception criterion is $E_{max} = E_{bd\_unif}$ (see Section 5.1). In contrast, past studies that employed the lumped-element model [40], [43] assessed the flashover risk by considering uniform electric field conditions, as outlined in

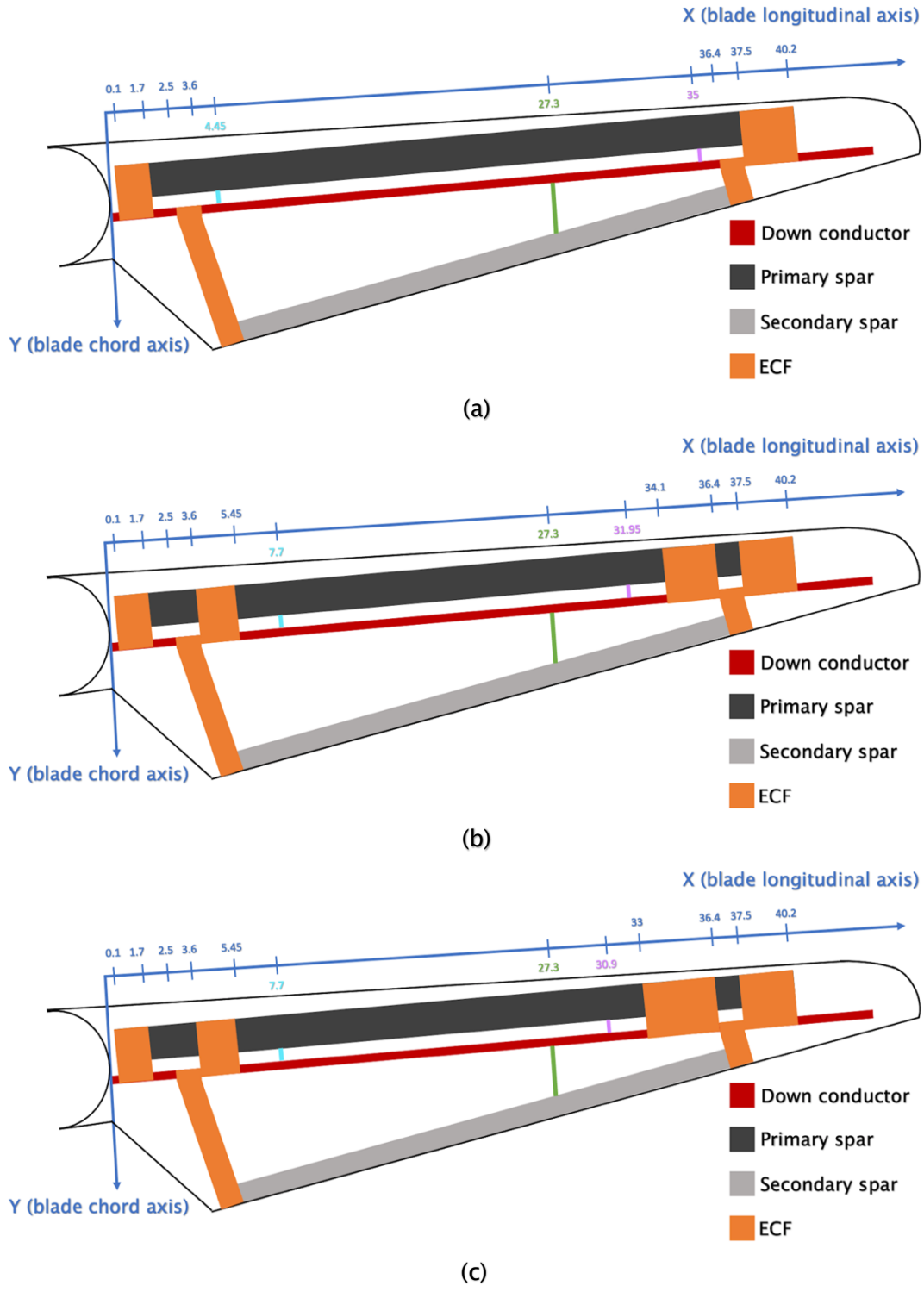

Figure 7.7 – ECF EB configurations (not to scale): (a) configuration 1 (2 bonding patches with p.spar and 2 bonding patches with s.spar), (b) configuration 2 (4 bonding patches with p.spar and 2 bonding patches with s.spar), and (c) configuration 3 (4 bonding patches with p.spar and 2 bonding patches with s.spar, with a longer p.spar tip patch compared with configuration 2). The lines and numbers in violet, light blue, and green represent the locations of $E_{y,max}$.

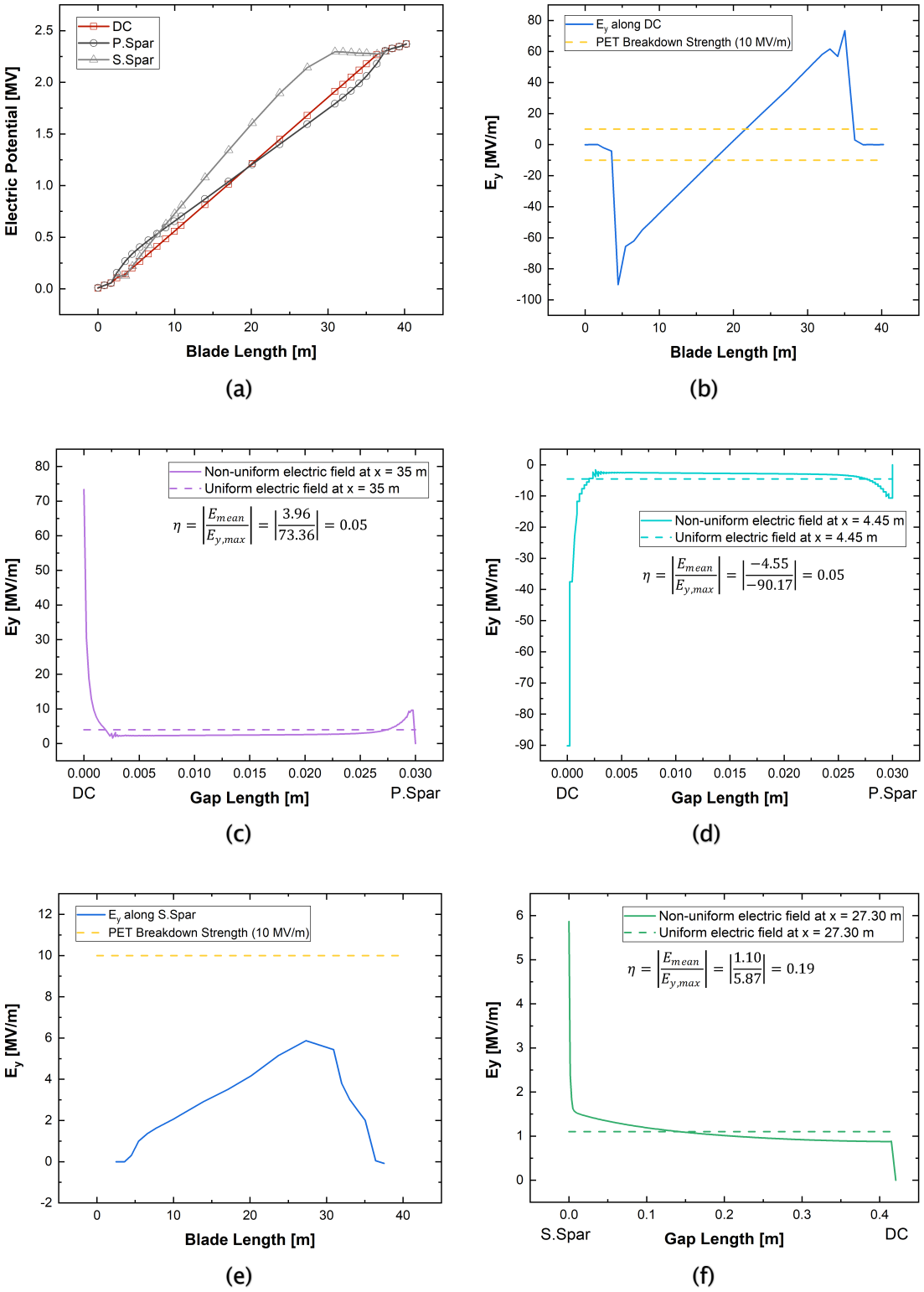

Figure 7.8 – ECF EB configuration 1: (a) electric potential distribution along the blade, (b) E_y distribution along the DC, (c) E_y between DC and p.spar at the tip, (d) E_y between DC and p.spar at the root, (e) E_y distribution along the s.spar, and (f) E_y between DC and s.spar at the tip.

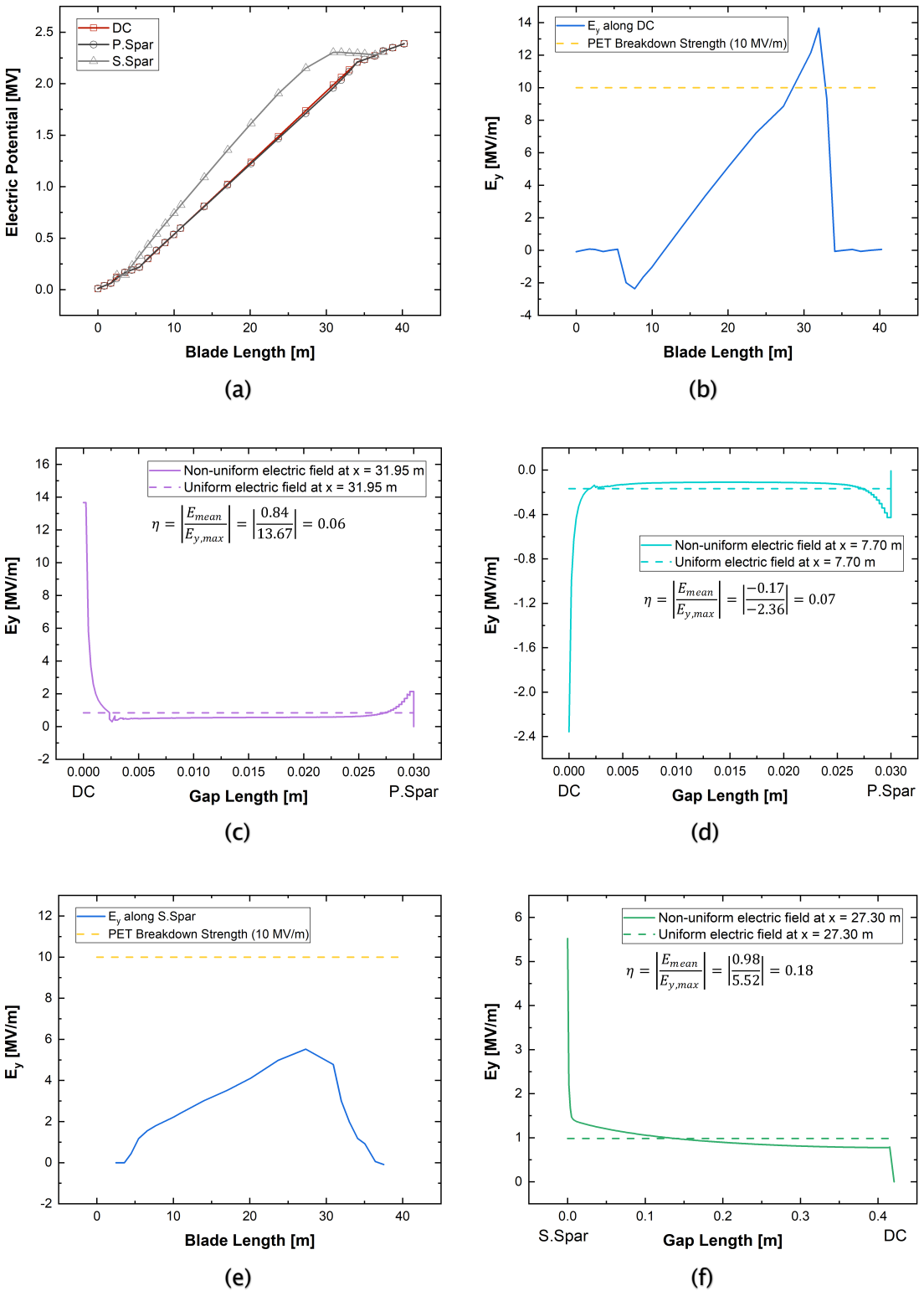

Figure 7.9 – ECF EB configuration 2: (a) electric potential distribution along the blade, (b) E_y distribution along the DC, (c) E_y between DC and p.spar at the tip, (d) E_y between DC and p.spar at the root, (e) E_y distribution along the s.spar, and (f) E_y between DC and s.spar at the tip.

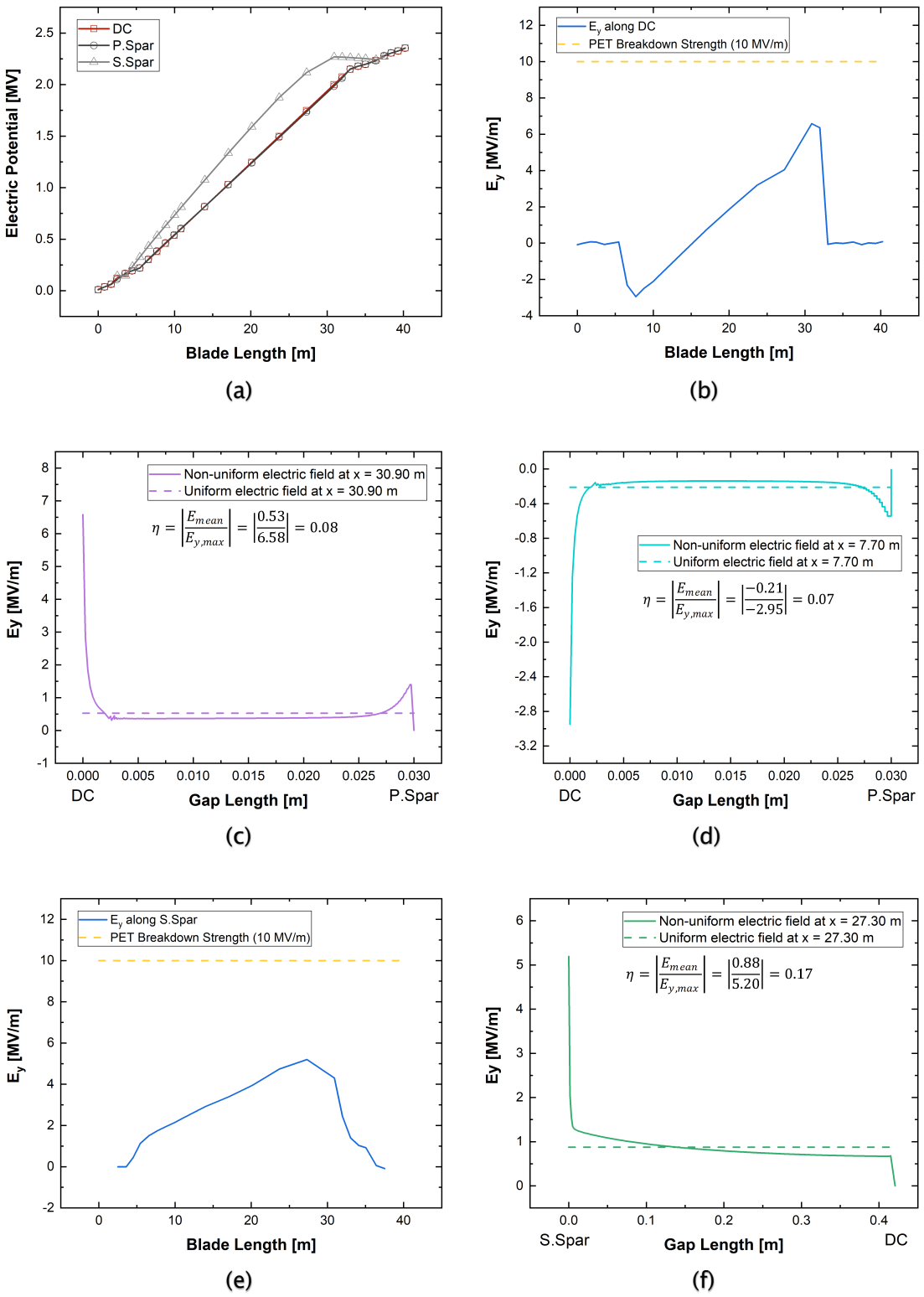

Figure 7.10 – ECF EB configuration 3: (a) electric potential distribution along the blade, (b) E_y distribution along the DC, (c) E_y between DC and p.spar at the tip, (d) E_y between DC and p.spar at the root, (e) E_y distribution along the s.spar, and (f) E_y between DC and s.spar at the tip.

Section 2.4.1. In fact, lumped-element circuits simulations only compute electric potential differences between the blade conductors, which are then divided by the conductors' distance to define an average electric field that is uniform in the gap. However, this assumption underestimates the electric field, leading to an incorrect design in terms of number and length of EB patches. For instance, even ECF EB configuration 1 leads to an average electric field that is smaller than the PET foam breakdown strength (10 MV/m [240], [241]), as shown in Figures 7.8*c* and 7.8*d*.

ECF EB configuration 1 presents two EB patches between the DC and primary spar, one at the tip and one at the root of the blade. Such a concept is not capable of preventing flashovers between the DC and primary spar in the region where they are not bonded (i.e., 1.7 m ≤ x ≤ 37.5 m), with maximum values of E_y found at x = 35 m and x = 4.45 m (see Figure 7.8*b*). In ECF EB configuration 2, four EB connections are used between the two conductors, but the electric field still exceeds 10 MV/m in the area 28 m ≤ x ≤ 34 m (see Figure 7.9*b*). Eventually, the electric field between the DC and primary spar is reduced below the breakdown threshold throughout the blade when increasing the length of the second tip connection by ~1 m (see Figures 7.7*c* and 7.10). On the other hand, the electric field on the secondary spar side is below the PET breakdown strength even when employing two EB connections, one at the tip and one at the root of the blade. This is because the distance between the DC and secondary spar (62.2-1,300 mm) is larger than the distance between the DC and primary spar (30 mm).

BIAX CFRP is also capable of preventing flashovers between the DC and primary spar when employed as an EB material, thanks to the good in-plane electrical conductivity. However, compared with ECF, BIAX CFRP requires a higher number of connections to reduce the electric field below the PET breakdown strength (see Figures 7.12 to 7.14) since its electrical conductivity is smaller than the ECF one. More specifically, six bonding connections of

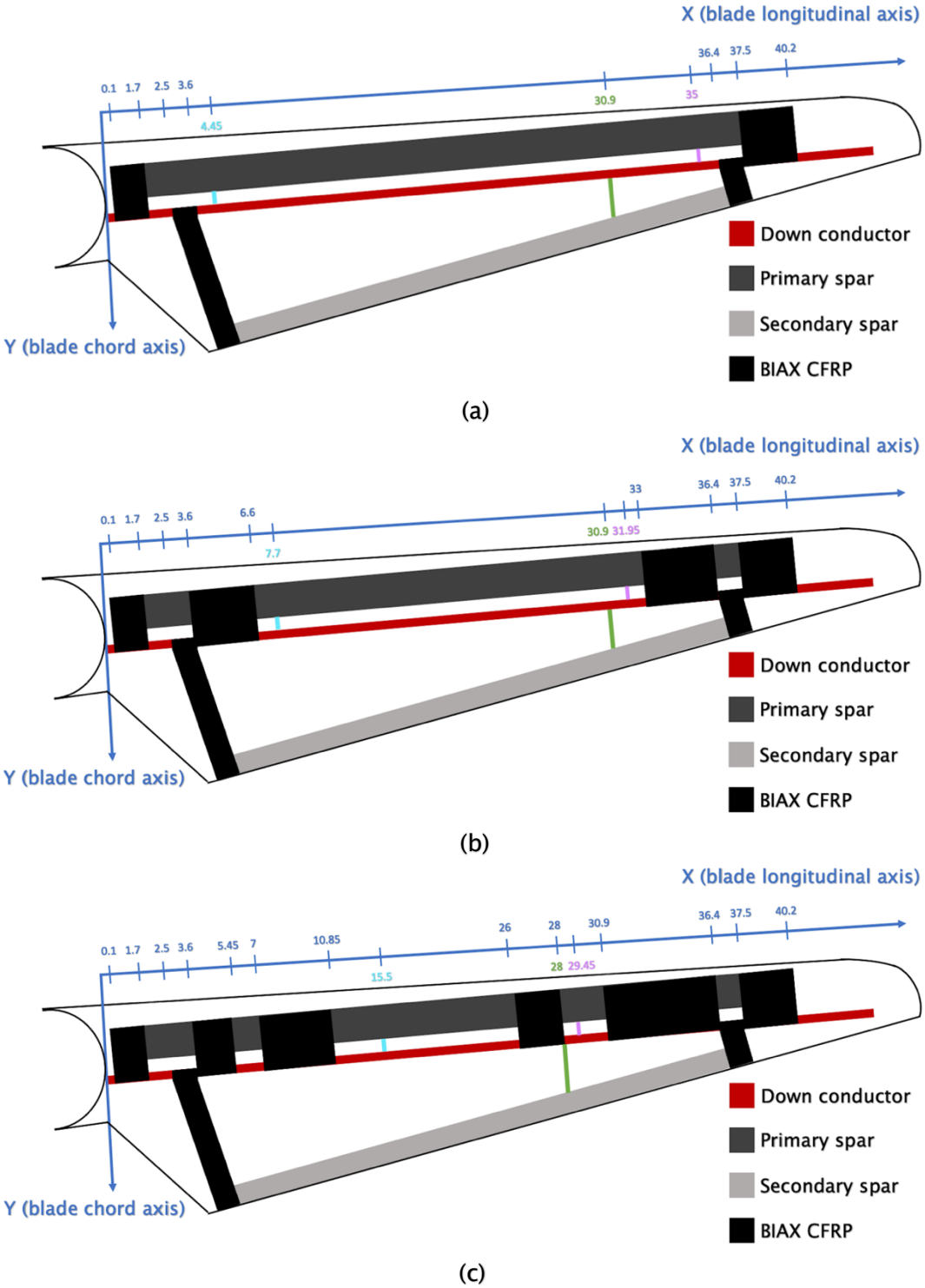

Figure 7.11 – BIAX EB configurations (not to scale): (a) configuration 1 (2 bonding patches with p.spar and 2 bonding patches with s.spar), (b) configuration 2 (4 bonding patches with p.spar and 2 bonding patches with s.spar), and (c) configuration 3 (6 bonding patches with p.spar and 2 bonding patches with s.spar). The lines and numbers in violet, light blue, and green represent the locations of $E_{y,max}$.

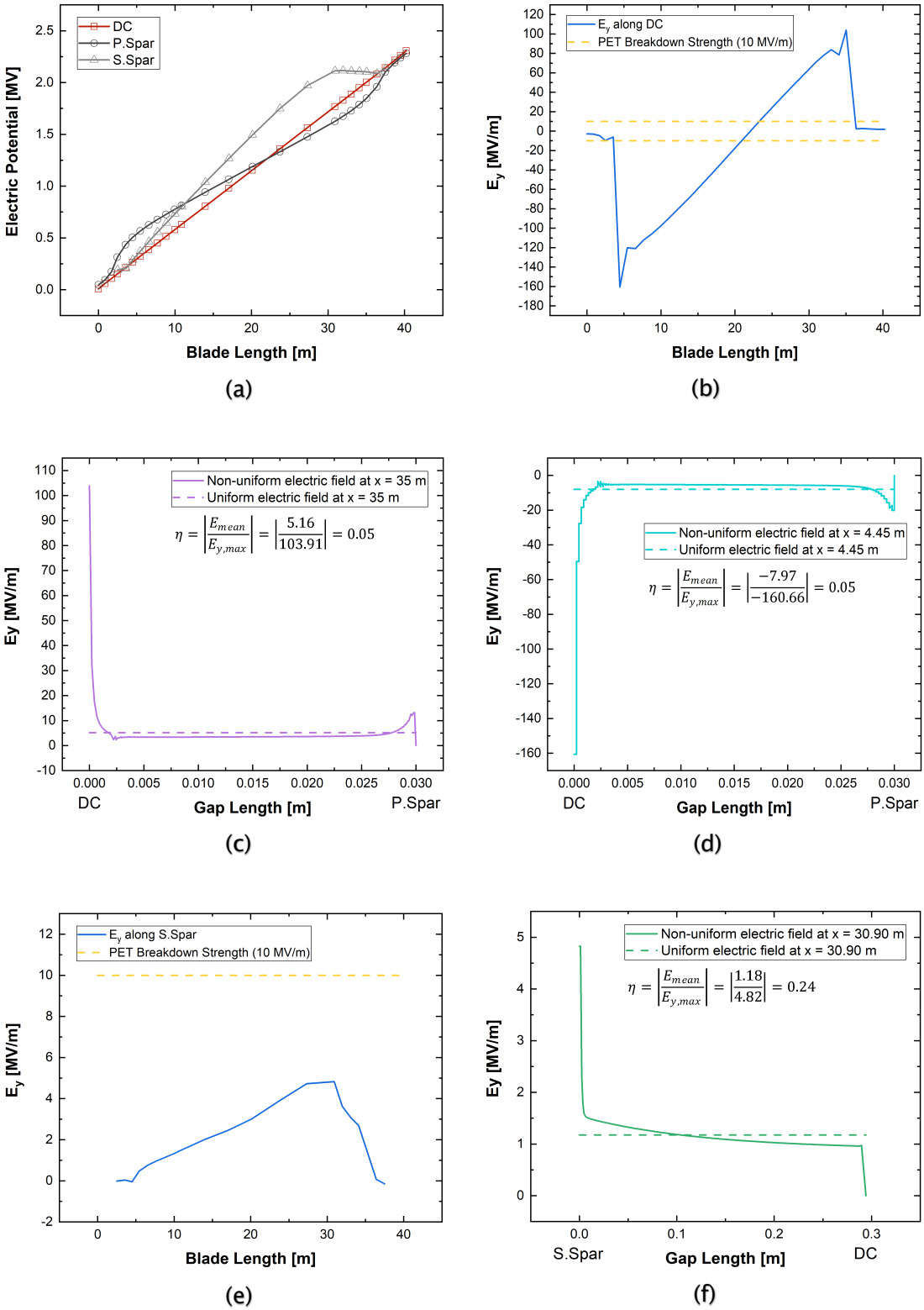

Figure 7.12 – BIAX EB configuration 1: (a) electric potential distribution along the blade, (b) E_y distribution along the DC, (c) E_y between DC and p.spar at the tip, (d) E_y between DC and p.spar at the root, (e) E_y distribution along the s.spar, and (f) E_y between DC and s.spar at the tip.

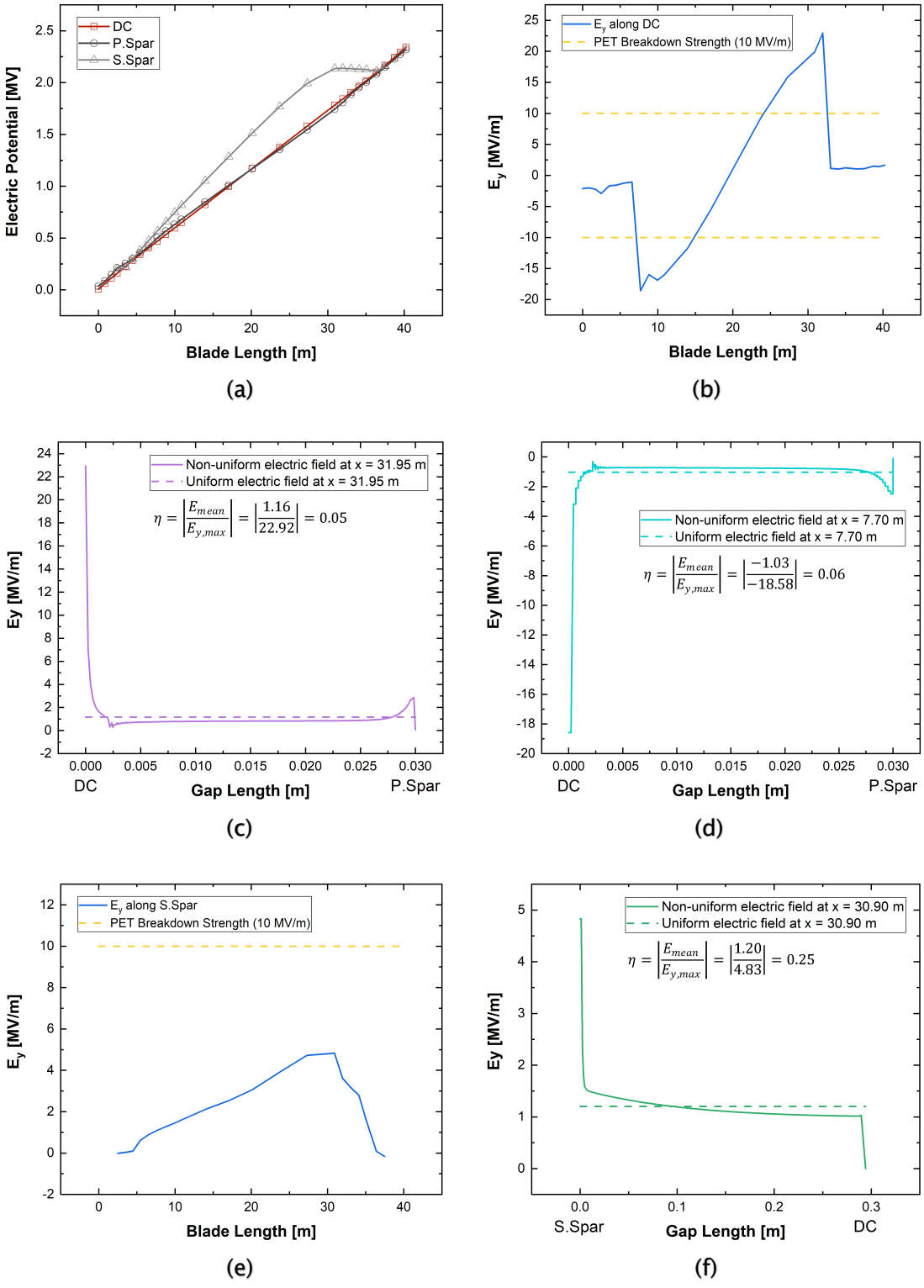

Figure 7.13 – BIAX EB configuration 2: (a) electric potential distribution along the blade, (b) E_y distribution along the DC, (c) E_y between DC and p.spar at the tip, (d) E_y between DC and p.spar at the root, (e) E_y distribution along the s.spar, and (f) E_y between DC and s.spar at the tip.

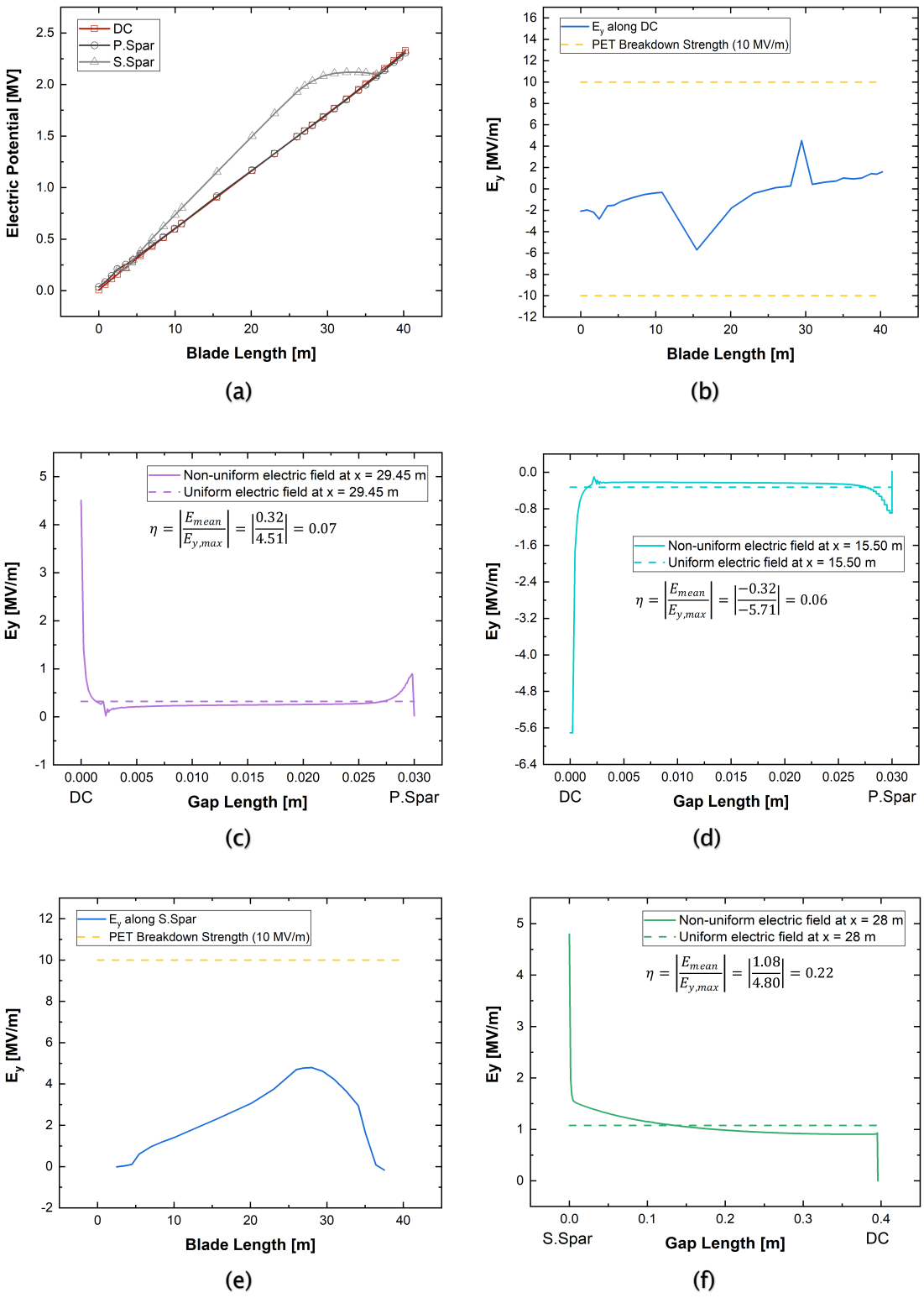

Figure 7.14 – BIAX EB configuration 3: (a) electric potential distribution along the blade, (b) E_y distribution along the DC, (c) E_y between DC and p.spar at the tip, (d) E_y between DC and p.spar at the root, (e) E_y distribution along the s.spar, and (f) E_y between DC and s.spar at the tip.

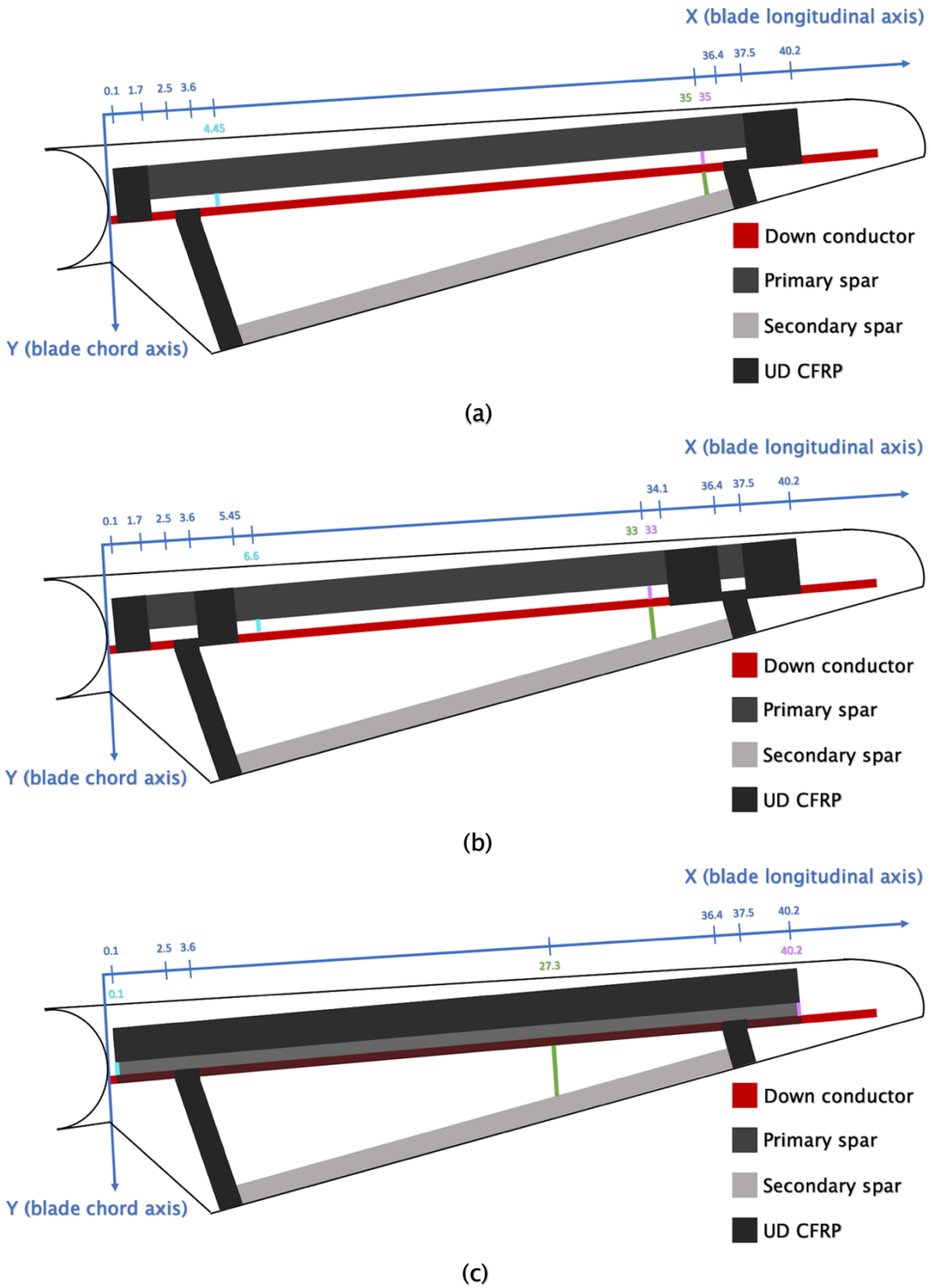

Figure 7.15 – UD EB configurations (not to scale): (a) configuration 1 (2 bonding patches with p.spar and 2 bonding patches with s.spar), (b) configuration 2 (4 bonding patches with p.spar and 2 bonding patches with s.spar), and (c) configuration 3 (continuous bonding with p.spar and 2 bonding patches with s.spar). The lines and numbers in violet, light blue, and green represent the locations of $E_{y,max}$.

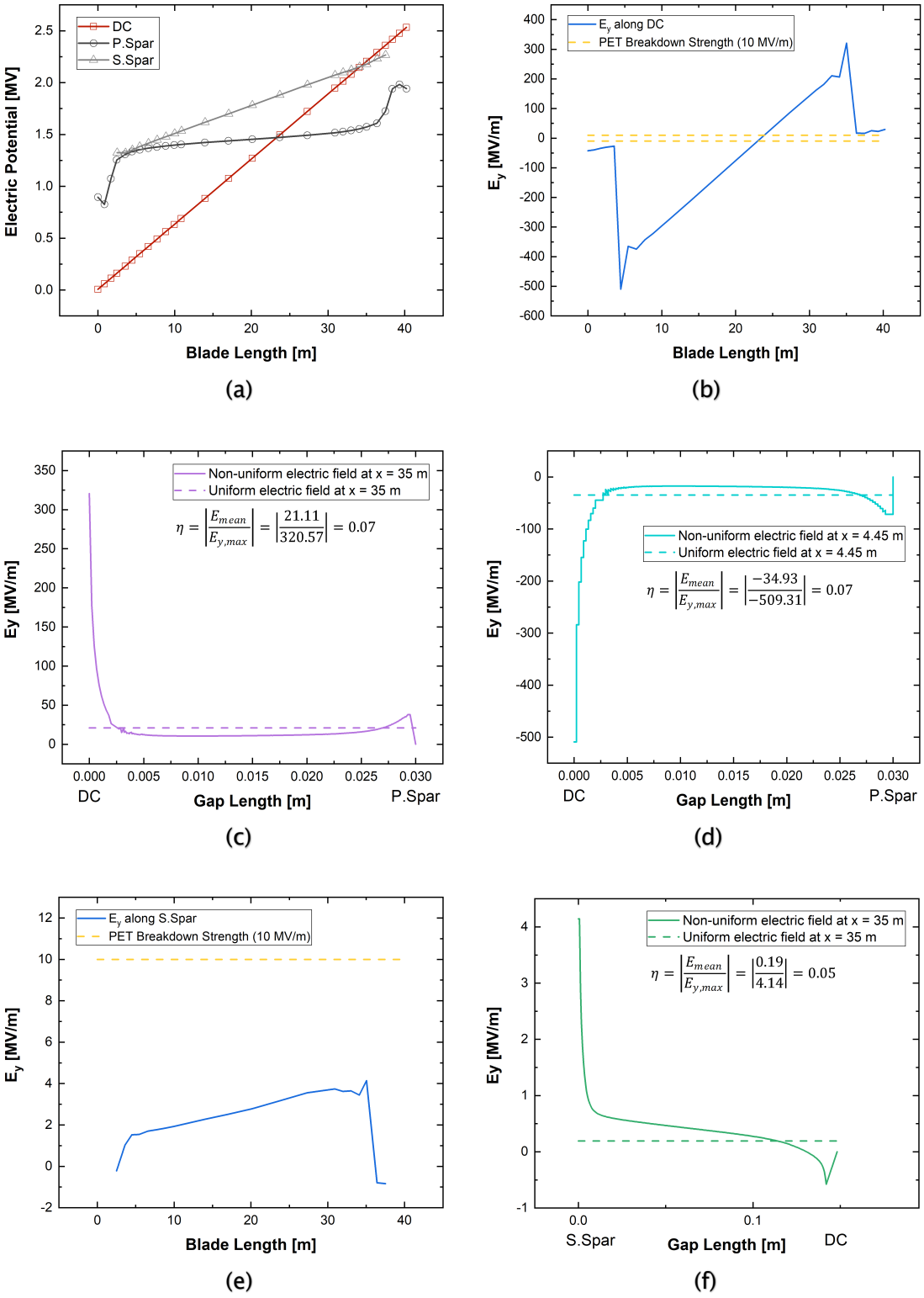

Figure 7.16 – UD EB configuration 1: (a) electric potential distribution along the blade, (b) E_y distribution along the DC, (c) E_y between DC and p.spar at the tip, (d) E_y between DC and p.spar at the root, (e) E_y distribution along the s.spar, and (f) E_y between DC and s.spar at the tip.

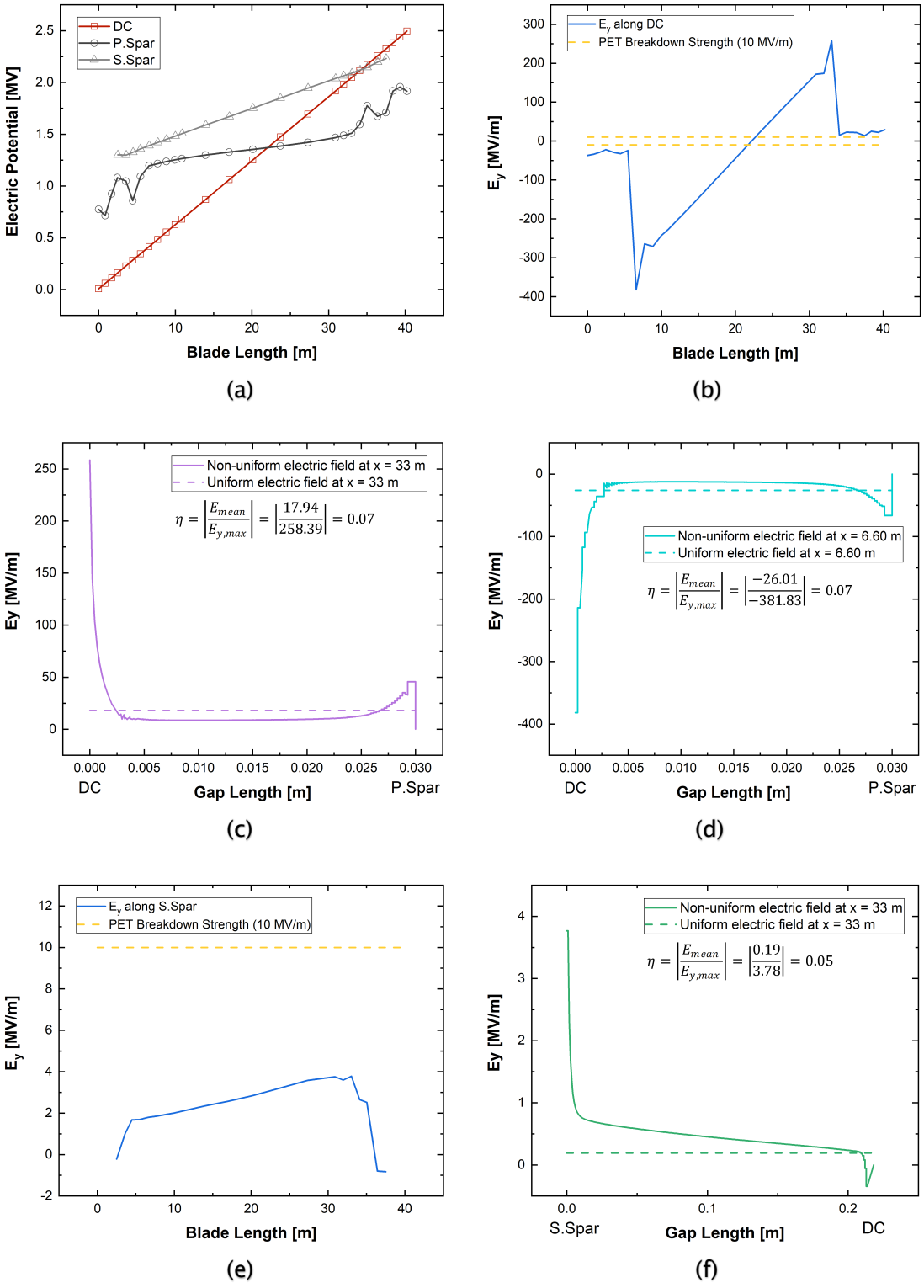

Figure 7.17 – UD EB configuration 2: (a) electric potential distribution along the blade, (b) E_y distribution along the DC, (c) E_y between DC and p.spar at the tip, (d) E_y between DC and p.spar at the root, (e) E_y distribution along the s.spar, and (f) E_y between DC and s.spar at the tip.

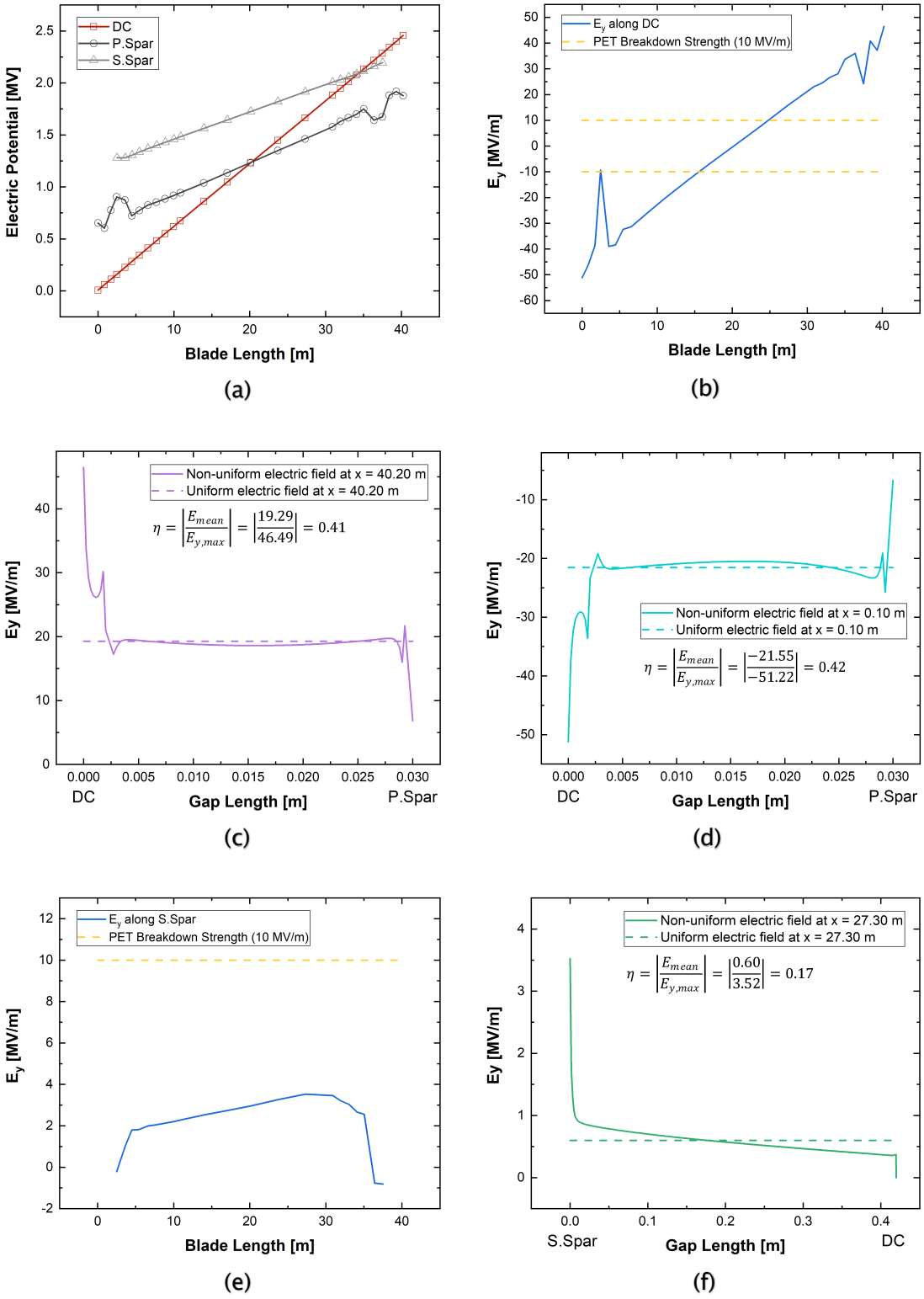

Figure 7.18 – UD EB configuration 3: (a) electric potential distribution along the blade, (b) E_y distribution along the DC, (c) E_y between DC and p.spar at the tip, (d) E_y between DC and p.spar at the root, (e) E_y distribution along the s.spar, and (f) E_y between DC and s.spar at the tip.

various lengths, three at the tip and three at the root of the blade, are required to minimise the risk of flashover. Similar to ECF case, HV breakdown of the insulation between the DC and secondary spar is prevented when employing two EB patches made of BIAX CFRP, one at the tip and one at the root of the blade.

Finally, the results in Figures 7.16 to 7.18 show that UD CFRP prevents flashovers between the DC and secondary spar thanks to the large distance between the two conductors. However, no concept can prevent flashovers between the DC and primary spar, including the continuous bonding configuration. This is due to the combined effect of the small distance between the two elements (30 mm) and the low transverse electrical conductivity of UD CFRP material, which results in large voltage drops and electric fields. In addition, the low transverse conductivity of UD CFRP does not favour a uniform transverse distribution of the lightning current. In fact, the latter tends to concentrate at the edge of the EB on the injection side rather than spreading over the entire EB and spar widths, as shown in Figure 7.19. In view of these limitations, UD CFRP is not suggested as an EB material and therefore it is not further discussed.

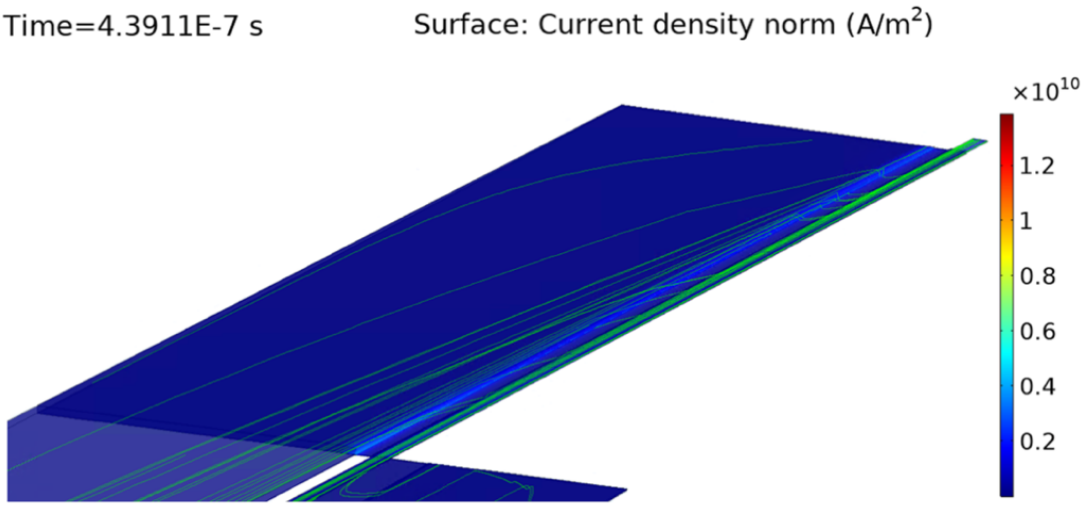

Figure 7.19 – UD EB: current density concentration at the EB edge on the injection side.

7.3.2 Electromagnetic-Thermal Problem: Current and Temperature Distributions Analysis

The results presented in Chapter 6 have shown that the most problematic interface is the DC-EB one when using BIAX CFRP as an EB material. The large values of current density (see Figure 6.8) and temperature (see Figure 6.12) in that area are caused not only by the high contact resistance, but also by the crowding effect in the DC and by the high anisotropy of BIAX CFRP. One way of improving the contact at this interface is to change the implementation of the EB layers. More precisely, by placing one layer above and one layer below the DC (see Figure 7.2), two surfaces are provided to the lightning current to leave the DC and flow towards the spars. When considering configuration 3 with such an arrangement (see Figure 7.11*c*), the peak temperature at this interface is ~1,460 °C (see Figure 7.20*a*), i.e., more than twice smaller than the one given by two EB layers on top of the DC (see Figure 6.12).

Note that this high temperature is found at the DC-EB interface on the primary spar side because more current flows through it (peak current of ~70 kA) than through the secondary spar (peak current of ~3.5 kA), as shown in Figure 7.20*b*. This is due to the low through-thickness electrical conductivity of the secondary spar CFRP/GFRP material, which provides a high impedance path (and thus less favourable) to the lightning current. Intuitively, the temperature at the DC-EB interface on the primary spar side can be further reduced if more current is diverted to the secondary spar and less to the primary spar. This can be done by extending the EB layers over the entire length of the secondary spar including the chamfer profiles, as shown in Figure 7.21*a* (note that the EB layers are not extended over the DC). This allows to inject the current through the whole secondary spar cross-section as well as a larger area is now established to transfer the current, which minimise the effect of the low through-thickness electrical conductivity. In this case the peak current within the secondary spar increases to ~24 kA, while it is reduced and delayed in

both the DC and primary spar (see Figure 7.21*b*). This concept results in a peak temperature of 1,120 ˚C at the DC-EB interface (see Figure 7.21*c*), i.e., ~23% lower than the one found in BIAX EB configuration 3.

A better solution would be obtained if the EB material was ECF. Thanks to its superior electrical and thermal properties, such as low contact resistivity and high thermal conductivity and diffusivity, ECF results in more uniform current density and temperature distributions through the EB thickness. For instance, when considering ECF EB configuration 3 with EB layers extended over the entire length of both primary and secondary spars (see Figure 7.22*a*), a

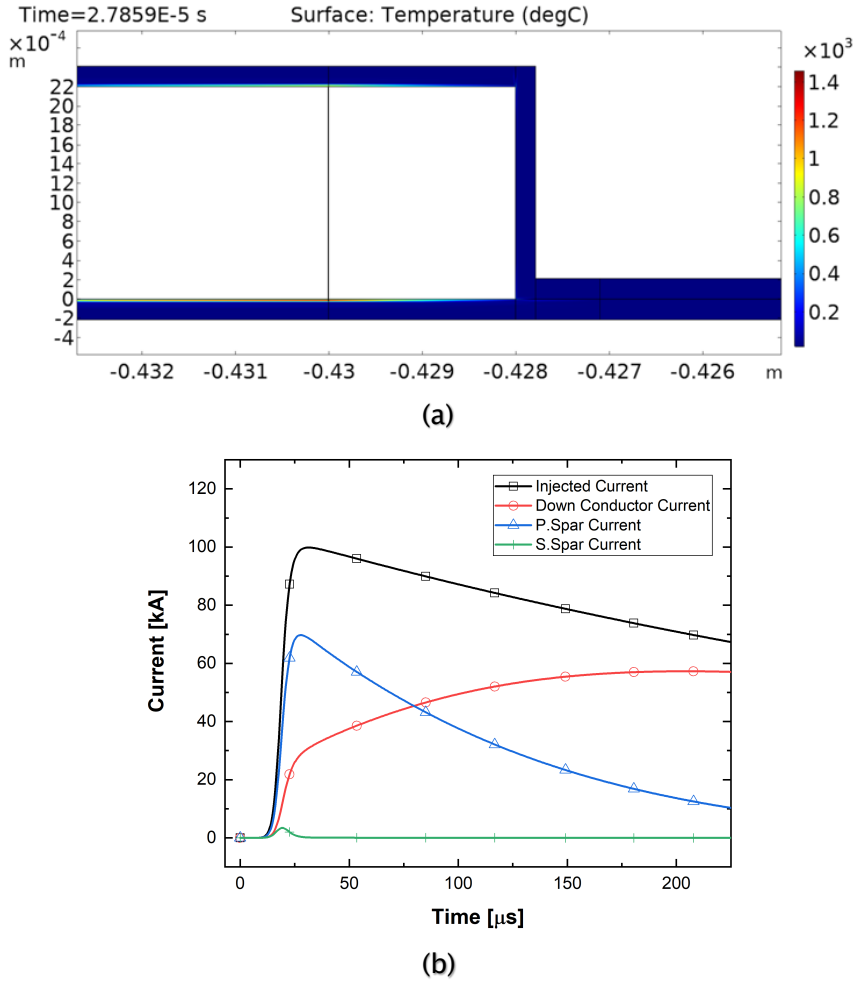

Figure 7.20 – BIAX EB configuration 3 under the first positive short stroke: (a) temperature distribution at the DC-EB interface (at x = 0.85 m and at the time instance of maximum temperature) and (b) current split among the blade conductors.

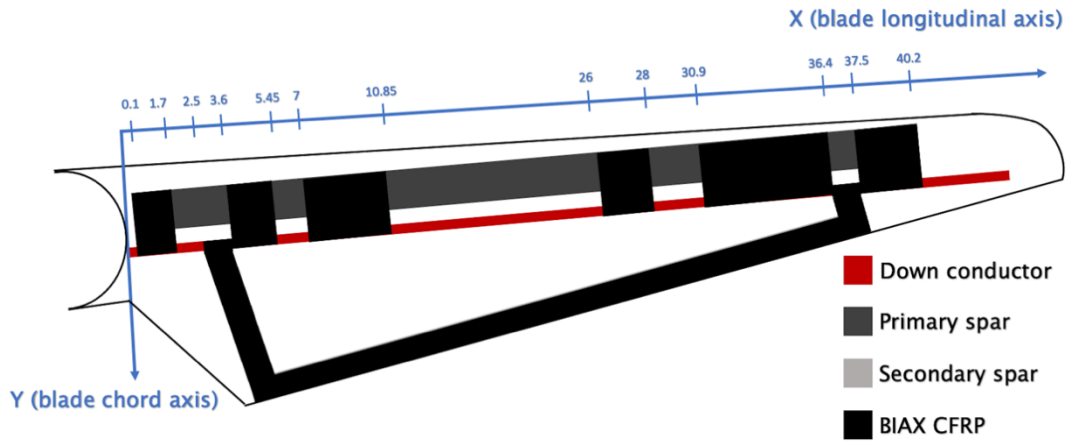

(a)

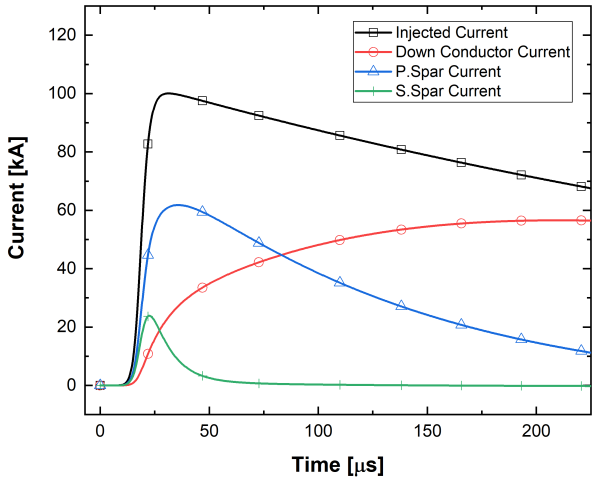

(b)

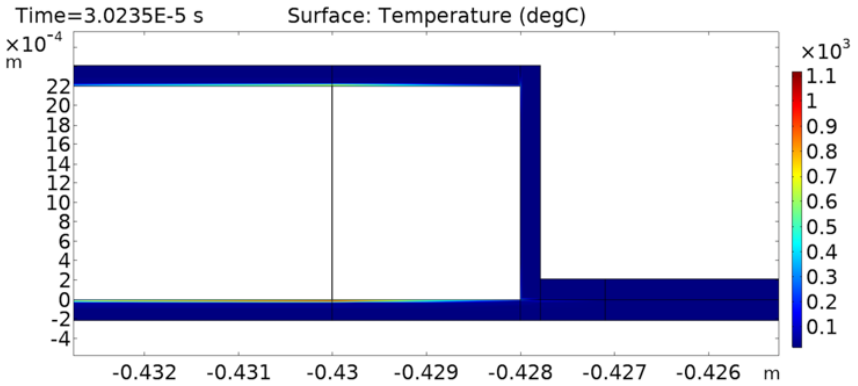

(c)

Figure 7.21 – BIAX EB configuration 3 with EB layers extended over the entire length of the secondary spar, under the first positive short stroke: (a) EB arrangement (not to scale), (b) current split among the blade conductors, and (c) temperature distribution at the DC-EB interface (at x = 0.85 m and at the time instance of maximum temperature).

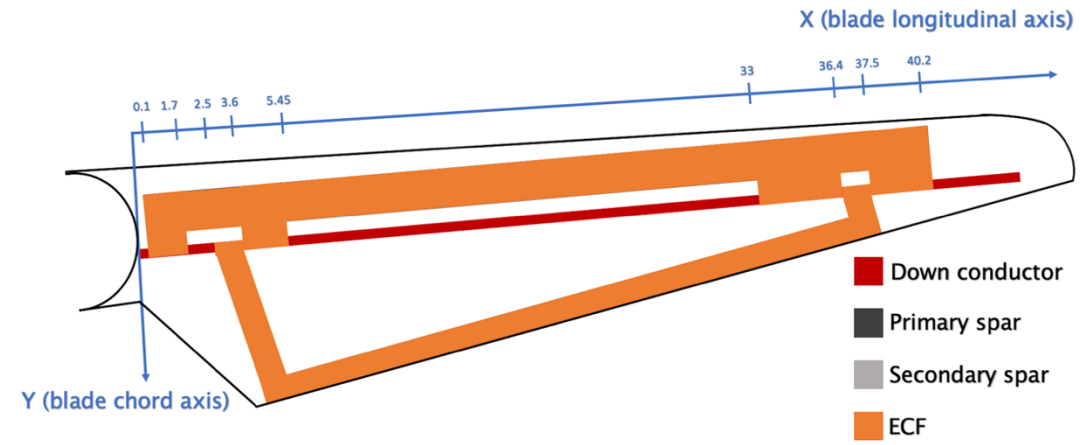

(a)

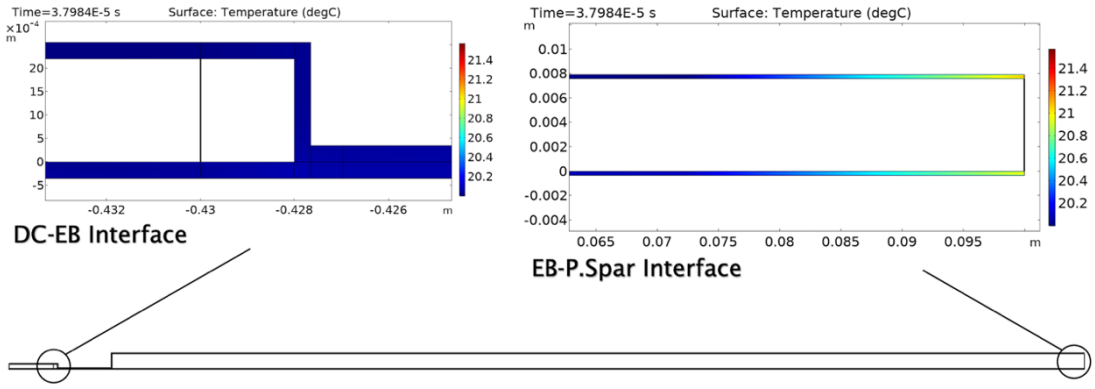

(b)

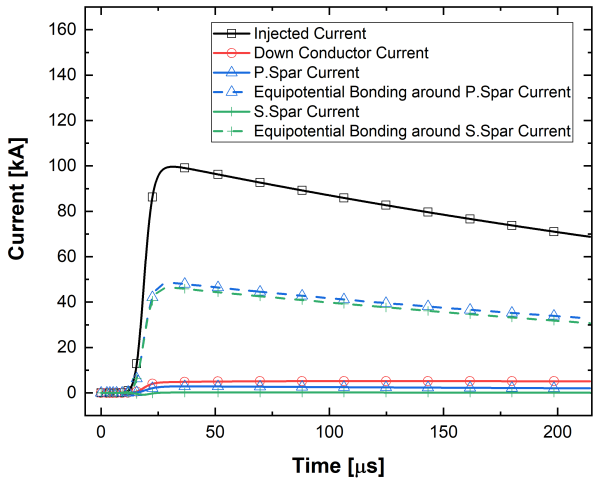

(c)

Figure 7.22 – ECF EB configuration 3 with EB layers extended over the entire length of both spars, under the first positive short stroke: (a) EB arrangement (not to scale), (b) temperature distribution at the EB interfaces (at x = 36.5 m and at the time instance of maximum temperature), and (c) current split among the blade conductors.

maximum temperature of 21.4 °C is predicted at the EB-S.Spar interface, as shown in Figure 7.22*b*. Furthermore, low current densities and temperatures are also obtained at the DC-EB interface since ECF does not present a strong anisotropy like CFRPs, i.e., the ECF through-thickness electrical and thermal conductivities are comparable to the in-plane ones. In addition, the contact resistivity at the DC-EB interface is very small (see Table A.2) since it is a metal-to-metal contact. These results, along with the superior electrical contact behaviour found in Chapter 3, indicate that ECF is the most performing EB material among those investigated in this research project.

Finally, the current split between the blade conductors given in Figure 7.22*c* shows that most of the lightning current flows through the ECF layers, while low currents are conducted through the DC and spars. This is due to the low inductance of the ECF layers, which is 2 orders of magnitude smaller than the DC and spars inductances. These results indicate that ECF layers with such an arrangement act as both transmission and EB systems, while the DC is not required as it only conducts a low share of the total lightning current. In addition, note that the two ECF layers shown in Figure 7.22*a* should also be capable of withstanding lightning long strokes (continuous currents) since their total cross-section is more than 195 mm^2. However, ECF layers used as both transmission and EB systems are not sacrificial protective meshes that can undergo damage due to direct attachments. This means that metal receptors are still needed to intercept the lightning leader and transfer the lightning current safely to the ECF layers and spars.

7.4 Summary

This chapter provided guidelines and suggestions on the implementation of EB connections to help answering the second open question of the field, i.e., how equipotential connections should be designed. To do so, the developed FEM models were employed to study the electromagnetic-thermal response of a 50 m rotor blade when equipped with different EB materials, i.e., ECF, BIAX

CFRP, and UD CFRP. In the first part of the chapter the three materials were compared based on their capability of preventing internal flashovers between the DC and spars when subjected to the subsequent short stroke current. EB connections were gradually introduced in the blade structure until the electric field was below the PET (insulating material) breakdown strength at all the blade locations. Both ECF and BIAX CFRP could reduce the electric field below the breakdown threshold thanks to their high in-plane electrical conductivities. On the other hand, UD CFRP could not reduce the potential risk of flashover because of its low transverse electrical conductivity, which resulted in large potential differences and electric fields. Thus, it was concluded that UD CFRP material is not suitable for EB applications. In addition, the results indicated that the electric field between the blade conductors is strongly non-uniform due to its magnification at sharp corners. This contradicted past studies that used lumped-element circuits simulations, which assume uniform electric field conditions when assessing the flashover risk between the blade conductors. It was seen that this assumption underestimates the electric field, leading to an incorrect design in terms of number and length of EB patches.

The second half of the chapter presented the best practises for the control and minimisation of the temperature at the EB interfaces caused by the combined effect of current crowding and contact resistance. The blade equipped with the EB concepts determined in the flashover risk analysis was subjected to the first positive short stroke current. In the case of BIAX EB configuration 3, most of the lightning current flew through the primary spar, whereas a negligible current was conducted by the hybrid secondary spar due to its small through-thickness electrical conductivity. In such conditions, high temperatures were achieved at the DC-EB interface on the primary spar side, similar to the case discussed in Chapter 6. However, compared with the latter, BIAX EB configuration 3 ensured a reduction in maximum temperature at the DC-EB interface of a factor larger than 2, thanks to a different arrangement of the EB layers. In fact, in this concept one EB layer was placed above and one

below the DC, which provided two surfaces to the lightning current to leave the DC and flow towards the primary spar. A further reduction in excess of 20% was obtained by diverting more current towards the secondary spar and less towards the primary one. This was achieved by extending the EB layers over the entire length of the secondary spar including the chamfer profiles, which allowed to inject the current through its whole cross-section, minimising the effect of the low through-thickness electrical conductivity. On the other hand, much lower temperatures were predicted when the EB material was ECF, thanks to its low contact resistivity and high thermal conductivity and diffusivity. These results, along with the superior electrical contact behaviour found in Chapter 3, indicated that ECF was the most performing EB material among those considered in this research project. Finally, most of the lightning current flew through the ECF layers when extending them over the entire length of both spars, since their inductance was 2 orders of magnitude smaller than those of DC and spars. In this configuration the ECF layers acted as both transmission and EB systems, while the DC was not needed as it only conducted a low share of the total lightning current.

Chapter 8

Conclusions and Future Work

8.1 Conclusions

This PhD project investigated the behaviour under lightning strikes of wind turbine blades equipped with EB connections. The damage experienced in EB joints due to the conduction of lightning current has not been thoroughly considered before and represents one of the major lightning protection challenges faced by rotor blade manufacturers. The work presented in this thesis made significant contributions to the field of lightning protection of wind turbine blades by a combination of experimental studies and numerical simulations.

8.1.1 Experimental Characterisation

Experimental techniques were proposed to characterise the causes and mechanisms of resin thermal degradation at the EB joint interfaces. The determined material properties were implemented in FEM models to predict areas of potential thermal damage.

An alternative approach to estimate the electrical contact behaviour of EB joints was developed. For such assemblies, the use of the standard two-probe method alone results to be unsuccessful because of the spreading effects in CFRP components and of the complicated geometrical arrangement. To

overcome these limitations and determine the contact resistance, the developed procedure combines experimental measurements with FEM simulations. Its application to typical EB materials such as UD CFRP, BIAX CFRP, and ECF showed good accuracy, with uncertainties below 10%.
The thermal degradation process of a commercial epoxy resin used in wind turbine blade manufacturing was studied to determine the degradation mechanisms responsible for voids formation and sparks in EB joints and their reaction kinetics. The results showed that the pyrolysis process was initiated at temperatures lower than expected by release of water molecules formed via a thermally activated dehydration reaction.

8.1.2 FEM Model Development

In this project the FEM was employed to predict the response of wind turbine blades under lightning strikes. The advantage of the FEM over other approaches, such as equivalent circuits using the lumped-element model, is the capability of computing spatial current density distributions in the blade cross-section. This would allow the identification of high current density and temperature areas at the EB interfaces, which might lead to thermal damage. The developed FEM models solve a weakly coupled formulation of the electromagnetic-thermal problem in the time-domain when implementing electrical contact resistivities and degradation reaction kinetics, which are crucial to predict the thermal damage in EB joints. A procedure was developed to inject the lightning current in the blade by imposing a voltage boundary condition. This was accomplished by first computing the lightning current spectrum and then calculating the blade impedance (and thus the voltage drops across the blade) for a small set of frequencies. After that, the complete voltage spectrum was obtained through interpolation of the predicted voltage-frequency mapping. Finally, the voltage spectrum was transformed back to the time-domain to determine the transient voltage waveform. The use of voltage boundary conditions improves the convergence of the solution, reducing the computational time by at least a factor of 2.

8.1.3 EB Joints – Thermal Damage and Implementation Suggestions

The developed FEM models were successfully validated against conducted current test data, which proved that they can replicate the reality and thus support the design phase of EB joints. This would significantly reduce the lightning testing cost since, once validated, the developed models can be re-employed several times during the design stage at little extra cost. High current densities and temperatures were predicted at the sparking locations observed during the test, which allowed a qualitative prediction of potential thermal degradation areas upon the solution of the Arrhenius equation. Furthermore, the predictions of high temperature and thermal degradation at the sparking locations indicated that the damage is thermally activated. That is, high temperatures cause epoxy pyrolysis, leading to voids formation, separation of the blade current carrying conductors, and inception of sparks. On the other hand, the bulk CFRP spar could withstand lightning currents without experiencing thermal damage. These results answered one of the two EB design open questions, i.e., whether CFRP spars and EB joints can withstand lightning currents without experiencing thermal damage. Finally, major differences in terms of local current density and temperature distributions were found between the FEM formulations with and without the contact resistivities at the bonding interfaces. Therefore, it is essential to implement the electrical contact in FEM models to compute accurate current densities and temperatures and design reliable EB solutions.

The developed FEM models were then employed to provide guidelines and suggestions on the implementation of EB connections to help answering the second open question of the field, i.e., how to design EB connections. To do so, it was assessed the electromagnetic-thermal performance of a 50 m wind turbine blade when equipped with different EB materials, i.e., ECF, BIAX CFRP, and UD CFRP. The three materials were compared based on their capability of preventing internal flashovers between the DC and spars when subjected to the subsequent short stroke current. The results showed that both ECF and BIAX CFRP could reduce the electric field below the breakdown threshold

thanks to their high in-plane electrical conductivities. On the other hand, UD CFRP could not reduce the potential risk of flashover because of its low transverse electrical conductivity, and it was concluded that it is not suitable for EB applications. Besides, it was shown that lumped-element circuits simulations, widely employed in previous studies, underestimate the electric field, leading to an incorrect design in terms of number and length of EB patches. In fact, this approach assesses the flashover risk between the blade conductors by defining an average electric field, which is given by the electric potential difference divided by the distance. That is, it assumes that wind turbine blades are subjected to uniform electric field conditions under lightning strikes. This was contradicted by the FEM results, which indicated that the electric field between the blade conductors is strongly non-uniform due to its magnification at sharp corners. Finally, it was shown how the FEM can be used to optimise the current conduction capability of the spars and the temperature at the EB interfaces. For instance, the temperature was reduced by a factor larger than 2 when two surfaces were provided to the lightning current to leave the DC and flow towards the spars. Further reductions could be achieved by extending the EB layers over the entire length of the spar including the chamfer profiles. This allows to inject the current through the whole spar cross-section, minimising the effect of the low through-thickness electrical conductivity of carbon fibre-based composites. Finally, low temperatures were obtained by employing a material with low contact resistivity and high thermal conductivity and diffusivity such as ECF.

8.2 Recommendations for Future Work

Based on the findings of Chapter 6, the numerical methodology presented in this PhD thesis can predict the locations of thermal damage, although a discrepancy in terms of size was identified. To improve the estimation of damage extent, it might be beneficial to study the change in contact resistivity due to the thermal degradation and sparking events occurring at high temperatures. In addition, it is suggested to investigate manufacturing routes

and/or surface preparation methods to improve the electrical contact at the EB interfaces and minimise the thermal damage.

Possible future work might also include the investigation of experimental techniques to measure temperature profiles at the EB interfaces (i.e., inside the rotor blade sample) during simulated lightning current tests. This would allow a direct correlation between test and numerical temperatures at the bonding interfaces.

Finally, the accuracy of the numerical solution might be enhanced by the development of multiscale FEM models. For instance, the identified high temperature regions might be remodelled (small-scale geometry) and the electromagnetic-thermal problem recomputed using a finer mesh. In this way a better resolution of current density and temperature distributions would be obtained thanks to the higher number of finite elements and to the low aspect ratio of the small-scale model.

Appendix A
Material Properties

The electrical properties of the blade materials considered in this thesis are listed in Tables A.1 and A.2, while the nomenclature of electrical conductivity axes is shown in Figure A.1. The anisotropic electrical conductivities of UD CFRP, BIAX CFRP, and UD CFRP/GFRP were experimentally measured according to the procedures described in [33]. The ECF electrical conductivity was considered anisotropic as done in past research [73], [105]. The relative permittivity was assumed equal to 1 for copper, CFRP, and CFRP/GFRP materials [31], [108], [144], whereas it was 4 for GFRP [66] and 1.7 for PET foam [240], [241]. On the other hand, the relative permeability was assumed equal to 1 for all the blade materials [145]–[148]. Finally, the thermal properties of the blade materials are given in Tables A.3 and A.4. The density, specific heat capacity at constant pressure, and longitudinal thermal conductivity of both CFRP and CFRP/GFRP materials were determined through the parallel rule of mixture as done in previous research [108], [112], [120], [122], [149], [150], [155]. On the other hand, their transverse and through-thickness thermal conductivities were experimentally measured according to the procedures described in [33].

Table A.1 – Electrical conductivity values of the blade materials.

Materials	σ_{11} [S/m]	σ_{22} [S/m]	σ_{33} [S/m]
UD CFRP (primary spar)	36,380	17.91	3.95
UD CFRP (primary spar - pultruded)	40,365	132.90	51.70
UD CFRP/GFRP (secondary spar)	8,120	0.19	0.01
UD CFRP (EB)	33,874	26.30	11.62
BIAX CFRP (EB)	20,702	20,702	8.34
ECF (EB) [74]	2.19×10^7	6.04×10^6	1.97×10^7
Copper (DC)	5.99×10^7	5.99×10^7	5.99×10^7

Table A.2 – Contact resistivity values at the different EB interfaces.

Materials	UD CFRP (EB)	BIAX CFRP (EB)	ECF (EB)
$\rho_{C\_DC\text{-}EB}$ [mΩ·m^2]	0.18	0.03	0.01
$\rho_{C\_EB\text{-}P.Spar}$ [mΩ·m^2]	49.01	0.68	0.20
$\rho_{C\_EB\text{-}P.Spar\_Chamfer\ c}$ [mΩ·m^2]	69.67	1.64	0.93
$\rho_{C\_EB\text{-}P.Spar\_Chamfer\ a}$ [mΩ·m^2]	70.05	1.52	0.95
$\rho_{C\_EB\text{-}P.Spar\_Chamfer\ b}$ [mΩ·m^2]	47.79	1.25	0.53
$\rho_{C\_EB\text{-}S.Spar}$ [mΩ·m^2]	196.03	2.74	0.82
$\rho_{C\_EB\text{-}S.Spar\_Chamfers\ d,\ e,\ g}$ [mΩ·m^2]	389.85	8.31	6.10
$\rho_{C\_EB\text{-}S.Spar\_Chamfer\ f}$ [mΩ·m^2]	177.24	4.47	2.09

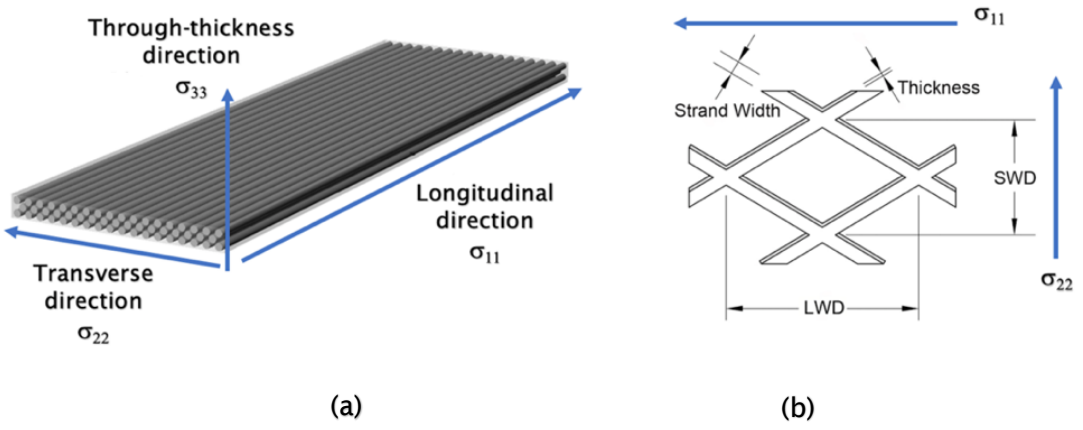

Figure A.1 – Nomenclature of electrical conductivity axes for: (a) CFRP and (b) ECF [73].

Table A.3 – Density and specific heat capacity at constant pressure values of the blade materials.

Materials	ρ[kg/m^3]	C_P [J/(Kg·K)]
UD CFRP (primary spar)	1,335	1,200
UD CFRP (primary spar - pultruded)	1,335	1,200
UD CFRP/GFRP (secondary spar)	1,535	940
UD CFRP (EB)	1,335	1,200
BIAX CFRP (EB)	1,335	1,200
ECF (EB) [74]	8,910	393
Copper (DC) [191]	8,960	385
PET foam (core material) [242], [243]	70	2,450
BIAX GFRP (shell) [152]	1,600	850

Table A.4 – Thermal conductivity values of the blade materials.

Materials	k_{11} [W/(m·K)]	k_{22} [W/(m·K)]	k_{33} [W/(m·K)]
UD CFRP (primary spar)	2.50	0.87	0.64
UD CFRP (pultruded primary spar)	2.50	0.90	0.71
UD CFRP/GFRP (secondary spar)	1.18	0.77	0.42
UD CFRP (EB)	2.50	0.87	0.64
BIAX CFRP (EB)	2.50	2.50	0.53
ECF (EB) [74]	366.94	297.06	330.20
Copper (DC) [191]	400	400	400
PET foam (core material) [243]	0.03	0.03	0.03
BIAX GFRP (shell) [244]–[248]	0.74	0.74	0.34

Appendix B
Conducted Current Test Procedures According to the IEC 61400-24:2019 Standard

Conducted current tests are aimed to evaluate the conducting performance of the LPS. For instance, these tests are performed to assess the lightning current conduction capability of the transmission and EB systems, the occurrence of HV breakdown of the insulating material, sparks at the EB interfaces, temperature rises and hotspots in the LPS conductors and insulations, current carrying capability of CFRP spars, etc. [12].

The test setup is the following [12]:

- The specimen under testing is mounted on a fixed insulating support. It can be either a full-scale blade sample or a representative sample presenting primary features such as equipotential connections between the DC and spar, fastened joints, bearings, etc.
- The specimen under testing is connected to the generator return path to ensure a closed circuit and conduct the test current away from the blade sample (see Figure B.1). The return path is typically placed at a

distance of at least 1.5 times the minimum flashover distance specified in the IEC 60060-1:2010 standard.

- Setup sensing and recording equipment, such as IR cameras to detect hotspots, equipment to measure laboratory environmental conditions, and instruments to record the test results (peak currents, waveforms, specific energies, charges, etc.).

The lightning test currents are the subsequent short stoke of negative lightning (see Section 2.6.1) to assess the occurrence of internal flashovers, and the first positive short stoke (see Section 2.6.2) to assess the Joule heating damage experienced by the LPS (e.g., at the EB interfaces). The conducted current standard test plan requires a gradual scaling of the test current parameters, i.e., peak current, specific energy, and transferred charge. In other words, the test is repeated multiple times and the current parameters are increased up to the desired level. The waveform parameters need to be supplied within the following tolerances: ±10% for the peak current; -10/+45% for the specific energy; ±20% for the transferred charge; ±20% for the front duration; and ±10% for the duration of long strokes.

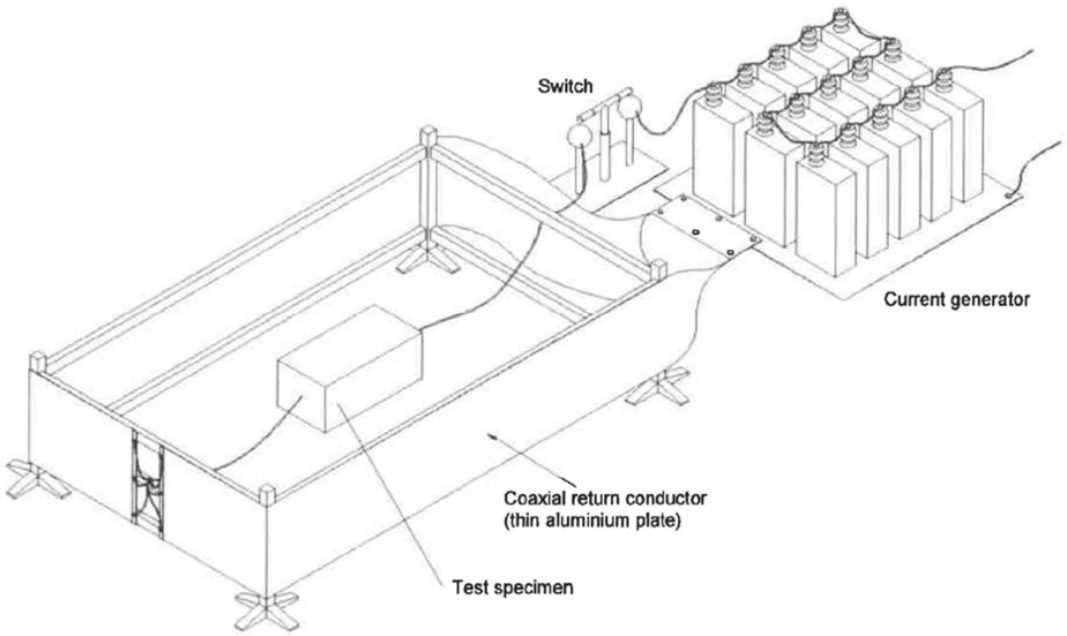

Figure B.1 – Conducted current test schematic [12].

The LPS of the assessed specimen has passed the test if the electro-mechanical functionality of the sample has been maintained intact and if the following criteria are met [12]:

- No arc develops which deteriorates the LPS and sample functionalities.
- The contact resistance of fixed metal connections (e.g., connection between the generator and air termination, connection between the DC and return path, etc.) is smaller than 1 mΩ (this value increases up to 2.5 mΩ if the connections are made of stainless steel).
- It has been proved, by inspection, measurement, and testing, that the functionality of the CFRP components has not been impacted.
- Fixed connections, such as EB joints, do not exhibit any visible crack or deformation.
- The structural integrity of the specimen under testing is not compromised by the injected test currents. It is the responsibility of the blade manufacturer to verify it, and to document that the rotor blade can remain operative until the next scheduled inspection.

According to the outlined test setup, test plan requirements, and pass-fail criteria, the conducted current test procedure is the following [12]:

- Laboratory environmental conditions are measured.
- Safety procedures are reviewed and implemented.
- Calibrate the generator and the instrumentation by implementing the test on a conductive bar having material properties similar to the specimen ones. Repeat the test until the test current parameters are within the tolerances.
- Clean the specimen under testing from contaminants which could affect the results.
- Measure the resistance of the specimen, to verify it respects the pass/fail criteria prior to the test.
- Perform the test on the specimen.
- Record the results and inspect the specimen.
- Repeat the last two points to fulfil the test plan.

List of References

[1] K. Merker, “HALIADE-X Shaping the Future,” Presented at the Wind Mission Lithuania 2020 International Conference, unpublished, 2020.

[2] B. Glushakow, “Effective Lightning Protection for Wind Turbine Generators,” *IEEE Trans. Energy Convers.*, vol. 22, no. 1, pp. 214–222, 2007.

[3] J. Clarke, A. McIlhagger, E. Archer, T. Dooher, T. Flanagan, and P. Schubel, “A Feature-Based Cost Estimation Model for Wind Turbine Blade Spar Caps,” *Appl. Syst. Innov.*, vol. 3, no. 17, pp. 1–26, 2020.

[4] Q. Li *et al.*, “The lightning striking probability for offshore wind turbine blade with salt fog contamination,” *J. Appl. Phys.*, vol. 122, no. 7, 2017.

[5] T. Naka *et al.*, “Study on Lightning Protection Methods for Wind Turbine Blades,” *IEEJ Trans. Power Energy*, vol. 125, no. 10, pp. 993–999, 2005.

[6] V. Peesapati and I. Cotton, “Lightning Protection of Wind Turbines – A Comparison Of Real Lightning Strike Data Analysis,” in *International Conference on Sustainable Power Generation and Supply*, 2009, pp. 1–8.

[7] V. Peesapati, “Lightning protection of wind turbines,” University of Manchester, PhD Thesis, 2010.

[8] M. Long, M. Becerra, and R. Thottappillil, “On the attachment of dart lightning leaders to wind turbines,” *Electr. Power Syst. Res.*, vol. 151, pp. 432–439, 2017.

[9] J.-D. Pitteloud, “Global Wind Installations,” *World Wind Energy Association*, 2019. [Online]. Available: https://library.wwindea.org/global-statistics-2018-preliminary/. [Accessed: 13-May-2020].

[10] GLPS, “Visit to GLPS Lightning laboratory Agenda day 1,” 2016.

[11] H. Braam *et al.*, “Lightning Damage of OWECS Part 3: ‘Case Studies,’” 2002.

[12] International Electrotechnical Commission, “IEC 61400 Ed. 2.0, Wind energy generation systems - Part 24: Lightning protection,” Geneva, 2019.

[13] O. T. Thomsen, “Sandwich materials for wind turbine blades - Present and future,” *J. Sandw. Struct. Mater.*, vol. 11, no. 1, pp. 7–26, 2009.

[14] P. Brøndsted and R. P. L. Nijssen, *Advances in Wind Turbine Blade Design and Materials*. Cambridge: Woodhead Publishing Limited, 2013.

[15] J. Zangenberg and P. Brøndsted, “Fatigue life in textile composites used for wind energy engineering,” *Fatigue Text. Compos.*, pp. 403–440, 2015.

[16] L. Mishnaevsky, K. Branner, H. N. Petersen, J. Beauson, M. McGugan, and B. F. Sørensen, “Materials for wind turbine blades: An overview,” *Materials (Basel).*, vol. 10, no. 11, pp. 1–24, 2017.

[17] B. Ennis *et al.*, “Optimized Carbon Fiber Composites in Wind Turbine Blade Design,” 2019.

[18] F. Rachidi *et al.*, “A Review of Current Issues in Lightning Protection of New-Generation Wind-Turbine Blades,” *IEEE Trans. Ind. Electron.*, vol. 55, no. 6, pp. 2489–2496, 2008.

[19] Y. Yasuda and S. Yokoyama, “Proposal of Lightning Damage Classification to Wind Turbine Blades,” in *7th Asia-Pacific International Conference on Lightning*, 2011, pp. 368–371.

[20] D. Djalel, G. Abdallah, and L. Hocine, “Study of the Lightning Impact on the Wind-Turbine,” *Energy Res. J.*, vol. 5, no. 1, pp. 17–25, 2014.

[21] J. Montanyà, “Lightning interaction and damages to wind turbines,” in *V Russian Conference on Lightning Protection*, 2016, pp. 1–15.

[22] A. Candela Garolera, S. F. Madsen, M. Nissim, J. Myers, and J. Holboell, “Lightning Damage to Wind Turbine Blades From Wind Farms in U.S.,” *IEEE Trans. Power Deliv.*, vol. 31, no. 3, pp. 1–1, 2016.

[23] Q. Zhou, C. Liu, X. Bian, K. L. Lo, and D. Li, “Numerical analysis of lightning attachment to wind turbine blade,” *Renew. Energy*, vol. 116, pp. 584–593, 2018.

[24] T. M. Harrell, O. T. Thomsen, J. M. Dulieu-Barton, and S. F. Madsen, “Damage in CFRP composites subjected to simulated lighting strikes - Assessment of thermal and mechanical responses,” *Compos. Part B Eng.*, vol. 176, no. March, p. 107298, 2019.

[25] S. Haigh, “Recommended Practices for Wind Turbine Testing - Lightning

Protection for Wind Turbine Installations," 1997.

[26] A. Smorgonskiy, F. Rachidi, and M. Rubinstein, "Modeling lightning current distribution in conductive elements of a wind turbine blade," in *2014 International Conference on Lightning Protection (ICLP)*, 2014, pp. 1415–1417.

[27] F. A. Fisher, "Some notes on sparks and ignition of fuels," 2000.

[28] P. G. Slade, Ed., *Electrical Contacts: Principles and Applications*, 2nd Ed. Boca Raton, USA: CRC Press, 2017.

[29] E. C. Senis, "Graphene Oxide based enhancement of electrical, thermal and mechanical properties of CFRP materials for wind turbine applications," University of Southampton, PhD Thesis, 2020.

[30] R. D. Chippendale, "Modelling of the Thermal Chemical Damage Caused to Carbon Fibre Composites," University of Southampton, PhD Thesis, 2013.

[31] R. Abid, "Electrical Characterisation of Aerospace Grade Carbon-Fibre-Reinforced Polymers," Cardiff University, PhD Thesis, 2015.

[32] E. C. Senis, O. Vryonis, I. O. Golosnoy, O. T. Thomsen, J. M. Dulieu-Barton, and S. F. Madsen, "Reducing the electrical anisotropy in unidirectional CFRP materials for wind turbine blade applications," in *International Conference on Lightning and Static Electricity*, 2017, pp. 1–5.

[33] E. C. Senis, I. O. Golosnoy, J. M. Dulieu-Barton, and O. T. Thomsen, "Enhancement of the electrical and thermal properties of unidirectional carbon fibre/epoxy laminates through the addition of graphene oxide," *J. Mater. Sci.*, vol. 54, no. 12, pp. 8955–8970, 2019.

[34] E. C. Senis, I. O. Golosnoy, T. Andritsch, J. M. Dulieu-Barton, and O. T. Thomsen, "The influence of graphene oxide filler on the electrical and thermal properties of unidirectional carbon fiber/epoxy laminates: Effect of out-of-plane alignment of the graphene oxide nanoparticles," *Polym. Compos.*, no. November 2019, pp. 1–11, 2020.

[35] S. C. Brown, C. Robert, V. Koutsos, and D. Ray, "Methods of modifying through-thickness electrical conductivity of CFRP for use in structural health monitoring, and its effect on mechanical properties – A review," *Compos. Part A Appl. Sci. Manuf.*, vol. 133, p. 105885, 2020.

[36] O. Vryonis, S. T. H. Virtanen, T. Andritsch, A. S. Vaughan, and P. L. Lewin, "Understanding the cross-linking reactions in highly oxidized graphene/epoxy nanocomposite systems," *J. Mater. Sci.*, vol. 54, no. 4, pp. 3035–3051, 2019.

[37] O. Vryonis, T. Andritsch, A. S. Vaughan, and P. L. Lewin, "Structural and chemical comparison between moderately oxygenated and edge

oxygenated graphene: mechanical, electrical and thermal performance of the epoxy nanocomposites," *SN Appl. Sci.*, vol. 1, no. 10, pp. 1–10, 2019.

[38] O. Vryonis, T. Andritsch, A. S. Vaughan, and P. L. Lewin, "An alternative synthesis route to graphene oxide: influence of surface chemistry on charge transport in epoxy-based composites," *J. Mater. Sci.*, vol. 54, no. 11, pp. 8302–8318, 2019.

[39] O. Vryonis, T. Andritsch, A. S. Vaughan, and P. L. Lewin, "Effect of surfactant molecular structure on the electrical and thermal performance of epoxy/functionalized-graphene nanocomposites," *Polym. Compos.*, no. March, pp. 1–15, 2020.

[40] A. Candela Garolera, "Lightning protection of flap system for wind turbine blades," Technical University of Denmark, PhD Thesis, 2014.

[41] S. F. Madsen and A. Candela Garolera, "Numerical tools for Lightning Protection of Wind Turbines," in *International Conference on Lightning and Static Electricity*, 2013, vol. 1, pp. 1–6.

[42] D. Romero, J. Montanyà, and J. Vinck, "Test and simulation of lightning current distribution on a wind turbine blade," in *2014 International Conference on Lightning Protection (ICLP)*, 2014, pp. 1720–1724.

[43] A. Candela Garolera, J. Holboell, and S. F. Madsen, "Lightning transient analysis in wind turbine blades," in *Proceedings of the International Conference on Power Systems Transients*, 2013, p. 8.

[44] International Electrotechnical Commission, "IEC62305, Protection against lightning Part 1: General principles," Geneva, 2010.

[45] M. Peeters, G. Santo, J. Degroote, and W. Van Paepegem, "The concept of segmented wind turbine blades: A review," *Energies*, vol. 10, no. 8, pp. 1–20, 2017.

[46] P. Norlin and R. Lewis, "The 'core' material in a blade," *PES Wind: Europe*, pp. 94–96, 2013.

[47] P. J. Schubel, "Technical cost modelling for a generic 45-m wind turbine blade producedby vacuum infusion (VI)," *Renew. Energy*, vol. 35, no. 1, pp. 183–189, 2010.

[48] J. R. Hutchinson, P. J. Schubel, and N. A. Warrior, "A cost and performance comparison of LRTM and VI for the manufacture of large scale wind turbine blades," *Renew. Energy*, vol. 36, no. 2, pp. 866–871, 2011.

[49] P. J. Schubel, "Cost modelling in polymer composite applications: Case study - Analysis of existing and automated manufacturing processes for a large wind turbine blade," *Compos. Part B Eng.*, vol. 43, no. 3, pp. 953–960, 2012.

[50] R. E. Murray, S. Jenne, D. Snowberg, D. Berry, and D. Cousins, "Techno-economic analysis of a megawatt-scale thermoplastic resin wind turbine blade," *Renew. Energy*, vol. 131, pp. 111–119, 2019.

[51] D. T. Griffith and W. Johanns, "Large Blade Manufacturing Cost Studies Using the Sandia Blade Manufacturing Cost Tool and Sandia 100-meter Blades," Albuquerque, USA, 2013.

[52] V. Peesapati, I. Cotton, T. Sorensen, T. Krogh, and N. Kokkinos, "Lightning protection of wind turbines - a comparison of measured data with required protection levels," *IET Renew. Power Gener.*, vol. 5, no. 1, pp. 48–57, 2011.

[53] Y. Wang and W. Hu, "Investigation of the Effects of Receptors on the Lightning Strike Protection of Wind Turbine Blades," *IEEE Trans. Electromagn. Compat.*, vol. 59, no. 4, pp. 1180–1187, 2017.

[54] H. C. Miller, "Surface Flashover of Insulators," *IEEE Trans. Electr. Insul.*, vol. 24, no. 5, pp. 765–786, 1989.

[55] H. C. Miller, "Study on surface flashover and gas desorption of solid insulation materials in vacuum," *IEEE Trans. Electr. Insul.*, vol. 28, no. 4, pp. 512–527, 1993.

[56] X. Li, L. Jin, J. Cai, and H. Shi, "Surface discharge detection of external insulation of outdoor vacuum circuit breaker based on ultraviolet imaging," in *International Symposium on Discharges and Electrical Insulation in Vacuum*, 2016, pp. 1–4.

[57] Y. Nakano, H. Kojima, S. Iitsuka, K. Tsuchiya, and N. Hayakawa, "Control and suppression of impulse surface flashover in vacuum based on discharge development mechanisms," *IEEE Trans. Dielectr. Electr. Insul.*, vol. 23, no. 1, pp. 35–42, 2016.

[58] A. S. Ayub, W. H. Siew, and S. J. MacGregor, "Lightning protection of wind turbine blades - An alternative approach," in *2011 7th Asia-Pacific International Conference on Lightning*, 2011, pp. 941–946.

[59] S. F. Madsen and H. Erichsen, "Improvements of numerical models to determine lightning attachment points on wind turbines," in *2008 29th International Conference on Lightning Protection (ICLP)*, 2008.

[60] S. F. Madsen and H. Erichsen, "Numerical model to determine lightning attachment point distributions on wind turbines according to the Revised IEC 61400-24," in *International Conference on Lightning and Static Electricity*, 2009.

[61] S. F. Madsen, K. Bertelsen, T. H. Krogh, H. V. Erichsen, A. N. Hansen, and K. B. Lonbaek, "Proposal of new zoning concept considering lightning protection of wind turbine blades," in *2010 30th International Conference on Lightning Protection (ICLP)*, 2010, pp. 108–117.

[62] W. Arif, Q. Li, Z. Guo, M. A. Aizaz, Y. Ma, and W. H. Siew, “Experimental study on interception failure of lightning protection system of wind turbine blade,” in *2017 13th International Conference on Emerging Technologies (ICET)*, 2017, pp. 1–6.

[63] W. Arif, Q. Li, Z. Guo, M. Ellahi, G. Wang, and W. H. Siew, “Experimental study on lightning discharge attachment to the modern wind turbine blade with lightning protection system,” in *2017 13th International Conference on Emerging Technologies (ICET)*, 2017, pp. 1–6.

[64] Y. M. Hernandez *et al.*, “A First Approach in the Modelling of Failures in Rotor Blades Caused by Lightning Strikes,” in *2010 30th Intrenational Conference on Ligtning Protection (ICLP)*, 2010, pp. 1–8.

[65] A. Muto, J. Suzuki, and T. Ueda, “Performance comparison of wind turbine blade receptor for lightning protection,” in *2010 30th International Conference on Lightning Protection (ICLP)*, 2010, pp. 1–5.

[66] S. F. Madsen, “Interaction between electrical discharges and materials for wind turbine blades – particularly related to lightning protection,” Technical University of Denmark, PhD Thesis, 2006.

[67] S. Yokoyama *et al.*, “Clarification of the mechanism of wind turbine blade damage taking lightning characteristics into consideration and relevant research project,” in *2012 International Conference on Lightning Protection (ICLP)*, 2012, pp. 1–6.

[68] S. Yokoyama, N. Honjo, Y. Yasuda, and K. Yamamoto, “Causes of wind turbine blade damages due to lightning and future research target to get better protection measures,” in *2014 International Conference on Lightning Protection (ICLP)*, 2014, pp. 823–830.

[69] K. Yamamoto, T. Chikara, and A. Ametani, “Numerical Electromagnetic Field Analysis of Transient Magnetic Fields in a Nacelle Caused by a Lightning Stroke to a Wind Turbine Generator System,” in *International Conference on Power Systems Transients*, 2009, pp. 1–6.

[70] E. Kuffel and W. S. Zaengl, *High Voltage Engineering - Fundamentals*, 2nd Ed. Oxford, UK: Butterworth-Heinemann, 2000.

[71] C. Karch and C. Metzner, “Lightning protection of carbon fibre reinforced plastics - An Overview,” in *2016 33rd International Conference on Lightning Protection (ICLP)*, 2016, pp. 1–8.

[72] S. F. Madsen and L. Carloni, “Lightning exposure of Carbon Fiber Composites in wind turbine blades,” in *24th Nordic Insulation Symposium on Materials, Components and Diagnostics*, 2015, pp. 105–110.

[73] Y. Guo, Y. Xu, Q. Wang, Q. Dong, X. Yi, and Y. Jia, “Enhanced lightning strike protection of carbon fiber composites using expanded foils with anisotropic electrical conductivity,” *Compos. Part A Appl. Sci. Manuf.*,

vol. 117, pp. 211–218, 2019.

[74] Dexmet Corporation, “Dexmet Expanding Materials,” Wallingford, USA, 2017.

[75] A. Advani, “A comparative evaluation of copper and aluminium wires and cables in building installations,” 2015.

[76] D. Chapman, “High Conductivity Copper for Electrical Engineering,” 2016.

[77] H. Kumazawa and T. Takatoya, “Biaxial strength investigation of CFRP composite laminates by using cruciform specimens,” in *17th International Conference on Composite Materials*, 2009.

[78] S. A. Michel, R. Kieselbach, and H. J. Martens, “Fatigue strength of carbon fibre composites up to the gigacycle regime (gigacycle-composites),” *Int. J. Fatigue*, vol. 28, no. 3, pp. 261–270, 2006.

[79] M. Gude, W. Hufenbach, I. Koch, R. Koschichow, K. Schulte, and J. Knoll, “Fatigue Testing of Carbon Fibre Reinforced Polymers under VHCF Loading,” *Procedia Mater. Sci.*, vol. 2, pp. 18–24, 2013.

[80] P. Alam, D. Mamalis, C. Robert, C. Floreani, and C. M. Ó Brádaigh, “The fatigue of carbon fibre reinforced plastics - A review,” *Compos. Part B Eng.*, vol. 166, pp. 555–579, 2019.

[81] R. Bond, S. Haigh, and J. Hardwick, “Comparison of experimental and modelling results for current flow in a 3D composite-metal structure,” in *International Conference on Lightning and Static Electricity*, 1999.

[82] L. F. Nunes de Souza, H. Librantz, J. Amonrim, and G. Adabo, “Analysis of Direct Effects of Lightning on Composite,” in *IX International Symposium on Lightning Protection*, 2007, no. November.

[83] B. Lepetit, I. Revel, G. Peres, L. Andrivet, and F. Flourens, “In-strike dynamical measurements of contact resistances,” in *2010 30th International Conference on Lightning Protection (ICLP)*, 2010.

[84] S. Evans, I. Revel, M. Cole, and R. Mills, “Lightning strike protection of aircraft structural joints,” in *2014 International Conference on Lightning Protection (ICLP)*, 2014, pp. 1952–1959.

[85] E. Bogatin, *Signal and Power Integrity - Simplified*. Boston, USA: Pearson Education, Inc., 2010.

[86] F. Ulaby and U. Ravaioli, *Fundamentals of Applied Electromagnetics*. Upper Saddle River, USA: Pearson Education, Inc., 2015.

[87] C. Mattiussi, “The finite volume, finite element, and finite difference methods as numerical methods for physical field problems,” in *Advances in Imaging and Electron Physics*, vol. 113, 2000, pp. 1–146.

[88] V. Mucsi *et al.*, “Lightning protection methods for wind turbine blades: An alternative approach,” *Appl. Sci.*, vol. 10, no. 6, pp. 1–18, 2020.

[89] A. Küchler, *High Voltage Engineering Fundamentals - Technology - Applications*. Berlin, Germany: Springer-Verlag, 2018.

[90] Y. Nishikori, S. Kojima, and T. Kouno, “A study of the field utilization factor and the maximum electric field at sparkover of the standard sphere gaps,” *Electr. Eng. Japan (English Transl. Denki Gakkai Ronbunshi)*, vol. 139, no. 4, pp. 26–32, 2002.

[91] M. J. Alvi, T. Izhar, A. A. Qaiser, H. S. Kharal, and A. Safdar, “Field optimization and electrostatic stress reduction of proposed conductor scheme for pliable gas-insulated transmission lines,” *Appl. Sci.*, vol. 9, no. 15, pp. 1–21, 2019.

[92] F. A. M. Rizk, “New approach for assessment of positive streamer penetration of long air gaps under impulse voltages,” *IEEE Trans. Dielectr. Electr. Insul.*, vol. 27, no. 3, pp. 791–798, 2020.

[93] Ö. Kalenderli, E. Önal, and Ö. Altay, “Computing the corona onset and the utilization factor of rod-plane electrode by using charge simulation method,” in *Proceedings: Electrical Insulation Conference and Electrical Manufacturing and Coil Winding Conference*, 2001, pp. 453–456.

[94] H. Javadi, M. Farzaneh, and A. Peyda, “Determination of electric field at inception based upon current-voltage characteristics of AC corona in rod-plane gaps,” *Iran. J. Electr. Electron. Eng.*, vol. 6, no. 2, pp. 119–128, 2010.

[95] L. G. Christophorou and D. R. James, Eds., *Gaseous Dielectrics VII*. Springer Science & Business Media, 1994.

[96] J. H. Kwon, C. W. Seo, Y. M. Kim, and K. J. Lim, “Lightning impulse breakdown characteristic of dry-air/silicone rubber hybrid insulation in rod-plane electrode,” *J. Electr. Eng. Technol.*, vol. 10, no. 3, pp. 30–36, 2015.

[97] Y. Wang and O. I. Zhupanska, “Lightning strike thermal damage model for glass fiber reinforced polymer matrix composites and its application to wind turbine blades,” *Compos. Struct.*, vol. 132, pp. 1182–1191, 2015.

[98] M. Zhang, Q. Li, H. Li, W. Yu, Z. Guo, and W. H. Siew, “Damage mechanism of wind turbine blade under the impact of lightning induced arcs,” *J. Renew. Sustain. Energy*, vol. 11, no. 5, pp. 1–12, 2019.

[99] Y. Zhao, B. Yang, and Y. Zhang, “Experimental Research and Simulation Analysis of Lightning Ablation Damage Characteristics of Megawatt Wind Turbine Blades,” *Metals (Basel).*, vol. 11, no. 1251, 2021.

[100] G. Abdelal and A. Murphy, “Nonlinear numerical modelling of lightning

strike effect on composite panels with temperature dependent material properties," *Compos. Struct.*, vol. 109, no. 1, pp. 268–278, 2014.

[101] F. S. Wang, N. Ding, Z. Q. Liu, Y. Y. Ji, and Z. F. Yue, "Ablation damage characteristic and residual strength prediction of carbon fiber/epoxy composite suffered from lightning strike," *Compos. Struct.*, vol. 117, no. 1, pp. 222–233, 2014.

[102] Q. Dong, Y. Guo, X. Sun, and Y. Jia, "Coupled electrical-thermal-pyrolytic analysis of carbon fiber/epoxy composites subjected to lightning strike," *Polymer (Guildf).*, vol. 56, pp. 385–394, 2015.

[103] O. Soykasap, S. Karakaya, and M. Colakoglu, "Simulation of lightning strike damage in carbon nanotube doped CFRP composites," *J. Reinf. Plast. Compos.*, vol. 35, no. 6, pp. 504–515, 2016.

[104] K. Fu, L. Ye, L. Chang, C. Yang, and Z. Zhang, "Modelling of lightning strike damage to CFRP composites with an advanced protection system. Part I: Thermal–electrical transition," *Compos. Struct.*, vol. 165, pp. 83–90, 2017.

[105] T. M. Dhanya and C. S. Yerramalli, "Lightning strike effect on carbon fiber reinforced composites – effect of copper mesh protection," *Mater. Today Commun.*, vol. 16, pp. 124–134, 2018.

[106] T. Hu and X. Yu, "Lightning performance of copper-mesh clad composite panels: Test and simulation," *Coatings*, vol. 9, no. 11, 2019.

[107] G. Wan, Q. Dong, J. Zhi, Y. Guo, X. Yi, and Y. Jia, "Analysis on electrical and thermal conduction of carbon fiber composites under lightning based on electrical-thermal-chemical coupling and arc heating models," *Compos. Struct.*, vol. 229, no. 17923, p. 111486, 2019.

[108] Y. Wang, "Multiphysics analysis of lightning strike damage in laminated carbon/glass fiber reinforced polymer matrix composite materials: A review of problem formulation and computational modeling," *Compos. Part A Appl. Sci. Manuf.*, vol. 101, pp. 543–553, 2017.

[109] T. L. Bergman and A. S. Lavine, *Fundamentals of Heat and Mass Transfer*, 8th Ed. New York, USA: John Wiley and Sons, 2017.

[110] J. H. Lienhard IV and J. H. Lienhard V, *A Heat Transfer Textbook*, 5th Editio. Cambridge, USA: Phlogiston Press, 2019.

[111] J. A. Rey Fernández and J. Montanya Puig, "Simulation of current distribution in a wind turbine blade using the FDTD method," *Electr. Power Syst. Res.*, vol. 185, pp. 1–7, 2020.

[112] D. D. L. Chung, *Carbon Fiber Composites*. Newton, USA: Butterworth-Heinemann, 1994.

[113] C. Kassapoglou, *Design and Analysis of Composite Structures With*

Applications to Aerospace Structures. Chichester, UK: John Wiley and Sons, 2010.

[114] E. J. Barbero, *Introduction to Composite Materials Design*, 3rd Ed. Boca Raton, USA: CRC Press, 2017.

[115] N. V. Nayak, "Composite Materials in Aerospace Applications," *Int. J. Sci. Res. Pubblications*, vol. 4, no. 9, pp. 1–10, 2014.

[116] S. W. Tsai, *Introduction to Composite Materials*. Westport, USA: Technomic Publishing Company, 1980.

[117] F. C. Campbell, *Structural Composite Materials*. Russell Township, USA: ASM International, 2010.

[118] A. J. Whittaker and R. Taylor, "Thermal transport properties of carbon-carbon fibre composites III. Mathematical modelling," *Proc. R. Soc. London - Ser. A Math. Phys. Sci.*, vol. 430, pp. 199–211, 1990.

[119] R. Rolfes and U. Hammerschmidt, "Transverse thermal conductivity of CFRP laminates: a numerical and experimental validation of approximation formulae," *Compos. Sci. Technol.*, vol. 54, no. 1, pp. 45–54, 1995.

[120] J. Koráb, P. Štefánik, Š. Kavecký, P. Šebo, and G. Korb, "Thermal conductivity of unidirectional copper matrix carbon fibre composites," *Compos. - Part A Appl. Sci. Manuf.*, vol. 33, no. 4, pp. 577–581, 2002.

[121] N. Athanasopoulos and V. Kostopoulos, "Prediction and experimental validation of the electrical conductivity of dry carbon fiber unidirectional layers," *Compos. Part B Eng.*, vol. 42, no. 6, pp. 1578–1587, 2011.

[122] B. A. Newcomb, "Processing, structure, and properties of carbon fibers," *Compos. Part A Appl. Sci. Manuf.*, vol. 91, pp. 262–282, 2016.

[123] F. Uhlig, "Contribution a l'etude des e ets directs du foudroiement sur les materi- aux structuraux constituant un aeronef (Contribution to the study of the lightning direct effects on the aircraft structural materials)," Université de Paris, PhD Thesis, 1998.

[124] A. Piche, I. Revel, and G. Peres, "Experimental and Numerical Methods to Characterize Electrical Behaviour of Carbon Fiber Composites Used in Aeronautic Industry," *Adv. Compos. Mater. - Anal. Nat. Man-Made Mater.*, 2011.

[125] L. A. Scruggs and W. J. Gajda, "Low Frequency Conductivity of Unidirectional Graphite/Epoxy Composite Samples," *Electromagn. Compat.*, vol. 19, pp. 396–402, 1977.

[126] J. Cheng, H. Ji, J. Qiu, T. Takagi, T. Uchimoto, and N. Hu, "Novel electromagnetic modeling approach of carbon fiber-reinforced polymer laminate for calculation of eddy currents and eddy current testing

signals," *J. Compos. Mater.*, vol. 49, no. 5, pp. 617–631, 2015.

[127] K. Yamamoto, "Current distribution characteristics of CFRP panels," *Electron. Commun. Japan*, vol. 96, no. 6, pp. 32–40, Jun. 2013.

[128] M. Nakagawa, Y. Baba, H. Tsubata, T. Nishi, and H. Fujisawa, "FDTD Simulation of Lightning Current in a Multilayer CFRP Panel with Triangular Prism Cells," *IEEE Trans. Electromagn. Compat.*, vol. 58, no. 1, pp. 327–330, 2016.

[129] D. D. L. Chung, *Functional Materials: Electrical, Dielectric, Electromagnetic, Optical and Magnetic Applications*. Hackensack: World Scientific, 2010.

[130] L. Chemartin, P. Lalande., and F. Tristant, "Modeling and Simulation of Sparking in Fastenning Assemblies," in *International Conference on Lightning and Static Electricity*, 2013, pp. 1–7.

[131] G. K. Reevs and H. B. Harrison, "Obtaining the Specific Contact Resistance from Transmission Line Model Measurements," *IEEE Electron Device Lett.*, vol. 3, no. 5, pp. 111–113, 1982.

[132] J. H. Klootwijk and C. E. Timmering, "Merits and limitations of circular TLM structures for contact resistance determination for novel III-V HBTs," in *IEEE International Conference on Microelectronic Test Structures*, 2004, vol. 17, pp. 247–252.

[133] L. Giraudet *et al.*, "Spin-coated conductive polymer film resistivity measurement using the TLM method," *Synth. Met.*, vol. 156, pp. 838–842, 2006.

[134] N. Stavitski, M. J. H. van Dal, A. Lauwers, C. Vrancken, A. Y. Kovalgin, and R. A. M. Wolters, "Evaluation of transmission line model structures for silicide-to-silicon specific contact resistance extraction," *IEEE Trans. Electron Devices*, vol. 55, no. 5, pp. 1170–1176, 2008.

[135] P. N. Vinod, "Specific contact resistance measurements of the screen-printed Ag thick film contacts in the silicon solar cells by three-point probe methodology and TLM method," *J. Mater. Sci. Mater. Electron.*, vol. 22, no. 9, pp. 1248–1257, 2011.

[136] E. Watanabe, A. Conwill, D. Tsuya, and Y. Koide, "Low contact resistance metals for graphene based devices," *Diam. Relat. Mater.*, vol. 24, pp. 171–174, 2012.

[137] T. Abbas and L. Slewa, "Transmission line method (TLM) measurement of (metal/ZnS) contact resistance," *Int. J. Nanoelectron. Mater.*, vol. 8, no. 2, pp. 111–120, 2015.

[138] R. Holm, *Electrical Contacts - Theory and Applications*. Berlin: Springer-Verlag, 1967.

[139] P. Zhang, Y. Y. Lau, and R. S. Timsit, “On the spreading resistance of thin-film contacts,” *IEEE Trans. Electron Devices*, vol. 59, no. 7, pp. 1936–1940, 2012.

[140] P. Lorrain, D. R. Corson, and F. Lorrain, *Electromagnetic Fields and Waves*, 3rd Ed. New York, USA: W. H. Freeman and Company, 1998.

[141] J. Zhou, Y. Li, L. Cheng, and X. Hao, “Dielectric properties of continuous fiber reinforced polymer composites: Modeling, validation, and application,” *Polym. Compos.*, vol. 39, no. 12, pp. 4646–4655, 2018.

[142] Z. Li, A. Haigh, C. Soutis, and A. Gibson, “X-band microwave characterisation and analysis of carbon fibre-reinforced polymer composites,” *Compos. Struct.*, vol. 208, no. October 2018, pp. 224–232, 2019.

[143] A. A. Eddib and D. D. L. Chung, “Electric permittivity of carbon fiber,” *Carbon N. Y.*, vol. 143, pp. 475–480, 2019.

[144] A. Todoroki, “Skin effect of alternating electric current on laminated CFRP,” *Adv. Compos. Mater.*, vol. 21, no. 5–6, pp. 477–489, 2012.

[145] C. B. Scott and D. B. Fischbach, “Diamagnetic studies on as-processed carbon fibers,” *J. Appl. Phys.*, vol. 47, no. 12, pp. 5329–5335, 1976.

[146] S. Arajs, C. A. Moyer, G. Kote, and I. L. Kalnins, “Diamagnetic susceptibility of carbon fibre reinforced epoxy resin composites,” *J. Mater. Sci.*, vol. 13, no. 9, pp. 2061–2063, 1978.

[147] A. Galehdar *et al.*, “The strong diamagnetic behaviour of unidirectional carbon fiber reinforced polymer laminates,” *J. Appl. Phys.*, vol. 112, no. 11, pp. 2–8, 2012.

[148] J. T. Tzeng and K. T. Hsieh, “Electromagnetic field effect and analysis of composite structure,” *IEEE Trans. Plasma Sci.*, vol. 43, no. 5, pp. 1536–1540, 2015.

[149] A. P. Mouritz and A. . Gibson, *Fire Properties of Polymer Composite Materials*. Dordrecht, The Netherlands: Springer, 2006.

[150] A. P. Mouritz *et al.*, “Review of fire structural modelling of polymer composites,” *Compos. Part A Appl. Sci. Manuf.*, vol. 40, no. 12, pp. 1800–1814, 2009.

[151] V. Bellenger, J. Decelle, and N. Huet, “Ageing of a carbon epoxy composite for aeronautic applications,” *Compos. Part B Eng.*, vol. 36, no. 3, pp. 189–194, 2005.

[152] G. Kalogiannakis, D. Van Hemelrijck, and G. Van Assche, “Measurements of thermal properties of carbon/epoxy and glass/epoxy using modulated temperature differential scanning calorimetry,” *J. Compos. Mater.*, vol. 38, no. 2, pp. 163–175, 2004.

[153] P. Foster, G. Abdelal, and A. Murphy, "Understanding how arc attachment behaviour influences the prediction of composite specimen thermal loading during an artificial lightning strike test," *Compos. Struct.*, vol. 192, no. March, pp. 671–683, 2018.

[154] J. Lee, T. E. Lacy Jr., C. U. Pittman Jr., and M. S. Mazzola, "Temperature-Dependent Thermal Decomposition of Carbon/Epoxy Laminates Subjected to Simulated Lightning Currents," *Polym. Compos.*, vol. 39, pp. 2185–2198, 2018.

[155] R. D. Sweeting and X. L. Liu, "Measurement of thermal conductivity for fibre-reinforced composites," *Compos. Part A Appl. Sci. Manuf.*, vol. 35, no. 7, pp. 933–938, 2004.

[156] J. B. Henderson and T. E. Wiecek, "A Mathematical Model to Predict the Thermal Response of Decomposing, Expanding Polymer Composites," *J. Compos. Mater.*, vol. 21, no. 4, pp. 373–393, 1987.

[157] T. R. Crompton, *Thermal Methods of Polymer Analysis*. Shambury, UK: Smithers Rapra Technology Ltd, 2009.

[158] M. Heydari, M. Rahman, and R. Gupta, "Kinetic study and thermal decomposition behavior of lignite coal," *Int. J. Chem. Eng.*, vol. 2015, 2015.

[159] J. D. Menczel and R. Bruce Prime, Eds., *Thermal Analysis of Polymers - Fundamentals and Applications*. Hoboken, USA: Wiley, 2009.

[160] S. L. J. Millen, A. Murphy, G. Catalanotti, and G. Abdelal, "Coupled Thermal-Mechanical Progressive Damage Model with Strain and Heating Rate Effects for Lightning Strike Damage Assessment," *Appl. Compos. Mater.*, vol. 26, no. 5–6, pp. 1437–1459, 2019.

[161] T. Ogasawara, Y. Hirano, and A. Yoshimura, "Coupled thermal-electrical analysis for carbon fiber/epoxy composites exposed to simulated lightning current," *Compos. Part A Appl. Sci. Manuf.*, vol. 41, no. 8, pp. 973–981, 2010.

[162] J. H. Lee, K. S. Kim, and H. Kim, "Determination of kinetic parameters during the thermal decomposition of epoxy/carbon fiber composite material," *Korean J. Chem. Eng.*, vol. 30, no. 4, pp. 955–962, 2013.

[163] A. Kanapitsas, C. Tsonos, H. Zois, C. G. Delides, and G. C. Psarras, "Thermal and Mechanical Characterization of Epoxy Resin Nanocomposites," *J. Adv. Phys.*, vol. 2, no. 1, pp. 1–4, 2013.

[164] Z. N. Azwa and B. F. Yousif, "Thermal degradation study of kenaf fibre/epoxy composites using thermo gravimetric analysis," in *3rd Malaysian Postgraduate Conference*, 2013, vol. 98, no. 12, pp. 256–264.

[165] H. Wang and L. Zhang, "Pyrolysis and combustion characteristics and

reaction kinetics of carbon fiber/epoxy composites," *AIP Adv.*, vol. 9, no. 12, 2019.

[166] S. V. Levchik and E. D. Weil, "Thermal decomposition, combustion and flame-retardancy of epoxy resins - A review of the recent literature," *Polym. Int.*, vol. 53, no. 12, pp. 1901–1929, 2004.

[167] S. M. Kathmann, B. J. Palmer, G. K. Schenter, and B. C. Garrett, "Activation energies and potentials of mean force for water cluster evaporation," *J. Chem. Phys.*, vol. 128, no. 6, 2008.

[168] D. P. Bishop and D. A. Smith, "The Thermal Degradation of Expoxide Resins," *Ind. Eng. Chem.*, vol. 59, no. 8, pp. 32–39, 1967.

[169] N. Rose, M. Le Bras, S. Bourbigot, and R. Delobel, "Thermal oxidative degradation of epoxy resins: evaluation of their heat resistance using invariant kinetic parameters," *Polym. Degrad. Stab.*, vol. 45, no. 3, pp. 387–397, 1994.

[170] N. Grassie, M. I. Guy, and N. H. Tennent, "Degradation of epoxy polymers: 2-Mechanism of thermal degradation of bisphenol-A diglycidyl ether," *Polym. Degrad. Stab.*, vol. 13, no. 1, pp. 11–20, 1985.

[171] V. A. Rakov and M. A. Uman, *Lightning Physics and Effects*. Cambridge: Cambridge University Press, 2003.

[172] V. A. Rakov, "The Physics of Lightning," *Surv. Geophys.*, vol. 34, no. 6, pp. 701–729, 2013.

[173] J. R. Dwyer and M. A. Uman, "The physics of lightning," *Phys. Rep.*, vol. 534, no. 4, pp. 147–241, 2014.

[174] N. Malcolm and R. K. Aggarwal, "Estimation of the failure rate of wind turbine electrical systems exposed to lightning strikes," in *IEEE Power and Energy Society General Meeting*, 2015.

[175] R. D. Goud, R. Rayudu, C. P. Moore, and D. Burmester, "Lightning protection analysis of main shaft bearings in wind turbine generators," in *International Conference on Power System Technology*, 2016, pp. 1–6.

[176] F. Heidler, J. M. Cvetić, and B. V. Stanić, "Calculation of lightning current parameters," *IEEE Trans. Power Deliv.*, vol. 14, no. 2, pp. 399–404, 1999.

[177] F. Heidler and J. Cvetić, "A class of analytical functions to study the lightning effects associated with the current front," *Eur. Trans. Electr. Power*, vol. 12, no. 2, pp. 141–150, 2002.

[178] D. Djalel, H. Ali, and C. Fayçal, "The return-stroke of lightning current, source of electromagnetic fields (study, analysis and modelling)," *Am. J. Appl. Sci.*, vol. 4, no. 1, pp. 42–48, 2007.

[179] Mueller Brass Co., “Alloy C11000 Electrolytic Tough Pitch Copper,” 2018.

[180] RS Components, “RS Pro Bottle of Silver Conductive Adhesive Paint (Stock No: 186-3600),” 2018.

[181] I. El Sawi, P. A. Olivier, P. Demont, and H. Bougherara, “Processing and electrical characterization of a unidirectional CFRP composite filled with double walled carbon nanotubes,” *Compos. Sci. Technol.*, vol. 73, no. 1, pp. 19–26, 2012.

[182] H. Yu, “Modelling and characterisation of electrical resistivity of carbon composite laminates,” University of Delaware, PhD Thesis, 2018.

[183] J. B. Khan, A. C. Smith, P. M. Tuohy, M. Gresil, C. Soutis, and A. Lambourne, “Experimental electrical characterisation of carbon fibre composites for use in future aircraft applications,” *IET Sci. Meas. Technol.*, vol. 13, no. 8, pp. 1131–1138, 2019.

[184] S. Wang and D. D. L. Chung, “Electrical behavior of carbon fiber polymer-matrix composites in the through-thickness direction,” *J. Mater. Sci.*, vol. 35, no. 1, pp. 91–100, 2000.

[185] S. Wang, D. P. Kowalik, and D. D. L. Chung, “Self-sensing attained in carbon-fiber-polymer-matrix structural composites by using the interlaminar interface as a sensor,” *Smart Mater. Struct.*, vol. 13, no. 3, pp. 570–592, 2004.

[186] Q. Zhao *et al.*, “Review on the electrical resistance/conductivity of carbon fiber reinforced polymer,” *Appl. Sci.*, vol. 9, no. 11, 2019.

[187] G. Norberg, S. Dejanovic, and H. Hesselbom, “Contact resistance of thin metal film contacts,” *IEEE Trans. Components Packag. Technol.*, vol. 29, no. 2, pp. 371–378, 2006.

[188] S. Karmalkar, P. V. Mohan, H. P. Nair, and R. Yeluri, “Compact models of spreading resistances for electrical/thermal design of devices and ICs,” *IEEE Trans. Electron Devices*, vol. 54, no. 7, pp. 1734–1743, 2007.

[189] W. Ren, Y. Chen, Z. Wang, S. Xue, and X. Zhang, “Electrical Contact Resistance of Coated Spherical Contacts,” *IEEE Trans. Electron Devices*, vol. 63, no. 11, pp. 4373–4379, 2016.

[190] Comsol 5.6, “AC / DC Module User ’s Guide,” 2020.

[191] Comsol 5.6, “Comsol Multiphysics Reference Manual,” 2020.

[192] H. H. Berger, “Contact Resistance and Contact Resistivity,” *J. Electrochem. Soc.*, vol. 119, no. 4, pp. 507–514, 1972.

[193] R. Hahn and M. E. Johansson, “New contact design for the ex situ fabrication of small size, low resistivity normal metal contacts to

epitaxial c-axis YBCO films," *IEEE Trans. Components Packag. Manuf. Technol. Part A*, vol. 19, no. 1, pp. 105–112, 1996.

[194] D. K. Schroder, *Semiconductor Material and device*, 3rd Ed. Hoboken: John Wiley and Sons, 2006.

[195] S. Sze and K. K. Ng, *Physics of Semiconductor Devices*, 3rd Ed. John Wiley and Sons, 2007.

[196] N. Stavitski, "Silicide-to-silicon specific contact resistance characterization - test structures and models," University of Twente, PhD Thesis, 2009.

[197] B. J. Lwo, C. L. Teng, K. F. Tseng, T. Ni, and S. Lu, "Contact Resistance of Microbumps in a Typical Through-Silicon-Via Structure," *IEEE Trans. Components, Packag. Manuf. Technol.*, vol. 7, no. 1, pp. 27–32, 2017.

[198] Aim TTi, "BS407 wide range precision micro-ohmeter," 2018.

[199] H. Kawakami and P. Feraboli, "Lightning strike damage resistance and tolerance of scarf-repaired mesh-protected carbon fiber composites," *Compos. Part A Appl. Sci. Manuf.*, vol. 42, no. 9, pp. 1247–1262, 2011.

[200] M. Gagné and D. Therriault, "Lightning strike protection of composites," *Prog. Aerosp. Sci.*, vol. 64, pp. 1–16, 2014.

[201] K. Schulte and C. Baron, "Load and failure analyses of CFRP laminates by means of electrical resistivity measurements," *Compos. Sci. Technol.*, vol. 36, no. 1, pp. 63–76, 1989.

[202] A. Todoroki, M. Tanaka, and Y. Shimamura, "Measurement of orthotropic electric conductance of CFRP laminates and analysis of the effect on delamination monitoring with an electric resistance change method," *Compos. Sci. Technol.*, vol. 62, no. 5, pp. 619–628, 2002.

[203] Perkin Elmer Incorporated, "Pyris 1 TGA Thermogravimetric Analyzer," 2013.

[204] A. P. Snyder, A. Tripathi, J. P. Dworzanski, W. M. Maswadeh, and C. H. Wick, "Characterization of microorganisms by thermogravimetric analysis-mass spectrometry," *Anal. Chim. Acta*, vol. 536, no. 1–2, pp. 283–293, 2005.

[205] N. Bityurin, B. S. Luk'yanchuk, M. H. Hong, and T. C. Chong, "Models for laser ablation of polymers," *Chem. Rev.*, vol. 103, no. 2, pp. 519–552, 2003.

[206] Y. Ou, J. Wu, Y. Zhang, and J. Li, "Modeling the laser-polymer interaction of laser propulsion systems considering progressive surface removal, thermal decomposition and non-Fourier effect," *Acta Astronaut.*, vol. 186, no. May, pp. 319–328, 2021.

[207] Y. Hu, Z. Wang, X. Cheng, and C. Ma, “Non-isothermal TGA study on the combustion reaction kinetics and mechanism of low-rank coal char,” *RSC Adv.*, vol. 8, no. 41, pp. 22909–22916, 2018.

[208] H. E. Kissinger, “Reaction Kinetics in Differential Thermal Analysis,” *Anal. Chem.*, vol. 29, no. 11, pp. 1702–1706, 1957.

[209] A. Chairat *et al.*, “Thermal degradation kinetics of a commercial epoxy resin - Comparative analysis of parameter estimation methods,” *J. Appl. Polym. Sci.*, vol. 132, no. 27, pp. 6–9, 2015.

[210] C. L. Chiang, F. Y. Wang, C. C. M. Ma, and H. R. Chang, “Flame retardance and thermal degradation of new epoxy containing silicon and phosphorous hybrid ceramers prepared by the sol-gel method,” *Polym. Degrad. Stab.*, vol. 77, no. 2, pp. 273–278, 2002.

[211] P. Thomas, A. Ashokbabu, and R. Vaish, “Structural, thermal and dielectric properties and thermal degradation kinetics of nylon 11/CaCu3Ti4O12 (CCTO) nanocomposites,” *J. Therm. Anal. Calorim.*, vol. 141, no. 3, pp. 1123–1135, 2020.

[212] ASTM International, “ASTM E2550-17 Standard Test Method for Thermal Stability by Thermogravimetry,” 2017.

[213] C. P. Fredlake, J. M. Crosthwaite, D. G. Hert, S. N. V. K. Aki, and J. F. Brennecke, “Thermophysical properties of imidazolium-based ionic liquids,” *J. Chem. Eng. Data*, vol. 49, no. 4, pp. 954–964, 2004.

[214] D. M. Blake, L. Moens, D. Rudnicki, and H. Pilath, “Lifetime of imidazolium salts at elevated temperatures,” *J. Sol. Energy Eng. Trans. ASME*, vol. 128, no. 1, pp. 54–57, 2006.

[215] L. Chancelier *et al.*, “Targeting adequate thermal stability and fire safety in selecting ionic liquid-based electrolytes for energy storage,” *Phys. Chem. Chem. Phys.*, vol. 16, no. 5, pp. 1967–1976, 2014.

[216] R. Z. Alshali, N. A. Salim, J. D. Satterthwaite, and N. Silikas, “Post-irradiation hardness development, chemical softening, and thermal stability of bulk-fill and conventional resin-composites,” *J. Dent.*, vol. 43, no. 2, pp. 209–218, 2015.

[217] P. Y. Kuo, L. De Assis Barros, Y. C. Sheen, M. Sain, J. S. Y. Tjong, and N. Yan, “Thermal degradation of extractive-based bio-epoxy monomer and network: Kinetics and mechanism,” *J. Anal. Appl. Pyrolysis*, vol. 117, pp. 199–213, 2016.

[218] M. B. McKinnon, Y. Ding, S. I. Stoliarov, S. Crowley, and R. E. Lyon, “Pyrolysis model for a carbon fiber/epoxy structural aerospace composite,” *J. Fire Sci.*, vol. 35, no. 1, pp. 36–61, 2017.

[219] L. Chemartin *et al.*, “Direct Effects of Lightning on Aircraft Structure : Analysis of the Thermal , Electrical and Mechanical Constraints,” *J.*

Aerosp. Lab, vol. 9, no. 5, pp. 1–15, 2012.

[220] P. Aguilera, C. Lair, F. Issac, B. Michielsen, M. Hélier, and M. Darces, "Indirect effects of lightning on aircraft engine," in *International Conference on Lightning & Static Electricity*, 2015.

[221] B. De Vivo, P. Lamberti, G. Spinelli, and V. Tucci, "Evaluation of the Lightning Strikes on Carbon Fibers Panels for Aircraft Structural Parts," in *Proceedings of Comsol Conference*, 2015.

[222] Comsol 5.6, "Heat Transfer Module," 2020.

[223] B. R. Terespolsky and K. J. Nixon, "Developing an approximation to the Heidler function - With an analytical transformation into the frequency domain," in *2014 International Conference on Lightning Protection (ICLP)*, 2014, pp. 1326–1330.

[224] E. Brigham, *The Fast Fourier Transform and its Applications*. Englewood Cliffs: Prentice-Hall Inc., 1998.

[225] S. J. Orfanidis, *Introduction: Social signal processing*. Englewood Cliffs: Prentice-Hall, Inc., 2010.

[226] P. Kosky, R. Balmer, W. Keat, and G. Wise, "Mechanical Engineering," in *Exploring Engineering: An Introduction to Engineering and Design*, 5th Ed., London, UK: Elsevier, 2021, pp. 317–340.

[227] A. Adibekyan, E. Kononogova, C. Monte, and J. Hollandt, "Review of PTB Measurements on Emissivity, Reflectivity and Transmissivity of Semitransparent Fiber-Reinforced Plastic Composites," *Int. J. Thermophys.*, vol. 40, no. 4, pp. 1–14, 2019.

[228] J. Chen, X. Bi, J. Liu, and Z. Fu, "Damage investigation of carbon-fiber-reinforced plastic laminates with fasteners subjected to lightning current components c and d," *Appl. Sci.*, vol. 10, no. 6, 2020.

[229] Y. Wang, "Modeling of lightning-induced thermal ablation damage in anisotropic composite materials and its application to wind turbine blades," University of Iowa, PhD Thesis, 2016.

[230] C. D. Hodgman, *Handbook of chemistry and physics*. Cleveland, USA: Chemical Rubber Publishing Company, 1954.

[231] P. Zhou, *Numerical Analysis of Electromagnetic Fields*. Berlin, Germany: Springer-Verlag, 1993.

[232] N. Gasmi, S. Bouissou, and F. Piriou, "Comparison of Potential Dual Formulations Developed with Different Elements," A. Nicolet and R. Belmans, Eds. Boston, USA: Springer, 1995.

[233] G. Meunier, Ed., *The Finite Element Method for Electromagnetic Modeling*. Hoboken, USA: Wiley, 2008.

[234] H. B. Dwight, “Skin effect in tubular and flat conductors,” *Trans. Am. Inst. Electr. Eng.*, vol. 37, pp. 1379–1403, 1918.

[235] T. Ishikawa, T. Nagao, A. Kobayashi, M. Shimizu, A. Hattori, and H. Kawano, “Reduction of thermal stress induced in a steel plate strengthened by bonded aluminum-CFRP composite,” *Adv. Struct. Eng.*, vol. 17, no. 12, pp. 1771–1783, 2014.

[236] T. Wu, S. R. Tinkloh, T. Tröster, W. Zinn, and T. Niendorf, “Determination and Validation of Residual Stresses in CFRP/Metal Hybrid Components Using the Incremental Hole Drilling Method,” *J. Compos. Sci.*, vol. 4, no. 3, p. 143, 2020.

[237] E. Rosa, “The self and mutual inductances of linear conductors,” *Bull. Bur. Stand.*, no. Vol. 4 No. 2, pp. 301–344, 1908.

[238] F. Fisher, J. Plumer, and R. Perala, *Lightning protection of aircraft*. Pittsfield, USA: Lightning Technologies, Inc., 2004.

[239] M. J. Schauber, S. A. Newman, L. R. Goodman, I. S. Suzuki, and M. Suzuki, “Measurement of mutual inductance from the frequency dependence of impedance of AC coupled circuits using a digital dual-phase lock-in amplifier,” *Am. J. Phys.*, vol. 76, no. 2, pp. 129–132, 2008.

[240] J. Yan *et al.*, “A comparative study on damage mechanism of sandwich structures with different core materials under lightning strikes,” *Energies*, vol. 10, no. 10, 2017.

[241] J. Yan *et al.*, “Electrical and thermal performance of different core materials applied in wind turbine blades under lightning strikes,” *Wind Energy*, vol. 22, no. 11, pp. 1603–1621, 2019.

[242] O. Almanza, M. A. Rodríguez-Pérez, and J. A. de Saja, “Measurement of the thermal diffusivity and specific heat capacity of polyethylene foams using the transient plane source technique,” *Polym. Int.*, vol. 53, no. 12, pp. 2038–2044, 2004.

[243] Armacell, “ArmaForm ® Core GR,” 2020.

[244] M. B. Kasen, “Mechanical and thermal properties of filamentary-reinforced structural composites at cryogenic temperatures 1: Glass-reinforced composites,” *Cryogenics (Guildf).*, vol. 15, no. 6, pp. 327–349, 1975.

[245] G. Hartwig and S. Knaak, “Fibre-epoxy composites at low temperatures,” *Cryogenics (Guildf).*, vol. 24, no. 11, pp. 639–647, 1984.

[246] S. D. McIvor *et al.*, “Thermal conductivity measurements of some glass fibre- and carbon fibre-reinforced plastics,” *J. Mater. Sci.*, vol. 25, no. 7, pp. 3127–3132, 1990.

[247] M. Suchitra and N. M. Renukappa, “The Thermal Properties of Glass

Fiber Reinforced Epoxy Composites with and without Fillers," *Macromol. Symp.*, vol. 361, no. 1, pp. 117–122, 2016.

[248] H. Mahmood, S. Unterberger, and A. Pegoretti, "Tuning Electrical and Thermal Properties in Epoxy/Glass Composites by Graphene-Based Interphase," *J. Compos. Sci.*, vol. 1, no. 2, p. 12, 2017.